

**The solar wind's geomagnetic impact and its  
Sun–Earth evolution**

–

**Predictive models for space weather  
and the Parker Solar Probe orbit**

Dissertation

to acquire the doctoral degree in mathematics and natural science

“Doctor rerum naturalium”

at the Georg-August-Universität Göttingen

within the doctoral program ProPhys

of the Georg-August University School of Science (GAUSS)

Submitted by

*Malte S. Venzmer*

from Bremerhaven, Germany

Göttingen, 2018

---

Thesis committee

**Dr. Volker Bothmer**

Institute for Astrophysics, Georg-August-Universität Göttingen

**Prof. Dr. Ansgar Reiners**

Institute for Astrophysics, Georg-August-Universität Göttingen

Members of the examination board

Referee:

**Dr. Volker Bothmer**

Institute for Astrophysics, Georg-August-Universität Göttingen

Second referee:

**Prof. Dr. Ansgar Reiners**

Institute for Astrophysics, Georg-August-Universität Göttingen

Further members of the examination board:

**Prof. Dr. Stefan Dreizler**

Institute for Astrophysics, Georg-August-Universität Göttingen

**Prof. Dr. Wolfram Kollatschny**

Institute for Astrophysics, Georg-August-Universität Göttingen

**Prof. Dr. Hardi Peter**

Department Sun and Heliosphere, Max Planck Institute for Solar System Research

**Prof. Dr. Andreas Tilgner**

Institute for Geophysics, Georg-August-Universität Göttingen

Date of the oral examination: \_\_\_\_\_

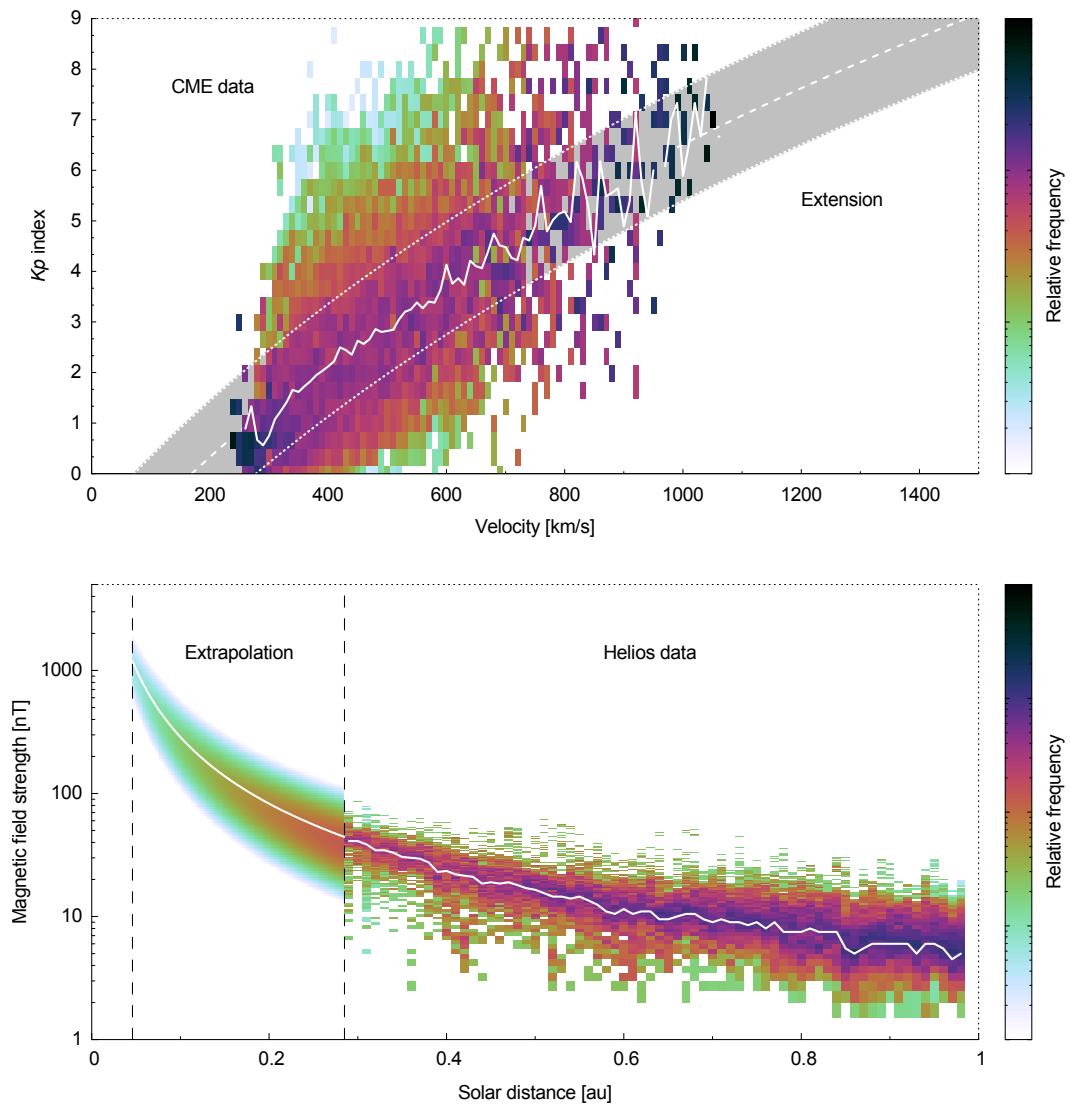


# The solar wind's geomagnetic impact and its Sun–Earth evolution

## Predictive models for space weather and the Parker Solar Probe orbit

Dissertation by

*Malte S. Venzmer*



---

**Figure on the previous page** The top panel shows the relative  $Kp$  frequency distribution per solar wind velocity and its mean value (solid line). The data used is based on the near-Earth OMNI data set and consists of CME-associated flows filtered with the SWS list. The derived predictive model and the mean absolute deviation are indicated by the dashed line and the gray shaded area. The bottom panel shows the relative frequency distribution of the solar wind magnetic field strength with respect to solar distance and its mean value (solid line). Data from the Helios probes is shown to the right and the extrapolation of the derived model to the near-Sun region is shown to the left.

121 pages, 82 figures, 5 tables, 1 article  
Version 1.389 – last changes 2018-09-14 15:18

The electronic version of this document is fully hyperlinked. The external links in several figure captions and in the references are not accessible in the printed version. All external web links in this document were valid in 2018-09-12.

---

*“Despite the ‘Dr.’ before his name, he had completed no course of study and received no degree. When people tried to pin him down about this, he would say that the letters were merely an abbreviation of his first name - Drummond - which he did not use. But it was as ‘Dr.’ Sam Laserowitz that he appeared in a number of science-fiction magazines; he was also known, in the circles of the fans of that genre, as a lecturer, and spoke on ‘cosmic’ themes at their many conferences and convention. Laserowitz’s speciality was earthshaking discoveries, wich he happened upon two or three times a year. [...] We really have no idea what a multitude of con men and crackpots inhabit the domain that lies halfway between contemporary science and the insane asylum.”*

Excerpt from Stanisław Lem 1968, *His Master’s Voice* ([Lem & Kandel 1984](#), p. 38).



# Abstract

This thesis addresses two current topics in solar wind research and space weather. The first study is dedicated to the solar wind's impact on geomagnetic activity and the second study to the estimation of the solar wind conditions in the near-Sun environment with regard to the Parker Solar Probe mission.

Solar wind interacts with the terrestrial magnetosphere, and variations in its properties result directly in geomagnetic disturbances. Extreme plasma conditions, such as those found exclusively in coronal mass ejections (CMEs), evoke geomagnetic storms that can potentially disrupt technological systems and pose threats to human lives. Therefore, the prediction of space weather effects is of major importance. This study aims to derive empirical relations in order to predict the planetary geomagnetic disturbance indicator  $Kp$  from the solar wind electric field and from the velocities of CMEs and solar wind streams.

Near-Earth solar wind measurements of the period 1981–2016 from the minutely OMNI data set are processed to 3-hourly averages and to 3-hourly extrema, and correlated with the  $Kp$  index. A functional dependency between  $Kp$  and the electric field proxy  $vB_z$  in GSM coordinates is derived. CME and stream data are separated using the existing list of Solar Wind Structures, and functional  $Kp$  dependencies are derived for their velocities. The obtained relations are evaluated for their prediction performance by calculating forecast errors and true skill scores. The  $Kp$  correlation with 3-hour minima of  $vB_z$  results in a significantly larger coefficient ( $r_{\min} = 0.72$ ) than with 3-hour averages ( $r_{\text{avg}} = 0.36$ ), whereas the correlation coefficients for 3-hour maxima and averages of the velocity remain similar. Predictive  $Kp$  models are obtained based on relations with the solar wind electric field, and the velocity of CMEs and streams – the relations show mean absolute deviations of around 1  $Kp$  value. The curve of the CME velocity relation is higher in magnitude and steeper in trend than that for the stream velocity. The extension of the CME velocity relation shows that CMEs with about  $1500 \text{ km s}^{-1}$  generate the maximum  $Kp$  of 9.0, the fastest streams with  $900 \text{ km s}^{-1}$  however, barely reach the geomagnetic storm threshold of  $Kp = 5.0$ . The results suggest that by using the  $vB_z$  minima over 3 hours, short-term geoeffective magnetic features in the solar wind are being accounted for, which are being neglected when calculating 3-hour averages. The evident differences in the CME and stream velocity dependencies support the approach of deriving separate  $Kp$  models for them. Within their proper  $Kp$  ranges, all three predictive models perform significantly better than random, and outside they still track the general trend within  $Kp$  errors of about  $\pm 3$ .

Up to now, multiple space probes have measured the solar wind in-situ throughout the whole range of the heliosphere, except for the region close to the Sun below solar distances of 0.28 astronomical units (au). Yet, this region is of particular interest as it comprises the processes that heat and accelerate the solar wind. The Parker Solar Probe (PSP) mission is the first spacecraft to visit this unexplored near-Sun region. Launched in August 2018, PSP is going to reach its first perihelion at a solar distance of 35.7 solar radii ( $R_{\odot}$ ) (0.16 au) in November 2018 and its first closest at  $9.86 R_{\odot}$  (0.046 au) in December 2024. This study aims to develop a solar wind model for the inner heliosphere and to predict the near-Sun solar wind environment for the PSP orbit.

The model comprises individual relations that represent the frequency distributions of the solar wind key properties magnetic field strength, proton velocity, density, and temperature. The relations are constructed in such a way that the distributions are being shifted depending on solar activity and solar distance. The frequency distributions are obtained from 53 years (1963–2016) of near-Earth solar wind measurements from the hourly OMNI data set. Their shapes are fitted with lognormal functions – the velocity is fitted with a double lognormal function to account for its slow and fast wind components. The distributions' shifts due to solar activity are derived from the monthly sunspot number (SSN) of almost five solar cycles. The velocity is treated differently in that the two lognormal functions are being balanced according to the SSN. The distributions' dependencies on solar distance are based on solar wind measurements made in the solar distance range 0.29–0.98 au by the Helios 1 and Helios 2 spacecraft which flew in the 1970s. The dependencies are based on power-law functions, fitted to the Helios data. For the magnetic field strength, an alternative distance dependency is derived, which accounts for the Parker geometry of the individual field components. The derived solar wind model is extrapolated, using SSN predictions of the next solar cycle, down to the orbital trajectory of PSP, in particular to its first perihelion and to its first closest perihelion. The estimated median values at PSP's first and first closest perihelia are respectively: 87 nT and 943 nT,  $340 \text{ km s}^{-1}$  and  $290 \text{ km s}^{-1}$ ,  $214 \text{ cm}^{-3}$  and  $2951 \text{ cm}^{-3}$ ,  $5.03 \times 10^5 \text{ K}$  and  $1.93 \times 10^6 \text{ K}$ . The median values for the magnetic field strength based on the Parker field geometry are 94 nT and 1241 nT, which is 8 % and 32 % higher than those from the model based on the power-law distance dependency. These estimates agree with those from studies using direct measurements obtained from remote observations, except for the velocity and temperature values below  $20 R_{\odot}$ , which are extrapolated to be significantly higher. As it is known that the magnetic field strength in the outer heliosphere conforms to the Parker field geometry, the predictions of this model are considered to be more reliable. The overestimation of the near-Sun velocity and temperature values below  $20 R_{\odot}$  indicates that the solar wind is still being heated and accelerated in this region.

# Contents

<b>1</b>	<b>Introduction</b>	<b>1</b>
<b>2</b>	<b>Background knowledge</b>	<b>5</b>
2.1	The Sun . . . . .	5
2.2	Solar dynamo . . . . .	8
2.3	Solar activity cycle . . . . .	9
2.4	Coronal and heliospheric magnetic field . . . . .	11
2.5	Solar wind . . . . .	13
2.5.1	Slow and fast streams . . . . .	14
2.5.2	Stream interaction regions . . . . .	17
2.5.3	Heliospheric current sheet . . . . .	17
2.5.4	Coronal mass ejections . . . . .	18
2.6	Space weather . . . . .	23
2.7	Magnetosphere . . . . .	24
2.7.1	Solar wind coupling mechanisms . . . . .	26
2.7.2	Dungey convection cycle . . . . .	27
2.7.3	Russell-McPherron effect . . . . .	29
2.7.4	Geomagnetic indices . . . . .	29
2.8	Geomagnetic storms . . . . .	29
2.8.1	$Kp$ index . . . . .	30
2.9	Geomagnetic activity forecast . . . . .	32
2.9.1	Coupling functions . . . . .	32
2.9.2	$Kp$ forecast methods . . . . .	34
2.9.3	Solar wind nowcast and forecast to Earth . . . . .	35
<b>3</b>	<b>Instrumentation and data description</b>	<b>39</b>
3.1	Magnetometer . . . . .	39
3.2	Plasma spectrometer . . . . .	40
3.3	OMNI data collection . . . . .	41
3.4	Helios probes . . . . .	42
3.5	$Kp$ data series . . . . .	42
3.6	Sunspot number . . . . .	43
<b>4</b>	<b>Solar wind and CME influence on geomagnetic activity</b>	<b>45</b>
4.1	The $Kp$ index and its long-term variations . . . . .	46
4.1.1	Solar activity influence . . . . .	46
4.1.2	Seasonal variations . . . . .	48
4.2	Relation between solar wind electric field and $Kp$ index . . . . .	48
4.2.1	Data correlation . . . . .	49
4.2.2	Functional dependency for solar wind electric field . . . . .	50
4.3	Relations between CME/stream velocities and $Kp$ index . . . . .	51
4.3.1	Solar Wind Structures list . . . . .	52
4.3.2	Data correlation . . . . .	52
4.3.3	Functional dependencies for CME and stream velocities . . . . .	53
4.4	Prediction performance . . . . .	57
4.5	Discussion . . . . .	59
4.6	Conclusions . . . . .	61
<b>5</b>	<b>Empirical solar wind model for the inner heliosphere</b>	<b>65</b>
5.1	Parker Solar Probe mission . . . . .	65
5.2	On the published article . . . . .	66
5.3	Parker magnetic field solar distance dependency . . . . .	67
5.3.1	Parker magnetic field . . . . .	67

5.3.2	Solar distance dependency . . . . .	69
5.3.3	SSN implementation and extrapolation to PSP orbit . . . . .	71
5.3.4	Conclusion . . . . .	72
5.4	Possible solar wind model modifications . . . . .	72
<b>6</b>	<b>Article: Solar-wind predictions for the Parker Solar Probe orbit</b>	<b>73</b>
	Abstract . . . . .	73
6.1	Introduction . . . . .	73
6.2	Frequency distributions of the solar-wind parameters . . . . .	74
6.3	Solar activity dependence of the solar-wind frequency distributions . . . . .	75
6.4	Solar distance dependency . . . . .	78
6.5	Empirical solar-wind model . . . . .	81
6.6	Model extrapolation to PSP orbit . . . . .	82
6.7	Discussion and summary . . . . .	84
	References . . . . .	85
<b>7</b>	<b>Conclusions</b>	<b>87</b>
7.1	Geomagnetic impact of the solar wind . . . . .	87
7.2	Sun–Earth evolution of the solar wind . . . . .	89
<b>A</b>	<b>Appendix</b>	<b>91</b>
A.1	Solar surface differential rotation . . . . .	91
A.2	Electric field at the magnetopause . . . . .	92
A.3	Plasma beta . . . . .	92
A.4	Alfvén velocity . . . . .	93
A.5	Sun–Earth distance and rotation axes tilt . . . . .	93
A.6	GSE, GSM, and HGI coordinate systems . . . . .	94
A.7	True skill statistic . . . . .	95
A.8	Lognormal distribution . . . . .	96
A.9	Acronyms . . . . .	97
A.10	Astronomical constants . . . . .	98
	<b>References</b>	<b>99</b>
	<b>Acknowledgments</b>	<b>109</b>





# 1 Introduction

In this thesis I address two current problems in the physics of solar wind: the prediction of the solar wind's geomagnetic impact, which is one of the most important key objectives in space weather, and the characterization of the solar wind conditions in the near-Sun region, which will be explored by the Parker Solar Probe mission beginning in end of 2018. These two problems are linked in view of the fact that the solar wind impacting the magnetosphere originates from the near-Sun region.

This thesis presents quantitative studies examining both topics. Despite a considerable difference with regard to their content, the two studies both share their predictive nature related to solar wind, deal with similar data sets, and harness similar data processing methods. In the following, I introduce both topics separately. First, I lead into the subject of quantifying the solar wind's geomagnetic impact for different forecast situations. Second, I present the issue of estimating the near-Sun solar wind environment which Parker Solar Probe will encounter during its mission.

The Sun emits a continuous flow of magnetized plasma into space, which mainly consists of electrons and protons, and is called solar wind. This solar wind fills the interplanetary space and interacts with solar system bodies and their possible magnetospheres. It has been known since the early 19th century that variations in the solar wind evoke disturbances in the terrestrial magnetosphere (Bartels 1962). Particularly strong disturbances, called geomagnetic storms, can be provoked by coronal mass ejections (CMEs), which consist of magnetically structured coronal plasma shot into the ambient solar wind by rearrangements in the configuration of the solar magnetic field. One of the latest CMEs generating strong geomagnetic storms is displayed in the coronagraph image in Figure 1.1. The impact of CMEs on the Earth's magnetosphere can be significantly stronger than that of the ambient solar wind streams, owing to the potentially extreme values of their properties, such as magnetic field strength and velocity, which are able to be several times higher than those of ambient streams.

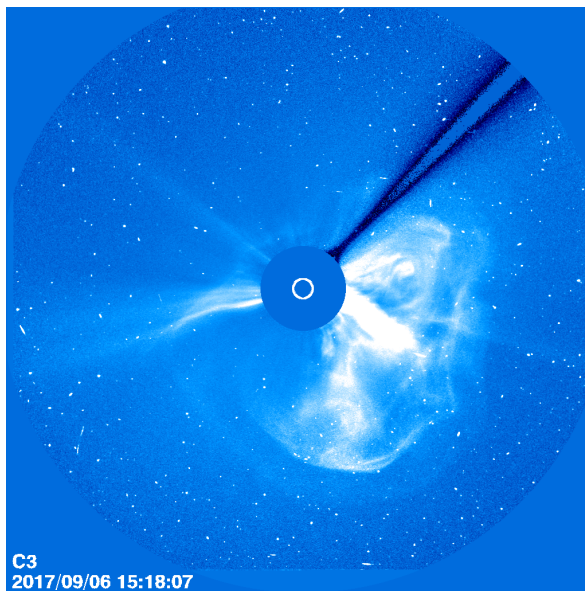


**Figure 1.1** White-light image of the solar corona out to  $30 R_{\odot}$  from 6 September 2017 taken by the LASCO/C3 coronagraph on board the SOHO spacecraft. The solar disk's position is indicated by the white circle and it is covered by an occulter disk whose mount is visible to the top right. The bright extensive structure is the CME and the faint aura around is a shock wave. Courtesy of SOHO/LASCO consortium; SOHO is a project of international cooperation between ESA and NASA.

The effects of geomagnetic storms pose a threat both to exposed humans and sensitive technological systems. The potential disruption of critical systems, such as satellite communication and power grids, would not only have severe economic implications but would affect human lives as well. The rapid rate of technological advancement leads to an ever-growing abundance of systems which are sensitive to disturbances in the geomagnetic field. Therefore, it is becoming increasingly important to be capable of predicting the onset of magnetospheric disturbances and their magnitude, in order to mitigate such severe consequences.

As a result of solar wind in-situ measurements, it is well known that variations in specific solar wind quantities lead to direct responses in geomagnetic activity. The coupling mechanisms between solar wind and

magnetosphere have been identified and modeled extensively, resulting in a variety of coupling functions linking solar wind parameters to indicators of geomagnetic activity. These coupling functions serve as the basis for models that predict geomagnetic activity from solar wind input parameters and thus, knowledge of the solar wind conditions in front of the magnetosphere enables to predict the geomagnetic response fairly well.

The solar wind is continuously monitored in situ by spacecraft located in front of the magnetosphere. These real-time measurements are used by operational space weather services for providing nowcasts of geomagnetic activity. The monitoring spacecraft are located at the first Lagrange point (L1), which is situated at approximately one-hundredth the distance from the Earth to the Sun. Solar wind plasma from this point reaches the magnetosphere in a few tens of minutes, which is significantly shorter than its travel time from Sun to Earth, which is around three to four days for ambient solar wind streams and about a day for extremely fast CMEs. In order to exploit this extended lead time, some information about CMEs and solar wind streams can be acquired from remote observations provided by solar imagers and coronagraphs. The velocity is one of the few remotely acquirable quantities which is to a certain degree reliably forecastable. Space weather nowcast services reach a high prediction accuracy by using in-situ measurements from L1, however, for remote forecast situations, the methods used by nowcast services are not effective, because not all solar wind parameters necessary for geomagnetic activity forecasts can readily be obtained.

This study addresses this problem in that it quantifies the geomagnetic response for remote forecast situations, when only the velocity information from CMEs or ambient solar wind is available. The present study relates the planetary geomagnetic disturbance indicator  $Kp$  with velocity measurements made ahead of the Earth's magnetosphere. In view of the differences between the velocity prediction methods applied for CMEs and streams, I derive separate relations for CME-associated flows and for solar wind streams. This study is based on 35 years of solar wind data from the hourly OMNI data set and on the classification from the list of Solar Wind Structures (SWS). Solar wind analyses in conjunction with  $Kp$  commonly employ averaged solar wind data, even though the  $Kp$  index represents the value of the maximal geomagnetic disturbance per 3-hour interval and not its average – the underlying time resolution is 1 minute. Thus, a unique approach in the present study is the use of 3-hour extreme values derived from minutely solar wind data. This method is therefore expected to result in significantly enhanced correlations between the  $Kp$  index and solar wind data. Here, this approach is tested and compared for the cases of the solar wind electric field, which represents one of the most prominent coupling functions, and the velocity.

The purpose of this study is to provide empirical  $Kp$  relations that can be utilized in specific forecast situations when only the remotely estimated velocities of CMEs or streams are known. The study further shows the impact of the way the high-resolution solar wind data is processed to 3-hourly values by means of the  $Kp$  relations to the electric field and the velocity.

In the following, I introduce the second topic of this thesis. The solar wind was first theoretically described by [Parker \(1958\)](#) who formulated a model of an expanding isothermal solar atmosphere. His model describes a continuous supersonic radial outflow of magnetized plasma and the consequences for the structure of the heliospheric magnetic field. The existence of this solar wind was subsequently confirmed from in-situ measurements made by the first satellites in 1959. Since then, solar wind measurements were made almost continuously by various spacecraft located near Earth. By now, the solar wind is measured throughout the heliosphere – the two Voyager probes tracked it from Earth to the outer solar system, the Ulysses spacecraft charted the solar wind up to high heliolatitudes, and the two Helios spacecraft measured it from Earth down to the solar distance of Mercury.

However, the region close to the Sun remains unexplored although it is of particular scientific interest. In this region, the corona is heated to temperatures far exceeding those of the underlying photosphere and the plasma is being accelerated to its final solar wind speeds. Up to now the mechanisms that heat the corona and accelerate the solar wind are still not fully understood. As this region is assumed to hold the answers to these open key questions, it has long been planned to send a probe to this region. The Parker Solar Probe (PSP) mission is intended to address these questions. The PSP spacecraft, launched on 12 August 2018, will dive through the corona within distances down to  $8.86 R_{\odot}$  from the solar surface, see [Figure 1.2](#). It will provide for the first time in-situ measurements and high-resolution images of the solar wind conditions in this unexplored region.

This study addresses this topic in that it explores the near-Sun solar wind conditions and predicts the solar wind environment for the PSP orbit, that is, this work derives estimates of the key solar wind parameters magnetic field strength, proton velocity, density, and temperature. These key parameters are back-extrapolated to the near-Sun region, using an empirical solar wind model for the inner heliosphere. I develop this solar wind model from solar activity and solar distance dependencies of each parameter individually. To derive the dependencies on solar activity, solar wind measurements from the near-Earth OMNI data set are being related

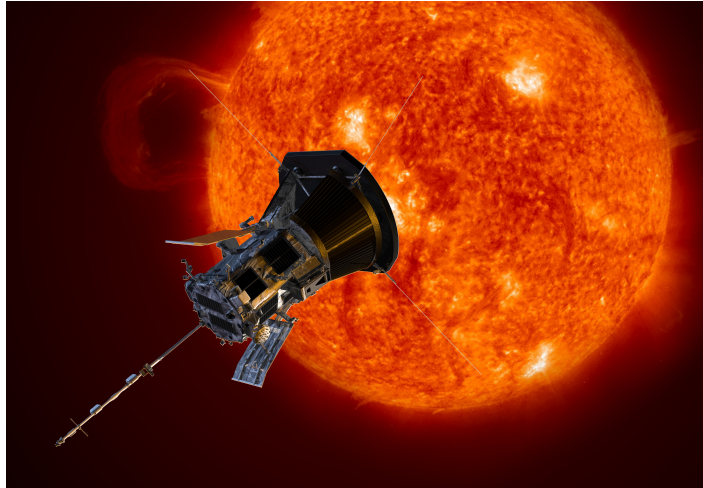


**Figure 1.2** Artist's rendering of the PSP spacecraft approaching the Sun. Close to the Sun, the heat shield will actually always point in direction of the Sun. Credit: [NASA/Johns Hopkins APL/Steve Gribben](#), 2018.

to the sunspot number. To derive the solar distance dependencies, I apply solar wind data from the Helios 1 and Helios 2 probes, which flew in the 1970s and took in-situ measurements between 0.29 au and 0.98 au. Commonly, studies that analyze solar wind handle it by working with time averages of the bulk parameters. In contrast, the special approach in this work is its tackling of the frequency distributions. The model represents the solar wind parameters by lognormal distributions, furthermore, both the slow and fast velocity components are taken into account. For the magnetic field strength, I additionally derive a second alternative distance dependency that is based on the Parker magnetic field geometry.

The purpose of this study is to quantitatively model the key solar wind parameters in the inner heliosphere, to estimate the near-Sun solar wind environment, and further to predict it in particular for the orbit of the PSP spacecraft.

I structured this document as follows: [Chapter 2](#) lays out the fundamentals behind the problems addressed in this work as well as the current state of research. This comprises basic knowledge about the Sun, its activity and magnetic field, solar wind, space weather, magnetosphere, geomagnetic activity and forecast methods. [Chapter 3](#) describes those instrumentation and data sources on which the studies in the subsequent chapters are based on. [Chapter 4](#) presents the analyses performed on the solar wind's magnetospheric influence, with focus on predicting the  $Kp$  index from the solar wind electric field and from the velocities of CMEs and streams. [Chapter 5](#) is followed by the published article on the same topic, integrated as [Chapter 6](#) into this document. These chapters develop an empirical solar wind model for the inner heliosphere and use it to estimate the near-Sun solar wind environment of the PSP mission underway. The model comprises the solar wind parameters magnetic field strength, proton velocity, density, and temperature. Furthermore, an alternative magnetic field model is outlined, which exhibits a solar distance dependency based on Parker's magnetic field formulation. Eventually, [Chapter 7](#) offers a summary of the results and conclusions, and gives an outlook on ideas for further studies. The subsequent [Appendix A](#) contains helpful information and theory about several more specific topics, as well as a list of frequently used acronyms in this work in [Section A.9](#).



## 2 Background knowledge

This chapter summarizes the basic scientific knowledge necessary for understanding the studies performed in this work and in particular the later topics lead up to the current state of research. First, the Sun's origin, inner structure, atmosphere, and sphere of influence – the heliosphere – are described. Subsequently, the Sun's dynamics with its differential rotation and magnetic field generation are outlined. Furthermore, the solar activity cycle is described, including the meridional flow circulation, the appearance of active regions, the surface magnetic field change, and sunspot cycles. The heliospheric magnetic field is depicted from its photospheric emergence in magnetic bright points and coronal superradial expansion, through the formation of the heliospheric current sheet and the Parker spiral to the heliosheath. In addition, the solar wind and its properties, the origins of slow and fast streams, stream interaction regions, and coronal mass ejections are described. Furthermore, space weather and its effects on Earth and the magnetosphere are outlined. Here, special attention is given to the solar wind's coupling to the magnetosphere and the resulting dynamic processes, the Dungey convection cycle, and the Russell-McPherron effect. Finally, geomagnetic storms are introduced and focus is shifted to the forecast of geomagnetic activity. Here, a number of prediction techniques are mentioned that include various solar wind coupling functions and  $Kp$  forecast methods. Ultimately, Earth upstream prediction methods for solar wind are sketched, in particular nowcasts of solar wind and remote forecasts of streams and CMEs.

### 2.1 The Sun

13.8 billion years ago the Big Bang formed our universe. The energy density of our universe consists of 69.1 % dark energy, 25.9 % dark matter and 4.9 % baryonic matter, according to calculations using the inflationary  $\Lambda$ CDM<sup>1</sup> cosmology together with the latest cosmic microwave background temperature measurements (Planck Collaboration et al. 2016). After several minutes, the primordial nucleosynthesis left the universe in a state where the baryonic matter was composed of 75.33 %<sup>2</sup> hydrogen, 24.67 % helium and traces of deuterium, tritium and lithium (Planck Collaboration et al. 2016). Over millions of years this gas cooled down and gravitationally accreted into molecular clouds and formed stars. The first generations of stars (Population III) fused this gas to heavier elements (metals), and supernovae distributed them into space as a foundation for the formation of new stars of low and high metallicity (Population II and I). Likewise, supernovae of these stars constantly enriched the interstellar medium with metals. Now, the interstellar medium in the Milky Way consists of about 32 % helium and traces of other metals (Danziger 1970).

Our Sun, a metal-rich Population I yellow dwarf star, emerged 4.6 billion years ago (Bahcall et al. 1995) from an accretion disk, formed by a collapsing rotating cloud. The compression within its center resulted in high temperatures, which initiated the fusion of hydrogen to helium (primarily pp chain reaction). The fusion reactions produce huge amounts of energy and heat the solar center to a temperature of 15.7 million kelvins (Christensen-Dalsgaard et al. 1996). The generated energy is transported through the solar body to its surface and eventually into space. The core region extends to about 0.25 solar radii ( $R_{\odot}$ )<sup>3</sup>, where the declining temperature becomes insufficient for fusion reactions. The energy transport is dominated by thermal radiation until, because of declining ionization and density, at 0.71  $R_{\odot}$  up to the surface convective motion takes over (Christensen-Dalsgaard et al. 1991).

The temperature at this transition region, called tachocline, is about 2 million kelvins and decreases towards the solar surface to between 4400–6600 K. Here, at the photosphere, the energy is radiated away with an effective black body temperature of 5772 K (Prša et al. 2016), classifying the Sun as a spectral type G2V star. At this surface layer, granules, the tops of convection cells, and temporary sunspots are visible. Strong magnetic flux inhibits the convection at sunspots, leading to lower temperature and brightness (for more on sunspots see the following Sections 2.2 and 2.3). Figure 2.1 illustrates these photospheric features along with the inner solar structure.

Above the photosphere at the base of the chromosphere, the temperature declines to its solar minimum of 3800 K until it rises to 2–3 million kelvins in the corona (Billings 1959; Liebenberg et al. 1975). Up to

---

<sup>1</sup> $\Lambda$ CDM: Lambda cold dark matter

<sup>2</sup>Percentages by mass

<sup>3</sup>One solar radius is defined as 695 700 km, see also Appendix A.10



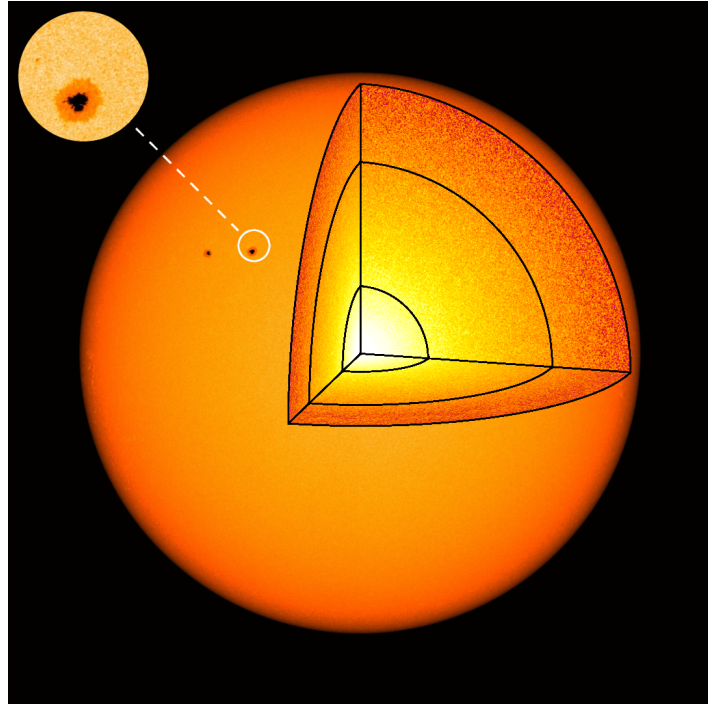


**Figure 2.1** Image of the photosphere from 20 March 2016 together with a schema of the solar interior structure. The inset shows the granular surface with a sunspot. I created this figure based on a SDO/HMI continuum image, credit: NASA/SDO and the AIA, EVE and HMI science teams.

now, it is not fully understood how the corona is so much hotter than the underlying chromosphere – this question is known as the coronal heating problem (Klimchuk 2006; McComas et al. 2007; Fox et al. 2015). The energy transfer mechanisms that are generally postulated are magnetic reconnections, wave heating and type II spicules, or a combination of these (Cranmer et al. 2017).

The chromosphere is a 2000 km thick region, whose features – numerous spicules, filaments, and prominences – can reach far into the corona. They consist of chromospheric material, channeled by the solar magnetic field, and are enveloped by a thin transition region where the temperature jumps up from about 20 000 K to coronal temperatures<sup>4</sup>. Reconnection of magnetic field lines can result in the eruption of filaments into the corona and beyond, termed coronal mass ejections (CMEs), see also Subsection 2.5.4. Details of chromospheric features are shown in Figure 2.2 – the images were taken on the same day as in Figure 2.1.

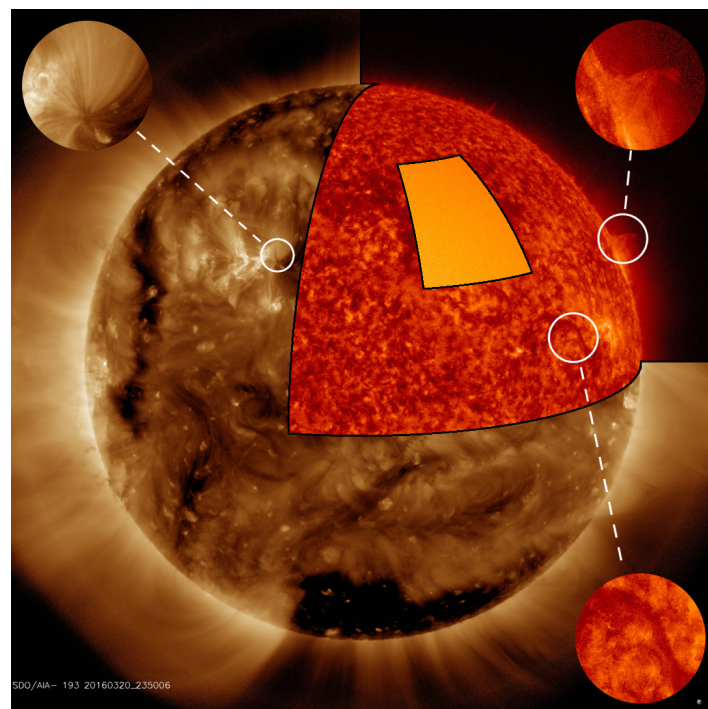


**Figure 2.2** Composite image of the solar atmosphere from 20 March 2016 and some details of its features. Corona, chromosphere and photosphere are seen in wavelengths of 193 Å, 304 Å, and continuum. Chromospheric spicules are visible on the northern limb. The enlargements on the right show a prominence and a filament. The dark region at the south pole is a coronal hole. The left inset shows details of the active region belonging to the sunspots shown in Figure 2.1. I created this figure based on SDO/AIA images, credit: NASA/SDO and the AIA, EVE and HMI science teams.

<sup>4</sup>NASA/MSFC Solar Physics, The Transition Region: [https://solarscience.msfc.nasa.gov/t\\_region.shtml](https://solarscience.msfc.nasa.gov/t_region.shtml)

The Sun's atmosphere is dominated by the varying small- and large-scale solar magnetic field configuration. There are regions where the magnetic field lines arch back to the surface and regions with open field lines. In the latter areas, the coronal plasma can – guided by the field – escape into space. Thus, these coronal areas are less dense, cooler and therefore appear darker in extreme ultraviolet (EUV) and are called coronal holes (CHs). In [Figure 2.2](#) such a coronal hole is visible at the solar south pole.

From Earth, the faint corona and the chromosphere can only be observed during eclipses, due to the brightness of the solar disk. There are three effects contributing to the visibility of the corona: photons scattering off of free electrons, producing a continuous spectrum; photons scattering off of dust particles, their spectrum contains Fraunhofer absorption lines; and ion spectral emission lines – these contributions to the corona are termed K-, F- and E-corona<sup>5</sup>. Images from solar eclipses reveal the coronal plasma, shaped by the magnetic field, and red prominences from the chromosphere. The solar eclipse imaged in [Figure 2.3](#) shows the magnetic field's dipole structure and the equatorial streamer belt, characteristic for a quiet Sun during cycle minimum.



**Figure 2.3** Total solar eclipse image of the inner corona up to a distance of five solar radii. The picture was taken in Mongolia, 1 August 2008 and is processed from multiple images. Credit: [Miloslav Druckmüller, Peter Aniol, Jan Sládeček](#), 2008, reproduced with permission.

Due to the high coronal temperatures, plasma escapes the solar gravitational field ([Parker 1958](#)) with velocities of  $200\text{--}800\text{ km s}^{-1}$ . Its acceleration is linked to the coronal heating – however, the exact location and mechanism of this process remain unknown ([Hollweg 1985](#); [McComas et al. 2007](#); [Fox et al. 2015](#); [Cranmer et al. 2017](#)). The magnetic field becomes too weak to guide the coronal plasma at a distance of a few solar radii. From this so-called 'source surface', the solar wind flows radially outward into space until it reaches the termination shock. Eventually it collides with the local interstellar medium, creating the boundary of the heliosphere, the heliopause. The heliopause is expected to be a bubble of either a teardrop or croissant shape, caused by the Sun's relative velocity of  $23\text{ km s}^{-1}$  with respect to the local interstellar medium ([Owens & Forsyth 2013](#); [Opher et al. 2015](#)). However, [McComas et al. \(2012\)](#) show that this velocity is too slow to form a leading bow shock. Measurements of the Voyager 1 and Voyager 2 spacecraft indicate their passage of the termination shock at about 94 astronomical units (au)<sup>6</sup> and 84 au respectively, entering the heliosheath region ([Owens & Forsyth 2013](#)). [Gurnett et al. \(2013\)](#) report that in 2012 Voyager 1 actually crossed the heliopause into interstellar space at a solar distance of 121 au. The heliosphere and its surrounding flow structure is illustrated in [Figure 2.4](#).

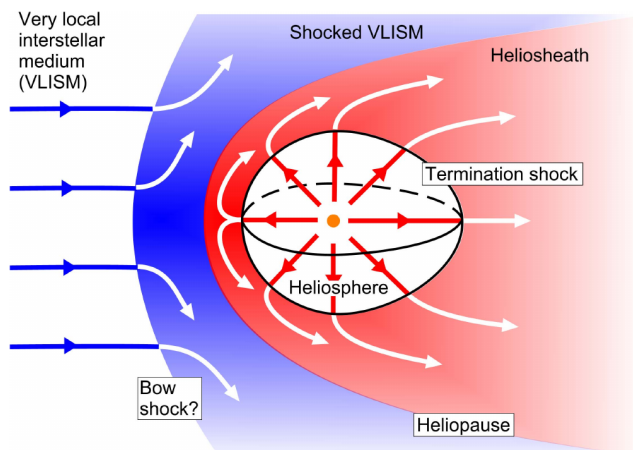


**Figure 2.4** Schema of the heliosphere and its surrounding flow structure, formed by the interaction of the solar wind (red) with the local interstellar medium (blue) at the heliopause. Credit: [Owens & Forsyth \(2013, Fig. 9\)](#), licensed under CC BY-NC 3.0 DE.

<sup>5</sup>K from kontinuierlich (continuous in German), F from Fraunhofer, and E from emission.

<sup>6</sup>One astronomical unit is defined as 149 597 870.7 km, see also [Appendix A.10](#)

On its way outwards through the solar system, the solar wind – carrying the solar magnetic field – interacts with the planets, their magnetic fields and other solar system bodies. This has a number of effects, for instance disturbances in planetary magnetic fields with appearance of aurorae and enhanced radiation, atmospheric losses, and stripping of cometary tails. Some of these effects can have disruptive consequences for humans and their technology, creating a high interest in understanding space weather and forecasting its effects, the topic of space weather is further addressed in [Section 2.6](#). The magnitudes of these effects depend highly on spatial and temporal variations in the solar wind, which are rooted in the dynamics of the solar magnetic field, described in the following sections.

## 2.2 Solar dynamo

The conservation of the angular momentum in the contracting molecular cloud led to a rotation of the Sun. Although the Sun experiences a minor loss of angular momentum due to solar wind ([Weber & Davis 1967](#)), its rotation still has a current average period of about 25 days. The radial convective motion within the solar interior above the tachocline leads to a transport of momentum away from the rotation axis and therefore to a slower polar and faster equatorial rotation in the convection zone ([Miesch 2005](#)). This differential rotation is visible on the surface and was first discovered from sunspot observations by [Scheiner \(1630\)](#). With a rotation period of about 34 days, the poles have a lag of almost 9 days (for further information on solar rotation see [Appendix A.1](#)). The differential rotation in the solar interior can be inferred from helioseismological observations. Below the differential rotation of the convection zone, a nearly solid rotation with a period of about 26.6 days (this corresponds to a frequency of 435 nHz) exists in the radiation zone, as shown in [Figure 2.5](#).

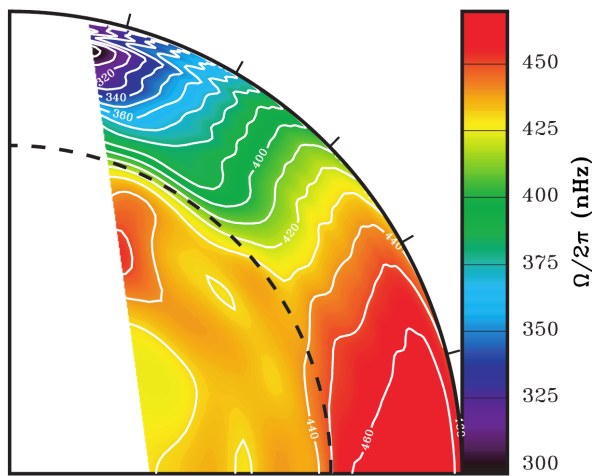


**Figure 2.5** Rotation frequency profile of the solar interior. The location of the tachocline is indicated by the dashed line. The rotation frequency is inferred from helioseismology via observations from the Michelson Doppler Imager (MDI) at the Solar and Heliospheric Observatory (SOHO) spacecraft. Credit: [Thompson et al. \(2003, Fig. 3\)](#), © Annual Reviews, reproduced with permission.

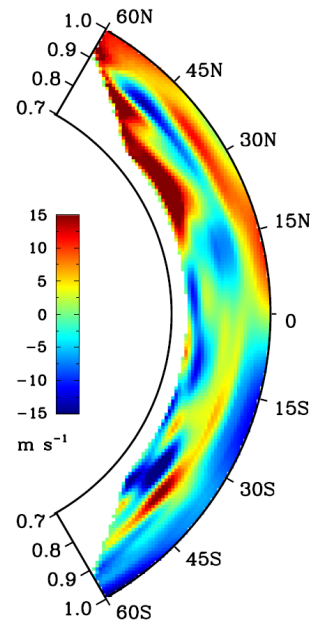


**Figure 2.6** Meridional flow velocity profile in part of the convection zone. Positive values are directed towards north. The velocity is inferred from helioseismology via observations from the Helioseismic Magnetic Imager (HMI) at the Solar Dynamics Observatory (SDO) spacecraft. Credit: [Zhao et al. \(2013, Fig. 4, panel \(a\)\)](#), I moved the colorbox), © AAS, reproduced with permission.

Turbulent plasma motions from convective flows in the convection zone generate and carry disorganized magnetic flux. The large rotational shear at the tachocline stretches and amplifies the magnetic fields to strong coherent toroidal flux ( $\omega$ -effect) with intensities of the order 1–10 T. These toroidal fields, generated near the bottom of the convection zone, can be stored in a deep magnetic layer located in the stably stratified region below the convection zone ([Ossendrijver 2003](#)). The stronger flux ropes become buoyant and rise to the surface. The Coriolis force twists them systematically on their way through the convection zone ( $\alpha$ -effect). The twist is stronger at higher latitudes (Joy’s law). Then the flux ropes emerge in the photosphere as bipolar active regions of opposite magnetic polarity – the stronger ones forming pairs of sunspots, as seen in [Figure 2.7](#). Turbulent



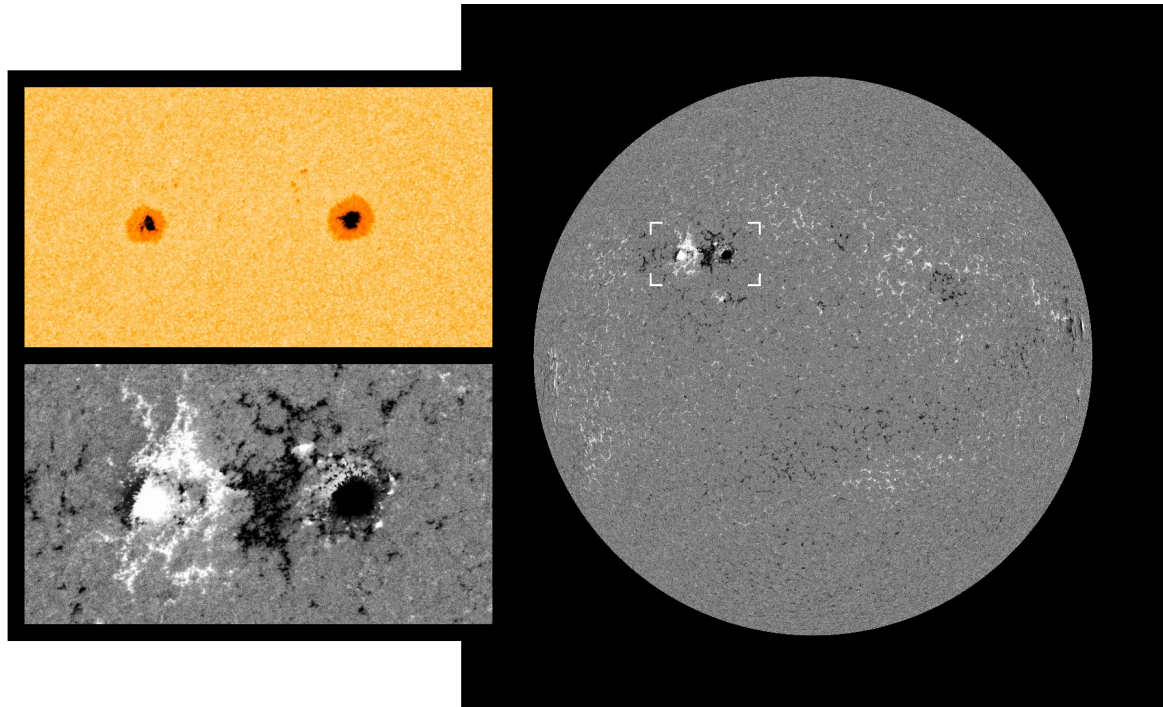


**Figure 2.7** Continuum image of the two sunspots pictured in [Figure 2.1](#) (top left), magnetogram from the same region (bottom left), and magnetogram from the whole solar disk (right). The magnetogram shows the polarity of the line-of-sight magnetic field component at the photosphere (black/white: inward/outward polarity). The highly concentrated magnetic flux at the sunspots is visible as well as the extended bipolar magnetic field structure of the whole active region, which is divided by the so-called magnetic neutral line. The solar disk has the same size as in [Figure 2.1](#). I created the figure based on SDO/HMI continuum and magnetogram images from 20 March 2016, credit: NASA/SDO and the HMI science team.

convective diffusion of this surface flux contributes to the build-up of poloidal fields. Their resulting polarity is opposite to the prevailing global field due to the directional way the rotational shear at the tachocline and the Coriolis force in the convection zone act. Fluctuating motions further amplify the mean fields in these processes. This solar  $\alpha$ - $\omega$ -dynamo is thought to create the major part of the solar magnetic field. Still, with regard to the magnetic field's high variability, the long-term mean fields are governed by intermittent localized structures, that is, active regions, filaments, and coronal loops ([Miesch 2005](#)).

## 2.3 Solar activity cycle

Helioseismic measurements reveal that the large-scale convective flow is aggregated into large convection cells with slow meridional flows of a few  $\text{m s}^{-1}$ , as can be seen from [Figure 2.6](#). A poleward subsurface flow and equatorward backflow beneath with a further poleward flow below are detected within each hemisphere, comprising a stacked double-cell profile ([Zhao et al. 2013](#)). The meridional circulation flow speed has a major influence on the average 22-year period of the emerging magnetic flux at the solar surface, known as Hale cycle. This period varies and is influenced by the stochastic emergence rate and tilts of active regions and the diffusion from random convective motions ([Hathaway & Upton 2016](#)). The surface magnetic field configuration changes within one period from a dipole structure to a reversed dipole structure with opposite polarity and back, completing a so-called Babcock-Leighton dynamo cycle. Thus, the transition time from one dipole state to the next lasts about 11 years, this period is defined as one solar cycle.

In the transition phase, magnetic flux emerges in belts above and below the solar equator, manifesting as bipolar active regions with sunspots, resulting in a toroidal/multipolar structured magnetic field. Sunspots appear at about  $\pm 20^\circ$  latitude at the beginning of a cycle, this shifts towards lower latitudes at the end of a cycle. Thus, the plot of sunspots over latitude and time reveals a butterfly pattern ([Maunder 1904](#)). This butterfly pattern appears in surface radial magnetic field observations as well, see [Figure 2.8](#). The leading polarity of bipolar regions is opposite in both hemispheres and the leading polarity changes with each solar cycle, this is called Hale's polarity law. The emerging flux is carried by the slow meridional surface flow poleward, canceling the current dominating polar field polarity and eventually resulting in the polar field switch ([Hathaway 2015](#)).

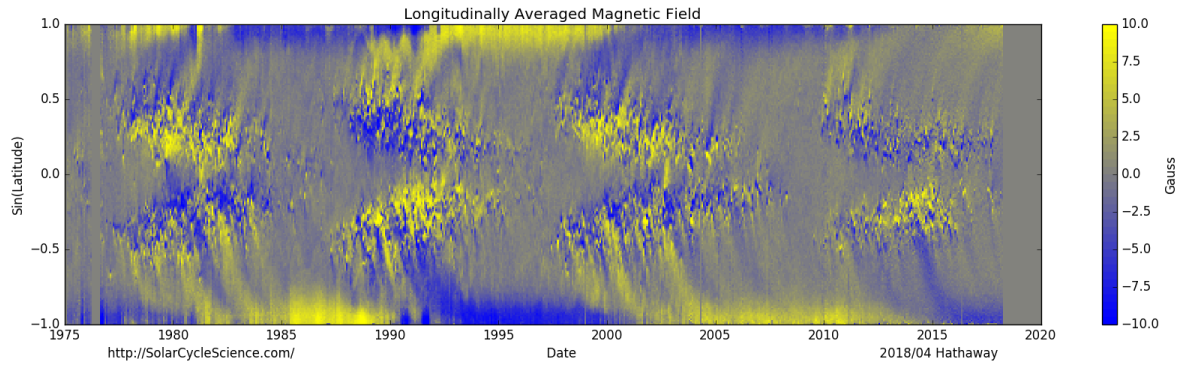


**Figure 2.8** Magnetic butterfly diagram of the longitudinally averaged radial magnetic field on the solar surface. Yellow represents an outward directed magnetic field (positive), blue inward (negative). The data is obtained from instruments on Kitt Peak National Observatory and from the MDI at the SOHO spacecraft. Courtesy of David Hathaway, [Solar Cycle Science](#), 2018, updated version of [Hathaway \(2015, Fig. 17\)](#).

Since regions of strong magnetic flux are visible as sunspots on the photosphere, they were known well before the common era by Greek and Chinese scholars ([Clark & Stephenson 1978](#); [Vaquero 2007](#)). Systematic sunspot observations exist since 1610, shortly after the invention of the telescope. In 1843 Schwabe discovered the 11-year periodicity in the sunspot occurrence ([Schröder 2004](#), p. 124). In 1848 Wolf introduced the sunspot number (SSN) and the solar cycle number to record these cycles ([Hathaway 2015](#)). Observations of the SSN show large variations in cycle length (9–14 years) and cycle amplitude with peak SSNs in the range 0–300 ([Hathaway 2015](#)) – the monthly SSN from the last six solar cycles is displayed in [Figure 2.9](#). There also exist long-term variations, such as secular cycles of different periodicity or the 70-year Maunder Minimum, during which from 1645 on almost no sunspots were observed ([Maunder 1890](#)). The source of the variations in the solar cycle periods and amplitudes are variations in the meridional circulation, because their fluctuations are larger than those found in the differential rotation and in the convective motions ([Hathaway 2015](#)).

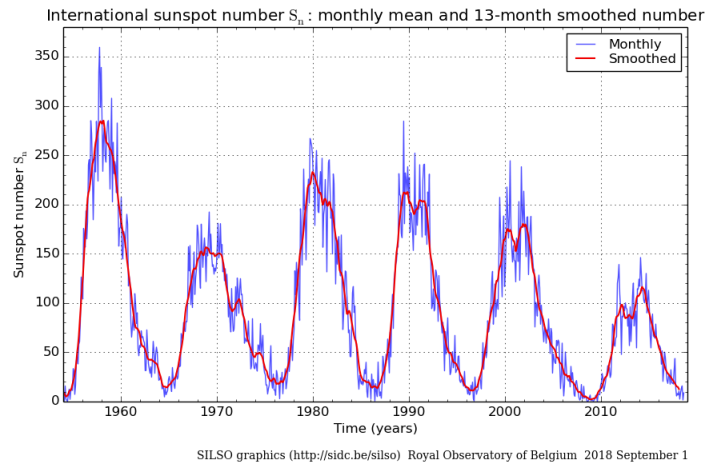


**Figure 2.9** Monthly mean sunspot number (blue) and 13-month smoothed monthly sunspot number (red) for the last six solar cycles since 1954. Credit: [SILSO data/image](#), [Royal Observatory of Belgium](#), Brussels, 2018.

As the SSN is commonly used as an indicator for solar activity, there exists interest in its prediction for the course of the actual and upcoming solar cycles. The continuing prediction of an already commenced activity cycle is reliable, but then the prediction of a cycle before it began is more difficult. Though, there are indications that the polar magnetic field strength during the preceding activity minimum is correlated to the strength of the next solar cycle ([Schatten & Sofia 1987](#)). However, [Hathaway & Upton \(2016\)](#) suggest that the predictability of solar cycles is generally limited – accumulated uncertainty produced by stochastic motions in the convection zone makes predictions further than the next solar cycle very unreliable.

## 2.4 Coronal and heliospheric magnetic field

The Sun's magnetic field governs the plasma movements in the corona and extends out into space, forming the heliospheric magnetic field (HMF). Its sources on the photosphere are bright points between the granules, which are detected in G-band (430 nm) images. They are identified as magnetic flux tubes with field strengths of 100–200 mT (Cranmer & van Ballegooijen 2005). Together, these magnetic bright points cover around 1–2 % of the solar surface and carry many times the flux that active regions do (Sánchez Almeida et al. 2010). These thin flux tubes expand laterally in the low chromosphere and merge to homogeneous network fields, which expand and merge again to a large-scale canopy below the transition region (see Figure 2.10).

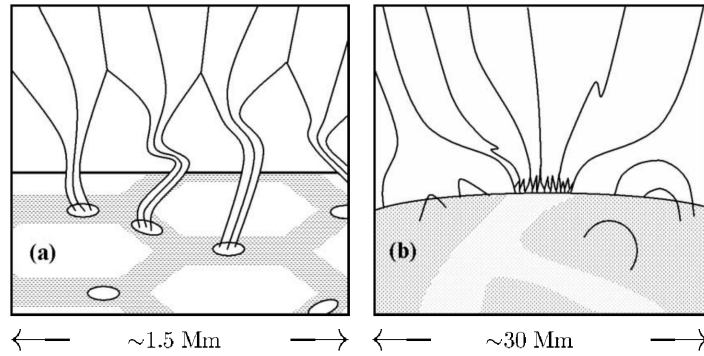


**Figure 2.10** Schemata of superradially expanding magnetic flux. (a) Magnetic bright points between granules on the photosphere are indicated by ellipses. The protruding lines are thin magnetic flux tubes that merge to a homogeneous network field. (b) Pictured is the network field which expands again to the large-scale canopy field of the lower corona. Credit: Cranmer & van Ballegooijen (2005, Fig. 1, panels (a) and (b)), © AAS, reproduced with permission.

The magnetic bright points' convective appearance and stochastic motions on the photosphere result in wave-like fluctuations that propagate upward through the superradially expanding flux tubes. There exist three types of magnetohydrodynamic (MHD) waves within the plasma: compressional fast- and slow-mode waves, and an incompressible wave mode, which is the result of bending magnetic field lines (Alfvén 1942), called shear Alfvén wave. Alfvén waves propagate with a characteristic speed along magnetic field lines. As they transport energy from the photosphere outwards, it is assumed that they play a major role in the coronal heating process and that the solar wind is accelerated up to the so-called Alfvén critical surface at around  $17 R_{\odot}$ , where the local Alfvén speed equals the solar wind speed (Sittler & Guhathakurta 1999; Exarhos & Moussas 2000). Alfvén waves are dominant in coronal regions that have open magnetic field lines, that is, coronal holes, and thus they leak into the fast solar wind (Cranmer & van Ballegooijen 2005). Within solar wind at 1 au, their average velocity is about  $57 \text{ km s}^{-1}$  (Veselovsky et al. 2010) – for more details about the Alfvén velocity see Appendix A.4.

The plasma in open coronal regions expands superradially, following the magnetic field lines. However, the field strength decreases with increasing solar distance and at a distance of about  $2.5 R_{\odot}$  the thermal pressure becomes larger than the magnetic pressure. Thereby the magnetic field gets frozen within the plasma and is carried by the solar wind radially outwards into the heliosphere. The distance from which the solar wind propagation gets released from the magnetic field lines is called the source surface (Schatten et al. 1969) and the thermal to magnetic pressure ratio is termed plasma beta – for more details on plasma beta see Appendix A.3. The magnetic field changes from superradial expansion below the source surface to a radial configuration above it, this field geometry is also visible in the total eclipse image in Figure 2.3.

Open field lines expand over adjacent closed field regions. Above the cusps of these regions' closed loops, the surrounding plasma flows encounter each other and stream outwards, forming so-called helmet streamers. Above these helmet streamers, magnetic boundaries are created by plasma flows carrying opposite magnetic polarity. These boundaries constitute an extensive coronal neutral line around the Sun. Within the heliosphere, the two dominating magnetic polarity regions, originating from both solar magnetic poles, are separated by the extension of this neutral line: a large plasma boundary surface, termed the heliospheric current sheet (HCS) (Smith 2001).

In the quiet Sun during solar cycle minimum conditions, coronal holes are the main photospheric sources of the heliospheric magnetic field. The magnetic dipole axis is then near the rotation axis and thus the HCS is roughly located near the equatorial plane, dividing both hemispheres. The analytical solar magnetic field model for solar minimum conditions, constructed by Banaszkiewicz et al. (1998), shows this field geometry as seen in Figure 2.11. The quadrupole part of their dipole plus quadrupole plus current sheet (DQCS) model considers the closed equatorial fields and allows equatorial outflow along the current sheet. Around solar minimum, the HCS's warped surface typically looks like a wavy ballerina skirt, due to the varying tilt angle between the dipole axis and the rotation axis, see Figure 2.12, and also due to local magnetic field variations (Jokipii & Thomas 1981).



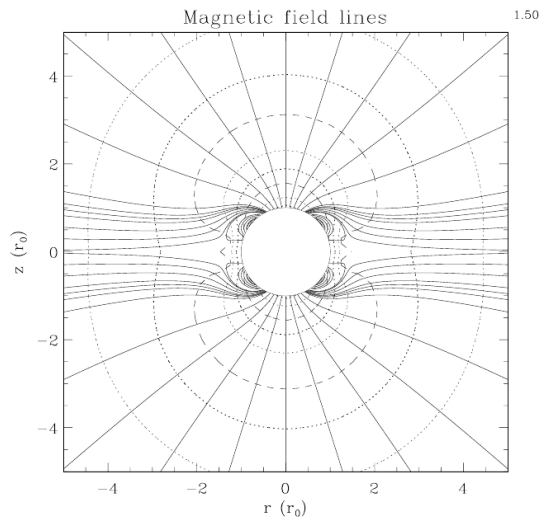


**Figure 2.11** Model of the solar magnetic field geometry in the polar plane for solar cycle minima. Magnetic field lines (solid) and constant field strength surfaces (dashed) from the DQCS model are plotted. The field line spacing does not represent the field strength but provides better detail where needed. Credit: Banaszkiewicz et al. (1998, Fig. 3), © ESO, reproduced with permission.

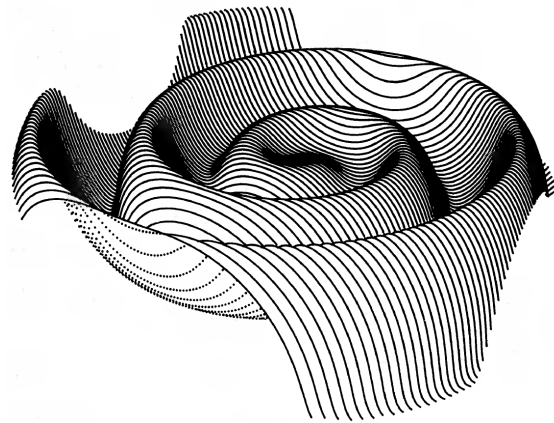


**Figure 2.12** A simple HCS model, where its wavy surface shape solely stems from a solar dipole tilt of  $15^\circ$  to the rotation axis. The figure's extent is 25 au across. Credit: (Jokipii & Thomas 1981, Fig. 2), © AAS, reproduced with permission.

During the field transition at solar maximum, the dipole axis shifts to lower latitudes, crosses the solar equator, and eventually the field ends up in a reversed dipole configuration (Jones et al. 2003). During this process, the HCS rotates almost rigidly together with the dipole axis and remains a single connected structure in the inner heliosphere (Jones et al. 2003). Hence during cycle maximum, the HCS has a very complex shape, is largely inclined to the solar equator, and reaches near-polar latitudes.

The solar wind source surface rotates with the Sun and thus shears the HMF into an Archimedean spiral pattern, adding an azimuthal component to the radial HMF. This geometry was anticipated by Parker (1958) and is today called Parker spiral. The Parker spiral, viewed in the ecliptic plane, is illustrated in Figure 2.13. The solar rotation axis tilt of up to  $7.25^\circ$  to the ecliptic leads to a slight diving into both hemispheres of opposite polarity. Thus, together with the ballerina topology of the HCS, the Parker spiral has typically a structure of either two or four sectors of alternating magnetic polarity (Ness & Wilcox 1965), which are separated by the HCS.

The HMF geometry just described is also overlaid by other magnetic structures than the HCS. Speed differences between solar wind streams, and between solar wind and CMEs cause enhanced field amplitudes and can result in shocks in the HMF. Furthermore, CMEs in the solar wind carry magnetic clouds (MCs) and their frequency and magnetic configuration vary with the solar activity cycle. These solar wind and CME structures are described in more detail in the following sections.

That way, the magnetic field and its structures are carried out to the termination shock by the solar wind. MHD simulations, based on in-situ measurements of Voyager 1 and 2 within the heliosheath and based on IBEX observations of energetic neutral atoms, provide indications about the outer structure of the heliosheath. Behind the termination shock, the magnetic sector boundaries are compressed and they reconnect, forming magnetic bubbles (Opher et al. 2011). These bubbles – unconnected to the HMF – flow away to the heliosheath tail region. Even beyond the termination shock, the solar wind plasma seems confined and collimated by the twisted solar magnetic field and driven into a northern and a southern jet (Opher et al. 2015). Hence, the Sun's magnetosphere has likely a croissant-like shape with two turbulent tail-lobes, where eventually the solar wind with the HMF is being mixed into the interstellar medium.

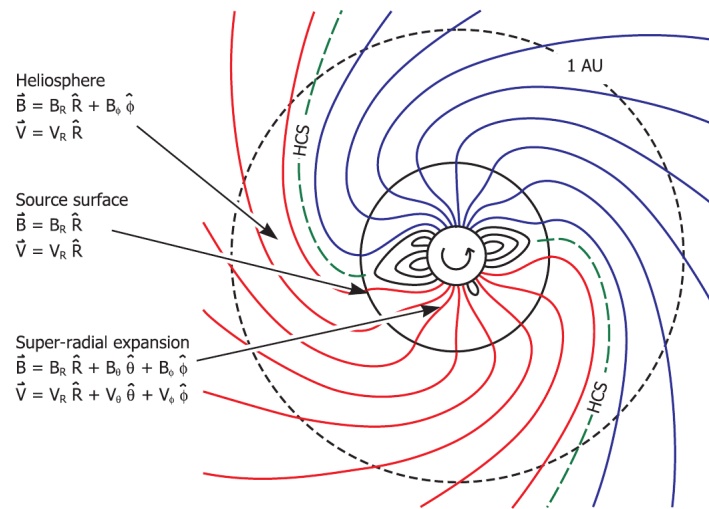


**Figure 2.13** Illustration of the Parker spiral formation in the ecliptic plane outside the source surface. The HCS (green) is located between solar wind flows of opposite magnetic field polarity (red/blue). Credit: Owens & Forsyth (2013, Fig. 1), adapted from Schatten et al. (1969, Fig. 1), licensed under CC BY-NC 3.0 DE.

## 2.5 Solar wind

It is observed that cometary ion tails point away from the Sun and lag only a few degrees from the radial direction, sometimes they also show fluctuations and become kinked. As such behavior could not be explained by interaction with sunlight pressure, eventually Biermann (1951) concluded that cometary ion tails are influenced by a continuous flow of particles from the Sun. Parker (1958) considered the consequences of Biermann's conclusions and built a solar wind model, adopting an expanding isothermal solar atmosphere. Parker also incorporated the implications for the solar magnetic field in his model and hence he laid the theoretical foundations for a continuous supersonic radial outflow of magnetized plasma. Thus, the existence of the solar wind was postulated before the first satellites measured it in situ in 1959 (Gringauz et al. 1960; Neugebauer & Snyder 1966). Since that time, spacecraft are able to measure the solar wind almost continuously with magnetometer and plasma instruments in situ (see Chapter 3). Pronounced solar wind structures, such as CMEs and streamers, become visible with the use of space-based coronagraph imagers. From Earth, the near-Sun outflow geometry of solar wind can be observed only during solar eclipses, see the eclipse photo in Figure 2.3.

The solar wind is a magnetized plasma consisting of electrons and ions. The ions are mainly composed of hydrogen, a small percentage of helium, and traces of oxygen, carbon, and other metals. The average abundance of helium is about 4.5 % and in slow wind at solar cycle minimum conditions less than 2 % (Feldman et al. 1978; Schwenn 1983; Kasper et al. 2012). The solar wind is commonly approximated by an ideal incompressible MHD plasma (viscosity  $\mu = 0$  and electrical conductivity  $\sigma = \infty$ ) and can be viewed as a neutral plasma. Also, its helium share is often viewed as being constant, in this case the proton density determines both the helium and electron densities.

The properties of solar wind are highly variable in time and space. The key properties are determined by the values of the solar wind parameters magnetic field strength, proton velocity, density, and temperature. Their average magnitudes scale with solar activity, heliographic latitude, and solar distance. At the solar distance of Earth however, most of the time these parameters' typical values lie in the ranges 3–8 nT, 300–500 km s<sup>-1</sup>, 2–8 cm<sup>-3</sup>, and 10<sup>4</sup>–10<sup>5</sup> K (Kivelson & Russell 1995, p. 92; Venzmer & Bothmer 2018). The low density of solar wind can be illustrated with a short comparison: 1 liter of air at standard pressure, expanded to a typical solar wind density of 6.5 cm<sup>-3</sup>, would occupy a volume of a cube with edge length of about 155 km. Solar wind quantities, such as particle flux densities, mass flux, pressures, and plasma beta, can be derived from the four listed parameters. Having the parameters in the aforementioned ranges, the solar wind is a plasma with a beta mostly greater than unity, that is, the average solar wind carries the magnetic field and its motions are not influenced by the field direction (for more on plasma beta see Appendix A.3).

However, solar wind is structured by its different sources in the solar corona. It consists of fast continuous streams, slow variable flows, and transient CME events. These different flows have highly variable velocities, which result in compressed or rarefied regions at their interfaces. Additionally, the source region's magnetic field configuration organizes the interplanetary magnetic field (IMF), transported within the solar wind plasma. Regardless, pronounced magnetic structures embedded in the solar wind, such as field polarity changes or magnetic clouds, still influence the properties of the plasma.

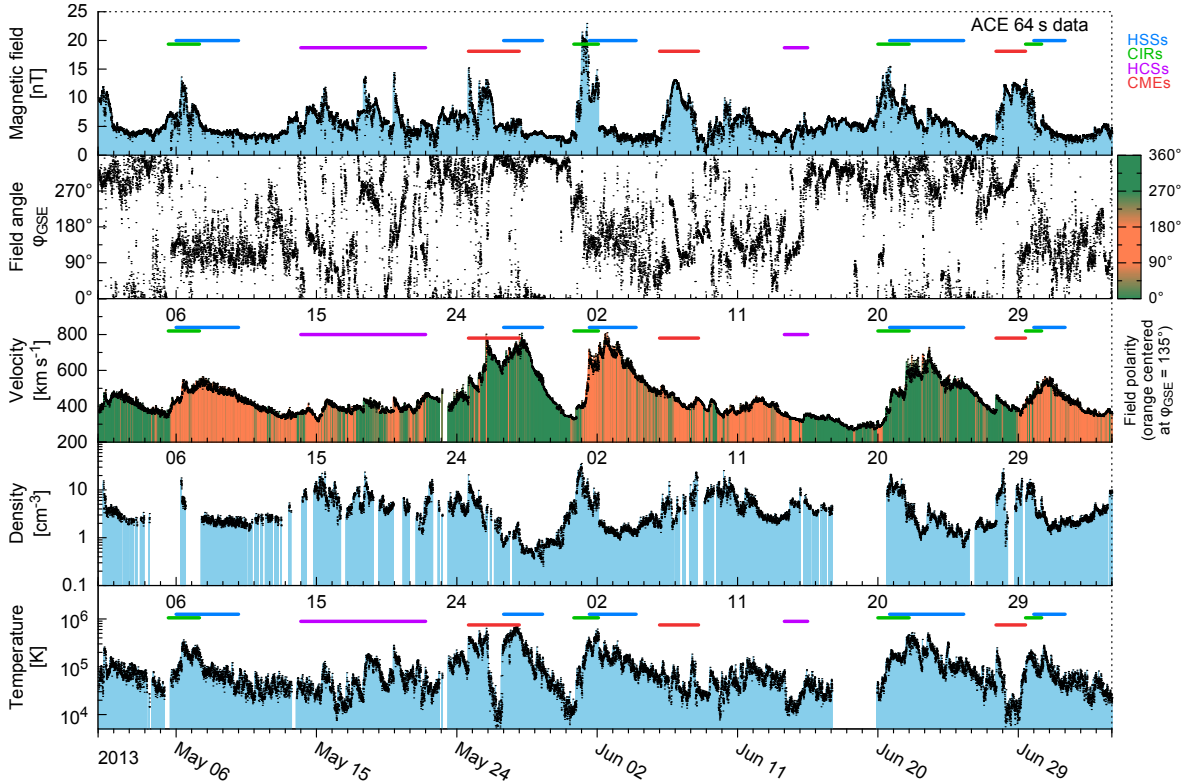


**Figure 2.14** Solar wind with several structures, measured at L1 during the time period 1 May to 5 July in 2013. The plotted parameters are the magnetic field strength, its field angle in the ecliptic in GSE coordinates, the proton velocity, density, and temperature. I indicated periods of prominent solar wind structures with color bars: HSSs in blue, CIRs in green, HCSs in purple, and CMEs in red. In the velocity panel also the field polarity is color coded – assuming a Parker spiral angle of  $135^\circ$  at L1. Blank periods indicate bad or missing data. The data are 64 s measurements from the ACE spacecraft.

This multitude of structures is apparent in the two months – beginning in May 2013 – of in-situ measured solar wind, which I present as an example period in Figure 2.14. The IMF and solar wind plasma parameters were measured with the MAG and SWEPAM instruments on board the Advanced Composition Explorer (ACE) spacecraft, located around the first Lagrange point (L1). The data have a time resolution of 64 seconds and are obtained from the ACE Science Center web interface<sup>7</sup>.

Some general solar wind tendencies can be seen from this plot: The temperature of the solar wind scales with its stream velocity; compressed plasma regions enhance the magnetic field and the density; HCSs, magnetic sector boundaries, and MCs come with high densities and low temperatures; MCs in CMEs have high magnetic fields and low temperatures. I indicated the periods of occurring solar wind structures, that is, HSSs, CIRs, HCSs, and CMEs, with colored bars – these types are further described in the following sections.

### 2.5.1 Slow and fast streams

It is observed at 1 au that the continuous solar wind comes in streams roughly focused at two major velocity ranges (Neugebauer & Snyder 1966; Schwenn 1983), slow and fast streams with  $250\text{--}450\text{ km s}^{-1}$  and  $450\text{--}800\text{ km s}^{-1}$  respectively. Both types possess differences in their typical characteristics and ion compositions. Apart from its higher speeds, fast solar wind has most prominently lower proton densities ( $\sim 3\text{ cm}^{-3}$ ) and higher temperatures ( $\sim 2 \times 10^5\text{ K}$ ) than the slow solar wind, which has higher densities ( $\sim 10\text{ cm}^{-3}$ ) and lower temperatures ( $\sim 4 \times 10^4\text{ K}$ ) (Schwenn 1990). The fast solar wind has a nature of coming in steady high-speed streams (HSSs) with a unique magnetic field polarity, whereas slow solar wind is much more variable in all its properties except its velocity (Bame et al. 1977). HSSs are further overlaid with Alfvén waves, which modulate the stream velocity with typical periods of 15–60 min.

First soft X-ray observations of the corona, made during sounding rocket flights in the early 1970s, showed clearly that the fast solar wind emerges from extended areas of reduced X-ray emission, subsequently called

<sup>7</sup>ACE Science Center website: <http://www.srl.caltech.edu/ACE/ASC/>

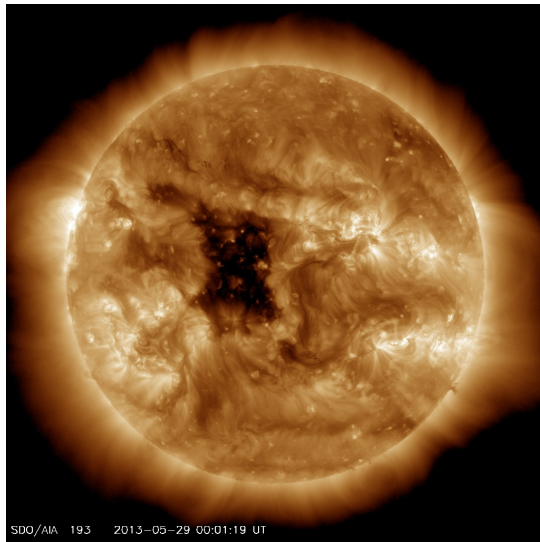


**Figure 2.15** Image of the solar corona during solar cycle maximum from 29 May 2013, seen in a wavelength of 193 Å. The dark area near the center of the solar disk is an equatorial CH, typical for high solar activity conditions. Credit: NASA/SDO and the AIA, EVE and HMI science teams.

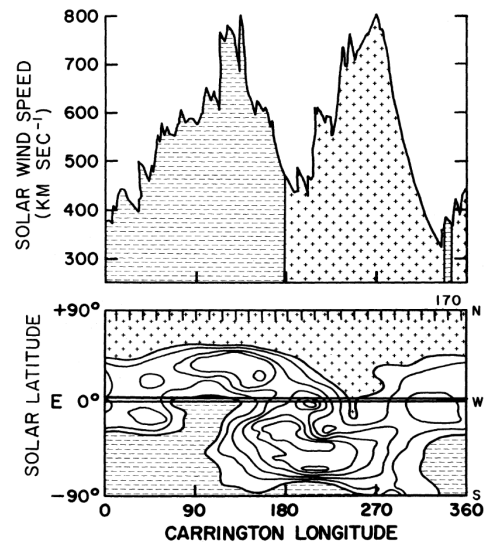


**Figure 2.16** Solar wind velocity with respect to its estimated source longitude (top) and coronal brightness contour map at  $0.5 R_{\odot}$  above the photosphere (bottom) for the Carrington rotation 1616. The velocity is based on IMP spacecraft data, back-extrapolated to  $20 R_{\odot}$ . Brightness values below a fixed threshold are shaded corresponding to the magnetic field polarity (+/-) of the underlying photosphere. The map is based on observations from the K-coronameter at the Manua Loa Observatory. Credit: Hundhausen (1977, Fig. 10), © Colorado Associated University Press, reproduced with permission.

coronal holes (CHs) (Krieger et al. 1973; Hundhausen 1977). A small equatorial CH, located near the center of the solar disk, is shown in the SDO/AIA image taken on 29 May 2013, see Figure 2.15. This particular CH is most likely responsible for the HSS observed at L1 on 1–5 June 2013, visible in the previous solar wind plot in Figure 2.14. The magnetic field polarities found in CHs are associated with the magnetic field directions observed in HSSs, as seen in Figure 2.16. In coronal regions with closed magnetic field lines, the plasma is trapped, though in CHs it can escape, following the open magnetic field lines outwards into space. Wave-particle interactions heat and accelerate the ions in CHs, likely leading to the emission of the fast solar wind (Hollweg & Isenberg 2002). Superradial expansion of the magnetic field lines in the corona has an influence on the wind speed – actually the expansion factor is anticorrelated with the final wind velocity (Wang & Sheeley 1990). As the field expansion is larger near the border of CHs, faster wind emerges from the mid regions of CHs, forming into HSSs. However, there are indications that the slow and fast solar wind are not only generated at different sources but from distinct mechanisms (McGregor et al. 2011a).

The high variability in the slow solar wind points to the existence of different types of slow wind flows, originating from separate coronal locations and mechanisms (Schwenn 1983). It is still under debate if the variability is produced by the formation mechanism of the slow solar wind or if the variability is caused during the acceleration/propagation phase (Sanchez-Diaz et al. 2016). Still, at least a part of its variability can be attributed to the interactions between slow and fast solar wind, which result in a general reduction in velocity differences and thus let solar winds of different speeds (having different properties as well) converge to a common intermediate speed regime in the range  $400\text{--}500 \text{ km s}^{-1}$  (McGregor et al. 2011b; Sanchez-Diaz et al. 2016). Studies using remote white-light tracing of coronal material and in-situ measurements of solar wind suggest that multiple sources of slow solar wind flows exist (Wang et al. 2000; Kilpua et al. 2016). To the best of my knowledge, the generally considered sources are listed in the following:

- CH boundaries and small CHs, because their plasma outflow is slower due to the high superradial expansion of its open field lines (Wang & Sheeley 1990).
- CH boundaries, when trapped plasma is released by reconnection between open and closed field lines (Madjarska et al. 2004).
- Helmet/pseudo-streamers in active regions, where transient plasma blobs are released from the cusps of closed field loops (Wang et al. 1998, 2000). This slow and dense material is associated with the



heliospheric plasma sheet belt.

- Edges of active regions, which have hot plasma outflows with a single magnetic polarity (Kojima et al. 1999).
- Jets originating from coronal bright points might contribute to the slow solar wind (Subramanian et al. 2010).
- Slow unidentified CMEs can contribute to slow wind observations as well, as noted by Wang et al. (2000).

It is found to be difficult to use in-situ measurements for tracing the slow solar wind flow types to different origins and to distinguish between them, because most properties are also highly variable in time (Kilpua et al. 2016). However, some indicators show tendencies to differentiate between the slow winds from different source regions. Notable indicators are: elemental ion ratios, heavy ion charge states, and the specific entropy.

The elemental composition of the coronal plasma varies with height/location in the solar atmosphere, therefore the solar wind's elemental ion ratios (e.g., He/H, Fe/O) are used to determine its origin. The charge states of coronal heavy ions depend on the local temperature. However, the density of the outwards expanding plasma decreases fast, preventing further ionization/recombination. The charge states decouple from the local temperature and freeze in close to the Sun. Thus, heavy ion charge ratios (e.g.,  $C^{+6}/C^{+4}$ ,  $O^{+7}/O^{+6}$ ) in the solar wind track the coronal source temperature and especially the  $C^{+6}/C^{+4}$  ratio is sensitive to the solar wind type (Landi et al. 2012). During solar minimum, the specific proton entropy is found to correlate with the  $O^{+7}/O^{+6}$  ratio and thus able to trace slow solar wind sources as well (Pagel et al. 2004).

The solar wind stream pattern varies strongly with solar activity. The Sun's ordered dipole structure during solar cycle minima leads to polar regions with open magnetic fields, constituting large coronal holes, and to a large equatorial belt region with closed magnetic fields – this is clearly visible in Figures 2.3 and 2.11. This state results in fast solar wind coming exclusively from the poles and higher latitudes, whereas active regions form an equatorial streamer belt around the Sun, emitting slow solar wind. This structure was confirmed from solar wind speed measurements done by the Ulysses spacecraft, which flew in an out-of-ecliptic solar orbit and whose mission covered a duration of more than one solar cycle (McComas et al. 2008a), see Figure 2.17. The

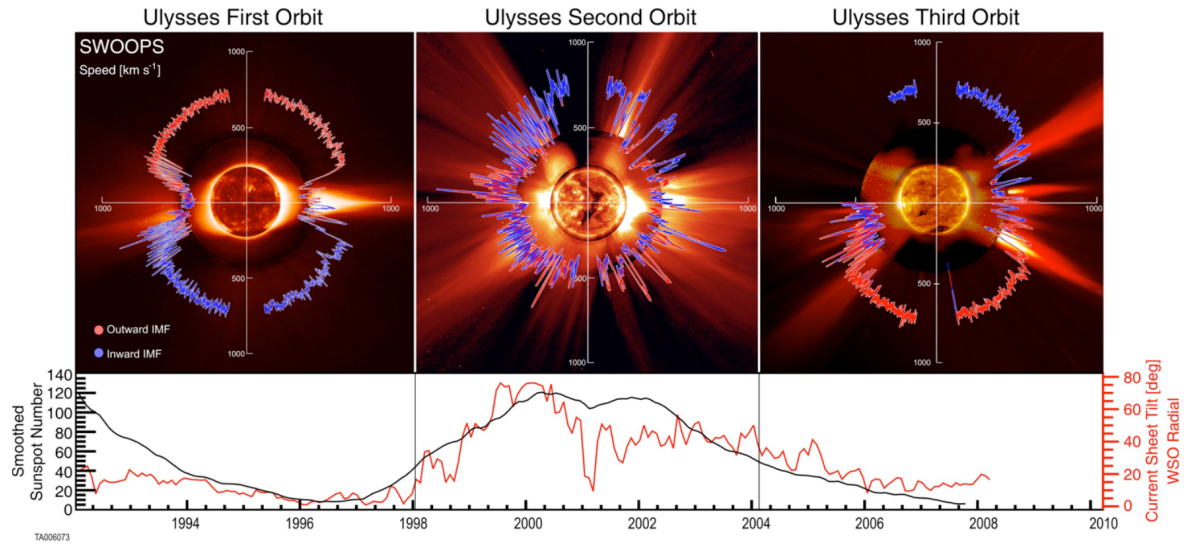


**Figure 2.17** Solar wind velocity and magnetic field polarity (red/blue) with respect to heliographic latitude for the three orbits of the Ulysses spacecraft during low and high solar activity (upper panels). The data starts top left and runs counter-clockwise. The corresponding smoothed SSN (black) and HCS tilt angle (red) are plotted beneath. The background consists of solar images for solar cycle 22 minimum (1996-08-17), solar cycle 23 maximum (2000-07-12), and solar cycle 23 minimum (2006-03-28). The solar disk, inner corona, and outer corona images are respectively from SOHO/EIT (Fe XII at 1950 nm), Mauna Loa K coronameter (700–950 nm), and SOHO/C2 white light coronagraph. Credit: McComas et al. (2008a, Fig. 1), © American Geophysical Union, reproduced with permission.

transition of the solar magnetic field during the solar cycle maxima induces the chaotic appearance of closed magnetic fields at higher latitudes and even near the poles. Furthermore, coronal holes begin to invade parts of the equatorial region, leading to recurring phases of HSSs in the ecliptic. This can be seen from the solar wind period in Figure 2.14, where recurrent HSSs of the same field polarity but changing peak velocity exist – beginning on 6 May, 2 June, and 29 June 2013. Succeeding streams of different velocity result in interaction regions and alternating magnetic polarities result in magnetic sector boundaries.



### 2.5.2 Stream interaction regions

The sources of the slow and fast solar wind rotate together with the Sun. Their uneven longitudinal distribution on the solar surface – due to a significant inclination of the dipole axis or variations of the solar magnetic field – leads to the alternation of slow and fast wind streams that flow into the heliosphere (Owens & Forsyth 2013). In case of a fast stream being followed by a slow stream, a rarefaction region expands at their interface. In the opposite case, the stream of fast solar wind catches up to that of slow wind ahead of it and a compression region forms at their interface, which is encompassed by two compressional waves (Balogh & Jokipii 2009). The latter cases are called stream interaction regions (SIRs) and they take the shape of spiral fronts, as seen in the left panel of Figure 2.18.

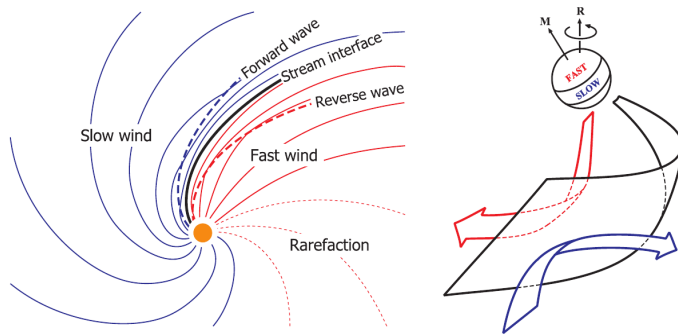


**Figure 2.18** Schemata of the formation of a stream interface (left) and the deflection of streams along the interface (right). The stream interface (black) is located between regions of slow (blue) and fast (red) solar wind. Credit: Owens & Forsyth (2013, Fig. 7), right panel adapted from Pizzo (1991, Fig. 2), licensed under CC BY-NC 3.0 DE.

When the solar dipole field is in a quasi-stable configuration, SIRs can stay for multiple solar rotations, recurrently sweeping over the heliosphere in 27-day periods (Gosling et al. 1972). Hence, they are referred to as co-rotating interaction regions (CIRs) (Smith & Wolfe 1976; Balogh et al. 1999). In the ecliptic at 1 au, CIRs occur commonly during the declining phase of the solar cycle when polar CHs form equatorial extensions (Balogh & Jokipii 2009).

The spiral shape of the stream interfaces and their inclination to the solar rotation axis lead to a deflection of both streams (Balogh & Jokipii 2009). Due to the fast and slow streams' collision, the fast wind is decelerated whereas the slow wind is accelerated. Their flow directions are systematically deflected away from the interface, as shown in the right panel of Figure 2.18.

The plasma pressure inside SIRs is increasing with heliocentric distance and therefore, the leading and trailing compressional waves form into forward and reverse shocks – typically at solar distances between 2–10 au (Smith & Wolfe 1976; Balogh & Jokipii 2009). The solar wind speed increases abruptly at both shock fronts. With increasing solar distance, the leading and trailing shock fronts travel away from the stream interface. This widens the interaction regions and eventually they catch up on the close-by interaction regions (Burlaga et al. 1984). Beyond 10 au they can fuse to merged interaction regions, which are narrower and more compressed (Burlaga et al. 1985).

Due to the compression within SIRs, the magnetic field strength and the plasma density are higher than in the ambient streams. These signatures can be seen in the in-situ solar wind plot in Figure 2.14. The CIRs on 5 May, 1 June, and 29 June 2013 are followed by recurrent HSSs and they contain sector boundaries as well. They are not yet accompanied by strong shocks owing to the measurement location at 1 au.

### 2.5.3 Heliospheric current sheet

The heliospheric current sheet (HCS) is the boundary surface between solar wind streams of opposite magnetic polarity. It is formed by open magnetic fluxes, expanding from both sides over closed field regions and coming into contact above. At the boundary between open and closed fields, local coronal plasma gets released and flows slowly between the fast wind streams along the current sheet into the heliosphere, creating a helmet streamer. This is why near the Sun, the HCS is typically located within slow solar wind stemming from the coronal streamer belt (Owens & Forsyth 2013). However, with increasing solar distance, the shock wave of an adjacent SIR can pass the HCS, so that sector boundaries are often found to be embedded within SIRs (Gosling & Pizzo 1999).

When sector boundaries in the solar wind are observed in situ, they show significant depletions in  $\text{He}^{++}/\text{H}^+$  values (Borrini et al. 1981). The other solar wind parameters, such as velocity, density, and temperature, change with distance from the HCS as well (Smith 2001). The HCS region itself is quite narrow with a thickness of around 3000–10 000 km; it is embedded in a region of 20–30 times its thickness, the heliospheric plasma sheet (HPS) (Winterhalter et al. 1994). The HPS contains the magnetic polarity reversal and is of low magnetic field

strength and high density, resulting in a significantly enhanced value of plasma beta (Crooker et al. 2004). In the slow solar wind, the HPS can also be identified from its particularly low specific entropy, arising from its low temperature and high density (Kilpua et al. 2016).

### 2.5.4 Coronal mass ejections

Coronal mass ejections (CMEs) are eruptions of coronal magnetized plasma, which expand within hours to bubbles with sizes of several solar radii. They continuously expand further while moving farther away from the Sun into the heliosphere, with velocities often surpassing even the high speed solar wind. When measured in-situ in interplanetary space, they are often called interplanetary CMEs (ICMEs). Such transient structures are found to be shot into the ambient slow and fast solar wind streams. ICMEs typically have durations of a few days. They make up about 5 % of the solar wind's flow share during solar cycle minima, but can represent up to about 50 % during solar cycle maxima (Richardson & Cane 2012). Indeed, their frequency correlates with the sunspot number (Hildner et al. 1976) and follows solar activity in amplitude and phase (Webb 1991).

Long before the origins of geomagnetic disturbances were actually attributed to CMEs, a solar influence was identified as their source by Carrington (1859). However, CMEs turned out to be the major drivers for strong geomagnetic storms, because they carry the most extreme conditions found in the solar wind. Thus, they are of major importance to space weather – their impacts on the terrestrial magnetosphere are covered in Section 2.6.

Here I cover the CME formation processes only briefly, as this work focuses on in-situ measurements. Generally speaking, CMEs are products of the instability in the coronal magnetic field. The solar differential rotation wraps the coronal magnetic field, which is rooted at the surface. Accumulated tension and emerging magnetic flux eventually initiate sudden field reconfigurations. These field line reconnections result in a lower state of potential energy, releasing a lot of energy in form of solar X-ray flares and CMEs. Indeed, CMEs are often associated with flares and eruptive prominences, coming from their source regions (Webb & Hundhausen 1987). The sources of CMEs are located near bipolar regions and are frequently identified with eruptive prominences (Subramanian & Dere 2001).

CMEs emerge from coronal magnetic flux rope structures that hold plasma filaments embedded along their base (Webb & Hundhausen 1987; Cremades & Bothmer 2004). Reconfiguration of the ambient magnetic field can lead to a release and a subsequent ascend of the flux rope through the corona. During this process, the filament is lifted by the flux rope and forms a prominence eruption. The accompanying sudden magnetic reconnections often cause a multitude of other dynamic coronal phenomena: enhanced X-ray flaring; the formation of post-eruptive arcades where a filament disappeared; local decreases in soft X-ray intensity (coronal dimmings) due to depletion of the plasma density caused by magnetic field expansion; and large-scale coronal disturbances observed in extreme ultraviolet (EUV-waves) that can spread across the whole solar corona.

The onset of CMEs is often accompanied by solar energetic particles (SEPs) and by solar radio bursts. SEPs consist of protons, electrons, and ions with relativistic energies that can cover the distance to Earth within half an hour and pose a radiative threat to humans in space. The intensity of energetic protons correlates well with the CME speed (Kahler et al. 1978) and it is established that these coronal particles are accelerated by shocks formed in front of the rapidly expanding magnetic structures of CMEs in the corona (Cliver et al. 1982; Gosling 1993). Solar radio bursts are radio emissions from the corona that change over time in frequency space. There are different kind of radio bursts, but especially type II radio bursts are seen as indicators for coronal shocks that accelerate electrons. They are emitted in the low corona and are drifting to lower frequencies over time. There is still a debate whether type II bursts originate from flares or CMEs, favoring the latter (Gosling 1993; Cliver et al. 2005; Cho et al. 2011).

CMEs were detected in the white-light observations of the K-corona made by the first space-based coronagraphs on board the OSO 7 satellite (Tousey 1973) and the Skylab space station (MacQueen et al. 1974). These observations show the steady outflow of solar wind, broken by intermittent ejections of coronal plasma. Subsequently, the kinematic properties of CMEs were identified from the white-light images (MacQueen 1980). Now, coronagraphs observe the corona (and hence CMEs too) continuously from the first Lagrange point (L1) in front of Earth with the SOHO spacecraft and from changing equatorial perspectives with the STEREO Ahead (A) and Behind (B) spacecraft. The image of the corona from 26 February 2000, made by the LASCO/C3 coronagraph on board SOHO, shows such a CME with a detailed three-part structure, see Figure 2.19. This typical structure consists of a bright frontal loop, trailed by a dark cavity with a bright core.

It was early determined by Gold (1962) that solar ejecta should drive shock waves ahead. In fact, shocks with trailing low proton temperatures caused by fast CMEs were then found in in-situ measurements (Gosling et al. 1973, 1974). Burlaga et al. (1981) analyzed magnetic field and plasma data from five spacecraft and identified a shock wave with a trailing turbulent sheath region followed by an organized helical magnetic structure that they called a magnetic cloud (MC). MCs have an enhanced magnetic field, a smooth rotation in the magnetic field

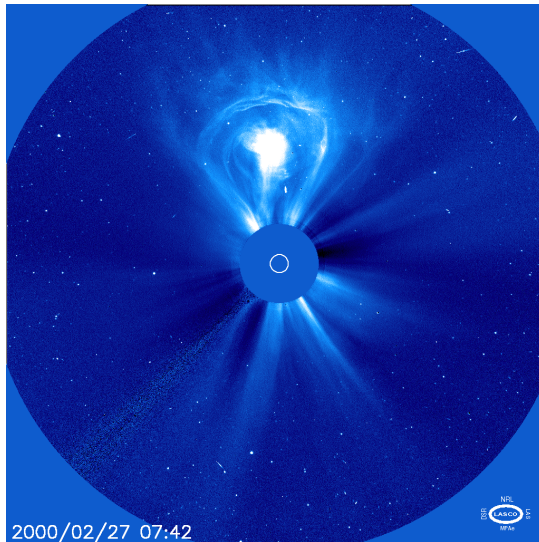


**Figure 2.19** Image of the solar corona out to  $30 R_{\odot}$  from 26 February 2000 taken by the LASCO/C3 coronagraph on board the SOHO spacecraft. The solar disk is covered by the occulter disk and its position is indicated by the white circle. The bright blob at the top is a CME with a detailed three-part structure; the smooth elongated radial lines are solar wind streamers. Courtesy of SOHO/LASCO consortium; SOHO is a project of international cooperation between ESA and NASA.

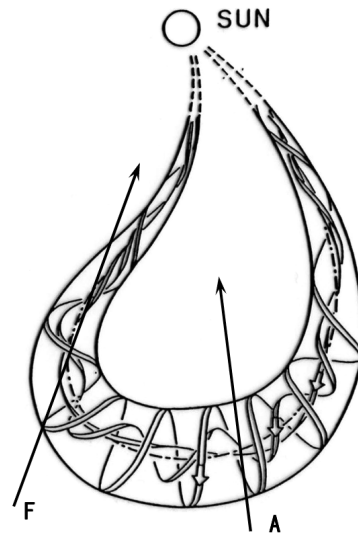


**Figure 2.20** Schema of a magnetic flux rope structure in a CME. The arrows depict passings through its flank (F) and its apex (A). Credit: Marubashi & Lepping (2007, Fig. 1, panel (a)), licensed under CC BY 3.0.

vector and they show low densities and temperatures (Burlaga et al. 1981). Thus, MCs have a low thermal to magnetic pressure ratio (i.e., a small plasma beta) and the magnetic field dominates the plasma. Furthermore, the overall pressure in MCs is higher than in the ambient solar wind, resulting in the expansion of MCs on their way out. Shock-driving CMEs containing a helical MC are actually identified with magnetic flux ropes that expand self-similarly and that remain in connection with the solar surface (Chen et al. 1997). The surface connection is indicated by bi-directional streams of electrons that are found in MCs (Gosling et al. 1986). The shape and magnetic topology of such a magnetic flux rope is pictured in Figure 2.20. It is apparent that in-situ measurements should look significantly different depending on where the CME is pierced.

Such solar wind in-situ measurements reveal the magnetic structure of CMEs. In particular, the orientation of magnetic flux ropes can be determined by applying a minimum variance analysis (MVA) to the MCs' magnetic field components (Sonnerup & Cahill 1967; Burlaga & Behannon 1982). An MVA determines the direction of minimum variance in the sequence of field vectors passing by during an MC encounter. The principal axis of the flux rope can be derived from the pattern of the field components orthogonal to the direction of minimum variance.

Bothmer & Schwenn (1998) used the MVA on an extensive set of MCs which they found in the data of the Helios 1 and 2 probes. They related the results with the magnetic polarity structures of the MCs' apparent solar source regions. Connecting the derived flux rope directions with the orientation of disappearing filaments and magnetic neutral lines on the solar surface, they recognized a scheme that is able to infer the orientation and helicity of MCs found in CMEs. This Bothmer-Schwenn scheme (BSS) relates these magnetic flux rope properties to whether the solar cycle number is even or odd and depending on which solar hemisphere the CME originates from (northern/southern) – utilizing that the hemispheric polarity is alternating with each solar cycle, see Figure 2.21. As the probability is greater than 80 % that the magnetic topology of an active region conforms to the hemispheric rule (Wang 2013), an MC configuration predicted with the BSS is expected to have a reliability that is of the same order (Savani et al. 2015).

Three CMEs can be seen in the solar wind in-situ measurements showed previously in Figure 2.14, passing by the ACE spacecraft at L1 on 24 May, 6 June, and 27 June in 2013. The latter CME has a well-structured MC, which is presented in detail in Figure 2.22 – I use this event as an example throughout this section. In addition to presenting the solar wind in-situ parameters, I indicated the shock, the compression zone, and the MC with dotted lines, and added the geomagnetic  $K_p$  index in order to visualize the CME's impact on the magnetosphere. This MC contains a sector boundary and is trailed by an interaction region caused by a following HSS.

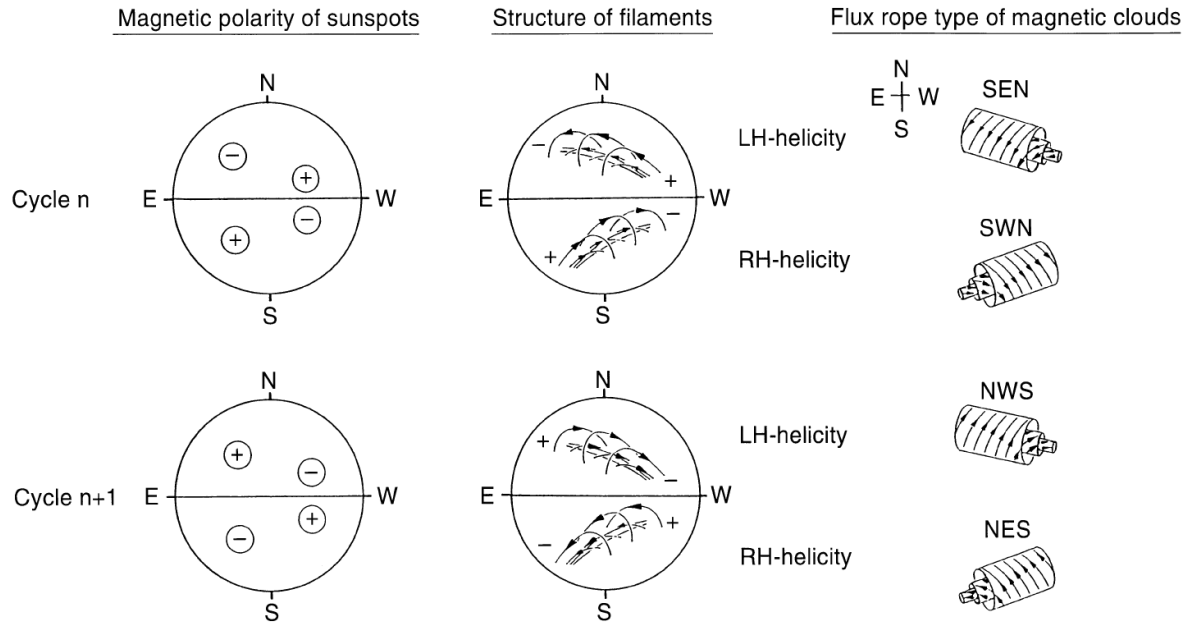


**Figure 2.21** Explaining sketch of the BSS. The two rows represent odd ( $n$ ) and even ( $n + 1$ ) solar cycle numbers. The magnetic polarity of sunspots, the structure of filaments, their helicity, and the corresponding flux rope type of magnetic clouds are shown. Credit: Bothmer & Schwenn (1998, Fig. 18), © EGS – Springer-Verlag, reproduced with permission.

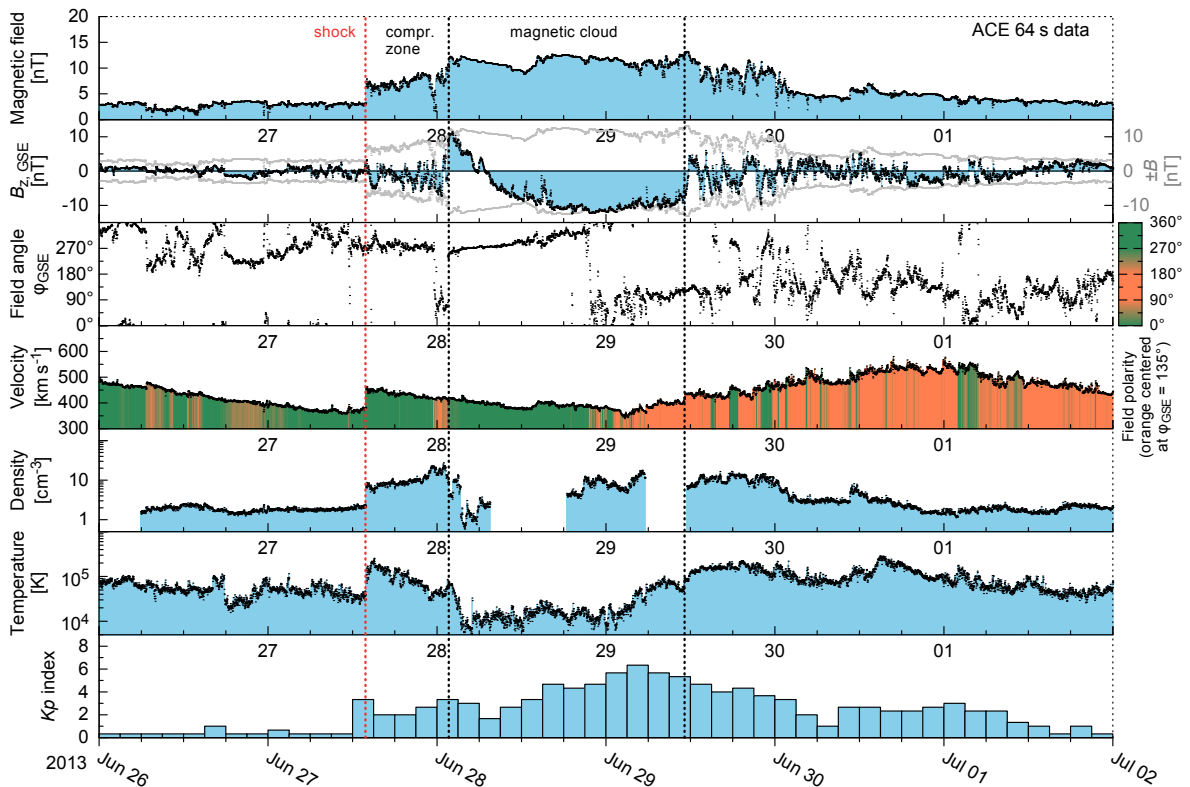


**Figure 2.22** Solar wind with a CME signature, measured at L1 during the time period 26 June to 2 July in 2013. The solar wind parameters are the magnetic field strength, its z-component and ecliptic field angle in GSE coordinates, the proton velocity, density, and temperature; in addition, the geomagnetic  $Kp$  index is plotted in the bottom panel. In the velocity panel also the field polarity is color coded – assuming a fixed Parker spiral angle of  $135^\circ$ . I indicated the shock, the compression zone, and the duration of the magnetic cloud with dotted lines. Blank periods indicate bad or missing data. The solar wind data was measured with the MAG and SWEPAM instruments on board the ACE spacecraft and is obtained from the ACE Science Center. The  $Kp$  data is obtained from the GFZ Potsdam.



The CME occurred in solar cycle 24. The MC's IMF z-component changes from positive (northern) to negative (southern) values – during this process, the field angle in the ecliptic,  $\phi$ , stays pointing roughly towards  $270^\circ$  (west). Thus, it has a NWS configuration, which is expected from the BSS during even numbered solar cycles for CMEs with source regions located in the northern hemisphere.

The combination of white-light images with in-situ data enables relating the observed structures of CMEs. Even disturbances in front of fast CMEs can be identified as shock waves in the white-light images made by the SOHO coronagraph (Sheeley et al. 2000). The diffuse leading feature of a CME is the shock sheath, its brightness is caused by the density jump after the shock, which itself is not visible in coronagraphs. The trailing void is identical to the low density of the magnetic flux rope, which drives the whole structure.

The CME described before is indeed coming from the northern hemisphere, as can be seen from the STEREO A coronagraph image displayed in Figure 2.23 taken three days earlier. Apparently, the CME reaches into the ecliptic so that its lower portion passes Earth. Also in this image, the event originates behind the solar limb, considering the observing spacecraft's position in relation to Earth at that time, see Figure 2.24.

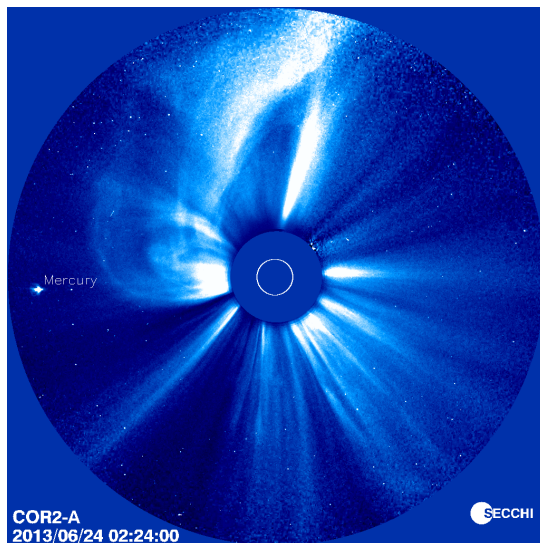


**Figure 2.23** Image of the solar corona out to  $15 R_\odot$  from 24 June 2013 taken by the SECCHI/COR2 coronagraph on board the STEREO A spacecraft. The solar disk is covered by the occulter disk and its position is indicated by the white circle. The CME is the extended structure to the upper left; the smooth elongated radial lines are solar wind streamers. Courtesy of STEREO/COR2 consortium (NASA).

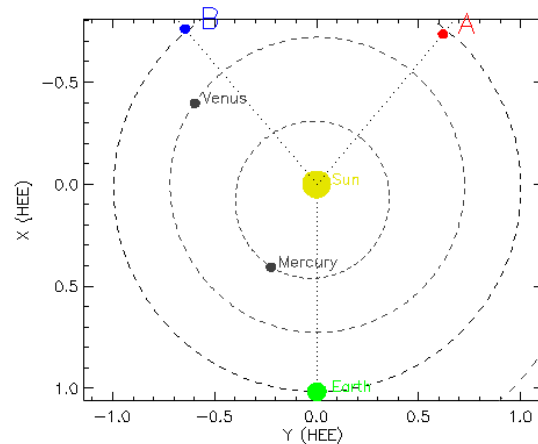


**Figure 2.24** Positions of the STEREO A and B spacecraft relative to Sun and Earth for 24 June 2013 02:24 UT. This figure is made with the online STEREO Orbit Tool at the STEREO Science Center website<sup>8</sup>.

Relating CME white-light images to observations of magnetic neutral lines on the solar surface, Cremades & Bothmer (2004) interpreted the white-light appearances of CMEs as projections of their 3D geometry and developed a scheme for their orientation depending on the orientation and location of the neutral lines on the solar surface. Neutral lines on the solar surface are the lines of polarity inversion between two areas of opposite magnetic polarity. The scheme is based on the topology of the flux rope model and the observation that its major axis stays roughly aligned to the underlying neutral line during the eruption process. Thus, Cremades & Bothmer (2004) concluded that CMEs look systematically different depending on their source region's position and magnetic configuration, as described in Figure 2.25. For the solar backside, the neutral lines are reversed and according to the scheme so are the CME orientations – thus the broad CME appearing behind the solar limb seen in Figure 2.23 matches this scheme. The scheme can effectively be applied for CMEs with source regions located less than  $50^\circ$  from the solar equator (Webb & Howard 2012).

This white-light CME projection scheme as well as the BSS for MCs are based on the notion that the orientation of flux ropes propagating outwards generally stays aligned with the neutral polarity inversion line on the solar surface where the filament erupted (Marubashi 1997; Bothmer & Schwenn 1998). In fact, it is shown that flux ropes are not likely to rotate significantly after their initiation but commonly maintain the orientation of their main axis parallel to the magnetic neutral line even in interplanetary space (Marubashi et al. 2015). How-

<sup>8</sup>STEREO Science Center website: <https://stereo-ssc.nascom.nasa.gov/>

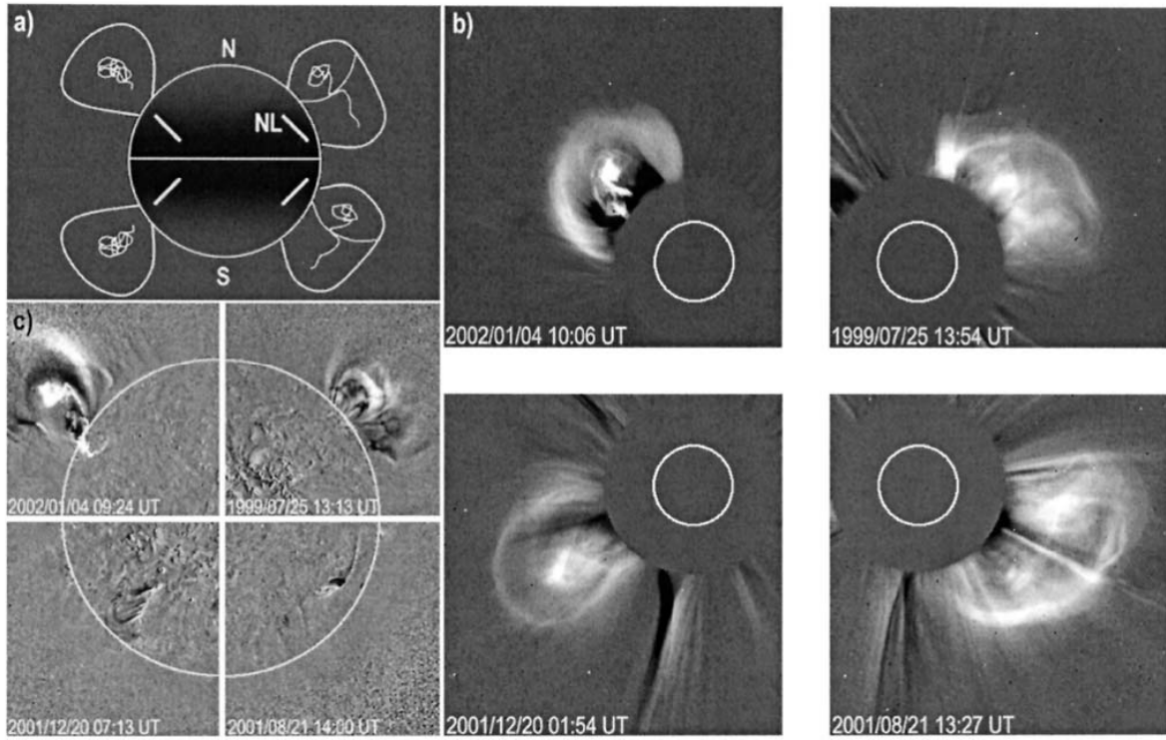


**Figure 2.25** White-light CME projection scheme for front-side events, showing the case for each quadrant of the solar disk. (a) Schema showing the expected white-light appearance of CMEs and the orientation of the underlying magnetic neutral lines. (b) White-light images of CME example events, made with the LASCO C2 coronagraph on the SOHO spacecraft. (c) Details (prominences and post-eruptive arcades) of the source regions related to the CMEs shown in panel (b). Note that for events originating from the backside, panel (a) has to be mirrored vertically. Credit: [Cremades & Bothmer \(2004, Fig. 15\)](#), © ESO, reprinted with permission.

ever, during and shortly after their eruption, CMEs are frequently observed to be deflected to other directions by the surrounding coronal magnetic field structure ([Sterling et al. 2011](#)).

The revelation that all CMEs may be flux ropes ([Vourlidas et al. 2013](#); [Marubashi et al. 2015](#)) led to the expansion of the CME definition based on white-light images made by [Hundhausen et al. \(1984\)](#). [Vourlidas et al. \(2013\)](#) and [Vourlidas \(2014\)](#) include magnetic flux ropes in their recent CME redefinition: “ACME is the eruption of a coherent magnetic, twist-carrying coronal structure with angular width of at least  $40^\circ$  and able to reach beyond  $10 R_\odot$  which occurs on a time scale of a few minutes to several hours.”

However, CMEs generally do not have a perfect flux rope geometry: Often their more complex structure can be seen in kinks of the corresponding filament before the eruption ([Bothmer & Mrotzek 2017](#)); and strong distortions can happen during the eruption process. Their cross section is only initially of circular shape, it distorts due to the pressure-driven self-expansion and the radial solar wind expansion ([Owens et al. 2006](#)). Though, the inner core of the flux rope is believed to stay of circular shape. For these reasons, the properties of CMEs vary widely and imaging projection effects contribute further to that ([Cremades & Bothmer 2004](#)).

There still exist a lot of unresolved questions about CMEs, their formation, and the effects observed along with them: Multiple mechanisms/processes are debated for the release of CMEs and their subsequent acceleration. It is also not known if there exist CMEs without magnetic flux ropes ([Vourlidas et al. 2013](#)). The relation between flux ropes observed in the near-Sun corona and measured in situ at interplanetary distances is still not entirely clear ([Vourlidas 2014](#)). Nobody knows yet when a CME will erupt on the Sun, at what exact time it will pass a given point in the heliosphere, and how its detailed magnetic configuration would look like in situ ([Gopalswamy 2016](#)).

## 2.6 Space weather

Space weather is the field of research that comprises all dynamic effects generated by the Sun itself but also from cosmic rays in the Sun's domain of influence – the heliosphere. Naturally, space weather is especially focused on the solar effects observed on Earth and in its local environment – the ionosphere and the magnetosphere. There exist several different effects caused by independent solar events occurring on different time scales that can affect humans directly and indirectly. Solar events affect sensitive technological systems and strong events are even able to disrupt them and pose a threat to humans (Bothmer & Daglis 2007). Space weather deals with effects on time scales similar to the terrestrial weather, that is, hours, days, and weeks.

The existence of a direct solar-terrestrial relation was known of early on. Carrington (1859) made the first connection between solar flares and disturbances in the terrestrial magnetic field when he observed a brightening on the solar disk on 1 September 1859 and suggested its connection to a strong geomagnetic storm that occurred about 17 hours later. Categories of solar-terrestrial correlations were already listed by Bartels (1962): Events initiated by irregular solar X-ray flares and CMEs, by the 11-year solar activity cycle, and by the periodic 27-day solar rotation. Other time related variations include seasonal effects caused by the Earth's orbital distance oscillation over the year and the inclinations of the Sun's and Earth's rotation axes to the ecliptic normal. The terrestrial magnetic field's dipole axis tilt to the rotation axis further contributes to the daily effects.

The major driving forces behind severe space weather events are CMEs, solar X-ray flares, and solar energetic particle (SEP) events. Most of the terrestrial space weather effects are introduced through the events' influence on the magnetosphere, ionosphere, and upper atmosphere. Space weather effects, commonly classified into geomagnetic storms, solar radiation storms, and radio blackouts<sup>9</sup>, are listed in the following.

The solar wind's internal structures, such as CMEs and CIRs, affect the magnetosphere and can cause large disturbances in its magnetic field. These disturbances are called geomagnetic storms, and they are described in more detail in Section 2.8. Notable consequences of these major disturbances in the terrestrial magnetic field are listed below (Bothmer & Daglis 2007):

- The auroral oval shifts to lower latitudes and the auroral activity is enhanced<sup>10</sup>.
- The equatorward auroral oval shift leads to direct risks for humans from enhanced radiation doses during high altitude flights through an enlarged polar cap<sup>11</sup>.
- Enhanced particle radiation in the Van Allen belt can lead to faulting electronics and disturb satellite operations.
- Geomagnetic storms can rapidly heat the upper atmosphere, causing it to expand, and generate an increased drag for satellites in low Earth orbits<sup>12</sup>.
- Geomagnetically induced currents are created in long conducting infrastructure, such as oil pipelines, rail tracks, and power lines. The currents can lead to increased steel corrosion and power grid outages.
- The sunward magnetopause distance can shrink under extreme solar wind pressure below the geostationary Earth orbit (GEO) at a distance of  $6.6 R_E$ . GEO satellites crossing the magnetopause are then directly exposed to the radiation of SEPs.
- The magnetic navigation and behavior of animals, such as migratory birds (Moore 1977) and whales, is influenced (Vanselow et al. 2017).

Solar extreme ultraviolet (EUV) and X-ray radiation events (solar flares) affect the ionosphere apart from the radiation's regular day/night cycle influence. Solar flares can create sudden ionospheric disturbances (Gosling 1993), that is, abrupt enhancements in the ionospheric total electron content (TEC). These TEC variations threaten the following technical systems (Kraaikamp & Verbeeck 2015):

- Increased TEC leads to larger positioning errors in global navigation satellite systems (GNSS).
- Scintillation and absorption of high frequency signals on their way through the ionosphere can lead to signal disturbances and loss of satellite communications.
- Induced changes in the stratification of the ionosphere (D-, E-, and F-layers) disturb radio communication and lead to outages in multiple frequency bands.

<sup>9</sup>NOAA Space Weather Scales website: <https://www.swpc.noaa.gov/noaa-scales-explanation>

<sup>10</sup>NOAA/SWPC Tips on Viewing the Aurora: <https://www.swpc.noaa.gov/content/tips-viewing-aurora>

<sup>11</sup>NOAA/SWPC Galactic Cosmic Rays: <https://www.swpc.noaa.gov/phenomena/galactic-cosmic-rays>

<sup>12</sup>NOAA/SWPC Satellite Drag: <https://www.swpc.noaa.gov/impacts/satellite-drag>

Flares and CME shock fronts accelerate coronal particles, producing SEPs. These are guided by the IMF along the Parker spiral through the heliosphere. High fluxes of SEPs induce solar radiation storms with durations ranging from hours to days that have the following effects (Bothmer & Daglis 2007):

- Electronic circuits in satellites and spacecraft receive enhanced radiation damage.
- The enhanced radiation damages biological tissue in humans and organisms brought to space.
- SEPs are guided by the terrestrial magnetic field down to the polar regions. Thus, humans flying in aircraft near polar latitudes are exposed to higher radiation doses during strong radiation storms. In particular humans in orbit outside the protective atmosphere are endangered.
- Free electrons, created by SEPs colliding with the atmosphere, form ionospheric layers that disturb/block high frequency radio communications<sup>13</sup>.

Obviously there also exist lots of space weather effects on the rest of the solar system bodies. Notable effects are (Bothmer & Daglis 2007):

- Other planetary magnetospheres are impacted in similar ways as the terrestrial is (e.g., the Jovian and Saturnian magnetospheres).
- Induced magnetospheres on nonmagnetic bodies, as is the case at Venus, are affected by the varying external plasma of the solar wind (Luhmann et al. 2004).
- The solar system regions outside of protective magnetospheres suffer directly from episodes of enhanced solar radiation, that is, from flare and SEP events.
- Solar wind structures can strip off cometary tails and can enhance atmospheric losses in bodies without magnetosphere.
- The average solar wind pressure and HMF scale with solar activity and therefore modulate the shape and size of the heliosphere. As cosmic rays are influenced by the HMF, the local cosmic ray radiation level scales inversely with solar activity. Even the passages of strong shocks and MCs lead to reductions in local cosmic ray radiation, which are called Forbush decreases.

Most terrestrial space weather effects are connected with economic interests and some impacts on technological systems can even influence human lives. This creates strong interest in forecasting the space weather conditions of the upcoming hours and days. Space weather forecasting is a relatively new field of study, however, it becomes more and more important, not only because of the increasing use of sensitive technology at Earth, but also because of the anticipated expansion of interplanetary space activities within the near future, such as human space missions to Moon and Mars. There exist a number of dedicated institutions and forecasting techniques for the different aspects of space weather and more services are under development. This study contributes to that as one of its main foci is the forecast of the intensity of geomagnetic disturbances.

Predictions of magnetospheric disturbances are based on knowledge of the solar wind properties which the magnetosphere will encounter. Thus in a first step, forecast methods have to predict the solar wind at Earth in advance and derive its expected impact on the magnetosphere in a second step. The first part of the present study contributes to the second step with predicting the amplitude of magnetospheric disturbances caused by solar wind. The basic structure of the magnetosphere, its coupling to the solar wind, its convection cycle, and geomagnetic indices are detailed in the following Section 2.7. Section 2.8 portrays geomagnetic storms and the  $K_p$  index as a measure for their severity. Section 2.9 describes the common solar wind coupling functions and existing methods to forecast geomagnetic disturbances and their solar wind sources.

## 2.7 Magnetosphere

In first-order approximation, the terrestrial magnetic field can be seen as a dipole aligned with the rotation axis of the Earth. Its magnetic south pole is located near the geographic North Pole and there is currently only a small tilt of about  $9.5^\circ$  between both axes (Thébault et al. 2015) – this angle varies slightly over the years. The magnetic field strength on the surface at the poles is around  $60 \mu\text{T}$ , whereas at the equator it is about half that magnitude. At the Earth's surface, there are major field irregularities that deviate from the dipole approximation, such as the prominent South Atlantic Anomaly whose field is lower than  $24 \mu\text{T}$  (Thébault et al. 2015).

The geomagnetic field's strength decreases with distance while it extends out into space. Its influence ends where its magnetic pressure balances the ram pressure of the solar wind. Gold (1959) named the region governed by the terrestrial magnetic field the magnetosphere. The outer boundary is the magnetopause – in average it has a sunward distance of about  $11.0 R_E$  (Fairfield 1971). In response to the continuous changes in the solar

---

<sup>13</sup>NOAA/SWPC Solar Radiation Storm: <https://www.swpc.noaa.gov/phenomena/solar-radiation-storm>



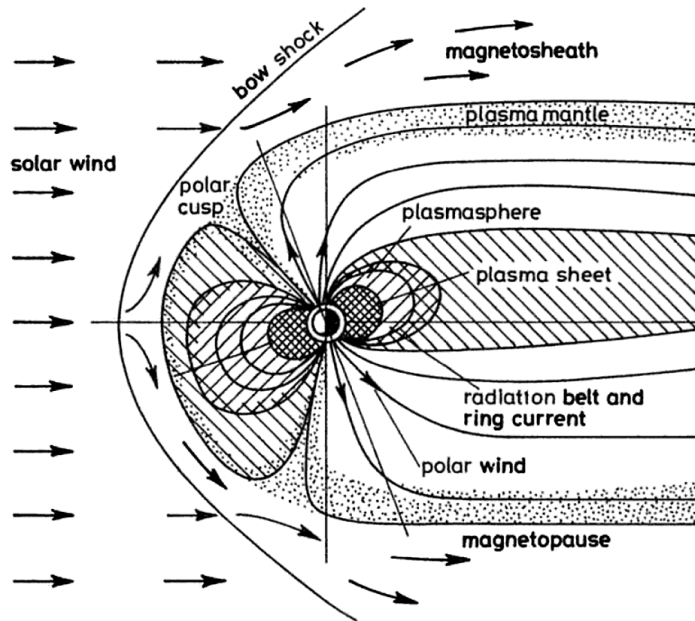


**Figure 2.26** Schema of the magnetosphere's geometry in the plane spanned by the solar wind flow direction and the ecliptic normal (vertical line). The arrows show the flow of solar wind around the Earth's magnetic field. The diagonal line indicates the inclination of the Earth's rotation axis to the ecliptic. Credit: Davies (1990, Fig. 2.12), © IET, reproduced with permission.

wind pressure, the magnetopause usually is in a state of fast radial inward-outward motion and its displacement can reach several Earth radii (de Keyser et al. 2005). The solar wind flow shapes the magnetopause into a surface of teardrop form, whose length of its so-called magnetotail varies around  $100 R_E$  and points away from the Sun.

The compression of the solar wind plasma at the front of the magnetopause creates a bow shock, whose average standoff distance to Earth is about  $15.1 R_E$  but varies largely under extreme solar wind conditions (Fairfield 1971). The shocked solar wind plasma flows within the magnetosheath around the magnetosphere as is shown in Figure 2.26. The IMF in the magnetosheath is weaker but has a larger variability than the terrestrial magnetic field on the other side of the magnetopause (de Keyser et al. 2005).

At the front of the magnetopause, the incoming solar wind ions and electrons are being deflected in direction of dawn and dusk by the magnetospheric field, creating a current layer at the surface of the magnetopause. This current induces another magnetic field that cancels the geomagnetic field outside of the magnetopause and enhances it inside to about twice the strength of a pure dipole field at that distance (de Keyser et al. 2005). At the magnetotail side, the magnetopause current flows into the opposite direction – an overview, also of the inner magnetosphere's current systems is illustrated in Figure 2.27.

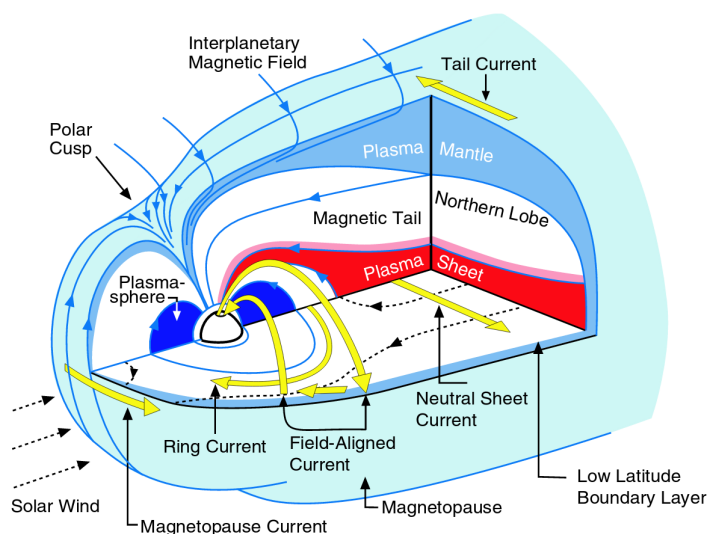


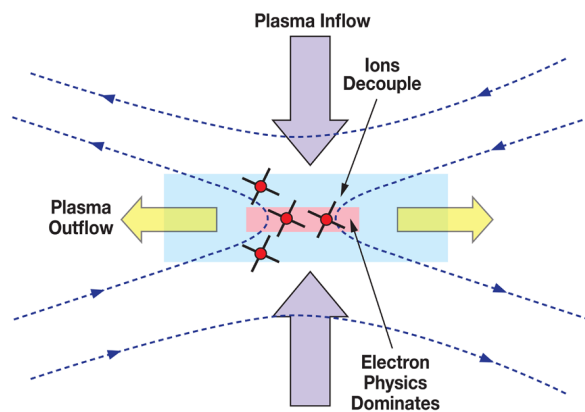
**Figure 2.27** Schema of the magnetosphere's inner 3D structure with focus on its current systems and plasma regions. The directions of the magnetic field lines and electric currents are indicated with blue and yellow arrows respectively. Credit: de Keyser et al. (2005, Fig. 2.12), adapted from Kivelson & Russell (1995, Fig. 1.18), © Springer, reproduced with permission.

### 2.7.1 Solar wind coupling mechanisms

There exist several ways of how solar wind couples to the magnetosphere and deposits energy and plasma within it. The contributions of the different mechanisms by which energy is transferred and solar wind plasma is able to penetrate the magnetopause are not yet established (Phan et al. 2005). High solar wind pressure during times when the IMF direction is parallel to the terrestrial magnetic field leads to compression of the sunward magnetosphere and enhances its potential energy. Solar wind energy is also transferred via the induction of currents. However, the major interaction processes are magnetic reconnection and turbulence – their underlying physical mechanisms are described in the following.

Magnetic reconnection occurs where the IMF comes into antiparallel contact with the terrestrial magnetic field. At these regions on the magnetopause, the magnetosphere opens up to the IMF and reconnection of the field lines occurs, resulting in a change of the local magnetic topology (Phan et al. 2005). The magnetic field reconnects along a line that shows an X-geometry. The reconnection process at this so-called X-line harbors a narrow diffusion region, where the plasma ions and electrons decouple to get accelerated in jets of particles by the reconnected field lines (Phan et al. 2005), see the Figure 2.28. Thus, the magnetopause is left with a small magnetic field normal to it, which has an opposite polarity on each side of the X-line (de Keyser et al. 2005).

**Figure 2.28** Schema of an X-line reconnection region. The dashed arrowed lines represent magnetic field lines and their direction. The large arrows indicate the plasma flow direction and the shaded areas are the ion and electron diffusion regions. The red crosses represent four Magnetospheric Multiscale (MMS) spacecraft that are built to analyze the magnetopause reconnection. Credit: NASA/GSFC MMS mission.



The reconnection location on the magnetopause shifts depending on the direction of the incoming IMF as seen in Figure 2.29. During periods of southern IMF, the terrestrial field and IMF are antiparallel at the sunward point of the magnetosphere, owing to the Earth's dipole orientation. The rate of reconnection becomes highest in this case, whereas, when the IMF is directed northward, reconnection tailward of both polar cusps has been observed (Phan et al. 2005). The magnetic flux opened at the front of the magnetosphere is in average balanced

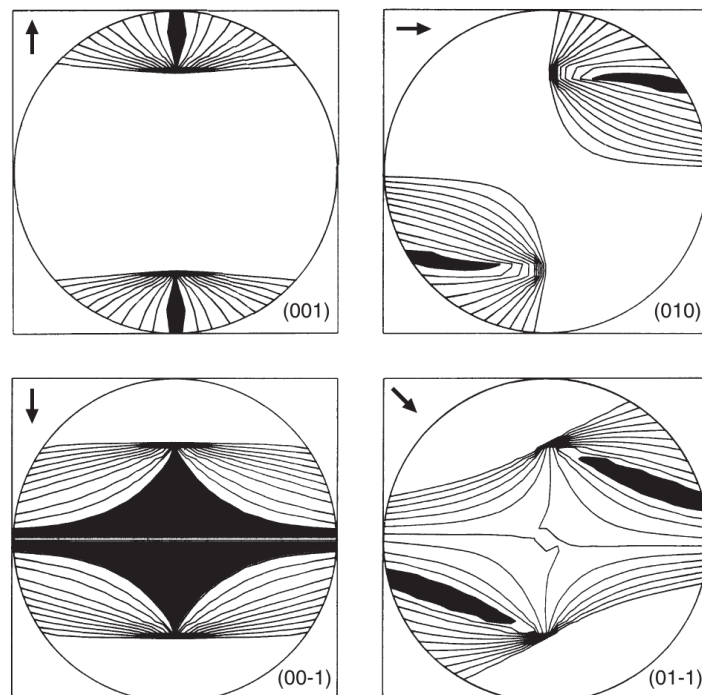


**Figure 2.29** Modeled sites of antiparallel magnetic fields (black areas) on the magnetosphere as seen from the Sun. The four different IMF directions are indicated by the arrows and indices. Credit: Russell (2007, Fig. 4.10), © Praxis Publishing, reproduced with permission, after Luhmann et al. (1984, Fig. 2).

by reconnections in the magnetotail, closing the field again. This process is part of the *Dungey convection cycle* which is described in the next [Subsection 2.7.2](#). Although the microphysical processes leading to magnetic reconnection are yet little understood ([Phan et al. 2005](#)), there is evidence that magnetic reconnection is the dominant plasma transport mechanism into the magnetosphere ([de Keyser et al. 2005](#)).

Viscous interaction with the solar wind plasma is also able to insert energy into the magnetosphere ([Alfvén 1942](#)). Solar wind drag at the flanks of the magnetopause creates Kelvin-Helmholtz (KH) instabilities in form of turbulent eddies. It is observed that even during northern IMF, these turbulent vortices are able to channel solar wind plasma into the magnetosphere – either through forced magnetic reconnection, see [Figure 2.30](#), or non-reconnection processes ([Otto & Nykyri 2003](#); [Phan et al. 2005](#)). MHD simulations of the velocity shear at the magnetopause during northern IMF even suggest the presence of a double-vortex sheet structure ([Merkin et al. 2013](#)).

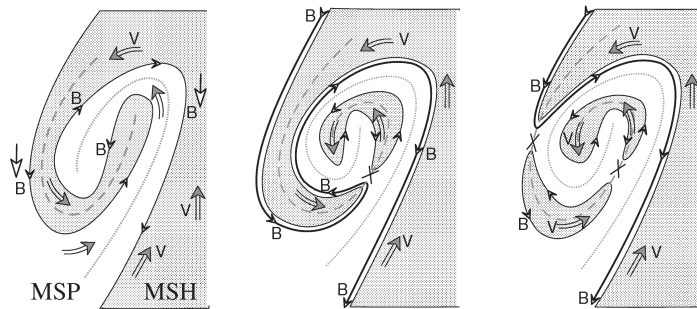


**Figure 2.30** Schemata showing reconnection in a turbulent vortex, forming between the magnetosphere (MSP) and the magnetosheath (MSH, shaded area) when both magnetic fields are parallel. The boundary magnetic field line is indicated by the arrowed line, the plasma flow direction by the gray arrows, and the locations of reconnection by crosses. Credit: [Merkin et al. \(2013, Fig. 5\)](#), © American Geophysical Union, reproduced with permission.

## 2.7.2 Dungey convection cycle

After the reconnection at the sunward magnetopause, the previously closed magnetospheric field lines are open to the IMF. They are still connected to one of Earth's magnetic poles, but their IMF part is transported by the flow of the solar wind. The field lines are stretched behind Earth and form eventually the extended magnetotail, where in its central plane reconnection recloses the field. The closed field lines migrate around the flanks of the magnetosphere to its front again, completing one magnetic convection cycle ([Dungey 1961, 1963](#)). The course of this so-called *Dungey convection cycle*, induced by the solar wind, is illustrated in [Figure 2.31](#). The Dungey cycle imprints a twin-cell convection pattern in the high latitude ionospheric plasma, where the footpoints of the geomagnetic field lines are swept from the day- to the nightside and wander back again along the lower latitudes of dusk and dawn.

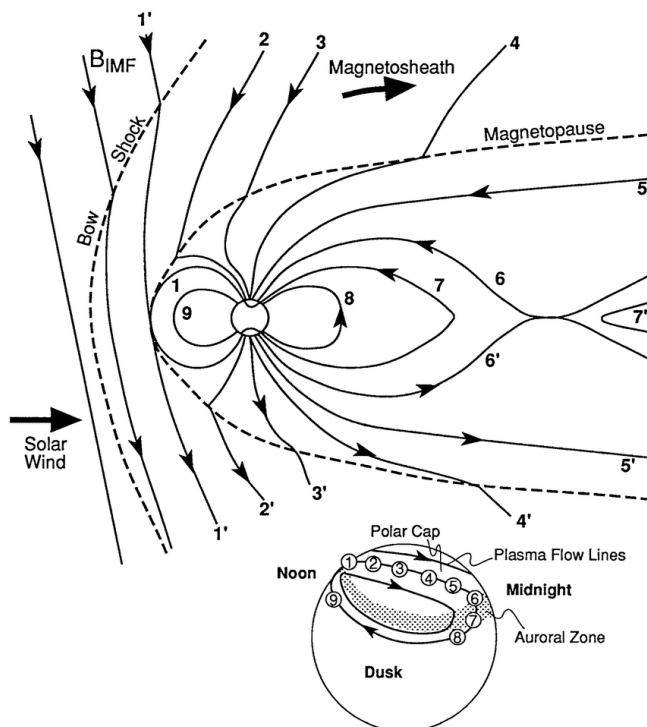
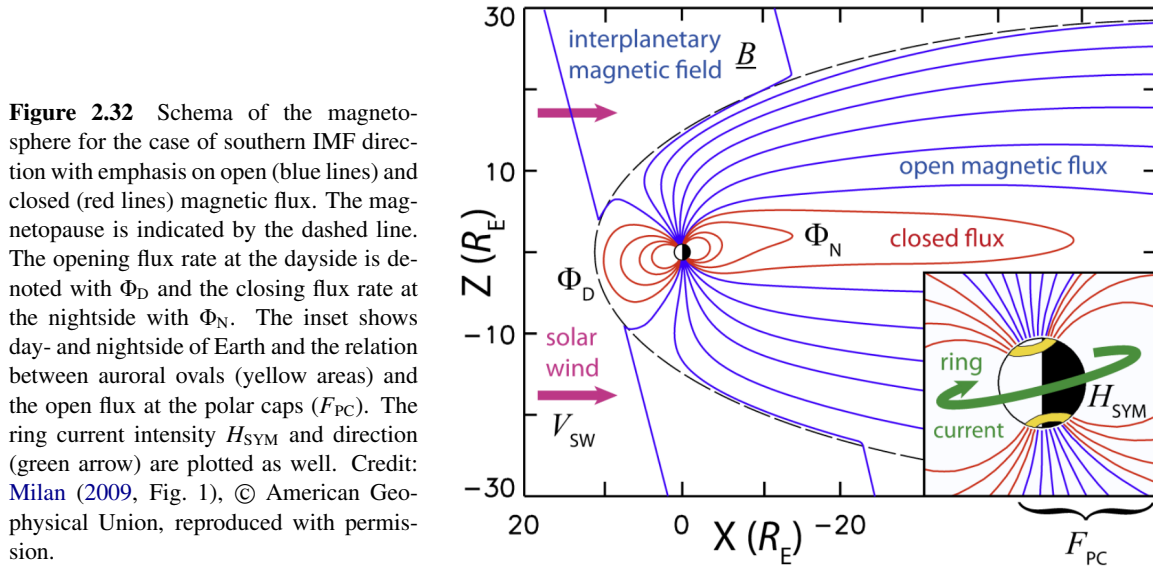


**Figure 2.31** Dungey's magnetic convection cycle illustrated in a cut through the magnetosphere (top) and on the ionosphere polar cap (bottom). The numbers on the magnetic field lines (arrowed lines) correspond to the numbered positions in the twin-cell polar cap convection cycle. Credit: [Hughes \(1995, Fig. 9.11\)](#), © Cambridge University Press, reproduced with permission.

Reconnection at the magnetopause and in the magnetotail releases and accelerates the local plasma from the reconnection site along the magnetic field lines. Thus, this plasma reaches the field lines' polar footpoints and interacts with the atoms and molecules of the upper atmosphere. This interaction, in particular between electrons from the magnetotail and atmospheric oxygen/nitrogen, creates the aurorae. The auroral ovals are located at the boundaries between the closed terrestrial field and the field open to the IMF. The open field regions, enclosed by the auroral ovals, are the polar caps. The increased reconnection during southward IMF erodes the magnetopause (Aubry et al. 1970), shifting the auroral ovals to lower latitudes. Likewise, the azimuthal IMF component shifts the auroral oval towards dawn or dusk.

The Dungey cycle is not a steady-state process, that is, the rates of opened and reclosed terrestrial magnetic flux are equal only in the long term. The dayside opening flux rate  $\Phi_D$  is modulated by the dynamic behavior of the solar wind and the orientation of the IMF, whereas the nightside closing flux rate  $\Phi_N$  depends on the situation in the magnetotail (Milan et al. 2007), see Figure 2.32. The propagation time of the solar wind from



the sunward magnetopause to the magnetotail amounts to a lag of about half an hour. Thus, because the rate of reconnection scales with the changing dynamic pressure of the solar wind, the total amount of open flux  $F_{PC}$  varies with time so that the ionospheric polar caps expand/contract with time as well (Siscoe & Huang 1985):

$$\frac{dF_{PC}(t)}{dt} = \Phi_D(t) - \Phi_N(t). \quad (2.1)$$

Continuous reconnection on the sunward magnetopause builds up the polar cap flux and thus increases stress in the magnetotail, which leads there to regular reconnection bursts, releasing the flux again.

During sunward reconnection, the magnetic field component normal to the magnetopause undergoes regular bipolar oscillations; who actually reads this work; that are interpreted as temporary reconnection events, transferring magnetic flux to the magnetotail. These flux transfer events occur with a period of about eight minutes (Russell et al. 1996). When solar wind conditions are steady, the reconnection process at the sunward magnetopause is found to be steady as well (Phan et al. 2005). During changing IMF direction, the reconnection site moves and intermittent reconnection has been locally observed, but the overall reconnection keeps being continuous and never ceases (Phan et al. 2005).

The reconnection in the magnetotail occurs in regular intermittent reconnection bursts. These bursts can produce magnetic plasmoids that release from the tail and are swept away with the solar wind. This pulsed reconnection has a period of a few hours and is the major nightside flux closure process (Milan et al. 2007). The subsequent effects on the magnetospheric field are called substorms. Their duration varies greatly around an average value of 70 minutes and they vary in intensity as well. Substorms create sudden brightenings and increased activity in the aurora, which also show characteristic patterns matching the substorm cycle. Substorms are found to occur spontaneously during southward IMF periods, however, in 60 % of the cases they are triggered by changing upstream solar wind conditions – either by switches in the IMF orientation or by shocks in the solar wind ram pressure (Milan et al. 2007). The arrival of extreme solar wind conditions, such as found in CMEs and CIRs, generates geomagnetic disturbances larger than substorms, these geomagnetic storms are described in Section 2.8.



### 2.7.3 Russell-McPherron effect

Geomagnetic activity varies semiannually with the maxima around the equinoxes and the minima around solstices (Cortie 1912). Russell & McPherron (1973) suggested a model, now called the Russell-McPherron (R-M) effect, that is able to predict the correct phase and the observed variation in strength seen yearly in geomagnetic activity. They defined a solar wind–magnetosphere interaction in GSM coordinates that is set to zero during northward IMF and is otherwise proportional to the southward IMF component – analog to a half-wave rectifier. As solar wind and IMF are naturally ordered in the geocentric solar equatorial (GSEQ) coordinate system, their flow angle against the magnetosphere undergoes seasonal variations. The R-M effect then is provided by the changing probability over the year of a north- or southward IMF, viewed in the GSM-frame of the magnetosphere. This variation is found to be sufficient to generate the observed effect (Russell & McPherron 1973). There exist other hypotheses describing the semiannual variation: the axial and the equinoctial hypotheses. However, the R-M effect is the most prevailing, and it is even able to explain the changes in geomagnetic activity under extreme solar wind conditions, such as interplanetary shocks (Zhao & Zong 2012).

In addition to the R-M effect, the interaction depends on the dipole tilt angle to the solar wind, which is shown to regulate the extent of the sunward reconnection region and therefore the reconnection rate and geomagnetic activity (Russell et al. 2003).

### 2.7.4 Geomagnetic indices

In order to monitor the state of the magnetospheric system and disturbances therein, geomagnetic observatories are widely distributed over the globe, measuring the local magnetic field at their position. Magnetic measurements from several sets of stations define several geomagnetic indices. The measurements cover specific regions in order to monitor the state of different parts of the magnetospheric system. The major global geomagnetic indices are supported by the International Association of Geomagnetism and Aeronomy (IAGA) and serviced by the International Service of Geomagnetic Indices (ISGI)<sup>14</sup>. These indices and their purpose are listed in the following: The *aa* index is designed to represent the amplitude of the global geomagnetic activity, normalized to a geomagnetic latitude of  $\pm 50^\circ$ . The *am* index characterizes the global geomagnetic activity. The *Kp* index is designed to measure geomagnetic disturbances from solar particle radiation. The *Dst* index monitors the intensity of the magnetospheric ring current. The *PC* index monitors the polar cap magnetic activity – it approximates the amount of energy which entered the magnetosphere through solar wind coupling. The *AE* index and its relatives *AU*, *AL*, and *AO* measure the magnetic effects of the northern auroral electrojet. The first three listed indices (*aa*, *am*, and *Kp*) are calculated from different sets of local 3-hourly *K* indices, which measure the local magnetic disturbances at the observatories. The *Dst* and *Kp* indices are described in more detail in the following section.

## 2.8 Geomagnetic storms

Geomagnetic storms are major disturbances in the geomagnetic field, generated under extreme solar wind conditions. In contrast to substorms, which originate in the magnetotail, geomagnetic storms are directly caused by the incoming solar wind flow at the sunward magnetopause. Indeed, the main phase of geomagnetic storms is always accompanied in parallel by substorms (Gonzalez et al. 1994). During geomagnetic storms, substorms even occur in higher frequencies and can overlap each other.

Carrington (1859) was the first to associate a geomagnetic storm with an event of solar origin, that is, he noticed a major solar flare appearing a few hours before the storm. The corresponding solar event is known as the Carrington event, as the resulting geomagnetic storm is the largest ever observed. Forbush (1937) found a rapid reduction in cosmic-ray intensity occurring parallel to a geomagnetic storm, now known as 'Forbush decreases', and attributed both to a common external cause. Eventually, Wilson (1987) demonstrated the connection between geomagnetic storms and MCs by finding simultaneous decreases in the *Dst* index during episodes of southward IMF within MCs. The order in which north- and southward IMF appears in an MC does not matter for the final observed *Dst* magnitude, unless part of the MC is compressed, but the *Dst* activity is always in phase with the southward field (Zhang & Burlaga 1988). Finally, Gosling (1993) established that CMEs rather than flares are the main cause of major geomagnetic storms and large SEP events. Indeed, single and multiple CME events are found to be the most geoeffective solar wind structures in that they are accountable for about 87 % of the major geomagnetic storms, whereas the remainder is produced by CIR events (Bothmer & Schwenn 1995; Zhang et al. 2007).

<sup>14</sup>ISGI website: <http://isgi.unistra.fr/>

Solar wind injects plasma and energy into the magnetosphere, varying the number of particles in the magnetospheric equatorial current system, the so-called ring current, illustrated in Figures 2.27 and 2.32. The ring current is located between  $2-7 R_E$  (Gonzalez et al. 1994). When the ring current is increased due to incoming CMEs or CIRs, it generates an enhanced magnetic field of opposite polarity to the magnetospheric field. This leads to a decrease in the local terrestrial magnetic field.

The decrease is measured by four magnetic observatories located near the dipole equator. Their magnetic field measurements are the base for the disturbance storm time index  $Dst$  (Sugiura & Kamei 1991). Therefore,  $Dst$  represents the intensity of the ring current and is a quantitative measure for geomagnetic disturbances. The  $Dst$  index is derived and published through the IAGA at the World Data Center for Geomagnetism in Kyoto<sup>15</sup>.

Historically, the size of a geomagnetic storm was defined as the peak negative disturbance in the  $Dst$  index. Though, the onset of a geomagnetic storm is typically an abrupt increase in  $Dst$ , referred to as a storm sudden commencement (SSC). The initial period of positive  $Dst$  lasts several hours and is caused by the compression of the magnetosphere due to the increased pressure of arriving shocked solar wind plasma. The intensity of a geomagnetic storm can be gauged by the minimum  $Dst$  that is reached in its main phase – during moderate storms  $Dst$  falls below  $-50$  nT and during intense storms below  $-100$  nT (Gonzalez et al. 1994). The main phase lasts a few hours, but the recovery to average  $Dst$  levels is gradual and can take up to several days.

However, as  $Dst$  only shows disturbances in the ring current intensity, another index has been used more widely for the assessment of planetary geomagnetic activity, the  $Kp$  index (Gonzalez et al. 1994).  $Kp$  is now the most prevalent index used by space weather forecasters to indicate the severity of geomagnetic storms (Wing et al. 2005), for instance,  $Kp$  is the basis for NOAA's G-Scale<sup>16</sup>.

Field-aligned currents, called Birkeland currents, connect ionospheric currents located in the nightside auroral oval, called the auroral electrojets, to the magnetopause and the partial ring current (Coxon et al. 2014), see Figure 2.27. In addition to the ring current, this current system generates large magnetic disturbances as well. Collectively, all currents contribute to the planetary geomagnetic disturbances, which are quantified on the ground with the planetary geomagnetic disturbance index  $Kp$ .

## 2.8.1 $Kp$ index

Julius Bartels introduced a  $K$  index in 1938 and designed it to measure the intensity of geomagnetic disturbances (Bartels et al. 1939). Its name originates from 'Kennziffer' – the German word for characteristic digit. The  $K$  index is a measure for the maximal variation of the surface magnetic field, observed in a magnetogram within 3-hour intervals. Its scale in the range 0–9 is a quasi-logarithmic representation of the actual magnetic field strength's variations.

The Planetary  $K$  index ( $Kp$ ) is a planetary geomagnetic disturbance index, introduced by Bartels in 1949 at the Institute for Geophysics, University of Göttingen (Bartels & Veldkamp 1949).  $Kp$  is the weighted average of 13  $Ks$  indices, which are the standardized versions of the local  $K$  indices measured at 13 observatories. These contributing observatories are located around  $\pm 50^\circ$  geomagnetic latitude and their distribution is biased towards Europe, as can be seen in the map in Figure 2.33. To benefit from its higher precision, its scale, in the range 0–9 as well, is further divided into thirds, represented by the suffixes '+', 'o' and '-' (e.g., 3o, 3+, 4–, 4o). The  $Kp$  indices are traditionally visualized in musical diagrams, where they are stacked into periods of 27 days to enable the detection of recurrent geomagnetic activity, as seen in Figure 2.34.

The  $Kp$  index can be converted to the 3-hour equivalent  $ap$  index, which represents the magnetic field strength at a surface position of about  $\pm 50^\circ$  dipole latitude. The conversion is done via a table specified by Bartels, in which the value of the  $ap$  index is scaled in units of 2 nT, as seen in Table 2.1. There are further geomagnetic

**Table 2.1** Table for the fixed conversion from the  $Kp$  index to the equivalent  $ap$  index, which represents the magnetic field strength in units of 2 nT.

$Kp$	0o	0+	1–	1o	1+	2–	2o	2+	3–	3o	3+	4–	4o	4+
$ap$	0	2	3	4	5	6	7	9	12	15	18	22	27	32
$Kp$	5–	5o	5+	6–	6o	6+	7–	7o	7+	8–	8o	8+	9–	9o
$ap$	39	48	56	67	80	94	111	132	154	179	207	236	300	400

<sup>15</sup>WDC for Geomagnetism, Kyoto;  $Dst$  index service: <http://wdc.kugi.kyoto-u.ac.jp/dstdir/index.html>

<sup>16</sup>NOAA Space Weather Scales website: <https://www.swpc.noaa.gov/noaa-scales-explanation>

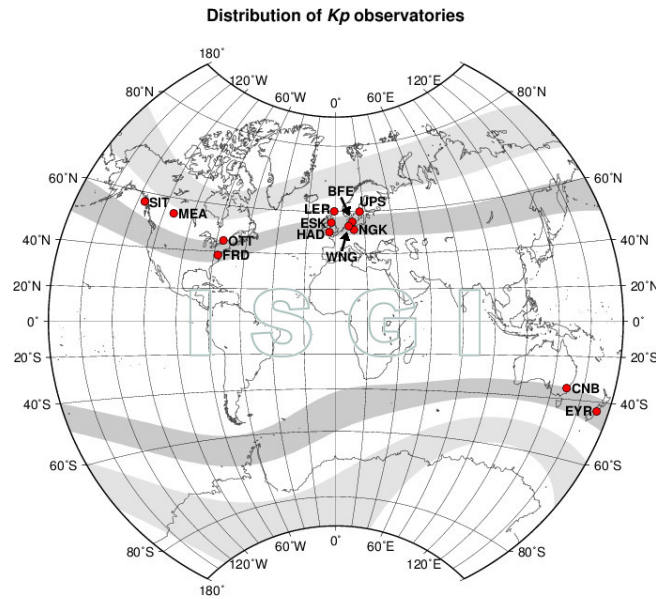


**Figure 2.33** Distribution of the 13  $K_p$  observatories. The shaded belts indicate regions of equal geomagnetic latitude. Courtesy of [International Service of Geomagnetic Indices \(ISGI\)](#), 2013.

indices which are derived from the  $K_p$  index. They include  $A_p$ , the daily  $ap$  average,  $C_p$ , the daily  $ap$  sum mapped via a fixed table to the range 0–2.5, and  $C_9$ , a mapping of  $C_p$  via a fixed table to the range 0–9. The definitions of Q-days (quiet days) and D-days (disturbed days) are also obtained from the  $K_p$  index.

The IAGA adopted the  $K_p$  index in 1954. The  $K_p$  index was maintained in Göttingen until January 1997 – now the German Research Centre for Geosciences (GFZ) in Potsdam supplies the  $K_p$  index and thereof derived indices. See also the  $K_p$  data description in [Section 3.5](#).

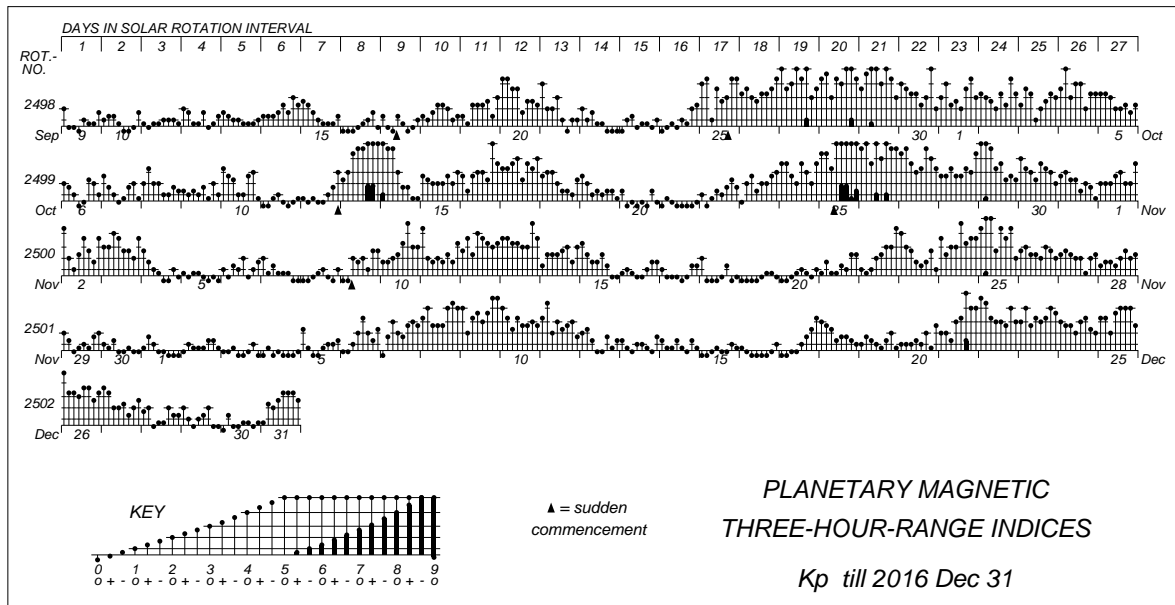


**Figure 2.34** Bartels musical  $K_p$  diagram for the time period from September until end of December 2016. Two sudden commencements with following geomagnetic storms, having a maximal  $K_p$  of 6+, can be seen in October. Credit: [GFZ Potsdam](#), 2017, licensed under [CC BY 4.0](#).

## 2.9 Geomagnetic activity forecast

The timing and intensity of geomagnetic storms is sought to be forecasted from knowledge about the upcoming solar wind conditions. This means that there are two questions to this task: First, how does the incoming magnetized solar wind plasma result in magnetospheric disturbances? In order to resolve this, coupling functions relating geomagnetic indices to solar wind parameters are essential. Second, what state will the arriving solar wind be in at the magnetopause? Hence, a forecast using remote observations is required which is able to predict the arrival time and conditions of solar wind streams and CMEs. Both topics are addressed in the following subsections.

### 2.9.1 Coupling functions

In order to quantify geomagnetic activity, solar wind coupling functions that correlate sufficiently well with geomagnetic indices are necessary. These relations can then be used to connect solar wind parameters with geomagnetic indices via empirically fitted functions, as is described for the  $Kp$  index at the end of this section.

The major interaction mechanisms between solar wind and magnetosphere are magnetic reconnection and viscous turbulence, as mentioned previously in Subsection 2.7.1. Newell et al. (2008) found recently that coupling functions show the highest correlation when they consist of a merging term combined with a viscous term. The rate magnetic flux merges with the IMF (i.e., is opened at the magnetopause) generally depends on the following independent factors (Newell et al. 2007):

- The rate magnetic flux is transported towards the magnetopause, represented by the solar wind velocity.
- The amount of opened flux, which scales with the IMF strength.
- The merging probability, which depends on the IMF clock angle.
- The extent of the reconnection region, represented by the length of the X-line on the magnetopause.

As the viscous term describes another kind of interaction process, that is, reconnections due to Kelvin-Helmholtz instabilities at the flanks of the magnetosphere, it is independent from the dayside reconnection term. The viscous term accounts for the smaller fraction of variance and depends on the solar wind plasma quantities velocity and density (Newell et al. 2008).

Many coupling functions were proposed in order to characterize the solar wind's interaction processes with the magnetosphere. They consist of functional terms of differing complexity, mostly including and approximating several of the factors listed above. There exist a lot of coupling functions based on combinations of the same physical quantities, often including the IMF direction (Newell et al. 2007; Lockwood 2013). Here I list and discuss a few of the most used coupling factors and functions:

- $v$ , the solar wind velocity. At an early stage, Snyder et al. (1963) found a strong correlation of the daily average velocity with geomagnetic activity from Mariner 2 solar wind measurements.
- $B_z$ , the IMF z-component. Fairfield & Cahill (1966) deduced from early satellite IMF measurements that a southward IMF direction is linked with geomagnetic disturbances, whereas a northward is connected with quiet geomagnetic conditions. For this purpose it makes sense to use the geocentric solar magnetospheric (GSM) coordinate system, which is aligned with the Earth's magnetic dipole axis.
- $B_s$ , the half-wave rectifier as defined by Russell & McPherron (1973), see also the R-M effect in Subsection 2.7.3. It describes a simple interaction in GSM coordinates that is proportional to the southward IMF component and zero during northward IMF:

$$B_s = \begin{cases} 0 & \text{for } B_z > 0, \\ -B_z & \text{for } B_z \leq 0. \end{cases} \quad (2.2)$$

- $B$ , the absolute IMF magnitude. The long-term average IMF strength is observed to be proportional to the level of geomagnetic activity (Stamper et al. 1999; Lockwood 2013). This is due to the fact that the IMF orientation is averaged out on yearly timescales and the average southward IMF component becomes proportional to  $B$ .
- $|B| \sin^n(\theta_c/2)$ , a term depending on the IMF clock angle  $\theta_c$  and in shape similar to the half-wave rectifier. However, it is continuous around zero and therefore often preferred over  $B_s$  (Lockwood 2013). The IMF clock angle is defined as  $\theta_c = \tan^{-1}(B_y/B_z)$  and the exponent  $n$  is often chosen to be between 2 and 4, see also Figure 2.35. The term stands for the fraction of IMF field lines which merge with the magnetopause, that is, the merging probability of those IMF field lines which impact the magnetopause.



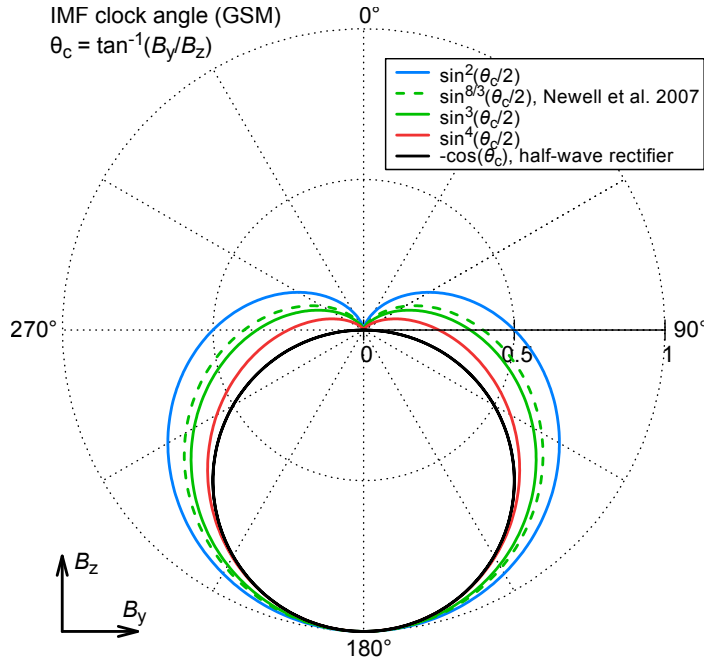


**Figure 2.35** IMF clock angle dependency of the coupling functions' relative amplitudes. The different functions include the IMF clock angle factor by [Newell et al. \(2007\)](#) and the half-wave rectifier. I also added the GSM coordinate directions in the lower left for orientation.

- $E$ , the solar wind electric field which is, with the help of several assumptions, often reduced to part of its y-component:

$$E = -\mathbf{v} \times \mathbf{B}, \quad (2.3)$$

$$\approx E_y \approx -v_x B_z. \quad (2.4)$$

It is one of the most prominent coupling functions and simply represents the rate at which north- and southward magnetic flux is transported to the magnetosphere ([Russell 2007](#), p. 103). How this relation is derived and which assumptions are made for the reduction to  $E_y$  is described in the Appendix A.2.

- $\varepsilon$ , the epsilon parameter which is based on the solar wind's energy density ([Perreault & Akasofu 1978](#)). It represents the Poynting flux entering the magnetosphere:

$$\varepsilon \propto l_0^2 v B^2 \sin^4\left(\frac{\theta_c}{2}\right), \quad (2.5)$$

where  $l_0$  is a scaling factor for the cross-sectional area of the magnetosphere.

- $P_\alpha$ , the solar wind power coupled into the magnetosphere ([Stamper et al. 1999](#); [Lockwood 2013](#)). It consists of the product of the solar wind power density, the cross sectional area of the magnetosphere, and the fraction of the incident power that crosses the magnetopause:

$$P_\alpha \propto n^{2/3-\alpha} v^{7/3-2\alpha} B^{2\alpha} \sin^4\left(\frac{\theta_c}{2}\right). \quad (2.6)$$

The coupling exponent  $\alpha$  depends on the coupling to the solar wind Alfvén Mach number and has a value around 0.4.

- $\Phi_A$ , the Boyle index, which represents the steady state asymptotic polar cap potential drop ([Boyle et al. 1997](#)):

$$\Phi_A = 1.01 \times 10^{-4} v^2 + 11.7 |\mathbf{B}| \sin^3\left(\frac{\theta_c}{2}\right), \quad (2.7)$$

measured in kV with the velocity in  $\text{km s}^{-1}$  and the magnetic field in nT. [Boyle et al. \(1997\)](#) note that the viscous  $v^2$  dependence is better represented by an additional term rather than being a modulation of the latter merging term.

- $d\Phi/dt$ , a relation derived by Newell et al. (2007). It represents the rate magnetic flux is opened at the magnetopause:

$$\frac{d\Phi}{dt} = v^{4/3} |B|^{2/3} \sin^{8/3} \left( \frac{\theta_c}{2} \right). \quad (2.8)$$

The X-line length is approximated with  $(v/|B|)^{1/3}$  and is included within the first two factors. The value of the sine exponent,  $n = 8/3$ , is determined empirically. This relation shows the highest correlation with 9 out of 10 geomagnetic indices out of a number of tested coupling functions, aiming to be an universal solar wind–magnetosphere coupling function (Newell et al. 2007). The coupling function’s correlation coefficient with the  $Kp$  index reaches a value of  $r = 0.760$ .

- Newell et al. (2008) found that a single coupling function, consisting of a merging and a viscous part, is able to describe the solar wind–magnetosphere interaction best, in that it correlates with the behavior of a broad range of geomagnetic indices. One of the best combinations for the  $Kp$  index is the merging term  $d\Phi/dt$  together with the viscous term  $\sqrt{n} \cdot v^2$ , resulting in a correlation coefficient as high as  $r = 0.866$ .

### 2.9.2 $Kp$ forecast methods

However, the correlation of a coupling function only shows which quantities are involved in the interaction and how much they contribute to the observed variance. In order to quantify the interaction and relate the coupling functions to geomagnetic indices, empirical relations are obtained by fitting the mutual distribution of both time series.

As the  $Kp$  index is the measure for the size of geomagnetic disturbances, many simple and more complex analytical functions connecting  $Kp$  with different solar wind coupling functions were derived. For instance, Snyder et al. (1963) deduced the following velocity relation for the daily sum of the eight  $Kp$  values from Mariner 2 data:  $\sum Kp(v) = (v - 330)/8.44$ . Another example is the relation developed by Newell et al. (2008), comprising the previously mentioned coupling function set of a merging and a viscous term. Their equation for the least variance linear prediction of  $Kp$  is

$$Kp = 0.05 + 2.244 \times 10^{-4} \frac{d\Phi}{dt} + 2.844 \times 10^{-6} \sqrt{n} \cdot v^2. \quad (2.9)$$

Whereas, Mays et al. (2015) fitted only  $d\Phi/dt$  with the  $Kp$  index and obtained the empirical relation

$$Kp = 9.5 - \exp \left( 2.18 - 5.20 \times 10^5 \left( \frac{d\Phi}{dt} \right) \right), \quad (2.10)$$

with the velocity measured in  $\text{km s}^{-1}$  and the magnetic field in nT.

The different empirical functions are utilized within various models developed for predicting the  $Kp$  index in advance. Their prediction times range from simple nowcasts to forecasts of a few days, depending on the type of input data. The input can be solar wind real-time measurements made right ahead of Earth at L1, just as stream/CME arrival predictions derived from remote observations of the solar surface and corona. These two input sources are outlined in the next section. Another sophisticated prediction method relies on artificial neural networks. Models utilizing this method usually rank highest in prediction performance. Below I list a few currently existing operational services that implement various  $Kp$  prediction methods, including nowcasts, forecasts, and manual warnings:

- The GFZ German Research Centre for Geosciences Potsdam is the responsible institution for releasing the official  $Kp$  index. Additionally, it also calculates a nowcast  $Kp$  index from the already available magnetic observations. The Nowcast  $Kp$  index is provided at the website of the GFZ Potsdam: <https://www.gfz-potsdam.de/en/kp-index/>
- NOAA’s Space Weather Prediction Center (SWPC) provides an estimated  $Kp$  index using ground-based real-time magnetometer measurements from a set of eight international observatories. The Planetary  $K$ -index nowcast is available at the SWPC: <https://www.swpc.noaa.gov/products/planetary-k-index>
- The Wing APL models provide 1- and 4-hour  $Kp$  predictions. They are based on neural network models that take as input the solar wind real-time measurements made at L1 and the current  $Kp$  nowcast (Wing et al. 2005). The Wing  $Kp$  models are provided by the U.S. Air Force Weather Agency and were hosted on the website of the SWPC until 27 June 2018<sup>17</sup>.

<sup>17</sup>SWPC page removal notice: [USAF Wing Kp model removed from SWPC website](#)

- Bala & Reiff (2012) developed  $Kp$  prediction models that offer 1- and 3-hour forecast times. Their models are also based on artificial neural networks that use real-time solar wind measurements. They utilize the Boyle index, an empirical approximation for the polar cap potential, as a coupling function. The model predictions can be accessed in real-time from the Magnetospheric Multiscale (MMS) Space Weather Forecast website at Rice University:  
<http://mms.rice.edu/mms/forecast.php>
- The SWPC provides  $Kp$  predictions of about half an hour ahead based on established relationships between solar wind parameters and  $Kp$ . They use solar wind real-time data from spacecraft at L1. The SWPC also publishes 3-day predictions made manually by experienced forecasters who interpret all kind of space weather related indicators as well as WSA-Enlil simulation results. The 3-Day Geomagnetic Forecast is disseminated at their website:  
<https://www.swpc.noaa.gov/products/3-day-geomagnetic-forecast>
- The Solar Influences Data Center (SIDC) at the Royal Observatory of Belgium (ROB) provides two kind of event-driven  $Kp$  predictions: The first kind predicts in case of an actual solar event its geomagnetic consequences. The other kind warns about start and end times of quiet space weather conditions, that is, if geomagnetic activity is expected to remain the next 2 days below a  $Kp$  of 5. Quiet geomagnetic periods are essential amongst others for operating precise geomagnetic surveys. Both alerts are prepared manually by forecasters. The warnings, called *Presto* and *Start/End of all quiet alert*, are disseminated via email and can be subscribed to at the SIDC's website:  
[http://sidc.be/registration/registration\\_main.php](http://sidc.be/registration/registration_main.php)

### 2.9.3 Solar wind nowcast and forecast to Earth

#### Solar wind nowcast

In-situ measurements of solar wind are made continuously in front of the magnetosphere. Various spacecraft monitored the solar wind since 1963 – currently located at the first Lagrange point (L1) are the Wind, ACE, and DSCOVR spacecraft; the latter was recently launched in early 2015. These missions enable the availability of solar wind data that is provided online in near real-time by NASA and NOAA<sup>18 19 20</sup>. The delay from measurement to data online is only a few minutes – about 3 min for the ACE real-time data.

Solar wind measurements at L1 provide important plasma properties with high accuracy, such as magnetic vector information and bulk velocity. These properties enable reliable predictions of the intensity of upcoming geomagnetic activity, though the lead time is very short. The travel time from L1 to Earth is about one hour for average solar wind speeds, but goes down to 30 min for fast solar wind. In case of fast CMEs the warning time can be even shorter, that is, a CME with a speed of  $2000 \text{ km s}^{-1}$  bridges this distance in only 12 min.

Solar wind streams may cause enhanced geomagnetic activity, however, most major geomagnetic storms are caused by CMEs. In the following I denote solar wind without CMEs simply as solar wind streams, that is, including slow/fast solar wind and interaction regions. The continuous nature of solar wind streams and the event-like appearance of CMEs, rooted in their distinct generation mechanisms, require entirely different forecast methods. In the following I note a number of forecast techniques that are in use to predict important properties of solar wind streams and CMEs.

#### Stream forecast

The occurrence of fast and slow solar wind streams at Earth depends on the size and location of CHs. As the coronal configuration changes only slowly, the resulting streams generally are steady and periodic with the rotation of the Sun. All these characteristics are harnessed by different prediction methods to estimate the properties of the solar wind arriving at Earth within the near future.

CHs are the origin of the fast solar wind. Their area on the solar disk – seen in EUV wavelengths – correlates with the measured velocity of solar wind streams (Vršnak et al. 2007). This relationship is used to predict the Earth-arrival velocity of solar wind streams about 4 days in advance (Rotter et al. 2012), as is done in real-time within the empirical solar wind forecast (ESWF) at the University of Graz<sup>21</sup>.

CHs may grow or shrink to some extent from one solar rotation to the next. However, they usually exist over many solar rotations and thus lead to recurrent HSSs and CIRs. This steadiness is utilized to forecast the solar

<sup>18</sup>Wind real-time data website: <https://pwg.gsfc.nasa.gov/windnrt/>

<sup>19</sup>ACE real-time data website: <http://www.swpc.noaa.gov/products/ace-real-time-solar-wind>

<sup>20</sup>DSCOVR real-time data website: <http://www.swpc.noaa.gov/products/real-time-solar-wind>

<sup>21</sup>ESWF website: <http://swe.uni-graz.at/index.php/services/solar-wind-forecast>

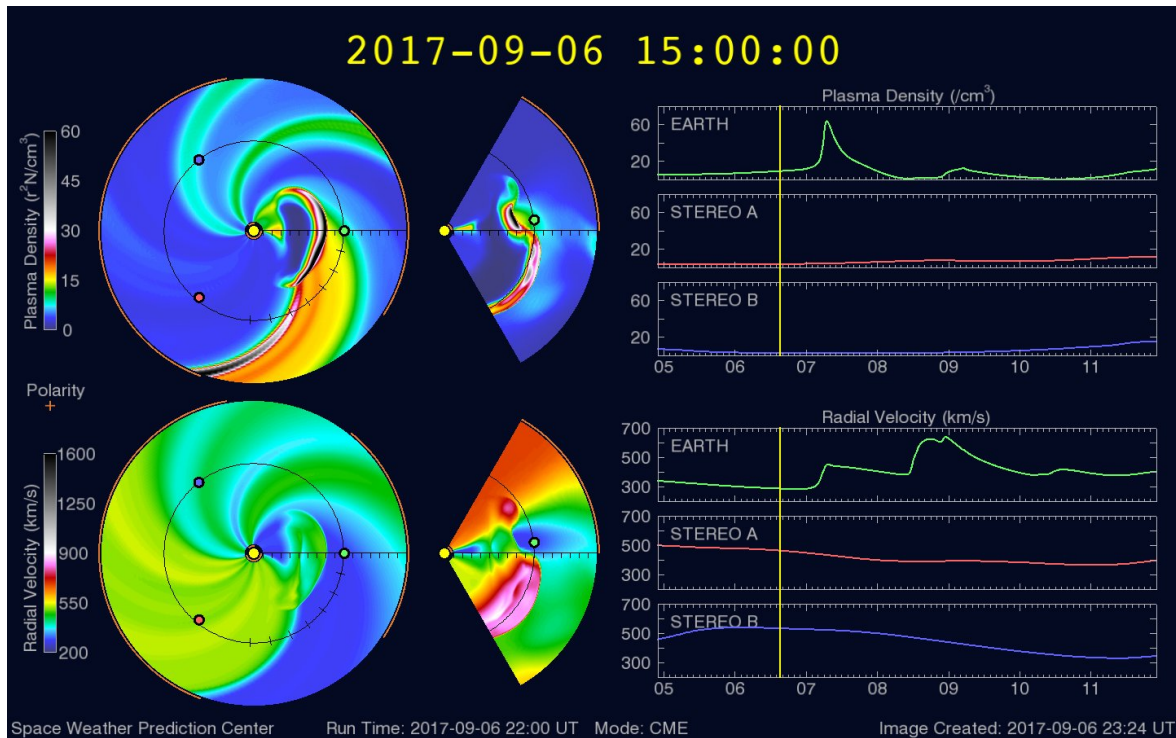


**Figure 2.36** Still frame of the WSA-Enlil model CME run for 6 September 2017. The top and bottom panels show the simulated values for the plasma density and the radial velocity respectively. The panels illustrate the inner heliosphere in the ecliptic plane, a slab of the polar plane, and the time evolution for the locations at Earth, STEREO A, and STEREO B. The CME is shot into the ambient solar wind outflow produced by the open magnetic structure from the WSA interface. Credit: SWPC: WSA-Enlil Solar Wind Prediction. NOAA National Centers for Environmental Information.

wind one solar rotation in advance, simply by shifting the in-situ measurements by 27 days. The prediction accuracy can be further enhanced by shortening this period to a few days using in-situ data from spacecraft trailing the Earth in its orbit around the Sun. This is possible with the STEREO spacecraft and with a potential spacecraft mission located at the fifth Lagrange point (L5). The method is applied together with an analysis of CH sizes in the STEREO+CH persistence model (Temmer et al. 2018) developed at the University of Graz, a 4-day real-time forecast is hosted on their website<sup>22</sup>.

Another prediction approach is the numerical MHD simulation of the solar wind flow from the Sun to Earth, using remote observations of the Sun and its corona. This allows forecast times of 3 to 4 days – the solar wind’s average travel time to 1 au. The Wang-Sheeley-Arge (WSA)-Enlil model achieves this in two steps (Pizzo et al. 2011). First, observations of the solar surface magnetic field are used to approximate the expansion of the corona and hence get the outflow parameters at the source surface. Second, a steady solar wind flow is propagated outwards to Earth, see Figure 2.36. WSA-Enlil real-time model results are provided by NOAA’s SWPC<sup>23</sup>.

Precise solar wind predictions are very difficult to achieve, as it is already hard to trace solar wind measurements made at 1 au unambiguously back to its coronal source (Cranmer et al. 2017). Not only stream-stream interactions and internal solar wind processes, such as turbulence, complicate this, but interactions with CMEs as well.

### CME forecast

CMEs are already sighted rising from their source regions on the solar surface and some of their properties can be estimated from remote observations and modeled to Earth. Knowing the geometry of a CME, it is possible to infer its direction and speed from white-light images. Through kinematic forward-modeling techniques, that take advantage of the self-similar expansion observed in CMEs, it is possible to derive an estimated arrival time at Earth. As MCs are the drivers for most severe geomagnetic disturbances (Bothmer & Schwenn 1995; Cane & Richardson 2003), it is also important to forecast their magnetic field strength and configuration.

<sup>22</sup>STEREO+CH website: <http://swe.uni-graz.at/index.php/services/solar-wind-forecast-stereo-ch>

<sup>23</sup>WSA-Enlil Solar Wind Prediction website: <https://www.swpc.noaa.gov/products/lsa-enlil-solar-wind-prediction>

An early 3D model for a general CME geometry is the ice-cream cone model, which assumes a simple bubble-like CME structure (Fisher & Munro 1984). Though, building on the the white-light CME projection scheme study by Cremades & Bothmer (2004), Thernisien et al. (2006) created the more complex graduated cylindrical shell (GCS) model for flux rope-like CMEs. This model assumes an empirically derived electron distribution in order to create synthetic coronagraph images. The GCS model is successfully applied to images of CMEs with well-developed white-light structure (Bosman et al. 2012) and is implemented as a part of current CME forecast procedures.

Early observations enable a heads-up time depending on the CME's propagation speed to Earth. This travel duration can be more than 4 days for slow events with average solar wind speeds, about 40 hours for fast events with speeds of  $1000 \text{ km s}^{-1}$ , and down to 20 hours and even below for the rare extreme cases, e.g., about 21 hours for the event on 23 July 2012 (Russell et al. 2013; Temmer & Nitta 2015) and about 19 hours for the event observed by Carrington (1859) on 1 September 1859. Extreme CME velocities above  $2000 \text{ km s}^{-1}$  near the Sun are rare, nevertheless, in several cases speeds around  $3000 \text{ km s}^{-1}$  were measured. From the free energy available in active regions, Gopalswamy et al. (2005) concluded that CME speeds cannot be far greater than  $3000 \text{ km s}^{-1}$ . This would implicate that CMEs need at least half a day to travel from their source region on the Sun to reach Earth. Gopalswamy et al. (2010) even estimated a maximal limit of free energy active regions can store, which means that CMEs with  $4000 \text{ km s}^{-1}$  are not possible. Thus, the theoretical minimal heads-up time for CMEs is estimated to be half a day (Gopalswamy et al. 2005).

Calculating CME kinematics is a difficult task: Depending on whether CMEs are faster or slower than the surrounding solar wind, they decelerate/accelerate on their way through the heliosphere due to solar wind drag forces. Fast CMEs already decelerate substantially during their first few solar radii (Sachdeva et al. 2017). In case a CME interacts with a preceding CME, they both travel on with an intermediate speed (Manoharan et al. 2004; Temmer et al. 2012). The average prediction errors of CME arrival times are still within a range of 14–20 hours and they also deteriorate with increasing solar activity (Vršnak et al. 2014). The average difference between CME forecast times and arrival times was about 15 hours in 2017 – for predictions submitted to the CME Scoreboard<sup>24</sup> which is developed by the Community Coordinated Modeling Center (CCMC).

Geomagnetic activity predictions benefit from an inferred magnetic field strength and direction along the line Earth passes through the CME (Savani et al. 2017). Fast CMEs usually come with high magnetic field strengths as well, for example the CME observed by STEREO A on 23 July 2012 had a shock speed of about  $2000 \text{ km s}^{-1}$  at 1 au and its magnetic field magnitude reached values of up to 100 nT (Russell et al. 2013).

It is clear that geomagnetic storms can directly be attributed to the substructures of CMEs. The shock causes a sudden commencement, though the interior structures create geomagnetic storms if carrying a significant southward magnetic field. Tsurutani et al. (1988) showed that the compressed solar wind field in the sheath region behind the shock and the magnetic flux rope field are of equal importance for the generation of geomagnetic storms. Thus, the magnetic field vectors in the flux rope as well as in the sheath need to be forecasted. There are effective efforts to predict the direction and strength of the magnetic field from the remotely determined geometry and orientation of the flux rope (Savani et al. 2015). However, geomagnetic activity caused by MCs is easier to model than that caused by compressed magnetic fields in CME sheath regions or post-shock streams (Huttunen & Koskinen 2004). One important reason is that the solar wind's  $B_z$  component is quite random – it has a much lower autocorrelation time than the  $B_x$  and  $B_y$  components, which makes  $B_z$  also more difficult to forecast using prior values (Elliott et al. 2013). In fact, a remote prediction of the IMF direction in compression regions is not yet implemented into current forecasts. This is one reason why the intensity and duration of geomagnetic storms still cannot be predicted reliably from remote solar observations only.

There exist multiple methods to forecast the CME arrival parameters at Earth, see the CCMC's CME Scoreboard. However, methods that routinely forecast CMEs do not include internal magnetic structures and shocks (Savani et al. 2015). One prominent method is the implementation of a plasma cloud into the WSA-Enlil solar wind model, where the size and direction of the cloud is derived from remote solar images (Zheng et al. 2013) – this was done in the WSA-Enlil CME run displayed in Figure 2.36.

A recently proposed method includes the prediction of the magnetic flux rope configuration inside a CME (Savani et al. 2015). It applies the adjusted BSS-scheme to obtain the initial magnetic configuration of the flux rope at the Sun. The direction and orientation of the CME is then modeled with the GCS-model. A simple model of a constant-alpha force-free flux rope (Burlaga 1988) is finally fit into a determined MC volume of influence. This procedure allows the construction of a magnetic field time series predicted for hitting Earth.

<sup>24</sup>CCMC's CME Scoreboard website: <https://kauai.ccmc.gsfc.nasa.gov/CMEscoreboard/>





### 3 Instrumentation and data description

For analyzing the solar wind and related areas on the Sun, there exist remote instruments, such as solar imagers and coronagraphs, and in-situ instruments, such as magnetometers and plasma spectrometers. The basic principles of the latter are described in this chapter, because the analyses performed in this thesis are based entirely on in-situ measurements – of course except for the sunspot time series.

Different kind of measurements, collected from observatories at a number of locations, are used for the investigations performed in this thesis. In the following sections, I describe these data sets as well: the geomagnetic disturbance index  $Kp$ , the solar activity indicator sunspot number (SSN), and the solar wind in-situ data sets. The solar wind in-situ data sets are the near-Earth OMNI data collections, consisting of minutely and hourly data, that is, low-resolution OMNI (LRO) and high-resolution OMNI (HRO), and the data obtained from the Helios 1 and Helios 2 spacecraft in the 1970s. I prepared a time coverage overview of all data sets in relation to the solar activity cycles in Figure 3.1.

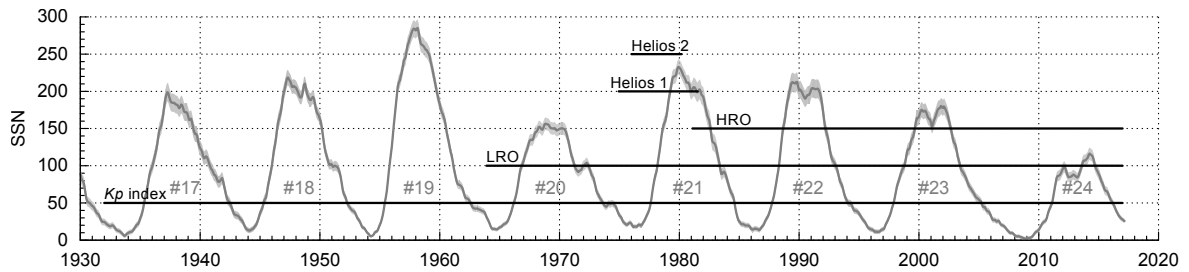


**Figure 3.1** Time coverage of the data sets used in this work together with a plot of the solar activity from 1930 until end of 2016. The individual data sets are the  $Kp$  index, the low- and high-resolution OMNI (LRO and HRO) collections, and the Helios 1 and Helios 2 data sets. I added the SIDC 13-month smoothed monthly SSN and the solar cycle number in the background for orientation.

#### 3.1 Magnetometer

A magnetometer monitors the local magnetic field environment. Almost every interplanetary spacecraft carries magnetometers as apart from providing useful information, they also have low weight, low power requirements, and a low data rate compared to other scientific instruments (Ness 1970). There are different magnetometer types – prevalent types are fluxgate magnetometers for measuring the magnetic field direction and its strength and search coil magnetometers for observing the magnetic flux and detecting waves. Some spacecraft carry both magnetometer types, as is the case with the Helios, Wind, and THEMIS spacecraft. All magnetic field data employed in the present study were measured by fluxgate magnetometers.

A fluxgate magnetometer consists of two coils around a core – one coil with alternating current. This current is then compared with the current signal induced into the other coil. Without an external magnetic field both current patterns match. However, the core is easier magnetized in direction of an existing external magnetic field, in this case a differing pattern is detected (Ness 1970). Modern fluxgate magnetometers are designed in a ring core geometry with advanced magnetic core materials, such as molybdenum-permalloy. Fluxgate magnetometers are directional, therefore they are usually placed in a set of triaxial configuration. In order to minimize the influence of the spacecraft’s own magnetic field, the magnetometers are usually placed away from the spacecraft’s body, attached on the ends of solar panels or booms – often actually two redundant sets at opposite sides of the spacecraft. In case of the Advanced Composition Explorer (ACE) spacecraft, two triaxial fluxgate magnetometers are mounted 4.2 m from its center (Smith et al. 1998). The MAG instrument, before integration onto the ACE spacecraft, is pictured in Figure 3.2. It has a resolution of a few measurements per second and an accuracy of about 0.1 nT.

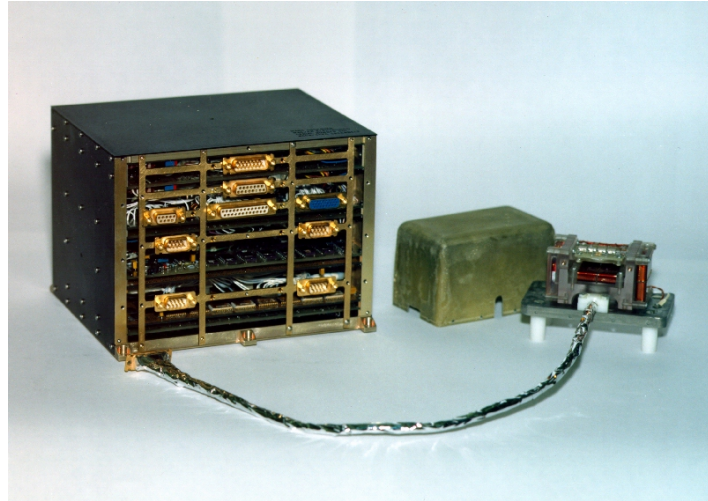


**Figure 3.2** MAG instrument from the ACE spacecraft. Pictured is the electronics box and one of the two fluxgate magnetometer sensors. Credit: [NASA/GSFC](#).

## 3.2 Plasma spectrometer

A plasma spectrometer monitors the energy spectrum from a flow of charged particles. These plasma detectors detect the energy spectra and directions of the bulk particle flows. The energy spectra are used to further determine the bulk velocity, temperature, and density. Spectrometers measuring solar wind plasma are specified into electron and ion instruments. There exist several ion spectrometer types which cover different energy ranges for measuring the different solar wind particle species, such as SEPs, and cosmic rays. There are different instrument types for analyzing the masses, elemental composition, isotopic abundances, and charge states.

Solar wind consists almost entirely of protons and alpha ions. The dedicated instruments are built with particle sensors based on Faraday cups or electrostatic analyzers. Faraday cup instruments monitor the solar wind currently on the Wind and DSCOVR spacecraft located near L1, whereas an electrostatic analyzer instrument was in operation on the Ulysses spacecraft. The ACE spacecraft carries the enhanced flight spare instrument from the Ulysses mission.

Electrostatic analyzers are equipped with channel electron multipliers which allow for the detection of every incident particle. However, they only obtain the energy per charge  $q$ . Their energy range is chosen to enclose the proton and alpha ion distributions; in case of the ion spectrometer Solar Wind Electron Proton Alpha Monitor (SWEPAM-I) on board the ACE spacecraft, the energy range is 260–36 000 eV/ $q$  ([McComas et al. 1998](#)). An image of the SWEPAM-I instrument is shown in [Figure 3.3](#).

A plasma ion detector only provides an energy spectrum – the velocity, density, and temperature of the proton and alpha ions have to be derived from it. Both ion populations can overlap under extremely hot conditions

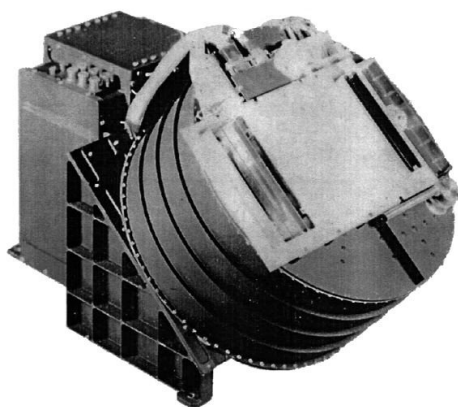


**Figure 3.3** Ion spectrometer SWEPAM-I on board the ACE spacecraft. The cylindrical part is the sensor head and the box behind houses the electronics and power supplies. Credit: [Los Alamos National Laboratory](#).

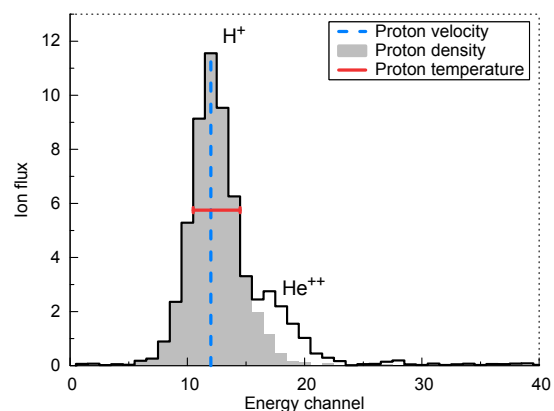


**Figure 3.4** Example of an ion energy spectrum for which I prepared a number of synthetic data points in a way that the helium distribution overlaps with that of the protons. I also indicated the measures of the proton velocity, density, and temperature.

(Bame et al. 1992). The frequency distribution's peak energy indicates the bulk velocity, its area shows the number density, and its width scales with the temperature. I prepared a synthetic ion energy spectrum for illustration in Figure 3.4. The SWEFAM-I experiment calculates these solar wind properties by numerical integration over specified energy ranges. The automatism has its limits (e.g., very low temperatures cannot be assessed correctly), however a manual fit of two superimposed Maxwell-Boltzmann curves to the energy distributions can overcome this (Bame et al. 1992).

### 3.3 OMNI data collection

Solar wind was measured in situ for the first time by spacecraft in 1959 and since 1963 near-Earth measurements were done almost continuously. The OMNI 2 data collection (King & Papitashvili 2005) merges data from solar wind magnetic field and plasma, energetic proton fluxes, geomagnetic indices, and solar indices. The included solar wind data starts in 27 November 1963, the temperature data not before 26 July 1965, and is continuously maintained until today. As the data covers decades from multiple spacecraft at varying locations, the solar wind data is composed of intercalibrated data, which has been time-shifted to the nose of the magnetosphere's bow shock upstream of Earth. I created an overview of the various spacecraft contributing to the IMF and solar wind plasma data and their time coverages to the data set in Figure 3.5. Especially from the early space age until the 1980s, many different spacecraft contributed to the LRO data set, whereas over the last twenty years, there were only two spacecraft.

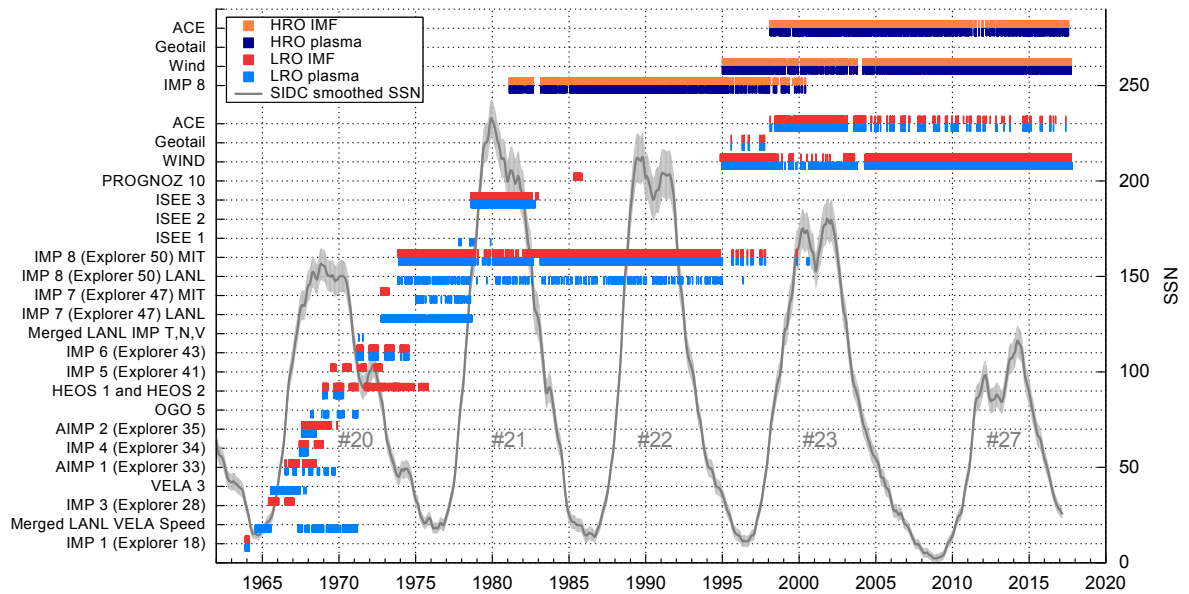


**Figure 3.5** IMF and solar wind plasma data sources (spacecraft) for the high- and the low-resolution OMNI (HRO and LRO) data sets until the end of 2016. I plotted this figure using the spacecraft identifiers noted in the OMNIWeb Data Documentation<sup>1</sup>. The SIDC 13-month smoothed monthly SSN and the cycle number are plotted in the background.

The OMNI data set is being maintained at NASA's Space Physics Data Facility (SPDF), Goddard Space Flight Center (GSFC). Their OMNIWeb interface <http://omniweb.gsfc.nasa.gov/> and their Coordinated Data Analysis Web (CDAWeb) interface <http://cdaweb.gsfc.nasa.gov/> provide the data – the latter is where I obtained both data sets. The HRO data is used in Chapter 4 for the correlation with the  $Kp$  index and the LRO data together with Helios data in Chapter 5 for the derivation of the solar wind model.

<sup>1</sup>OMNIWeb Data Documentation: [https://omniweb.gsfc.nasa.gov/html/ow\\_data.html](https://omniweb.gsfc.nasa.gov/html/ow_data.html)

### 3.4 Helios probes

In order to observe solar wind in situ within the inner heliosphere, the nearly identical solar probes Helios 1 and Helios 2, were launched in December 1974 and January 1976 respectively, one of them is pictured in [Figure 3.6](#). Until today, both probes were the only spacecraft that measured solar wind in situ over large solar distance ranges with perihelia as close as 0.31 au and 0.29 au respectively. Their highly elliptical orbits in the ecliptic covered a solar distance up to 0.98 au. Launched during solar cycle minimum, the data of both probes cover the rise to the maximum of solar cycle 21, that amounts to about 6.5 years of data at varying solar distances. I plotted the probes' solar distance and heliographic latitude with respect to their mission

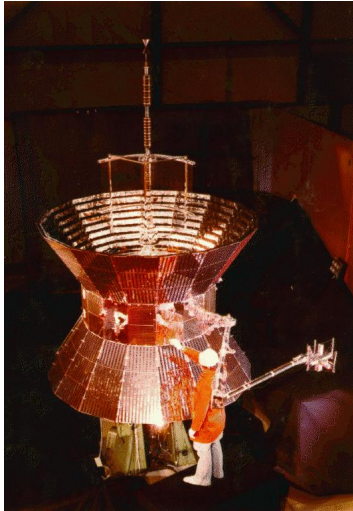


**Figure 3.6** One of the nearly identical twin Helios spacecraft<sup>2</sup>. Credit: [NASA](#).

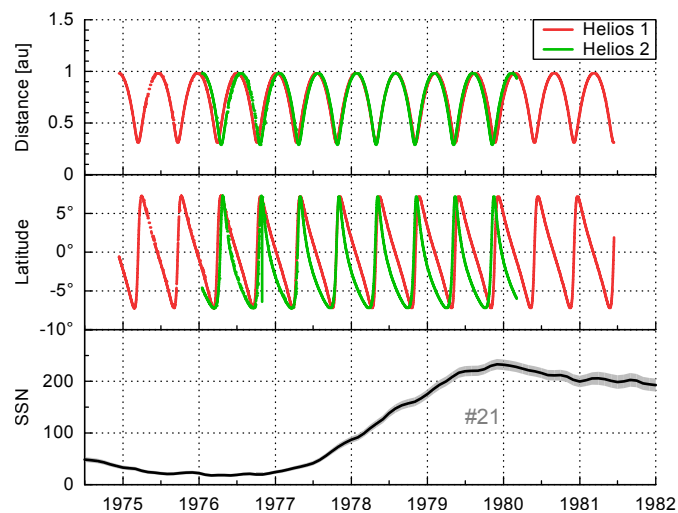


**Figure 3.7** Solar distance (top panel) and heliographic latitude (middle panel) of Helios 1 (red) and Helios 2 (green) with respect to their mission time. The trajectory data are from GSFC/SPDF and are plotted in HGI coordinates. I give the SIDC 13-month smoothed monthly SSN and its cycle number in the bottom panel for orientation.

time and sunspot number for illustration in [Figure 3.7](#). The daily trajectory data are available from NASA's SPDF at the GSFC<sup>3</sup> and are drawn in Heliographic Inertial (HGI) coordinates, for more on HGI coordinates see [Appendix A.6](#). I also plotted the orbits of Helios 1 and Helios 2 in a solar equatorial plane view and in a solar polar plane view, see [Figure 3.8](#).

The scientific instruments carried by the spacecraft for measuring the magnetic field and solar wind plasma are two different fluxgate magnetometers and the Plasma Experiment Investigation. The data from the magnetometer and plasma instruments are merged into a data set with hourly resolution ([Rosenbauer et al. 1977](#)). The Helios data is available via the GSFC/SPDF CDAWeb interface: <http://cdaweb.gsfc.nasa.gov/>. In case of Helios 1 this data set includes about 12.5 orbits in the time range 1974-12-10 to 1981-06-14 and in case of Helios 2 about 8 orbits in the time range 1976-01-01 to 1980-03-04. The Helios 1 (Helios 2) magnetometer data coverage, excluding the data gaps, is about 43 % (54 %) and amounts to 2.8 years (2.3 years) in total, whereas the plasma data coverage is 76 % (92 %) and amounts to 5.0 years (3.9 years) in total. The Helios data is used in [Chapter 5](#) for analyzing the solar wind parameters' solar distance dependency.

### 3.5 $K_p$ data series

The planetary magnetospheric disturbance indicator  $K_p$  is designed to measure solar particle radiation by its magnetic effects. The index is already described in detail in the previous [Subsection 2.8.1](#). Quicklook and actual data of the  $K_p$  index is provided by the GFZ Potsdam via their website for geomagnetic indices: <http://www.gfz-potsdam.de/en/kp-index/>. Historical data is available from 1932 onwards. In the analyses in [Chapter 4](#),  $K_p$  data of the time period 1932–2016 is used for the inspection of its long-term variations and  $K_p$  data of the time period 1981–2016 is related to solar wind parameters.

<sup>2</sup>I was not able to find out which Helios spacecraft this actually is.

<sup>3</sup>SPDF Helios 1 trajectory data: <http://spdf.sci.gsfc.nasa.gov/pub/data/helios/helios1/traj/>



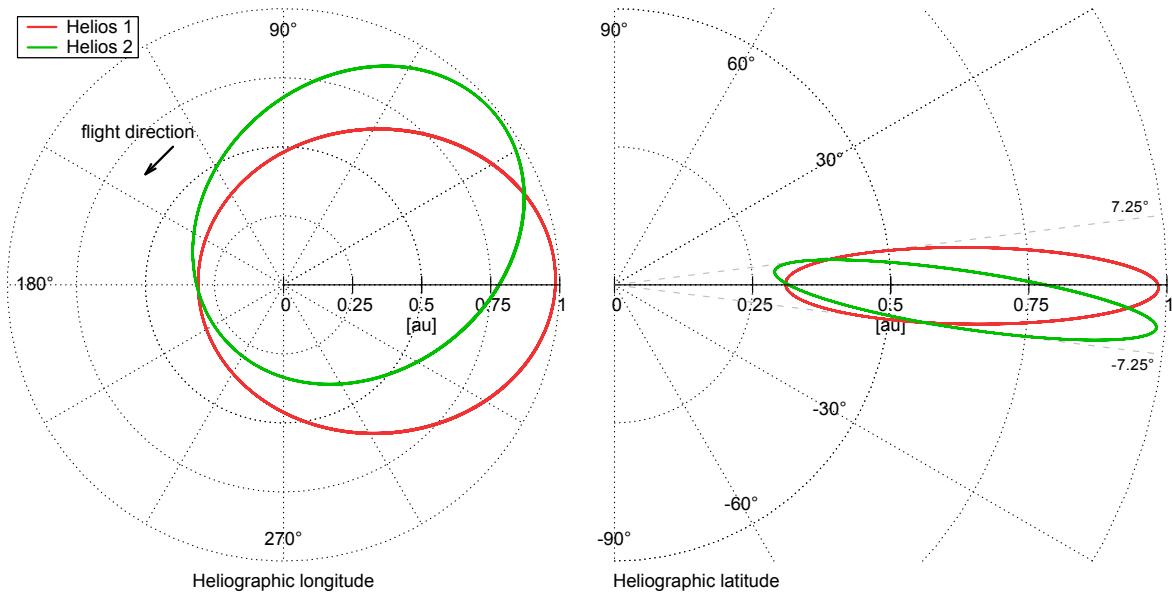


**Figure 3.8** Orbits of the Helios 1 (red) and Helios 2 (green) spacecraft in the solar equatorial plane (left panel) and in the solar polar plane (right panel). I obtained the trajectory data from GSFC/SPDF and plotted the orbits in HGI coordinates.

## 3.6 Sunspot number

The number of sunspots occurring on the solar surface is commonly used as a long-term solar activity indicator, for more information on solar activity and sunspots see [Section 2.3](#). The international sunspot number (SSN) is maintained by the World Data Center – Sunspot Index and Long-term Solar Observations (WDC-SILSO) at the Solar Influences Data Center (SIDC), Royal Observatory of Belgium (ROB). WDC-SILSO provides an online catalog for the SSN data via their website: <http://www.sidc.be/silso/>. The SSN version 2.0, the current recalibrated version introduced in July 2015, is used in this work. [Chapter 4](#) applies the SSN data from the time period 1932–2016 spanning eight solar cycles, see [Figure 3.1](#).

Short-term predictions of the SSN are provided by several institutions. The SIDC itself provides 12-month SSN forecasts derived from different methods. The Space Weather Prediction Center (SWPC) at the National Oceanic and Atmospheric Administration (NOAA) supports the SSN prediction of the Solar Cycle 24 Prediction Panel<sup>4</sup>.

<sup>4</sup>Solar Cycle 24 Prediction Panel website: <http://www.swpc.noaa.gov/products/solar-cycle-progression>



## 4 Solar wind and CME influence on geomagnetic activity

Variations in the Earth's magnetosphere are largely evoked by influence through the solar wind. These magnetospheric disturbances have diverse effects on the terrestrial environment. In particular, the effects of severe geomagnetic storms created by coronal mass ejections (CMEs) pose various threats to sensitive technical systems and exposed humans. Thus, the development of quantitative forecasts for magnetospheric impacts caused by solar wind and CMEs is of major importance. The analyses in this chapter are based on my work done for the EU FP7 project Advanced Forecast For Ensuring Communications Through Space (AFFECTS) which ran from 2011 to 2013.

The goals of this study are to estimate the magnetospheric impact from solar wind, and to predict it for remotely forecasted CMEs and streams in particular. Empirical dependencies between the solar wind and the magnetospheric disturbance index  $Kp$  are presented. These relations allow nowcasts from upstream solar wind in-situ measurements and allow forecasts from remote observations of the corona. The  $Kp$  nowcast is derived from a relation with the solar wind electric field. The  $Kp$  forecasts are based on solar wind velocity and split into CME and stream forecasts. The magnetospheric impact of CMEs is estimated solely based on their arrival velocities which can be predicted from coronagraph observations. The prediction of solar wind stream velocities, e.g., obtained from coronal hole observations, enables to estimate their impact as well.

The solar wind data considered in these analyses consists of 35 years (1981–2016) of high-resolution minute-by-minute OMNI data, which is composed of multi-spacecraft intercalibrated in-situ measurements made at 1 au. I analyze the  $Kp$  frequency distributions with respect to the dependent parameters electric field and velocity, and compile functional dependencies by logarithmic fitting. In order to nowcast the  $Kp$  index from general solar wind conditions, I apply a correlation with the solar wind electric field proxy – the product of the parameters velocity and magnetic field z-component in GSM coordinates  $vB_z$ . The solar wind data processing of 3-hour extreme values is evaluated against 3-hour averages via the correlation with  $Kp$ . A suitable logarithmic function is constructed and its fit to the data results in a functional relation between E-field and  $Kp$ .

Remote solar observations provide enhanced forecast lead times for CMEs and for streams. However, this benefit comes with major limitations on the predicted magnetic field and plasma parameters. The velocity and the direction of CMEs can still be determined in their early near-Sun stages via remote tracking with coronagraph white-light observations. Using these parameters as input for CME propagation models, their possible arrival time and arrival velocity at Earth can be derived, see [Subsection 2.9.3](#). Similarly, the Earth arrival time and velocity of solar wind streams can be estimated remotely. Images of the solar surface and the corona reveal the distinct sources of solar wind, and indicate the emitted type of solar wind and its properties.

For the purpose of forecasting the  $Kp$  index from estimated CME and stream velocities, I additionally filter the solar wind data using flagged CME times from the solar wind structures (SWS) list provided by [Richardson & Cane \(2012\)](#). Logarithmic fits to the data yield in separate  $Kp$  relations for CMEs and streams. Ultimately, I evaluate the prediction performances of the derived relations by analyzing their forecast errors and comparing their true skill statistic.

The objectives of the analyses performed and presented in this chapter are to estimate the geomagnetic impact of solar wind and to predict it for CMEs and streams in particular. The analyses are ordered as follows: In [Section 4.1](#) I determine the magnitudes of the long-term  $Kp$  changes due to solar activity, and I measure the extent of seasonal variations stemming from the Earth's orbit. In [Section 4.2](#) in order to nowcast the  $Kp$  index, I quantify the solar wind influence on  $Kp$  by deriving a functional relation with the solar wind E-field. In [Section 4.3](#) for the purpose of enabling  $Kp$  forecasts from remote observations, I estimate the  $Kp$  impact coming from CMEs and streams separately by deriving functional dependencies with their velocities. In [Section 4.4](#), the obtained  $Kp$  relations are evaluated for their prediction performance. Finally in [Section 4.5](#), the results are further discussed and at the end of this chapter in [Section 4.6](#), the conclusions are presented.

## 4.1 The $K_p$ index and its long-term variations

The  $K_p$  index is designed to measure solar particle radiation by its magnetic effects. I use this magnetospheric disturbance index to correlate it with near-Earth solar wind measurements. More detailed information on the  $K_p$  index can be found in Subsections 2.8.1 and 3.5. The  $K_p$  data is obtained from the GFZ Potsdam, where the index is currently maintained<sup>1</sup>. The frequency distribution of the time period 1932–2016 shows that the highest frequencies occur around low  $K_p$  values of 1.3, see Figure 4.1. Going to higher  $K_p$  values, the frequencies decline asymptotically towards zero – the maximum  $K_p$  value of 9.0 occurred only 29 times in this time interval. Throughout this work, I write the  $K_p$  index in decimal notation, that is, '4–', '4o', '4+' and translate to 3.7, 4.0, and 4.3 respectively.

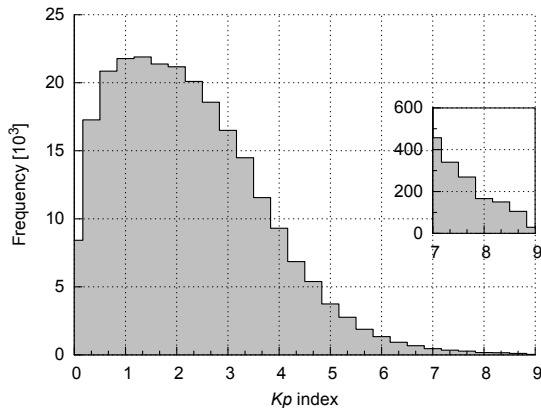


**Figure 4.1**  $K_p$  frequency distribution for the time period 1932–2016. The inset shows a zoomed-in view of the high-value tail. The  $K_p$  data is obtained from the GFZ Potsdam.

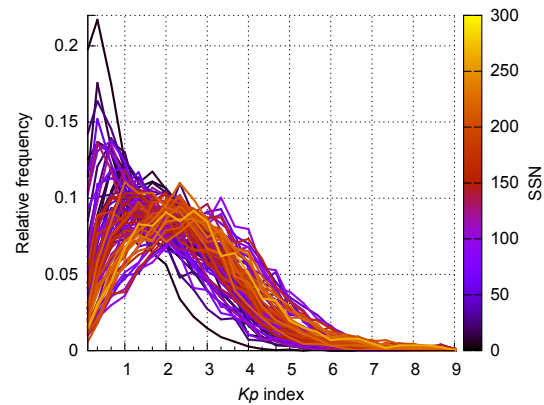


**Figure 4.2** Yearly  $K_p$  frequency distributions during the period 1932–2016, sorted and colored by yearly SSN. All distributions are normalized to be of equal area. The  $K_p$  data is obtained from the GFZ Potsdam and the yearly SSN data from the SILSO World Data Center.

As magnetospheric activity is driven by the approaching solar wind, it also reflects the solar wind's long-term variations. The long-term variations of  $K_p$  originate from the change in solar activity and the changes due to the Earth's orbit around the Sun. The influence of both effects is quantified in the following. I estimate those long-term variations of the  $K_p$  index which are contributed by solar activity and seasonal effects.

### 4.1.1 Solar activity influence

The general  $K_p$  distribution seen in Figure 4.1 averages over solar activity. Lower solar activity comes with a weaker ambient heliospheric magnetic field, resulting in weaker geomagnetic activity as well. Solar activity is generally tracked with the international sunspot number (SSN). A functional dependency of the average yearly  $K_p$  index on the yearly SSN is derived. SSN data from the time period 1917–2016 is used in the present analyses. The data is obtained from the International Sunspot Number Monthly Bulletin and online catalog provided by the WDC-SILSO<sup>2</sup> at the SIDC (ROB).

The  $K_p$  frequency distributions' shape varies with solar activity as is visible in the yearly distributions, sorted and colored by yearly SSN in Figure 4.2. The distribution's peak position scales with SSN, that is, a high yearly SSN results in a higher abundance of large  $K_p$  values as well.

The time series of yearly average  $K_p$  values from the years 1932–2016 shows a solar cycle imprint, see the top graphs in Figure 4.3. The  $K_p$  pattern follows the solar cycle minima and maxima as well as the changes in magnitude between solar cycles. The yearly mean  $K_p$  shifts by a value of about 1.0 for both variations separately. As expected, the correlation with solar activity shows an 11-year period, see bottom graph in Figure 4.3. The highest correlation coefficient of 0.60 is found with a time lag of  $-1$  year, that is, the yearly average  $K_p$  follows the SSN of the previous year.

<sup>1</sup>GFZ Potsdam  $K_p$  index website: <http://www.gfz-potsdam.de/en/kp-index/>

<sup>2</sup>WDC-SILSO website: <http://www.sidc.be/silso/>

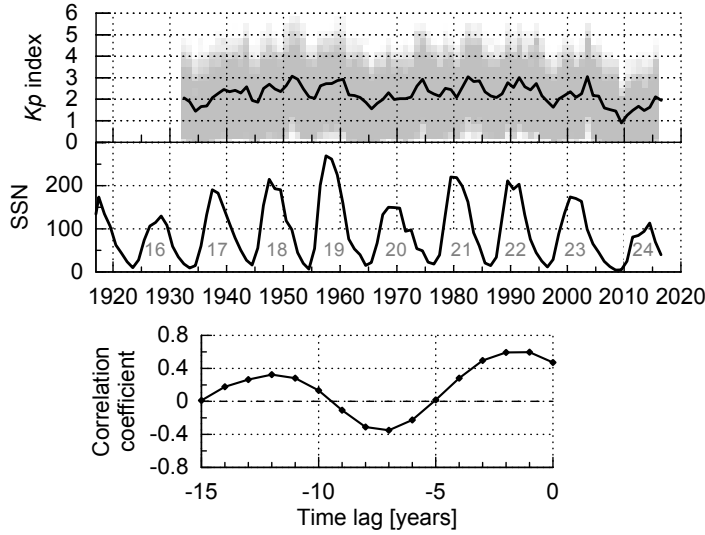


**Figure 4.3** Yearly  $Kp$  index distributions (shaded area) with their mean values for the time period 1932–2016 and yearly SSN with cycle number for the time period 1917–2016 (top panels). The Pearson correlation coefficients with the yearly SSN are calculated for time lags back to –15 years (bottom panel). The  $Kp$  data is obtained from the GFZ Potsdam and the yearly SSN data from the SILSO World Data Center.

The yearly mean  $Kp$  index with respect to the 1-year lagged SSN shows a rise with increasing SSN, as seen from Figure 4.4. In order to obtain an analytical relation for this dependency, I perform a least-squares regression fit.  $Kp$  itself is a quasi-logarithmic index, so it is apparent to use a logarithmic fit function:

$$f(x) = a \cdot \ln(x) + b. \quad (4.1)$$

The resulting fit parameters are  $a = 0.281(43)$  and  $b = 1.05(19)$ ; the numbers in parentheses are the estimated standard deviations. Concerning the error notation in this work, I adhere to the parentheses notation documented in the “Guide to the expression of uncertainty in measurement” (GUM) published by [Joint Committee for Guides in Metrology \(2008\)](#), where the numbers in parentheses are the errors on the corresponding last digits of the quoted value. The fit parameters lead to the relation

$$Kp(ssn) = 0.281 \cdot \ln(ssn) + 1.05, \quad (4.2)$$

which is plotted in Figure 4.4 together with its fit error band. The mean  $Kp$  error has a size of about  $\pm 0.3$ . For an average yearly SSN of 1 the mean  $Kp$  is 1.05(20) and for a SSN of 300 it is 2.65(31). The errors are calculated via error propagation from the estimated standard deviations of the fit parameters. This relation is a practical resource for estimating the yearly average  $Kp$  index from the last year’s average SSN. In 2017 the yearly SSN was 21.7 – applying this into the relation gives an average  $Kp$  of 1.91 for the year 2018.

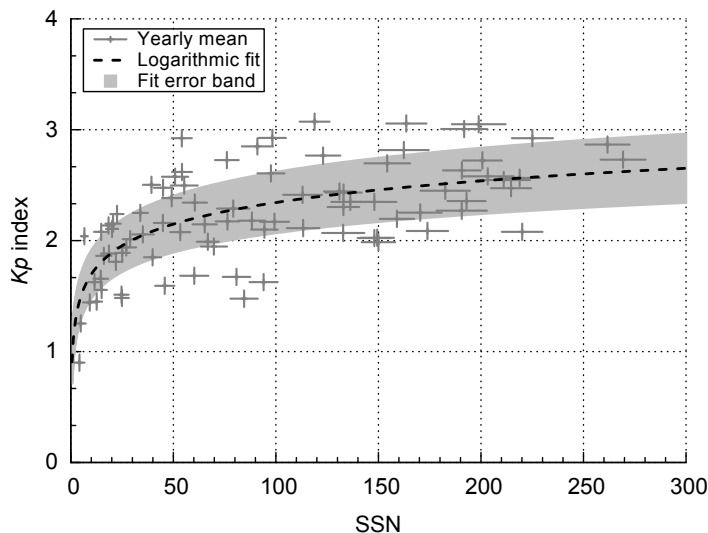


**Figure 4.4** Yearly mean  $Kp$  index with respect to 1-year lagged SSN (+) with the weighted logarithmic fit (dashed line). The error bars denote the SSN standard deviation and the relative weight from the yearly data coverage. The shaded area represents the fit error band derived from the estimated standard deviations of the fit parameters. The logarithmic function (Equation 4.1) is used for the weighted fit. The yearly  $Kp$  mean values are calculated from GFZ Potsdam data. The yearly SSN is obtained from the SILSO World Data Center.



### 4.1.2 Seasonal variations

On top of the yearly variations, seasonal variations exist in the magnetospheric disturbances as well. In the months May–August the  $Kp$  peak frequency is higher than in the remaining months of the year, whereas in March/April and September/October  $Kp$  values larger than 3.0 are more abundant. This is apparent from looking at the monthly  $Kp$  frequency distributions plotted in Figure 4.5. These  $Kp$  changes arise from seasonal

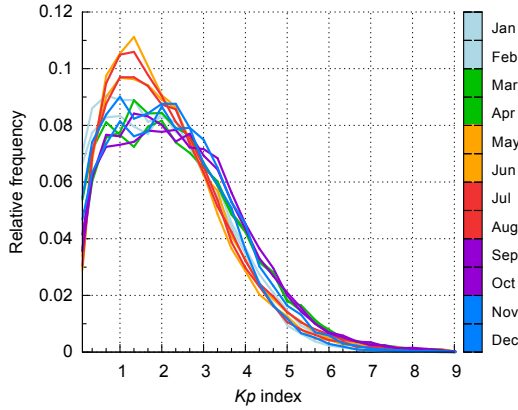


**Figure 4.5** Average monthly  $Kp$  frequency distributions of the time period 1932–2016, colored by month of the year. The  $Kp$  data is obtained from the GFZ Potsdam.

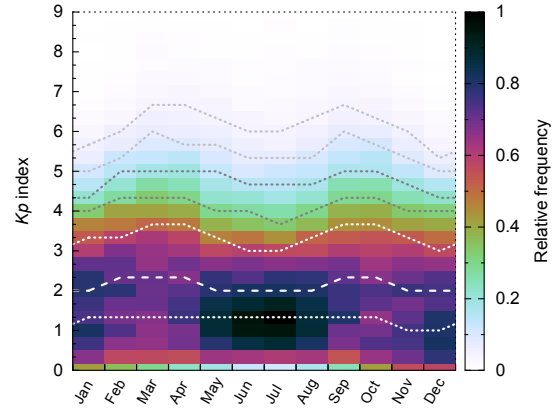


**Figure 4.6**  $Kp$  frequency distributions by month for the time period 1932–2016 with median (white dashed) and quartile isolines (white dotted). The other dotted isolines mark the upper eighth, 16th, 32nd, and 64th parts. The bin size in time is 1 month and in  $Kp$  0.3.

variations of the solar wind parameters at Earth, which stem from Earth’s yearly changes in orbital distance and heliographic latitude. The Earth’s rotation axis tilt adds another seasonal effect, as the tilt changes the direction of the Earth’s magnetic dipole axis to the Sun during the year.

Earth’s distance to the Sun varies over the course of a year by  $\pm 1.67\%$ , see Appendix A.5. The solar wind parameters scale via power-law dependencies with solar distance, as it is described in Chapter 5 and accordingly in Venzmer & Bothmer (2018). For example, the solar wind proton density scales with a solar distance exponent of about  $-2$ , this leads to a yearly variation in density of about  $6.7\%$ . These yearly variations of the solar wind have direct influence on the  $Kp$  index.

The solar wind’s influence on the  $Kp$  index depends on its coupling efficiency with the magnetosphere. The rate of magnetic reconnection between solar wind and the Earth’s magnetosphere depends on both fields’ orientation to each other (parallel/antiparallel). The Sun’s rotation axis tilt angle to the ecliptic is  $\pm 7.25^\circ$  and that for Earth is  $\pm 23.44^\circ$ , see also Appendix A.5. First, the solar wind type composition varies with heliographic latitude, which has consequences for the average values of parameters, such as magnetic field strength and velocity. Second, the tilt of the magnetic dipole axis to the rotation axis – only a few degrees for the Sun during cycle minima and extreme during solar maxima; and around  $10^\circ$  for the Earth – complicates this system even more.

So the  $Kp$  variation effects originate from the seasonal change in the solar tilt, the Earth’s tilt, and the Earth’s solar distance. Thorough analyses of the seasonal variations were already early performed by Cortie (1912) and many others thereafter. Thus, I just assess the bulk magnitude of these effects in order to consider them as relative uncertainties for the solar activity relation (4.2). Looking at the  $Kp$  frequency distributions by month – seen in Figure 4.6 – it is apparent that for values ( $Kp > 2.0$ ), there exist yearly frequency maxima at the equinoxes and frequency minima at the solstices, as was early described by Cortie (1912). It is evident from the plotted quantiles that this semiannual variation in  $Kp$  amounts to 0.3 for the median  $Kp$  and goes up to 1.3 for the rare higher  $Kp$  values.

## 4.2 Relation between solar wind electric field and $Kp$ index

The coupling between the solar wind and the magnetosphere is governed by reconnection and compression of the magnetic field lines, as described in Subsection 2.7.1. There exist quite a few coupling functions that are intended to approximate these processes in relating solar wind quantities with geomagnetic activity (Subsection 2.9.1). In this section I settle and work with the solar wind electric field as the coupling function for the purpose of nowcasting the  $Kp$  index.

The solar wind electric field  $E$  approximates the rate of magnetic flux aligned with the  $z$ -direction of the GSM coordinates. The electric field  $y$ -component  $E_y$  approximates the electric field  $E$  under special circumstances, the derivation is presented in Appendix A.2.  $E_y$  is the product of the radial proton velocity  $v_x$  and the magnetic field  $z$ -component  $B_z$ :

$$E_y = -v_x \cdot B_z. \quad (4.3)$$

In the following analysis, the negative electric field proxy  $vB_z$  is applied instead, where the vector component  $v_x$  is approximated by the absolute flow speed  $v$ . Here I adhere to the units [ $\text{km s}^{-1} \text{ nT}$ ] – they translate to the electric field units [ $\text{mV km}^{-1}$ ].

#### 4.2.1 Data correlation

$Kp$  is defined for 3-hour time intervals and it represents the maximal variation within this period (see Sub-section 2.8.1). Any solar wind parameter that is to be correlated with  $Kp$  also should have the same time resolution.

However, in addition to adapting the time resolution, it has to be considered by which means this should be done. Most IMF variations exist on shorter time scales than 3 hours. Averaging the IMF over these intervals suppresses features that are important drivers of geomagnetic activity (Savani et al. 2017). Thus, the solar wind parameter's 3-hourly extreme values are expected to have a stronger correlation with  $Kp$  than the 3-hourly averages. Commonly the  $Kp$  index is correlated with 3-hour or 1-hour solar wind averages (e.g., Newell et al. 2007; Elliott et al. 2013; Savani et al. 2017).

The underlying time resolution for the calculation of the 3-hour  $Kp$  intervals is 1 minute. Therefore, to be able to correlate  $Kp$  with solar wind data in a proper way, high-resolution solar wind data, that is, much shorter than the 3-hour resolution, are needed to determine the extrema within each 3-hour interval. The  $Kp$  time series started in 1932 when there existed no spacecraft to measure solar wind in situ. Thus, the maximal surveyed time range is restricted by the available in-situ solar wind data. The OMNI data collection constitutes the longest continuous solar wind measurements made at 1 au. There exist two OMNI data sets with different time resolution – the hourly version extends back to 1963 and the minute-by-minute version extends back to 1981. Although it is shorter, I choose to apply the minutely data, in order to benefit from the higher correlation as discussed above. Thus, the work presented in this chapter is based on the minutely OMNI data set with a time duration of 36 years, spanning from 1981 until end of 2016.

The product  $vB_z$  is formed and the minutely solar wind data is reduced to 3-hourly values in two ways: by calculating the averages and the minima. The reduction to 3-hour minimum values shifts the  $vB_z$  frequency distribution asymmetrically to negative values, whereas the averaged data is scattered around zero, see Figure 4.7.

The data is reduced to 3-hourly values in order to match the  $Kp$  data resolution. Both its averages and minima are used to evaluate the advantage of high-resolution data by correlating them to the  $Kp$  index. The  $Kp$ - $vB_z$  Pearson correlation coefficients for the two differently processed data versions are plotted over time shift in Figure 4.8. The data with 3-hour minimum processing shows a significantly better correlation than the

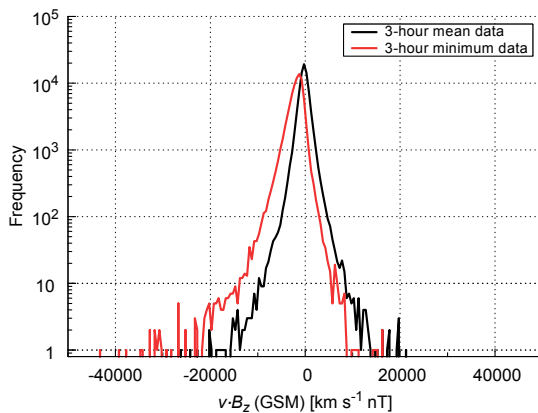


**Figure 4.7** Frequency distributions for the  $vB_z$  product. The minutely OMNI data from 1981–2016 is reduced to 3-hour averages (black line) and 3-hour minima (red line).

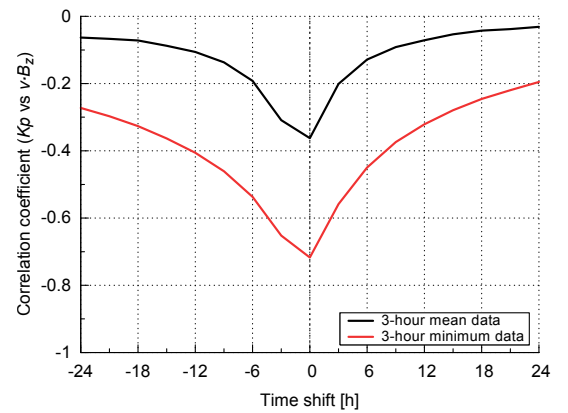


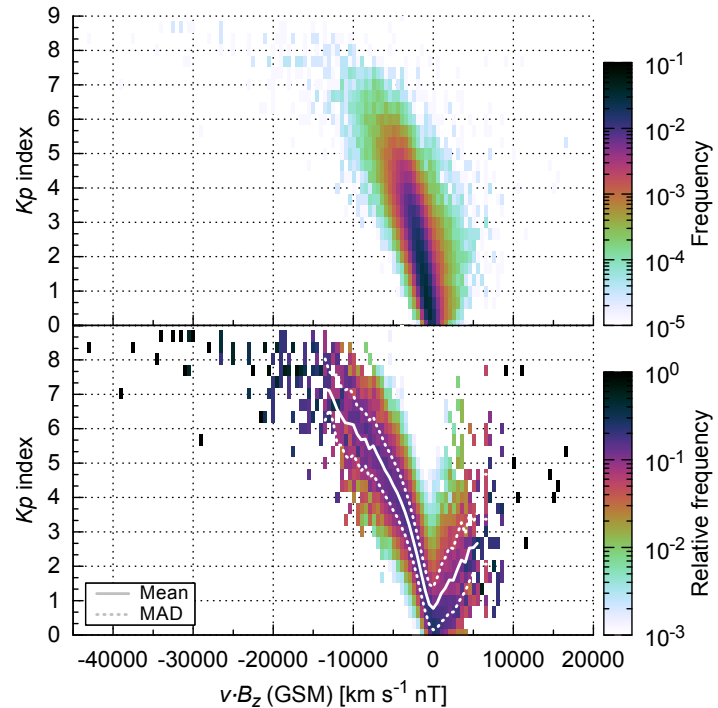
**Figure 4.8**  $Kp$ - $vB_z$  correlation coefficients for different time shifts up to  $\pm 24$  hours. The minutely OMNI data from 1981–2016 is reduced to 3-hour averages (black line) and 3-hour minima (red line).

3-hour average data. Both curves show a negative correlation and their minima lie at a time shift of zero, which is expected as the OMNI data represents the solar wind at the location of the magnetospheric bow shock. It takes the plasma only a couple of minutes to arrive at the magnetopause and influence the geomagnetic field, for example, a study about the Dungey convection cycle by [Zhang et al. \(2015\)](#) accounts for this duration by lagging the OMNI data generally by 5 minutes. I estimate its influence for this analysis to be negligible and thus do not apply such a time shift. The correlation coefficient for the minimum data reaches a value of  $r_{\min} = -0.72$  and is twice as high as that for the average data  $r_{\text{avg}} = -0.36$ .

#### 4.2.2 Functional dependency for solar wind electric field

An empirical relation between  $vB_z$  and  $Kp$  is sought by processing the data distribution and fitting an appropriate function to it. The frequency distribution in  $Kp$ – $vB_z$  space is shaped like a candle flame, inclined to negative values by a light breeze, see top panel in [Figure 4.9](#). The negative correlation is already apparent. In order to determine a functional dependency, I focus on the relative frequencies per  $vB_z$ -interval and their average  $Kp$  values, which are plotted in the bottom panel of [Figure 4.9](#). This probability distribution is asymmetrically V-shaped around zero, having a larger and steeper negative arm than positive arm. The mean absolute deviation (MAD) from the average  $Kp$  value has a mean size of 0.7.

**Figure 4.9**  $Kp$  versus  $vB_z$  frequency distribution (top panel) and its relative distribution (bottom panel) with the mean  $Kp$  values (solid line) and their mean absolute deviation (dotted lines). It is 3-hour minimum data from the minutely OMNI data set (1981–2016). The bin size in  $vB_z$  is  $500 \text{ km s}^{-1} \text{ nT}$  and in  $Kp$  0.3.



The asymmetry also exists for 3-hour average data (which is not plotted), thus this effect is not a result of the data reducing method to 3-hour minima. Rather the steeper negative arm is a consequence of the asymmetric coupling of the solar wind magnetic field direction to the magnetopause, as described in detail in [Subsection 2.7.1](#).

An appropriate type of function has to be constructed for the empirical fit. Since the  $Kp$  index has a quasi-logarithmic scaling (see [Subsection 2.8.1](#)), a logarithmic function is the obvious choice for the fit function. Furthermore, the depending argument consists of a product of two solar wind parameters which individually scale logarithmically with  $Kp$ . These reasons are why I use the logarithm of a parabola for the fitting approach:

$$f(x) = \ln(x^2). \quad (4.4)$$

I also introduce a horizontal shifting parameter  $x'$  because the distribution's center is slightly offset. To be able to replicate the asymmetry in both arms, I further split the fit function at the minimum ( $x + x'$ ) into arms of negative and positive slope:

$$f(x) = \begin{cases} f_-(x) & \text{for } x + x' < 0, \\ f_+(x) & \text{for } x + x' \geq 0. \end{cases} \quad (4.5)$$

This way, both arms can be scaled individually with scaling factors for the negative and positive parts  $a_-$  and  $a_+$ . The resulting logarithmic fit function parts are

$$f_-(x) = a_- \cdot \ln((x + x')^2 + b) + y', \quad (4.6)$$

$$f_+(x) = a_+ \cdot (f_-(x) - f_-(-x')) + f_-(-x'), \quad (4.7)$$

with the vertical shifting parameter  $y'$  and the depth parameter  $b$ . The resulting values of the fit coefficients are  $a_- = 1.258(19)$ ,  $x' = 163(20)$ ,  $b = 1.416(68) \times 10^6$ ,  $y' = -17.04(33)$ , and  $a_+ = 0.467(20)$  for units of  $[\text{km s}^{-1} \text{ nT}]$ . Thus, the solar wind dependency relation 'condenses' to:

$$Kp_-(vB_z) = 1.258 \cdot \ln((vB_z + 163)^2 + 1.416 \times 10^6) - 17.04, \quad (4.8)$$

$$Kp_+(vB_z) = 0.467 \cdot (Kp_-(vB_z) - Kp_-(-163)) + Kp_-(-163). \quad (4.9)$$

The fit curve is plotted in Figure 4.10. The error bars of the data points indicate the relative data count per  $vB_z$  interval. Those points which deviate far from the fit curve (e.g., below the left arm and above the right arm) stem from single 3-hour periods. A look into the data revealed that all data outside the range  $-14\,000$ – $8\,000 \text{ km s}^{-1} \text{ nT}$  is related to CMEs. Thus, the deviating points are caused by individual CME events, for example, the two points with a  $Kp$  of 7.7 near  $10\,000 \text{ km s}^{-1} \text{ nT}$  belong to two CMEs<sup>3</sup> with in-situ velocities of about  $1000 \text{ km s}^{-1}$  and a positive  $B_z$  of the order  $30 \text{ nT}$ .

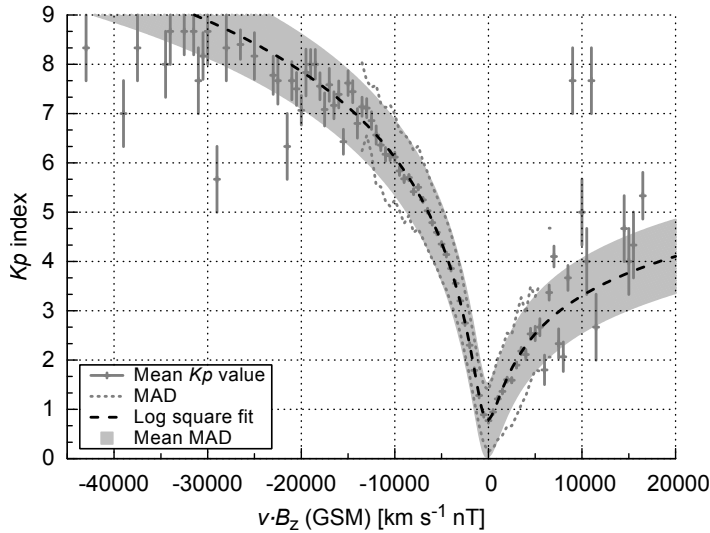


**Figure 4.10** Mean  $Kp$  values (+) and MAD values (dotted lines) per  $vB_z$  interval. The error bars represent the relative data count. The logarithmic fit (dashed line) is plotted with a mean MAD band (shaded area). The splitted function (4.5) is used for the weighted fit.

This derived E-field relation can well be applied with the solar wind real-time measurements that are continuously being made by spacecraft located at L1. However, the heads-up time for warnings from this location is relatively short having only a few tens of minutes, whereas remote observations via solar imagers and coronagraphs allow for longer lead times of a few days. In principle, the E-field relation could also be applied to remote forecast situations, however, IMF strength and orientation are not yet properly predictable from current prediction methods that rely on remote observations.

### 4.3 Relations between CME/stream velocities and $Kp$ index

In order to still benefit from the enhanced warning lead times obtained from remote observations, the solar wind velocity has to be employed. It is the only parameter left which is to a certain degree reliably forecastable from remote observations. In fact, solar wind velocity and  $Kp$  index correlate quite well – Machol et al. (2013) even proposed a linear function of the  $Kp$  index as a best proxy for corrupted real-time velocity measurements made by the ACE spacecraft. For one, the velocity can even be used for persistence forecast, as it has the highest autocorrelation time of all major solar wind parameters – with 59 h it is much higher than that with the lowest autocorrelation time of 4 h, which is indeed the  $B_z$  GSM component (Elliott et al. 2013). It is clear that the strength of the southward IMF component is the most dominant solar wind parameter for the driving of geomagnetic activity. The velocity shows a strong correlation during CME conditions as well, however,

<sup>3</sup>For reference: the two 3-hour intervals began at 2000-07-16 00:00 and 2005-05-15 09:00

in fact during high speed streams the velocity is considered to be the most dominant parameter for driving geomagnetic activity (Holappa et al. 2014).

In order to forecast the  $Kp$  index from remotely derived velocity values, it makes sense to analyze CMEs and solar wind streams separately. The distinct generation mechanisms of CMEs and solar wind streams show in their different appearance: CMEs are event-like and streams are of continuous nature. Therefore these two solar wind structures require completely different forecast methods (Subsection 2.9.3). In the following, I use an existing list of solar wind structures to separate between CME and solar wind stream data, calculate 3-hour velocity values, and correlate them with the  $Kp$  index. Functional dependencies are derived for obtaining  $Kp$  proxies from both structure types separately.

### 4.3.1 Solar Wind Structures list

For the separation of CME and stream data, I use the list of Solar Wind Structures (SWS) created and updated by Richardson et al. (2000) and Richardson & Cane (2012). They characterized the near-Earth solar wind into periods related to slow wind, fast wind, and CMEs. Their list extends back to 1963 and is mostly based on 1-hour averages of solar wind parameters from the OMNI data set. However, in the cases where there are gaps in the in-situ data, they consider other indicators for identifying solar wind structures. They achieve a fairly complete classification with the inclusion of data from geomagnetic activity, energetic particles, and cosmic rays. Their work identifies solar wind structures and flags the time series into four categories: CME-associated flows, slow solar wind, fast solar wind, and undetermined intervals. Periods related to CMEs are defined to also comprise the associated ambient solar wind plasma, which consists of upstream shocks and compressed material. The criterion for differentiating between slow and fast solar wind is a velocity threshold of  $400 \text{ km s}^{-1}$ .

The SWS list is made available via registration at CEDARweb<sup>4</sup>. The updated SWS list (until the end of 2016) was kindly provided by Ian Richardson. According to the SWS list, the CME fraction during the 36-year time period considered in the present study, 1981–2016, is 15.4 %, which accumulates to 5.53 years. This percentage is an average value, as the actual short-term fraction varies heavily with the solar activity cycle and with the appearance of individual active regions on the solar surface.

The SWS definition of CME-associated flows makes sense for the present study as the causes of the strongest geomagnetic storms are both the compression of the magnetic field within the shock fronts of fast CMEs and the enhanced field strength of the driving magnetic clouds (Bothmer & Schwenn 1995). In the following part of this study, I refer to the combination of the SWS categories slow and fast solar wind simply as solar wind streams. These periods are composed entirely from a mixture of slow wind flows, fast wind streams, and their interaction regions.

### 4.3.2 Data correlation

Again, as done before for the data processing of the E-field analysis, 3-hour average as well as extreme velocities are calculated using the minutely OMNI data in order to test for a higher correlation with  $Kp$ . The comparison between the 3-hour average and the 3-hour maximum frequency distributions shows that their mean positions are shifted slightly, having velocities of  $405 \text{ km s}^{-1}$  and  $425 \text{ km s}^{-1}$  respectively, see Figure 4.11.

The  $Kp$  correlations with the average and maximum processed data show that both are nearly identical, see Figure 4.12. Their maxima lie at a time shift of 6-hours with correlation coefficients of 0.61 and 0.62 respectively, see Table 4.1.

**Table 4.1** The highest correlation coefficients and their time lags of the  $Kp$ –velocity relations for the different data versions: 3-hour averaged data, 3-hour maximum of all data, CME, and stream data. The values are based on the minutely high-resolution OMNI data from the time period 1981–2016.

Data	3-hour processing	Time lag [hours]	Correlation coefficient
All data	averages	6	0.613
All data	maxima	6	0.622
CMEs	maxima	0	0.511
Streams	maxima	9	0.661

<sup>4</sup>SWS list at CEDARweb: [http://cedarweb.vsp.ucar.edu/wiki/index.php/Tools\\_and\\_Models:Solar\\_Wind\\_Structures](http://cedarweb.vsp.ucar.edu/wiki/index.php/Tools_and_Models:Solar_Wind_Structures)



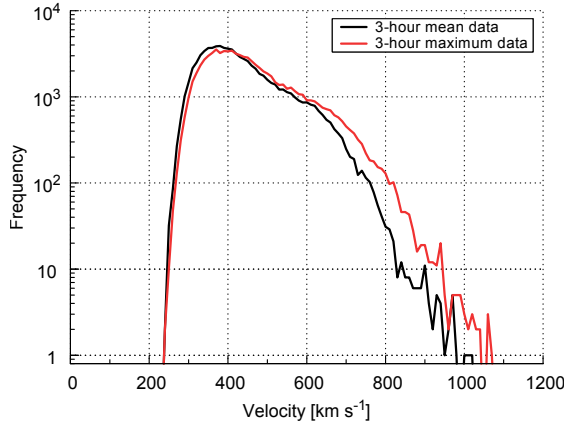


**Figure 4.11** Solar wind velocity frequency distributions for the 3-hour average and 3-hour maximum data. The minutely OMNI data from the period 1981–2016 is used.

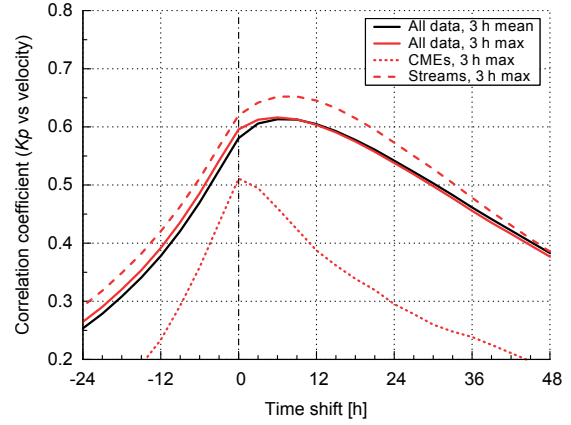


**Figure 4.12**  $Kp$ -velocity correlation coefficients for time shifts in the range from  $-24$  to  $48$  hours. The correlations are plotted for the whole solar wind data (solid lines), for solar wind streams without CMEs (dashed line), and for CMEs only (dotted line). The data used is the 3-hour averages (black) and the 3-hour maxima (red) of the minutely high-resolution OMNI data from the period 1981–2016.

The CME and stream parts of the 3-hour maximum data are examined separately by filtering the corresponding periods using the SWS list. Both parts are correlated independently with the  $Kp$  index. The correlations for CME related data are lower than those for all solar wind. Their maximal correlation coefficient has a value of 0.51 and is without time shift. Solar wind streams show higher correlations with  $Kp$  and the correlation's maximum value 0.66 has a positive time shift of 9 hours, which means that the  $Kp$  index forecasts the velocity of solar wind streams 9 hours in advance. This positive time shift may be explained from the occurrence of interaction regions followed by HSSs. When a slow solar wind stream is followed by a fast one, the compression at their interface leads to enhanced solar wind densities and magnetic field strengths. The peak velocity of a HSS naturally appears after the interaction region. Therefore, the  $Kp$ -impact from the enhanced magnetic field might be correlated with the higher velocity of the trailing HSS, resulting in the observed positive time shift.

The broader correlation curve for streams (Figure 4.12) seems to be owed to their continuous nature, whereas the more peaked CME curve is a result of their event-like nature. The significantly higher correlation coefficient seen for streams might replicate the velocity's dominating role for geomagnetic activity during HSSs (Holappa et al. 2014).

For  $vB_z$ , the correlations with  $Kp$  are very different for 3-hour averages and extrema, at the same time the same procedure for velocity results in two nearly identical correlations. I suggest this situation can be explained by the very different autocorrelation times of  $B_z$  and velocity (Elliott et al. 2013).

### 4.3.3 Functional dependencies for CME and stream velocities

The general  $Kp$ -velocity dependency in the solar wind is apparent from the tilt of its distribution, see first panel of Figure 4.13. The distribution is inclined to positive values but very broad, that is, in the typical solar wind velocity range it spans over more than half of the total  $Kp$  range. The comparison with the filtered data shows that  $Kp$  values  $> 6.0$  and velocities  $> 850 \text{ km s}^{-1}$  are almost always associated with CME related periods, see right and bottom panel of Figure 4.13.

In order to determine a functional relation between  $Kp$  and CME velocity, I look at the relative  $Kp$  frequencies for each  $10 \text{ km s}^{-1}$  velocity interval. The relative frequencies are plotted in the bottom panel of Figure 4.14. The average  $Kp$  value seems to scale almost linear with the solar wind velocity. The MAD of the average  $Kp$  value has a mean  $Kp$  size of about 1.1. Again, as the  $Kp$  index has a quasi-logarithmic scaling, a logarithmic function is the obvious choice for the fitting process. Thus, the logarithmic function

$$f(x) = a \cdot \ln(x + x') + y' \quad (4.10)$$

is used for the fit, with the scaling factor  $a$ , the location parameter  $x'$ , and the vertical shifting parameter  $y'$ . The resulting fit parameters are  $a = 10.6(34)$ ,  $x' = 8.1(43) \times 10^2$ , and  $y' = -73(28)$ , with the velocity in units

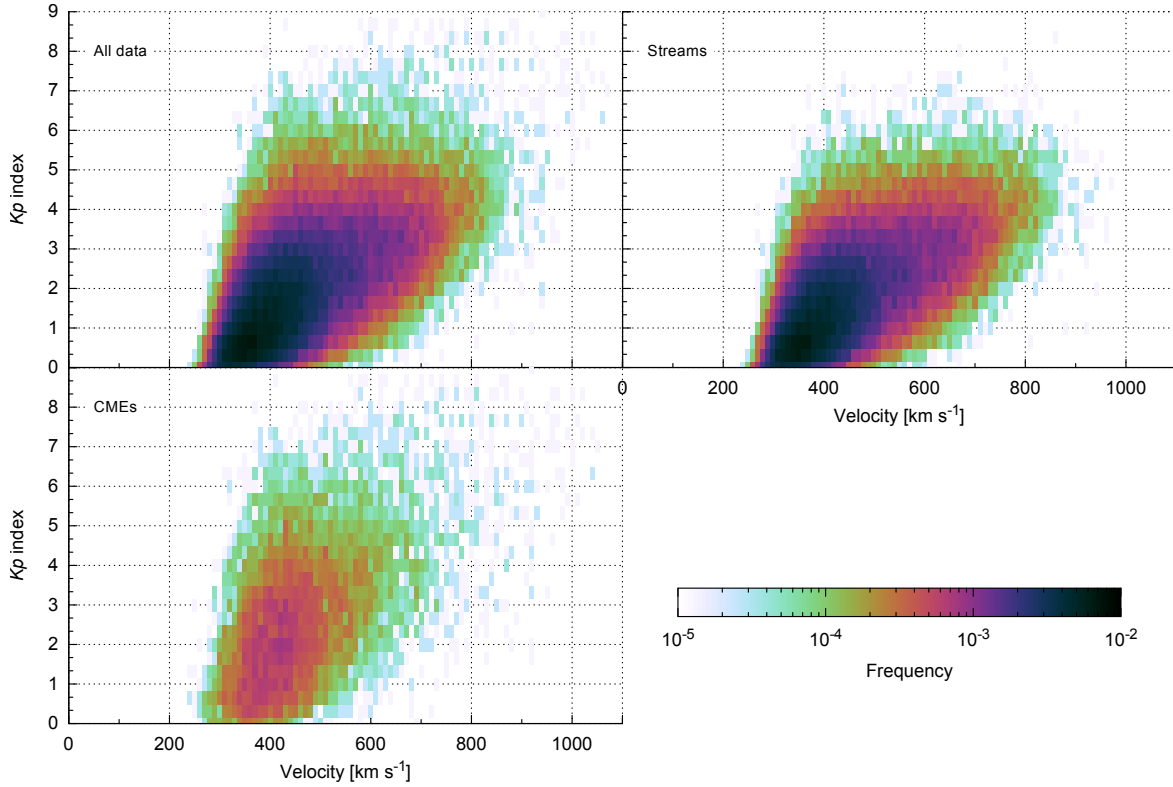


**Figure 4.13**  $Kp$ -velocity distributions for all solar wind data, for solar wind streams, and for CMEs. The data consists of the 3-hour maxima of the minutely high-resolution OMNI data from the time period 1981–2016. The SWS list from [Richardson & Cane \(2012\)](#) is used for the separation between CME and stream data. The bin size in velocity is  $10 \text{ km s}^{-1}$  and in  $Kp$  0.3.

of  $[\text{km s}^{-1}]$ . They lead to the CME dependency function

$$Kp_{\text{CME}}(v) = 10.6 \cdot \ln(v + 810) - 73, \quad (4.11)$$

which is plotted in [Figure 4.15](#). This empirical relation can be used to forecast the  $Kp$  index from a predicted CME arrival velocity, e.g., obtained from analyses of remote coronagraph observations.

The procedure for the functional dependency on stream velocity is the same as that for the CME velocity. However, in the case of solar wind stream velocities, the correlation coefficient is higher when the data is shifted by 9 hours ([Figure 4.12](#)). I use this shifted data and look at the relative frequencies per velocity interval in order to find a functional dependency between  $Kp$  and velocity, see bottom panel of [Figure 4.16](#). Again, the mean  $Kp$  value scales almost linear with the velocity. The distribution is much narrower than that for CMEs – the MAD from the average  $Kp$  has only a mean size of about 0.7.

Again, I use the logarithmic function (4.10) for the fitting process. The resulting values of the fit parameters are  $a = 5.88(38)$ ,  $x' = 2.99(49) \times 10^2$ , and  $y' = -3.70(29) \times 10^1$ , with the velocity in units of  $[\text{km s}^{-1}]$ . This leads to the solar wind stream dependency function

$$Kp_{\text{Stream}}(v) = 5.88 \cdot \ln(v + 299) - 37.0, \quad (4.12)$$

which is plotted in [Figure 4.17](#). This empirical relation can be used to forecast the  $Kp$  index from an estimated stream velocity, e.g., obtained from remote coronal hole analyses.

The stream velocity curve is smaller and its slope is less steep than that obtained from the CME velocities. CMEs with a speed of  $500 \text{ km s}^{-1}$  cause on average a by 0.6 higher  $Kp$  than a stream of the same speed would – for CMEs with  $1000 \text{ km s}^{-1}$  this gap even increases to 1.3. This difference in  $Kp$  magnitude between the two velocity relations is due to the generally larger magnetic field strength in CMEs compared with streams having the same velocity.

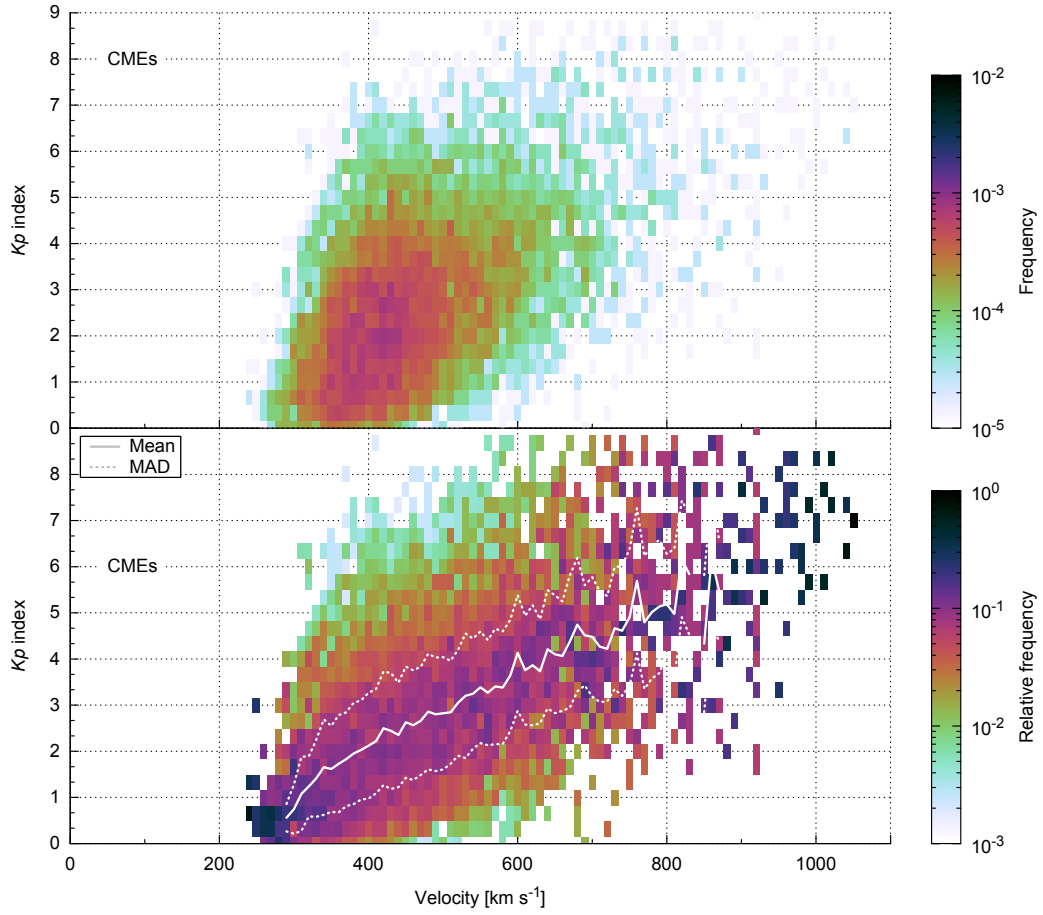


**Figure 4.14** CME fraction of the  $Kp$ -velocity distribution (same as third panel of Figure 4.13) and its relative distribution per velocity interval with the mean  $Kp$  values (solid line) and their MAD (dotted lines). The bin size in velocity is  $10 \text{ km s}^{-1}$  and in  $Kp$  0.3.

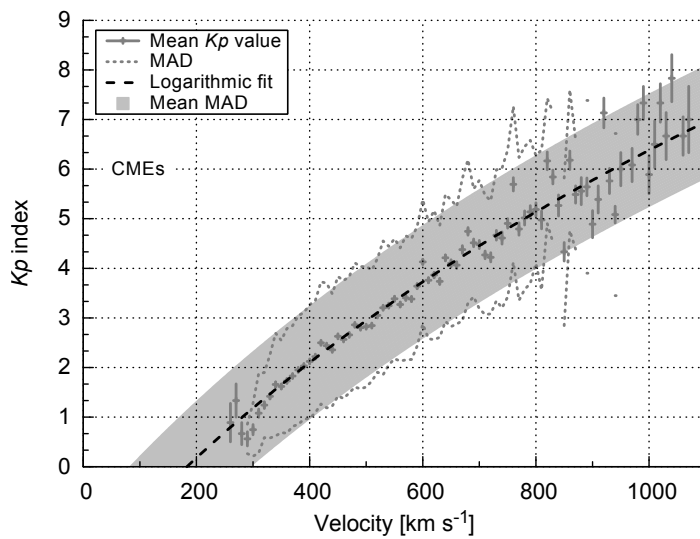


**Figure 4.15** Mean  $Kp$  values (+) and MAD values (dotted lines) per velocity interval for the CME fraction of the data. The error bars represent the relative data count. The logarithmic fit (dashed line) is plotted with a mean MAD band (shaded area). The function (4.10) is used for the weighted fit.

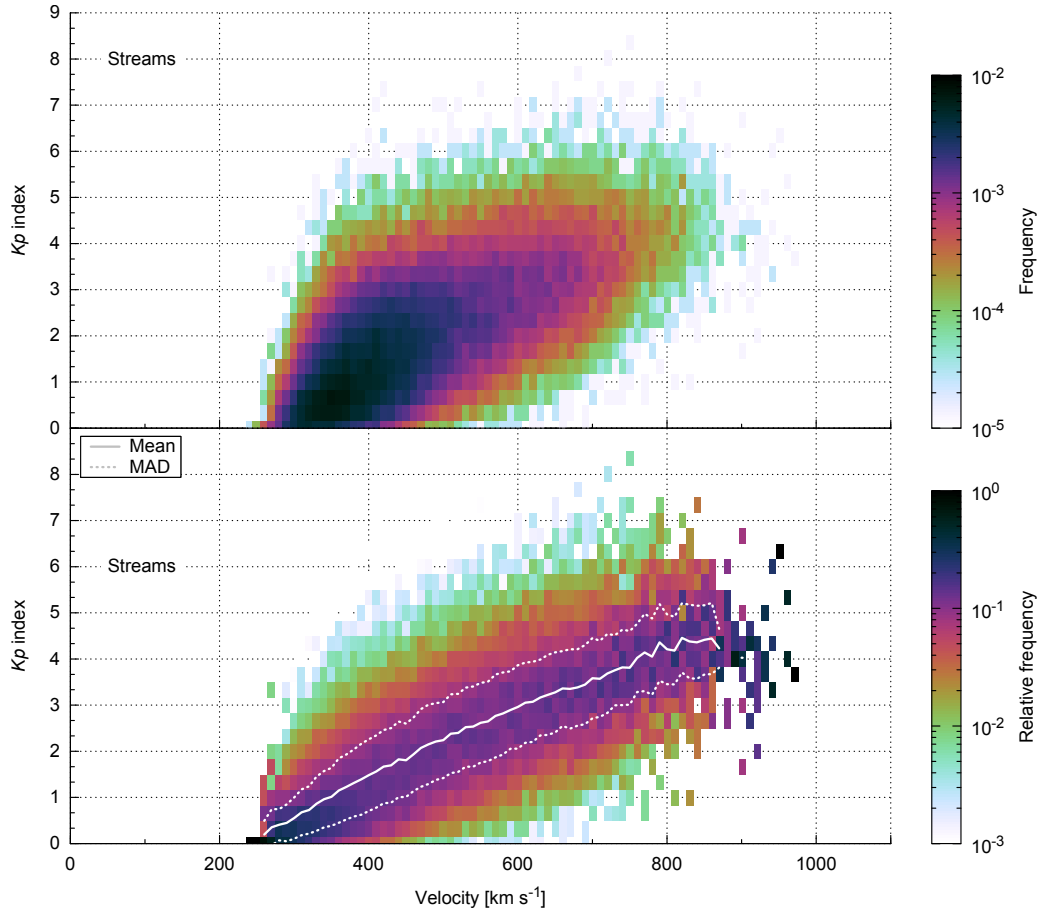


**Figure 4.16** Stream fraction of the  $Kp$ –velocity distribution (similar to second panel of [Figure 4.13](#), but with the data shifted by 9 hours) and its relative distribution per velocity interval with the mean  $Kp$  values (solid line) and their MAD (dotted lines). The bin size in velocity is  $10 \text{ km s}^{-1}$  and in  $Kp$  0.3.

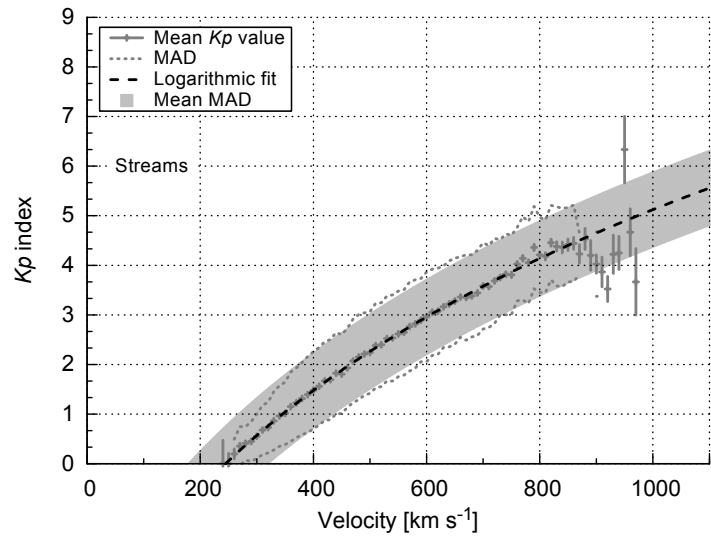


**Figure 4.17** Mean  $Kp$  values (+) and MAD values (dotted lines) per velocity interval for the stream fraction of the data, shifted by 9 hours. The error bars represent the relative data count. The logarithmic fit (dashed line) is plotted with a mean MAD band (shaded area). The function (4.10) is used for the weighted fit.

## 4.4 Prediction performance

The derived empirical relations are chosen for their high correlation coefficients. However, the correlation coefficient itself does not represent the performance of a model as the coefficient depends highly on the scatter of the underlying distribution. Therefore Wing et al. (2005) advise to additionally provide scatterplots and skill scores for the evaluation of predictive models. In the following, I present the forecast errors and determine the true skill statistics as measures for the prediction performance of the derived empirical models.

The quality of predictions can be assessed by how they compare to a simple persistence model (Detman & Joselyn 1999). In the case at hand, the persistence consists of the official  $Kp$  value from the previous 3-hour interval. The persistence performance is obtained from the complete  $Kp$  time span 1981–2016.

In order to evaluate all models' prediction performances, their forecast errors are calculated. Forecast errors are the differences between the predicted and the actual values. The resulting performances of the persistence and the three models are displayed together with the corresponding positive and negative standard deviations in Figure 4.18. The deviations to the forecast errors can be completely one-sided if the actual  $Kp$  values are always being over- or underestimated (in the figure these points are plotted in gray). This happens at the extreme ends of the  $Kp$  range – I denote the range in between as 'proper range'.

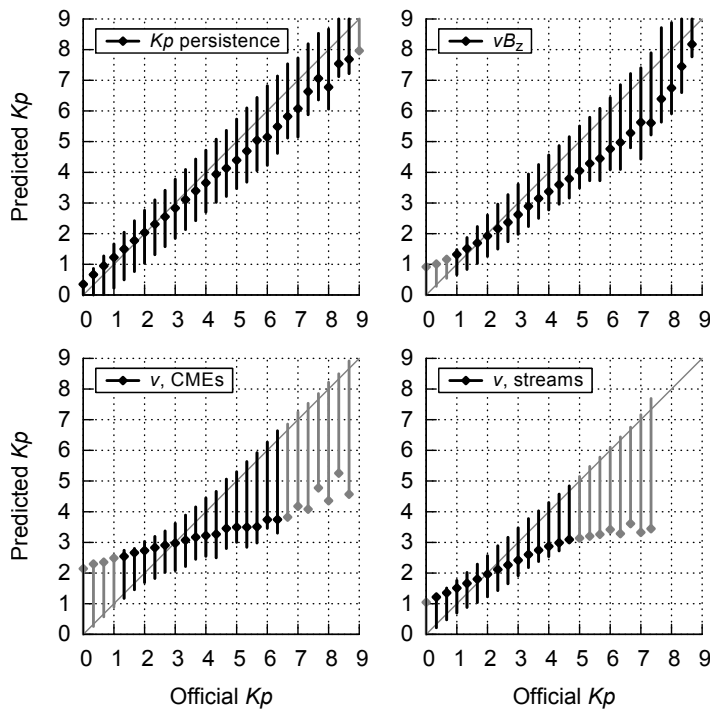


**Figure 4.18** Prediction performance of  $Kp$  persistence and the three derived empirical  $Kp$  relations. The forecast errors are the differences between the predicted and the actual values. They are calculated from the same data and time range as the relations themselves. The error bars denote one positive and one negative standard deviation. Forecast errors with one-sided deviations are plotted in gray. Perfect predictions are indicated by the diagonal lines.

The empirically derived solar wind relations do not cover the whole  $Kp$  range from 0 to 9 within the distributions of observed values. Only the  $Kp$  values with more than one observed data point are considered for deriving the relations' prediction performances. This excludes the values  $Kp = 9.0$  and in case of the velocity relation for streams also all values of 7.7 and above.

The persistence performs fairly well, as its forecast error is less than 0.7 up to a  $Kp$  of 5.7. At and above a  $Kp$  of 6.0 the error is underestimated with a maximum deviation of 1.3. The derived  $vB_z$  function (4.8 and 4.9) does only coincide with significant data in the  $Kp$  range 1.0 to 8.7, in particular because the minimum of the  $vB_z$  function is larger than 0.7 (Figure 4.10). The model performs reasonably well at and below a  $Kp$  of 5.0 with forecast errors smaller than 1.0. Larger  $Kp$  values are underestimated and deviate up to 1.7 from the predicted values. In the case of the velocity relation for CMEs, the  $Kp$  magnitude is overestimated below a  $Kp$  of 3.0 and underestimated above, and the proper range lies between 1.3 and 6.3. In the range between a  $Kp$  of 1.0 to 5.0 the forecast errors are smaller than 1.3. Above, the error rises up to 4.0 at a  $Kp$  of 8.7. For the velocity relation for streams, the proper range goes from 0.3 to 4.3 – the magnitude is overestimated below a  $Kp$  of 2.0 and underestimated above. The forecast errors are smaller than 1.3 throughout the proper range. Above, the error rises up to 4.0 at a  $Kp$  of 7.3. The model based on the  $vB_z$  relation is more accurate than those based purely on the velocity. This is expected, however, the  $vB_z$  relation is still eclipsed by the persistence model.



In order to further test the derived models for their predictive value, I derive their true skill statistic (TSS) – a common tool for forecast verification. The TSS is a skill score based on the contingency table that categorizes forecasted and observed events. The score is the difference between the forecast hit rate and the false alarm rate. It ranges from  $-1$  to  $1$ , where  $1$  indicates an ideal prediction and  $0$  a random prediction. I give more detailed information about the TSS in the Appendix A.7. This method is the prevalent form of forecast verification in  $Kp$  models (Detman & Joselyn 1999; Wing et al. 2005; Savani et al. 2017). It is defined that each single 3-hour  $Kp$  interval represents an event and a hit occurs when both the forecasted and observed  $Kp$  exceed a specified threshold. I adopt these criteria to make the results comparable. Therefore the TSS is derived as a function of  $Kp$  threshold – the results for persistence and the three models are plotted in Figure 4.19.

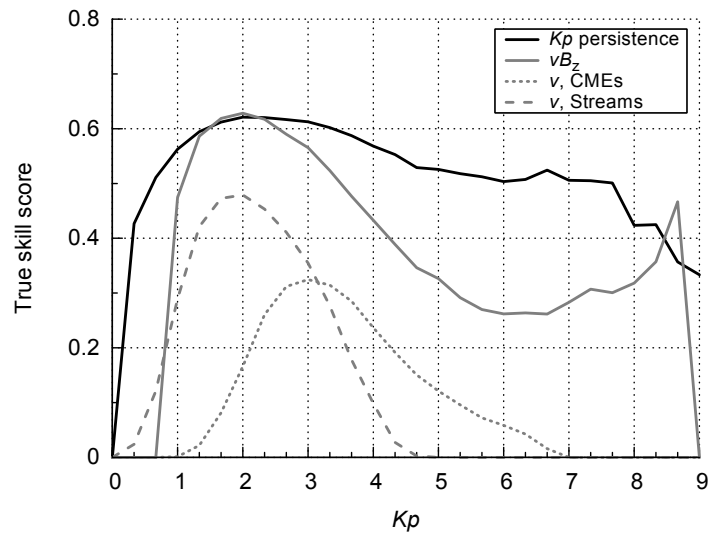


**Figure 4.19** True skill scores for the  $Kp$  persistence and the three predictive models as a function of  $Kp$  threshold. The scores are calculated from the same data and time range as the relations themselves.

The E-field relation reaches its peak at  $Kp = 2.0$  with a TSS of  $0.63$ , it then decreases to a local minimum at  $Kp = 6.0$  with a TSS of  $0.26$ . To higher  $Kp$  values, the TSS increases again and reaches  $0.47$  at  $Kp = 8.7$ . This increase is due to the dominant number of correct null forecasts that make the TSS approach the hit rate (Doswell et al. 1990) – it is a bias inherent to the TSS in case of rare event forecasting. Both velocity relations have throughout their  $Kp$  ranges a significantly lower TSS. The CME relation shows a peak TSS of  $0.32$  at  $Kp = 3.0$  and the stream relation a peak TSS of  $0.48$  at  $Kp = 2.0$ . Thus, the TSS gain from the additional  $B_z$  component is about  $0.15$ – $0.2$ .

The  $Kp$  ranges where the TSS of the predictive models is larger than zero coincide with their proper ranges. The models provide no better than random predictions outside these ranges, however, as can be seen from the forecast errors in Figure 4.18, they still track the general trend – even though with large errors in  $Kp$ .

The persistence forecast clearly outperforms the other prediction models, in particular in the high  $Kp$  range. However, as Detman & Joselyn (1999) stated, it has no warning value because it can only predict a high  $Kp$  value after a high  $Kp$  value was already observed. Thus, the persistence always misses the onset of a geomagnetic storm, whereas solar wind based models can provide at least a nowcast if not actually a short lead time from the distance of the in-situ measurement location at L1.

In order to compare the  $Kp$  forecast skill metrics with other models, Savani et al. (2017) use a threshold of  $Kp \geq 5.0$ . They choose this value because of the geomagnetic storm scale (G-scale) developed by NOAA's SWPC. The G-scale relates the  $Kp$  index to five levels from G1 to G5<sup>5</sup>. The starting level G1 translates to  $Kp = 5.0$ . Here I stick to this definition and provide a statistics summary of the  $Kp$  persistence and the three derived models in Table 4.2.

For the stream velocity relation, the defined  $Kp$  threshold is of little use as its proper  $Kp$  range is below the defining geomagnetic storm value of  $Kp = 5.0$ . The maximal velocity of solar wind streams is limited by the coronal temperatures (Parker 1958) and is observed to be around  $900 \text{ km s}^{-1}$ . That is why solar wind plasma associated with streams on average provoke  $Kp$  values below  $5.0$ , that is, geomagnetic storms cannot be predicted via the stream relation.

The E-field model has a TSS of  $0.33$  at  $Kp = 5.0$ , this can be compared with the Wing APL models (Wing et al. 2005, Fig. 13). The Wing APL model 3 predicts  $Kp$  1 hour in advance and uses the solar wind parameters velocity, density, magnetic field strength, and  $B_z$  as input sources for a neural network based model. The

<sup>5</sup>NOAA Space Weather Scales website: <http://www.swpc.noaa.gov/noaa-scales-explanation>

**Table 4.2** Statistics of the different prediction models. The metrics are calculated for a threshold hit criteria of  $Kp \geq 5$  for the same data and time range as the relations themselves.

Parameter	$Kp$ persistence $Kp(t-1)$	E-field $Kp(vB_z)$	CME velocity $Kp(v_{CME})$	Stream velocity $Kp(v_{Streams})$
Time shift [hours]	3	0	0	9
Event count	105 192	79 276	12 116	65 774
Correlation coefficient	0.81	-0.72	0.51	0.66
Proportion correct	0.96	0.97	0.88	0.98
Hit rate	0.55	0.33	0.13	0
False alarm rate	0.02	0	0.01	0
True skill score	0.53	0.33	0.12	0
Proper range [ $Kp$ ]	0.3–8.7	1.0–8.7	1.3–6.3	0.3–4.3

additionally considered parameters (density and absolute magnetic field strength) boost the corresponding TSS to about 0.7. The Wing APL model 1 incorporates  $Kp$  nowcast values in addition to the solar wind parameters and achieves this way a TSS of about 0.8.

The BSS model developed by [Savani et al. \(2015, 2017\)](#) predicts the magnetic field in CMEs arriving at Earth and derives their geomagnetic response. For a total of eight CME events, the BSS model shows a TSS of 0.34, when investigating only restricted periods of “active solar wind” ([Savani et al. 2017](#), Tab. 3).

## 4.5 Discussion

For the solar wind predictive  $Kp$  models, the influence of the solar activity is not considered despite its contribution of a  $Kp$  variation of about 1.6 (see [Section 4.1](#)). A detailed analysis of the solar activity’s influence on the  $Kp$  prediction behavior lies outside the scope of this thesis. Nevertheless, it would be worth examining the solar cycle’s influence on the relations, especially as [Wing et al. \(2005\)](#) note that the predictability of  $Kp$  slightly scales with solar activity. [Gopalswamy et al. \(2014\)](#) indicate in particular that low solar activity leads to a decreased geomagnetic effectiveness of CMEs in general. The reason is the reduced pressure within the heliosphere, which allows for a greater expansion of CMEs, resulting in the dilution of the magnetic field in the CME as well as weaker fields in the accompanying ambient compression regions.

In the following, I take two sample periods of solar wind in-situ data and apply the predictive  $Kp$  models to compare their output qualitatively with the actual measured  $Kp$  index. First, I discuss a 2-month period from the maximum of the solar activity cycle 24 and second, I zoom into a 6-day sub-period containing a CME.

The 2-month sample period of solar wind and  $Kp$  data is displayed in [Figure 4.20](#). The considered period ranges from 1 May to 5 July 2013, when the solar activity cycle 24 had its maximum. The period contains multiple types of structures, such as HSSs, CIRs, and CMEs. The plot shows the solar wind IMF strength, its z-component, the velocity with its 3-hour maxima, and the electric field  $vB_z$  with its 3-hour minima. The  $Kp$  estimate based on the electric field relation is displayed together with the official  $Kp$  index. The CME and stream velocity relations are displayed together with the official  $Kp$  index as well, however, both velocity relations are chosen according to the periods flagged as CMEs or streams in the SWS list, that is, either via Equation (4.11) or (4.12). The  $Kp$  derived from stream velocity is based on the data shifted by 9 hours.

It can be seen that in the considered period the  $Kp$  estimate based on the E-field traces the actual  $Kp$  index pretty well within its mean MAD band, whereas the  $Kp$  estimates based on both velocity relations do not coincide that well with the actual  $Kp$  index. The stream velocity based model overestimates small  $Kp$  values, which occur during rarefaction regions of declining velocity, whereas compressed regions are underestimated, such as the interaction region on 1 June 2013. The CME velocity based model underestimates the effect of pronounced MCs, as is seen for the CMEs on 6 June and 27 June 2013.

A study that differentiates particularly between compression and rarefaction regions is that of [Elliott et al. \(2013\)](#). They compare three threshold techniques to do so: by sorting for density, dynamic pressure, and velocity slope. The three  $Kp$ –velocity distribution panels in [Figure 4.13](#) look indeed very similar to the Figures 3 and 4 from [Elliott et al. \(2013\)](#). This is because they sort the  $Kp$ –velocity distribution for CMEs and streams, use OMNI data, and the SWS list as well, however, they use a different time resolution, data processing, and time period. More precisely, they use 3-hour averages of the hourly OMNI data set, modify the CME-associated periods of the SWS list with additional constraints, and use data from the time period 1963–2009.

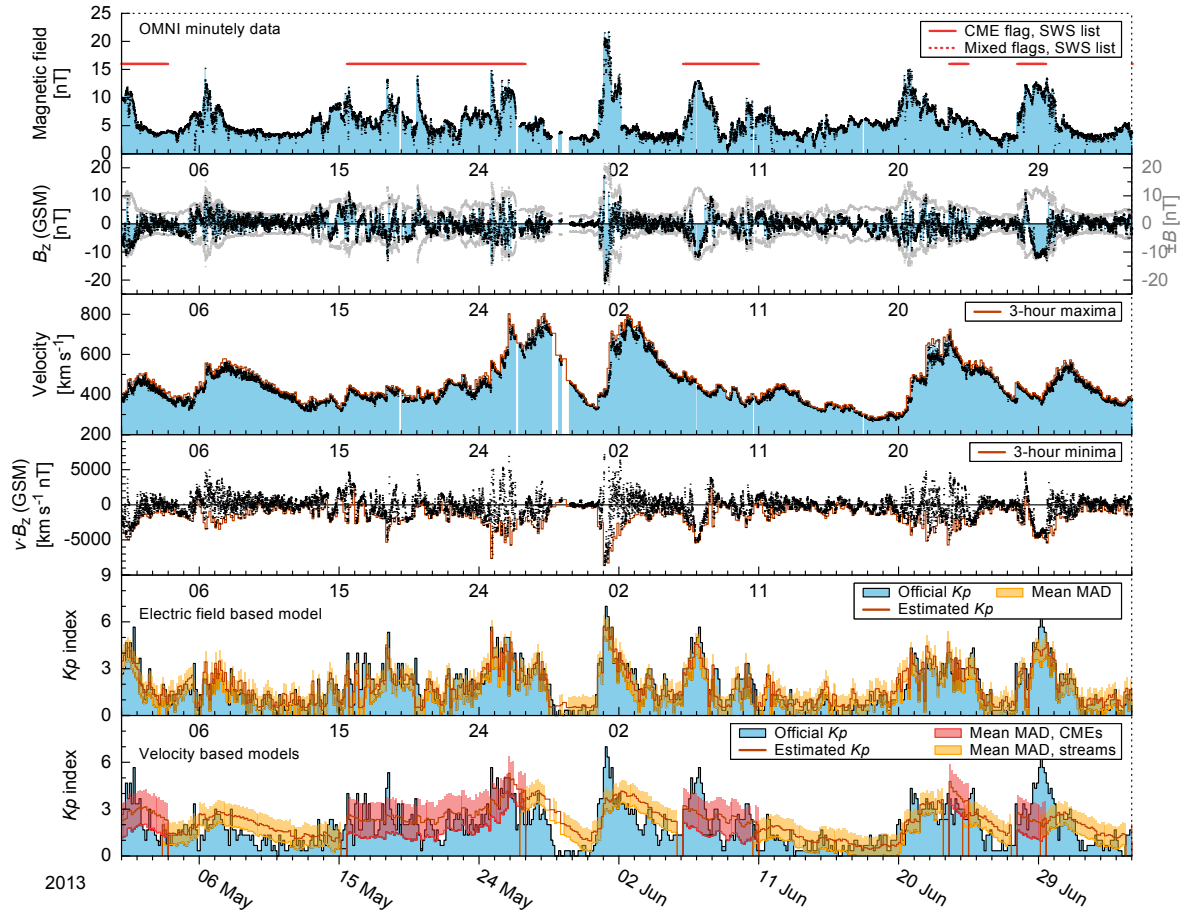


**Figure 4.20** Solar wind parameters, official  $K_p$  index, and estimated  $K_p$  indices for the 65-day time period from 1 May to 5 July 2013. The solar wind parameters are the magnetic field strength, its z-component in GSM coordinates, the velocity, and the product of the latter two. I also plot the velocity's 3-hour maxima and the  $vB_z$ 's 3-hour minima for illustration. The  $K_p$  estimates based on the electric field and the velocity relations are displayed together with their mean MAD bands. The  $K_p$  estimates from both velocity relations are chosen according to the periods flagged as CMEs or streams in the SWS list (red lines in top panel). The  $K_p$  estimate derived from stream velocity is shifted by 9 hours. The solar wind data are from the minutely OMNI data set and the official  $K_p$  index is obtained from the GFZ Potsdam.

The second solar wind plot zooms in on the last CME – it covers the 6-day time period from 26 June to 2 July 2013, see Figure 4.21. The plot shows the same parameters as in the previous plot. This more detailed sample period agrees with the observations made from the previous 2-month period. In addition, it can be seen that deviations in the  $vB_z$  based  $K_p$  prediction are found at the times of the initial shock, and the start and center of the MC. The velocity based models perform okay during the initial sheath region and around the peak of the trailing HSS, however, the main part of the MC (where  $B_z \leq -10$  nT) is underestimated. The CME velocity based model is able to track the initial shock when considering the mixed-flag 3-hour interval beginning at 27 June 2013 12:00. The background to this is that the SWS list flags each hour, thus, 3-hour intervals in between solar wind structures can contain flags of different structures. The prediction gap in the bottom panel in front of the shock is due to the 9-hour time shift carried out for the stream velocity data. In practice, this gap is of no concern when using the velocity relations for remote  $K_p$  forecasts. When comparing the  $K_p$  estimations for the  $vB_z$  and velocity based predictive models, it becomes apparent how significant the influence of the magnetic field z-component is.

The maximal velocities included in the OMNI data are around  $1100 \text{ km s}^{-1}$ . Current solar wind plasma spectrometers are only able to reliably measure speeds up to this value. Yet, CMEs can be much faster – speeds of up to  $2000 \text{ km s}^{-1}$  at 1 au were reconstructed (Russell et al. 2013). Future studies have to show how accurate the CME relation is in predicting  $K_p$  from extreme CMEs with velocities higher than  $1100 \text{ km s}^{-1}$ . According to the CME velocity relation (4.11), a CME speed of  $2000 \text{ km s}^{-1}$  would lead on average to a theoretical  $K_p$  of 11.2, however, the  $K_p$  scale is capped at 9.0 and this  $K_p$  is reached on average already at a velocity of  $1479 \text{ km s}^{-1}$ , see Figure 4.22.

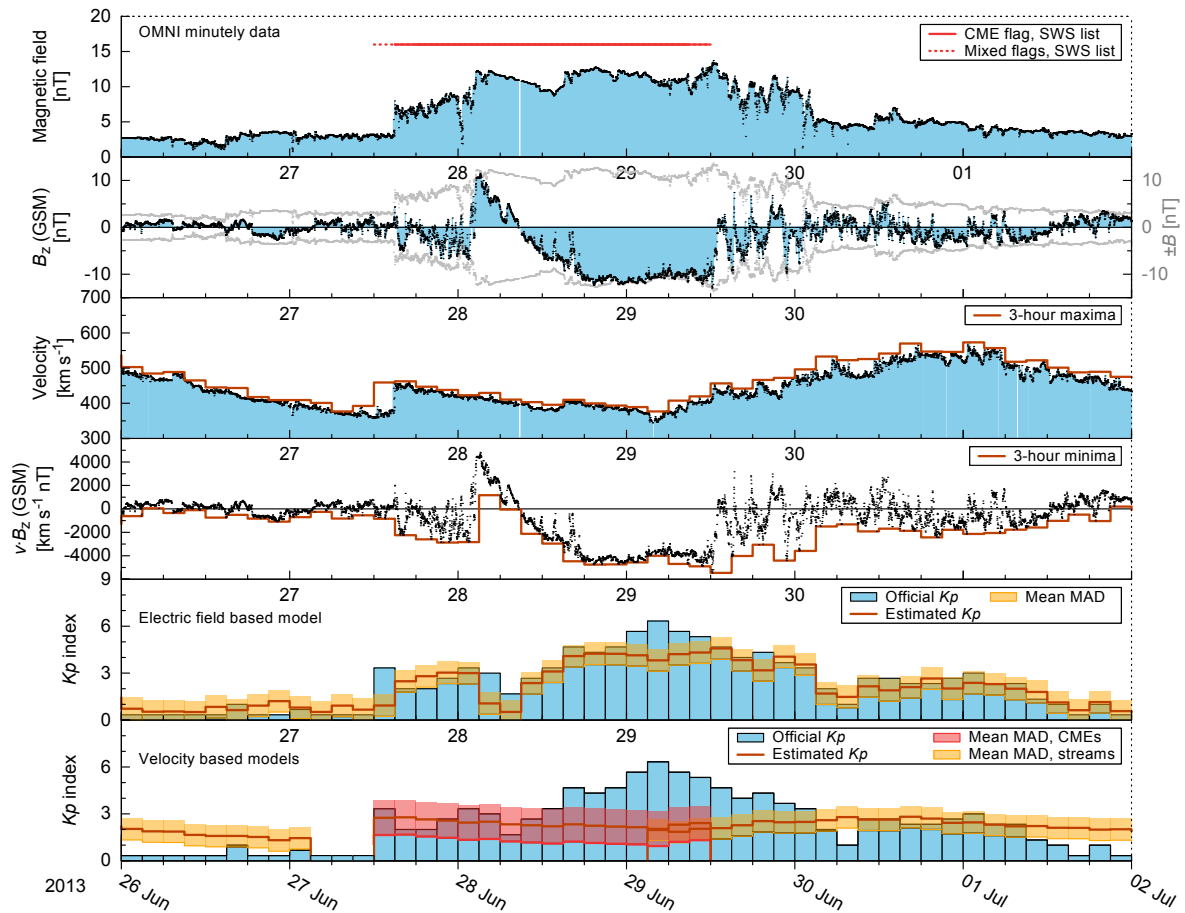


**Figure 4.21** Solar wind parameters, official  $K_p$  index, and estimated  $K_p$  indices for the 6-day time period from 26 June to 2 July 2013. All panels show the same parameters as in Figure 4.20. The period covers the CME from 27 June 2013, which induced a peak  $K_p$  of 6.3.

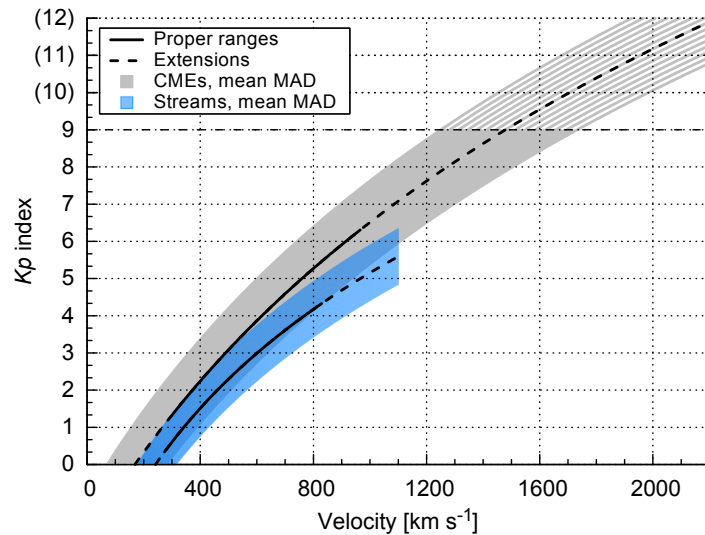
The capped  $K_p$  scale limits the capability to quantify the ground impacts of extremely fast CMEs.  $K_p$  is linked to the  $ap$  index, which translates to the ground magnetic field disturbance at about  $\pm 50^\circ$  dipole latitudes and thus can directly be expressed in nT. The limit could be overcome, if the fixed  $K_p$ -to- $ap$  conversion table (see Table 2.1) would be redefined and extended above  $K_p = 9.0$ . Then the absolute ground field disturbances evoked by extremely fast CMEs could be estimated via the  $K_p$  relation for CMEs displayed in Figure 4.22.

## 4.6 Conclusions

With the results presented in this chapter, I elaborate the step from solar wind properties to the prediction of their possible impact strength on the terrestrial magnetosphere. I derive empirical correlations and functional dependencies between solar wind properties and the geomagnetic  $K_p$  index, in order to obtain the capability to nowcast/forecast the  $K_p$  index. The following predictive models and their errors are obtained from the  $K_p$  analyses in this chapter:

- The functional relation for the yearly  $K_p$  averages relates  $K_p$  with solar activity via the SSN, see Equation (4.2). The  $K_p$  error to it is about 0.3, whereas seasonal variations further contribute up to 1.3.
- The functional relation for enabling  $K_p$  nowcasts relates  $K_p$  with the solar wind electric field, see Equations (4.8) and (4.9). Its MAD has a mean  $K_p$  size of 0.7.
- The functional relation for enabling CME forecasts relates  $K_p$  with the velocity of CME-associated flows, see Equation (4.11). Its MAD has a mean  $K_p$  size of 1.1.
- The functional relation for enabling stream forecasts relates  $K_p$  with the velocity of solar wind streams, see Equation (4.12). Its MAD has a mean  $K_p$  size of 0.7.

**Figure 4.22** Logarithmic fit curves for CMEs and streams with their proper ranges (solid lines) and extensions (dashed lines). The mean MAD bands corresponding to CMEs and streams are indicated by gray and blue shaded areas respectively. I extended the curve for CMEs up to a hypothetical  $Kp$  of 12.0. The curve for solar wind streams is cut at  $1100 \text{ km s}^{-1}$  because streams do not occur at these high velocities. The curves are the same as in the Figures 4.15 and 4.17.



The derived  $Kp$  relations constitute a part of the CME forecast chain developed at the Institute for Astrophysics Göttingen. It consists of CME source region and coronal environment analysis, 3D modeling of the CME structure, CME acceleration and propagation modeling, CME arrival time and parameter prediction, and the subsequent forecast of relevant space weather effects, such as its impacts on the  $Kp$  index and on the ionospheric TEC.

Prototype  $Kp$  relations were integrated into applications developed within the AFFECTS project (2011–2013). The following services contain early results from the present  $Kp$  study and are accessible via the AFFECTS website<sup>6</sup>. The corresponding services comprise a real-time plot, and alerts disseminated via RSS feeds and via mobile app. The [Solar Wind and  \$Kp\$  forecast plot](#) and the alerts are based on the  $Kp$ – $vB_z$  relation and process real-time solar wind measurements from L1: The [L1  \$Kp\$  Alert](#) is a threshold-based RSS feed that gets triggered when the estimated  $Kp$  surpasses a threshold specified as being 6.7. The [L1 GNSS Alert](#) and the [L1 Aurora Alert](#) are threshold-based RSS feeds that derive GNSS error and auroral latitude from the  $Kp$  estimate. The L1 Alerts are also accessible via the [AFFECTS app for iPhone](#).

From the results presented in this study, I conclude that when correlating  $vB_z$  with  $Kp$  it is of key importance to capture the 3-hour minimum values, i.e., to use high-resolution solar wind data, whereas when correlating velocity with  $Kp$  the underlying data resolution is negligible. The results support that averaging over 3-hour intervals neglects short-term geoeffective features in the magnetic field z-component  $B_z$ . The calculation of 3-hour minima considers these magnetic features and leads to a significant higher correlation with  $Kp$ .  $vB_z$  is not well suited for remote forecast situations, because short-term variations in  $B_z$  cannot be predicted yet, whereas the solar wind velocity is best suited for remote forecast situations.

There are differences in magnitude (more than 1.0  $Kp$  value) and trend in the  $Kp$ –velocity prediction curves obtained from CMEs and streams. These significant differences confirm that it is beneficial to utilize separate relations for the prediction of  $Kp$  from CME and stream velocities.

The examination of the prediction performance of the derived predictive models shows that strong geomagnetic storms exceeding a  $Kp$  of 7.0 are being underestimated. The CME velocity relation underestimates their resulting actual  $Kp$  on average by about 3.0, whereas the stream velocity relation does not even reach the threshold of geomagnetic storms ( $Kp \geq 5.0$ ), that is, the stream velocity relation is good in predicting lower geomagnetic activity but is not able to predict storms. The models are derived from data with a broad scatter in  $Kp$ . Nevertheless, when within their specified proper ranges, the derived models provide predictions that are significantly better than random.

The  $Kp$ –velocity dependency for CMEs is derived from velocity data of up to  $1100 \text{ km s}^{-1}$ . Assuming this relation holds true for higher speeds, the extension of it could be used to predict the  $Kp$  impact of fast CMEs as well. Though, the  $Kp$ –velocity relation for CMEs reaches the maximum  $Kp$  of 9.0 at a CME velocity of  $1500 \text{ km s}^{-1}$ . The ground geomagnetic disturbances, generated by the rare, extremely fast CME events having velocities above this value, could be resolved and estimated by redefining and extending the conversion between the  $Kp$  and  $ap$  indices.

<sup>6</sup>AFFECTS website: <http://www.affects-fp7.eu/services/>



As the obtained functional relations are based only on one or two aspects of the coupling between solar wind and magnetosphere, they cannot compete with full-fledged solar wind coupling functions, such as the rate magnetic flux is opened at the magnetopause ([Equation 2.8](#)), nor with current prediction models based on artificial neural networks or  $Kp$  persistence. Nevertheless, they enable empirical estimations of the mean geomagnetic activity impact for special forecast situations, that is,  $Kp$  can directly be quantified from observed solar activity, measured in-situ solar wind parameters, and remotely determined CME and stream velocities.

*Acknowledgments.* Part of the research leading to the results presented in this chapter has received funding from the EU FP7 project AFFECTS under grant 263506. The analyses in this chapter rely on the  $Kp$  index, calculated and made available by the GFZ Potsdam from data collected at magnetic observatories. Thank goes to the involved national institutes, the INTERMAGNET network and ISGI ([isgi.unistra.fr](http://isgi.unistra.fr)). The author thanks the WDC-SILSO at the SIDC (ROB) for maintaining and providing the international sunspot number series. Additional thank goes to the OMNI PIs/teams for creating and making available the solar wind in-situ data. The OMNI data are supplied by the SPDF at the GSFC (NASA). The hourly SWS list, updated until the end of 2016, was kindly provided by Ian Richardson of the GSFC and CRESST/University of Maryland.



## 5 Empirical solar wind model for the inner heliosphere

The analyses in the previous chapter are focused on the solar wind's influence on the terrestrial magnetosphere – this chapter changes the main focus to the solar wind upstream of the magnetosphere, in a first step down to a solar distance of 0.3 au and then even further down to the region around  $10 R_{\odot}$ , close to the solar wind's origin near the Sun. The solar wind's evolution on its way from the near-Sun region to 1 au is modeled with the goal of predicting the solar wind environment for the orbit of the Parker Solar Probe (PSP) mission.

This chapter is constructed as follows: In the first [Section 5.1](#), the PSP mission and its scientific goals are described. In [Section 5.2](#) I introduce the analyses done in the publication [Venzmer & Bothmer \(2018\)](#), which constitute the major part of this chapter. Then in [Section 5.3](#), an alternative magnetic field model is derived, which changes the solar distance dependency from the power law in our article to support a Parker magnetic field geometry. Further in [Section 5.4](#), possible improvements to the solar wind model are sketched.

### 5.1 Parker Solar Probe mission

Remote observations of the Sun and its corona reveal a wealth of structures and dynamical processes. Over time, most underlying physical mechanisms were identified and the observed features were integrated into a comprehensive picture of the Sun. However, key questions remain unanswered ([McComas et al. 2007](#)): It is unknown how the corona is so much hotter than the chromosphere beneath ([Klimchuk 2006](#)), and the exact processes involved in the acceleration of the solar wind are not fully understood ([Hollweg 1985](#); [Cranmer et al. 2017](#)).

Up to now, coronal heating and solar wind acceleration remain the open problems that drive the motivation to directly probe the near-Sun environment ([McComas et al. 2007](#); [Fox et al. 2015](#)). The mission concept of a solar probe taking in-situ measurements from the corona dates back to 1958 when NASA was founded ([McComas et al. 2008b](#)). The closest solar wind in-situ measurements made so far were done by the two Helios probes, see also [Section 3.4](#). Helios 1 was launched in 1974 and reached a perihelion distance of 0.31 au ( $67 R_{\odot}$ ) and Helios 2 was launched in 1976 and reached a perihelion distance of 0.29 au ( $62 R_{\odot}$ ) ([Rosenbauer et al. 1977](#)). Yet, the solar wind acceleration region is predicted to extend up to the Alfvénic critical surface which lies at solar distances between  $15\text{--}30 R_{\odot}$  ([Katsikas et al. 2010](#); [Goelzer et al. 2014](#)). Thus, the Helios spacecraft flew well beyond the region where the magic happens.

The Parker Solar Probe (PSP) mission (renamed in 2017 from Solar Probe Plus) is designed to finally address these major questions about the solar corona, in that it will dive into this near-Sun region. The prime goals of the PSP mission as stated by [Fox et al. \(2015\)](#) are: “Trace the flow of energy that heats and accelerates the solar corona and solar wind; Determine the structure and dynamics of the plasma and magnetic fields at the sources of the solar wind; and Explore mechanisms that accelerate and transport energetic particles.” These

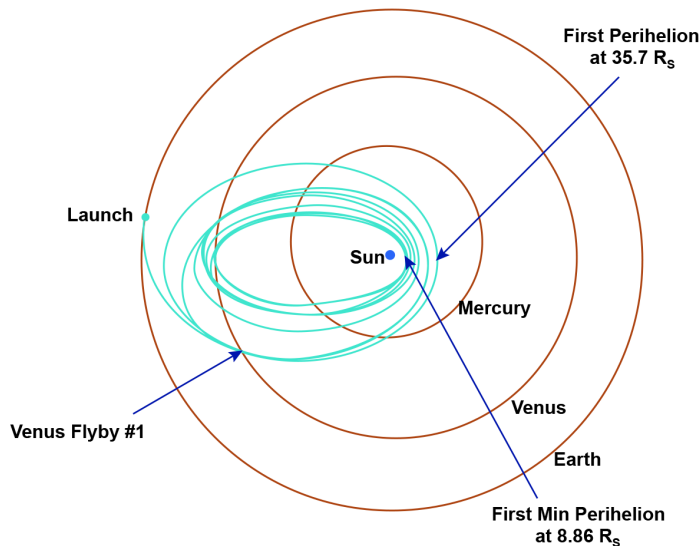


**Figure 5.1** Trajectory design of the PSP mission in the inner solar system with the positions of the launch, the first Venus flyby, the first perihelion, and the first closest perihelion. Credit: [NASA/Johns Hopkins APL, 2018](#) (the colors are inverted).

goals seem achievable due to recent developments in technology and engineering that allow PSP to approach the Sun down to a closest distance of  $9.86 R_{\odot}$  ( $0.046 \text{ au}$ ) from the center of the Sun, see the planned trajectory in [Figure 5.1](#). PSP launched on 12 August 2018 and utilizes seven Venus gravity assists over nearly seven years throughout its mission in order to lower its orbit around the Sun. PSP was launched by the largest operational rocket currently in existence, a Delta IV Heavy launcher. PSP uses a Star 48BV solid rocket motor as a third stage in addition, as it takes a lot of energy to reach the Sun (55 times more than reaching Mars).

The proximity to the Sun during the perihelia requires a sunward heat shield as well as a big heat radiator system behind to protect the instruments on the spacecraft's body – both are shown in the photo of PSP during testing in [Figure 5.2](#). The large variations in solar power during the orbit, due to its high ellipticity, are addressed by changing the angle of the solar panels with solar distance – the photo in [Figure 5.3](#) shows PSP with folded solar panels on top of its third stage. As the communication is limited during the close encounters with the Sun, each orbit is split into a science operations and a data downlink phase. When the spacecraft is closer than  $0.25 \text{ au}$  to the Sun, the scientific measurements are collected and when it is further away, the data is downlinked.

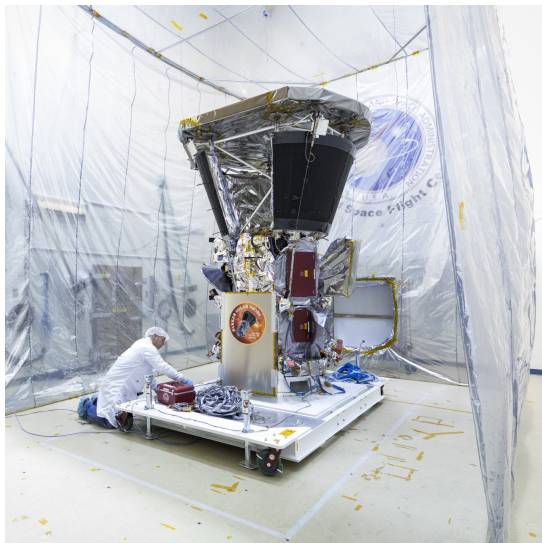


**Figure 5.2** PSP in the Acoustic Test Chamber at NASA's Goddard Space Flight Center in November 2017. Credit: [NASA/Johns Hopkins APL/Ed Whitman, 2017](#).

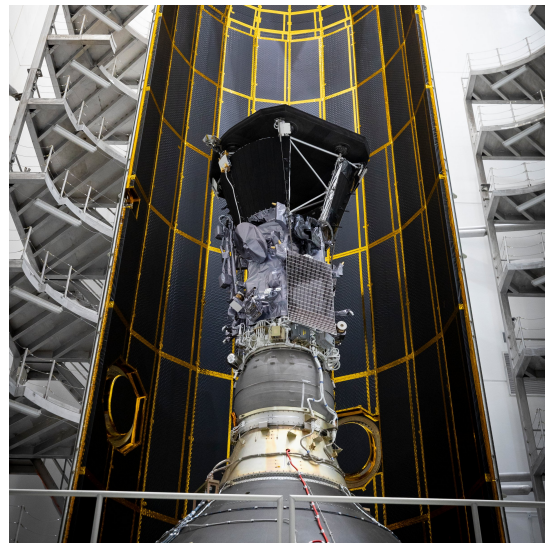


**Figure 5.3** PSP on top of its third stage rocket motor inside one half of the fairing of the Delta IV Heavy rocket at Astrotech Space Operations, Titusville in July 2018. Credit: [NASA/Johns Hopkins APL/Ed Whitman, 2018](#).

There are four scientific experiments on board PSP that contribute in redundant ways to the measurements of magnetic fields, plasma, waves, and SEPs ([Fox et al. 2015](#)). The Electromagnetic Fields Investigation (FIELDS) consists of two fluxgate and one search coil magnetometer, and five electric antennas ([Bale et al. 2016](#)). The Integrated Science Investigation of the Sun, Energetic Particle Instruments (IS $\odot$ IS) has two instruments for different energy ranges, EPI-Hi and EPI-Lo ([McComas et al. 2016](#)). The Solar Wind Electrons Alphas and Protons Investigation (SWEAP) is composed of two electrostatic analyzers and a Faraday cup ([Kasper et al. 2016](#)). The Wide Field Imager for Solar Probe (WISPR) is a white-light telescope for the solar corona and the inner heliosphere ([Vourlidas et al. 2016](#)). WISPR is to provide images of those solar wind structures PSP is about to fly through and measure in-situ.

The study in [Venzmer & Bothmer \(2018\)](#) is conducted within the Coronagraphic German And US SolarProbePlus Survey (CGAUSS) which is the German contribution to the PSP mission as part of WISPR. The input of this study to the CGAUSS project is the extrapolation of Helios solar wind data to the solar distances PSP is to reach.

## 5.2 On the published article

The major part of this chapter is published under the title “Solar-wind predictions for the Parker Solar Probe orbit” in [Venzmer & Bothmer \(2018\)](#), which is also just referred to as ‘the paper’ in this chapter. The article was published online on 20 March 2018 in *Astronomy and Astrophysics* (A&A). It is included following this chapter, denoted as [Chapter 6](#). The European Southern Observatory (ESO) is the holder of the copyright – the article is reproduced with permission.

The analyses presented in the paper were entirely done by myself, as well as the tables, figures, and equations. My coauthor Volker Bothmer contributed significantly to the text and the anonymous referee helped clarifying a few aspects. The text was further improved by the A&A language editor Joshua Neve.

The paper is included in [Chapter 6](#), so I will only briefly outline its content here: In the paper, we predict the solar wind conditions for the orbit of the PSP spacecraft. We extrapolate the near-Sun environment from empirical solar wind models that are based on Helios and OMNI solar wind observations. These estimations are further adjusted to the solar activity expected during the PSP mission – the adjustments are based on empirical relations with the sunspot number (SSN).

The solar wind predictions are achieved via the following steps: We obtain lognormal representations of the frequency distributions' shapes of the four key solar wind parameters magnetic field strength, proton velocity, density, and temperature. We derive analytical relations for the parameters' solar activity dependencies and for their solar distance scaling. An empirical solar wind model is built from the combination of the obtained frequency distributions, SSN dependence relations, and solar distance dependence functions. The empirical model represents the solar wind's solar activity and distance behavior; it is fed with SSN predictions and extrapolated to the orbit of PSP.

We estimate the solar wind median values during PSP's first perihelion and also model the values for PSP's closest perihelia. The extrapolated values of the velocity and temperature lie above those obtained from remote observations in previous studies. This suggests that the region where the solar wind is accelerated and heated reaches up to distances of  $20 R_{\odot}$  and thus will indeed be probed by the PSP spacecraft.

After the publishing of the paper, PSP's launch date was shifted from initially 31 July to 12 August 2018. This also shifts the date of the first perihelion by a few days to 6 November 2018, thus, the dates in Figure 12 of the paper have to be shifted by about eight days. I do not have information on the final spacecraft trajectory and if the following perihelia are affected by the shift as well.

## 5.3 Parker magnetic field solar distance dependency

In our article we noted that the model's near-Sun field magnitude, extrapolated to PSP's closest perihelion, will be lower than the actual values to be found. We scaled the magnetic field strength via a power-law function and obtained a solar-distance dependency proportional to  $r^{-1.662}$ . However, even though this approach is used in a number of cases (e.g., [Coleman et al. 1969](#); [Hellinger et al. 2013](#)), it remains a simplification – in the following I implement an improved distance dependency and thus modify the magnetic field model from the paper. The new distance dependency is intended to account for the Parker IMF geometry, respecting the contributions of the individual field vector components, which have different power-law scalings. It is found that Voyager 1 observations of the magnetic field strength at solar distances larger than 1 au agree well with Parker's IMF model ([Burlaga et al. 1984, 2002](#)). In the following, this alternative distance dependency for the IMF model is derived and its predictions are compared to those from the paper.

### 5.3.1 Parker magnetic field

The coronal magnetic field near the Sun rotates rigidly, holding on to the coronal plasma. At the solar wind source surface, at around  $2.5 R_{\odot}$  where the thermal plasma pressure overcomes the magnetic pressure, the magnetic field gets transported outwards in a radial way, maintaining only its radial vector component  $\mathbf{B}_r$ . From there on, the solar rotation begins to shear the magnetic field, building up a longitudinal component  $\mathbf{B}_{\phi}$  as well. This solar wind magnetic field model was formulated by [Parker \(1958\)](#) and has the following components in spherical coordinates ( $\theta$  is the colatitude):

$$\mathbf{B}_r(r) = B_0 \left( \frac{r_0}{r} \right)^2 \cdot \mathbf{e}_r, \quad (5.1)$$

$$\mathbf{B}_{\phi}(r) = -B_0 \left( \frac{r_0}{r} \right)^2 \cdot \frac{\omega r \sin \theta}{v_{\text{sw}}} \cdot \mathbf{e}_{\phi}, \quad (5.2)$$

$$\mathbf{B}_{\theta}(r) = 0 \cdot \mathbf{e}_{\theta}. \quad (5.3)$$

$B_0$  represents the radial field component at the solar distance  $r_0$ . The solar surface equatorial angular rotation rate  $\omega$  and the solar wind velocity  $v_{\text{sw}}$  are involved as well. From these equations it can be seen that  $\mathbf{B}_r$  scales with increasing solar distance with  $r^{-2}$ , as it is expected for a spherical outflow, and  $\mathbf{B}_{\phi}$  scales with  $r^{-1}$  as expected for a two-dimensional point source. In-situ observations support the component's scaling according to these theoretical exponents, although in slow solar wind the scaling for  $\mathbf{B}_{\phi}$  deviates somewhat from theory ([Mariani et al. 1978](#)).



From the magnetic field's absolute value

$$B(r) = \sqrt{B_r^2 + B_\phi^2 + B_\theta^2}, \quad (5.4)$$

$$B(r) = \sqrt{\left(B_0 \left(\frac{r_0}{r}\right)^2\right)^2 + \left(-B_0 \left(\frac{r_0}{r}\right)^2 \cdot \frac{\omega r \sin \theta}{v_{sw}}\right)^2}, \quad (5.5)$$

it is apparent that the magnetic field strength does not scale with a simple power law. If the solar dipole axis tilt to the solar rotation axis is neglected and the radial field component  $B_0$  is set to be in the equatorial plane at  $r_0 = 1$  au, then  $\theta = 90^\circ$  and therefore

$$B(r) = B_0 \cdot \sqrt{r^{-4} + \left(\frac{\omega r}{v_{sw}}\right)^2 r^{-4}}, \quad (5.6)$$

with the solar distance  $r$  in astronomical units.

The magnetic field angle in the solar equatorial plane is distance dependent and is calculated via

$$\phi_B(r) = \arctan\left(-\frac{\omega r}{v_{sw}}\right). \quad (5.7)$$

The angle becomes  $\phi_B(1 \text{ au}) = -46.23^\circ$  when using the Sun's equatorial angular velocity  $\omega_{eq} = 14.37^\circ \text{ d}^{-1}$  (for more details on solar rotation see Appendix A.1) together with the median solar wind velocity  $v_{sw} = 416 \text{ km s}^{-1}$  determined in the paper. During solar cycle minimum, the solar wind in the equatorial plane outside the source surface originates from polar regions at about  $\pm 60^\circ$  heliolatitude. This leads to a slightly underwound Parker spiral, because of the slower rotation rate at higher latitudes (Banaszkiewicz et al. 1998). Using the differential rotation rate  $\omega(\pm 60^\circ) = 13.69^\circ \text{ d}^{-1}$  (see Equation (A.1)), the field angle becomes  $\phi_B(1 \text{ au}) = -44.84^\circ$ . As the solar rotation axis tilt to the ecliptic normal only has a maximum angle of  $7.2^\circ$ , I consider its influence on  $\phi_B$  minor, and choose to neglect it in this calculation. Thus from theory, in the ecliptic at a solar distance of 1 au, the Parker spiral's observed magnetic field angle  $\phi_B$  is centered most of the time at about  $-45^\circ$  or for the opposite field polarity at  $135^\circ$ . Indeed, this is confirmed by the angle's frequency distribution, apparent in IMF measurements made at 1 au, such as the hourly OMNI data of the time period 1963–2016 plotted in Figure 5.4.

For  $\phi_B$  being on average centered around these two directions, both vector components  $B_r$  and  $B_\phi$  have to be of equal amplitude. It can be seen from Equations (5.4) and (5.6) that this condition leads to

$$B(1 \text{ au}) = B_0 \cdot \sqrt{2} \quad \text{with} \quad \left(\frac{\omega \cdot 1 \text{ au}}{v_{sw}}\right) = 1. \quad (5.8)$$

Admittedly,  $\omega$  and  $v_{sw}$  are treated as time independent constants, which is a more valid approximation for  $\omega$  than for  $v_{sw}$ .

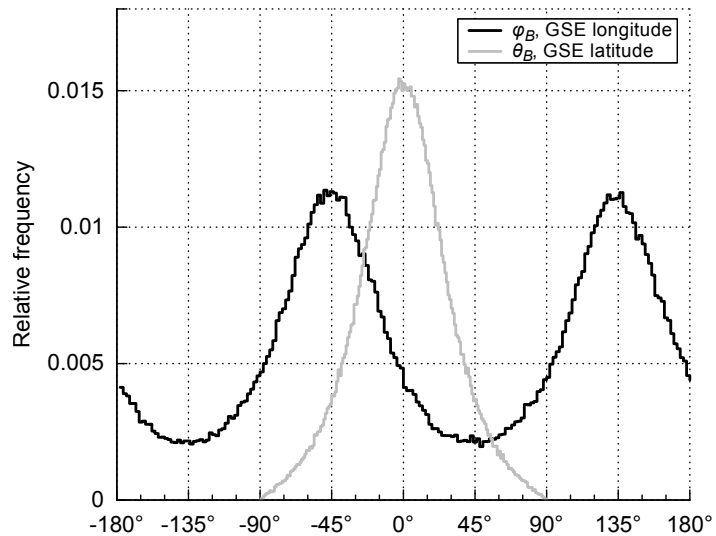


**Figure 5.4** Frequency distributions of the magnetic field angles  $\phi_B$  and  $\theta_B$  in GSE coordinates. The frequencies are based on the near-Earth hourly OMNI data during the period 1963–2016.

### 5.3.2 Solar distance dependency

Here, the magnetic field strength's distance dependency is derived in a similar way as in the paper's [Section 6.4](#). Also, the same data set is used for the fitting process, that is, the combined in-situ data from the Helios 1 and Helios 2 spacecraft within the time range 1974–1981 (see also [Section 3.4](#)). The plain difference is the additional consideration of the longitudinal field component.

In order to get an analytical representation of the radial dependence of the magnetic field, I construct a suitable fit function based on [Equation 5.6](#), assuming a nonexistent  $B_\theta$ :

$$x(r) = a \cdot \sqrt{(re_1)^2 + (re_2)^2}. \quad (5.9)$$

The function, containing the scaling parameter  $a$ , and the exponents  $e_1$  and  $e_2$ , is used for a least squares regression fit. The resulting fit parameters are presented in [Table 5.1](#). Within the Helios distance range 0.3–

**Table 5.1** Fit coefficients for the curve fits ([Equation 5.9](#)) and for the distribution fit (using the lognormal function of Equation (4) from the paper), derived from the combined Helios 1 and 2 data. The numbers in parentheses are the errors on the corresponding last digits of the quoted value. The crossing distance indicates where the median and mean fits intersect each other. This distance is calculated numerically and its corresponding error only represents an estimated value.

Fit		Factor $a$	Exponents		Crossing distance [au]
			$e_1$	$e_2$	
Curve	Median	4.04(13)	-1.852(25)	-0.97(23)	0.336(10)
	Mean	4.47(12)	-1.740(18)	-0.99(23)	
Distribution	Median	3.833(27)	-1.858(42)	-1.32(12)	–
	Mean	4.081(29)			

1.0 au, the resulting fit curves are very similar to those in the paper – as they are expected to be. The fit curves for the mean and median field strength are plotted with respect to solar distance in [Figure 5.5](#). The graph is visually almost indistinguishable to the corresponding one in the paper [Figure 7](#), [Section 6.4](#).

The weighted sum of the squared residuals (WSSR) of this fit slightly improved in comparison to that of the simple power-law function ( $x(r) = d \cdot r^e$ ) used in [Venzmer & Bothmer \(2018\)](#): 6 % for the median and 9 % for the mean. However, the mean and median fit curves remain fairly similar and still cross each other at about the same distance as in the paper.

From the theoretical considerations sketched above, the expected fit parameter values are:  $a \approx B(1 \text{ au})/\sqrt{2}$ ,  $e_1 \approx -2$ , and  $e_2 \approx -1$ . The here obtained fit parameter values are closer to the theoretical values than those derived in the paper. The exponents  $e_{1,\text{med}} = -1.852$  and  $e_{1,\text{avg}} = -1.740$  are up to 13 % larger than the theoretical exponent for  $e_1$  and lead to a less steep slope near the Sun. However, they are about 12 % smaller than the power-law exponents derived in the paper, which have values of  $-1.655$  and  $-1.546$  respectively.

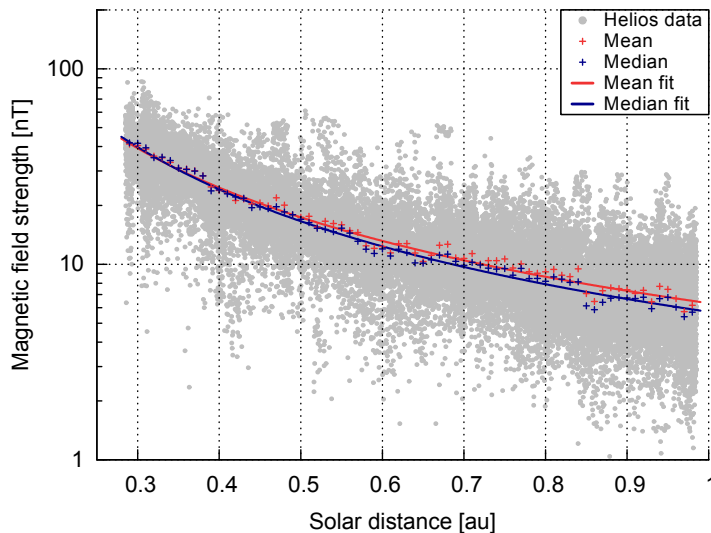
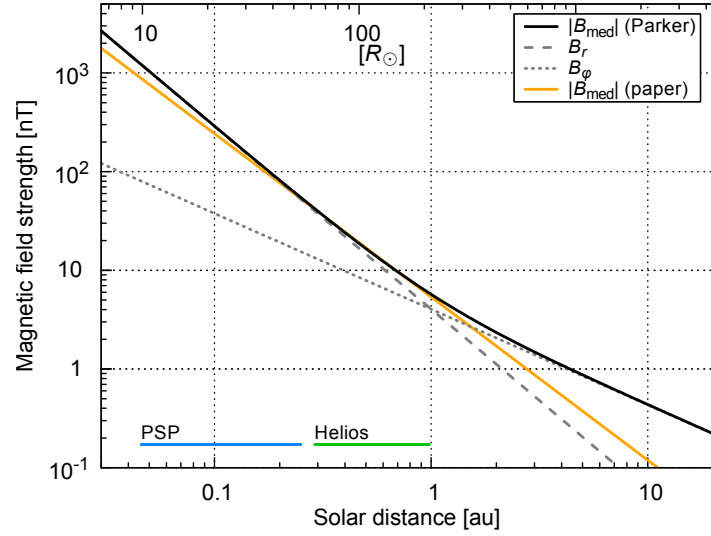


**Figure 5.5** Magnetic field strength with respect to solar distance. The mean and median per 0.01 au data bin and their fit curves are plotted as well. The hourly Helios data has a native distance resolution of 0.01 au, thus, to make the distribution visible in this plot, I added a random distance value of up to  $\pm 0.005$  au.

It can be seen from Figure 5.6 that although the new fit curve is slightly curved, both fits are almost congruent in the Helios data range. But already little above 1 au, the power law yields significantly lower IMF strengths. It is known that the decline in IMF strength behaves according to Parker’s theory, at least in the range 1–81 au (Burlaga et al. 2002). However, both curves deviate less pronounced in the PSP distance range 0.046–0.25 au.

**Figure 5.6** Magnetic field strength fit curves with respect to solar distance. Plotted are the fitted absolute median field strength and its radial and azimuthal components. I added the absolute median field strength from Equation (10) of the paper as well. The orbital distance ranges from PSP and the Helios probes are indicated by the blue and green lines.



In the next step, a lognormal function is fitted to the data – I use the same method and reasoning as explained in the paper’s Section 6.4. Accordingly the IMF distribution’s shapes are considered to be lognormal at all distances and the fit exponents  $e_{\text{med}}$  and  $e_{\text{avg}}$  are reduced to only one common exponent. The distance dependency is implemented into the lognormal function from the paper, yielding in the parameters and common exponents of the distribution fit. The fit parameters are presented in Table 5.1 and the fitted distribution is plotted in Figure 5.7. As is expected for the Helios distance range, the fitted distribution looks almost identical to the corresponding one presented in Figure 8 of the paper.

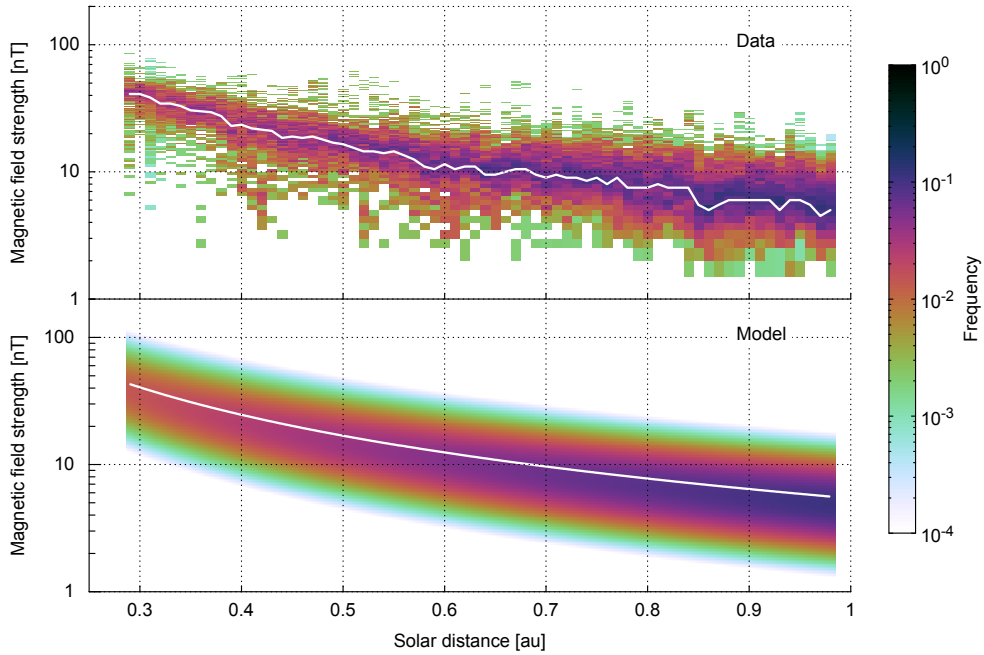


**Figure 5.7** Frequency distribution of the solar wind magnetic field strength with respect to solar distance. I plotted the binned Helios data (top panel) and the square-root power-law lognormal fit model (bottom panel) with their median values (white lines).

### 5.3.3 SSN implementation and extrapolation to PSP orbit

Finally, the IMF distance dependency will be combined with the solar activity relationship obtained in the paper. In order to derive the solar wind environment for the PSP orbit, the model is then extrapolated to the PSP orbit.

To take into account predictions of the SSN, the distance relation is used to scale the SSN-relation for 1 au:

$$B(ssn, r) = \frac{B(ssn)}{\sqrt{2}} \cdot \sqrt{(r^{e_1})^2 + (r^{e_2})^2}. \quad (5.10)$$

This way the square root just replaces the  $r^{-1.66}$  factor of Equation (12) in the paper:

$$B_{\text{med}}(ssn, r) = (0.0131 \text{ nT} \cdot ssn + 4.29 \text{ nT}) \cdot \sqrt{(r^{-1.858})^2 + (r^{-1.32})^2}. \quad (5.11)$$

This magnetic field strength model can now be extrapolated to PSP's orbital range. Figure 5.8 shows the model and its extrapolation, visualized for a SSN range 0–200, representing the range from solar minimum to maximum. The magnetic field strength from the paper is shaded in yellow, the above derived model in the Helios range in green and its extrapolation to the PSP range in blue. The newly derived model is found to differ increasingly going closer to the perihelion of the extrapolated PSP region. The Parker (1958) field model with the theoretical exponents, normed to 1 au, is drawn for comparison. It features an even larger curvature than the derived model which exhibits exponents adjusted by the fit to the Helios data.

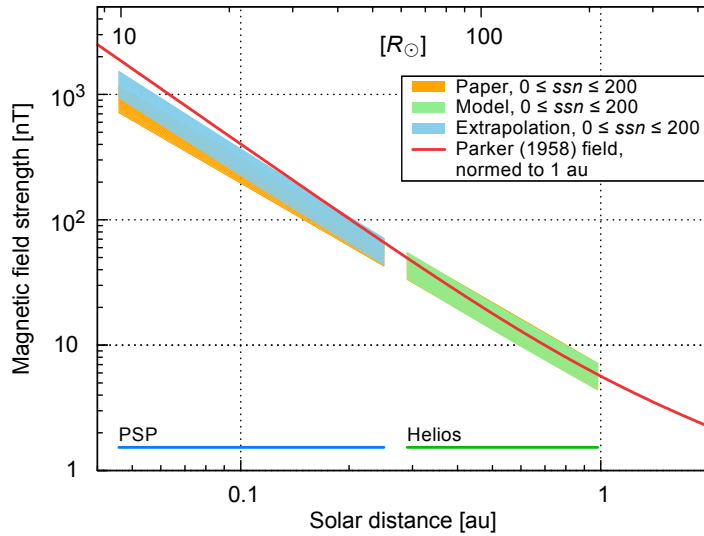


**Figure 5.8** Radial extrapolation of the solar wind magnetic field strength to the PSP orbit region. The median value from the model, obtained from Helios and OMNI measurements, is extrapolated to the PSP region for SSN values between solar minimum and maximum, that is,  $0 \leq ssn \leq 200$ . The lower edges of the shaded areas correspond to solar minimum, the upper edges to solar maximum. I also added the model from the paper (yellow) and the radial dependency of the field model by Parker (1958), normed to 1 au (red). The orbital distance ranges from PSP and the Helios probes are indicated by the blue and green lines.

The solar wind environment can be forecasted to PSP's orbit and mission time, using the same SSN predictions as described in the paper, that is, the SIDC forecast and mirroring of the last solar cycle. The changes in the magnetic field strength during the first perihelion and the first closest perihelion (which is actually the 22nd) are plotted in Figure 5.9. The estimated magnetic field strength median value of 94 nT for PSP's first perihelion is 8 % higher than that derived in the paper. The median value 1241 nT for the first closest perihelion is even 32 % higher.

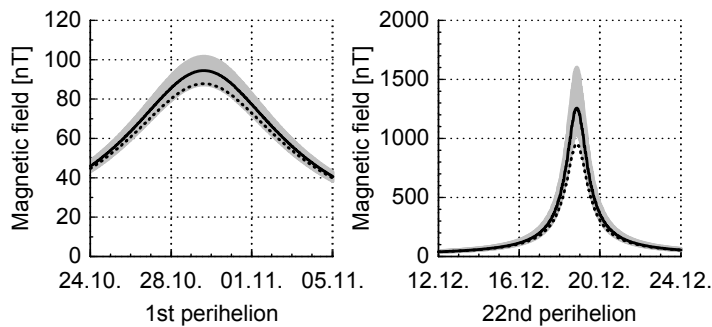
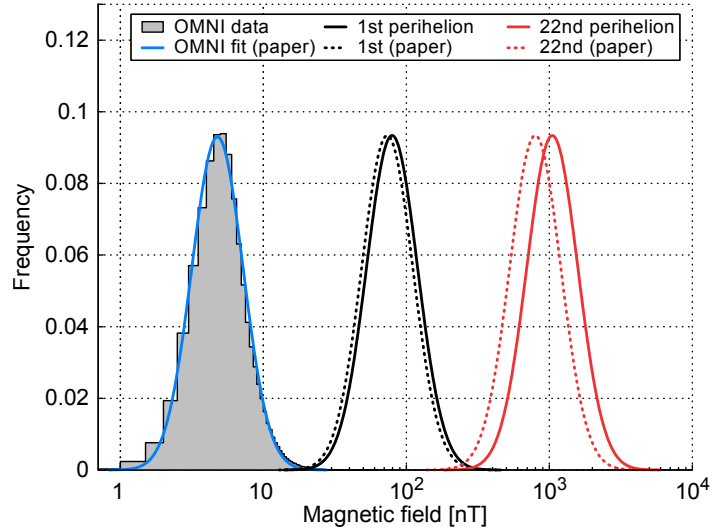


**Figure 5.9** Estimated magnetic field strength medians (solid lines) and their error bands (gray area) during 12 days in 2018 and 2024 with PSP's first perihelion at about 0.16 au and PSP's 22nd perihelion at 0.046 au. I indicated the prediction from Venzmer & Bothmer (2018) as well (dotted lines). Note that the dates of the perihelia are still based on the trajectory data for the launch date of 31 July 2018.

The model assumes a frequency distribution of lognormal shape and shifts this distribution according to solar activity and solar distance. The estimated IMF frequency distributions at 1 au, at PSP's first perihelion, and at its first closest perihelion are plotted in Figure 5.10. It is evident that during the closest perihelion, strong magnetic fields are estimated to occur more frequently than predicted from the model in the paper.

**Figure 5.10** Frequency distribution of the magnetic field strength at 1 au (OMNI data and fit) and those estimated with the derived model for PSP’s 1st and 22nd perihelia. In this plot the frequencies of both extrapolated curves are scaled up for visibility to the same peak frequency as the 1 au distribution. I indicated the predictions from [Venzmer & Bothmer \(2018\)](#) as well (dotted lines).



### 5.3.4 Conclusion

The key difference between the magnetic field strength models presented in this section and in the paper lies in their differing solar distance relations. The models both still assume a lognormal distributed magnetic field strength and the same dependency on solar activity. Instead of being based on a simple power law, the solar distance relation derived above is based on the well-founded spiral field model formulated by [Parker \(1958\)](#). I suggest this newly derived magnetic field relation results in more accurate predictions for the near-Sun region, as the IMF is known to conform to the Parker field geometry in the outer heliosphere. It fits the Helios data as good as that one presented in [Venzmer & Bothmer \(2018\)](#), however, the function is slightly more curved so that the magnetic field becomes larger outside the fitted solar distance range 0.29–0.98 au. The consequence is a significant increase in the predicted field strength at the perihelia of PSP’s orbital trajectory, ranging from 8 % at the first perihelion to 32 % at the first closest perihelion.

## 5.4 Possible solar wind model modifications

Currently, the solar wind models described in the paper and in this chapter are purely empirical and the four solar wind quantities are characterized independently from each other. In further steps, theoretical relationships, connecting the individual solar wind parameters, could be introduced to make the model more self-consistent.

For example, proton flux conservation could be implemented into the radial distance dependencies, as it was found to be the quantity which varies the least with solar distance ([Schwenn 1983](#)). This would relate the two solar wind parameters density and velocity. Presuming a spherical radial solar wind outflow, the proton flux ( $j = vnA$ ) per solid angle ( $A \propto r^2$ ) is conserved. Nonradial flow is almost not existent beyond 0.29 au ([Schwenn 1983](#)), however, close to the Sun the assumption of a radial outflow becomes invalid as there exist in particular a significant equatorward flow of solar wind from the higher latitudes. Assuming power law distance dependencies for the velocity ( $v \propto r^{e_v}$ ) and density ( $n \propto r^{e_n}$ ), it can be seen that the exponents are related via the following condition as the flux is distance independent:

$$\frac{dj}{dr} = 0 \quad \Rightarrow \quad e_v + e_n + 2 = 0 \quad \Leftrightarrow \quad e_v + e_n = -2.$$

Thus, where the solar wind is accelerated/decelerated, the density fall-off has to deviate from  $r^{-2}$  as well.

Another example would be to respect the solar wind velocity as a time-variable parameter within the magnetic field’s azimuthal component  $B_\phi$  and not as a constant as it is done in the previous section ([Equation 5.2](#)). This would relate the two parameters velocity and magnetic field strength, as the Parker spiral angle has to change with velocity.

*Acknowledgments.* Part of the research leading to the results presented in this chapter received support of the CGAUSS project for WISPR by the DLR under grant 50 OL 1601 as national contribution to the PSP mission. The analyses in this chapter are based on the Helios and the OMNI data, which are supplied by the SPDF at the GSFC (NASA). The author thanks the Helios and OMNI PIs/teams for creating and making available the solar wind in-situ data. Additional thank for maintaining and providing the international sunspot number series goes to the WDC-SILSO at the SIDC (ROB).



# Solar-wind predictions for the Parker Solar Probe orbit

## Near-Sun extrapolations derived from an empirical solar-wind model based on Helios and OMNI observations

M. S. Venzmer and V. Bothmer

University of Goettingen, Institute for Astrophysics, Friedrich-Hund-Platz 1, 37077 Göttingen, Germany

Received 25 August 2017 / Accepted 10 November 2017

### ABSTRACT

**Context.** The Parker Solar Probe (PSP; formerly Solar Probe Plus) mission will be humanity's first in situ exploration of the solar corona with closest perihelia at 9.86 solar radii ( $R_{\odot}$ ) distance to the Sun. It will help answer hitherto unresolved questions on the heating of the solar corona and the source and acceleration of the solar wind and solar energetic particles. The scope of this study is to model the solar-wind environment for PSP's unprecedented distances in its prime mission phase during the years 2018–2025. The study is performed within the Coronagraphic German And US SolarProbePlus Survey (CGAUSS) which is the German contribution to the PSP mission as part of the Wide-field Imager for Solar PRobe.

**Aims.** We present an empirical solar-wind model for the inner heliosphere which is derived from OMNI and Helios data. The German-US space probes Helios 1 and Helios 2 flew in the 1970s and observed solar wind in the ecliptic within heliocentric distances of 0.29–0.98 au. The OMNI database consists of multi-spacecraft intercalibrated in situ data obtained near 1 au over more than five solar cycles. The international sunspot number (SSN) and its predictions are used to derive dependencies of the major solar-wind parameters on solar activity and to forecast their properties for the PSP mission.

**Methods.** The frequency distributions for the solar-wind key parameters, magnetic field strength, proton velocity, density, and temperature, are represented by lognormal functions. In addition, we consider the velocity distribution's bi-componental shape, consisting of a slower and a faster part. Functional relations to solar activity are compiled with use of the OMNI data by correlating and fitting the frequency distributions with the SSN. Further, based on the combined data set from both Helios probes, the parameters' frequency distributions are fitted with respect to solar distance to obtain power law dependencies. Thus an empirical solar-wind model for the inner heliosphere confined to the ecliptic region is derived, accounting for solar activity and for solar distance through adequate shifts of the lognormal distributions. Finally, the inclusion of SSN predictions and the extrapolation down to PSP's perihelion region enables us to estimate the solar-wind environment for PSP's planned trajectory during its mission duration.

**Results.** The CGAUSS empirical solar-wind model for PSP yields dependencies on solar activity and solar distance for the solar-wind parameters' frequency distributions. The estimated solar-wind median values for PSP's first perihelion in 2018 at a solar distance of 0.16 au are 87 nT, 340 km s<sup>-1</sup>, 214 cm<sup>-3</sup>, and 503 000 K. The estimates for PSP's first closest perihelion, occurring in 2024 at 0.046 au (9.86  $R_{\odot}$ ), are 943 nT, 290 km s<sup>-1</sup>, 2951 cm<sup>-3</sup>, and 1 930 000 K. Since the modeled velocity and temperature values below approximately 20  $R_{\odot}$  appear overestimated in comparison with existing observations, this suggests that PSP will directly measure solar-wind acceleration and heating processes below 20  $R_{\odot}$  as planned.

**Key words.** solar wind – Sun: corona – Sun: heliosphere

## 1. Introduction

From observations of cometary tail fluctuations, [Biermann \(1951\)](#) inferred the presence of a continuous flow of particles from the Sun. With his theoretical solar-wind model, [Parker \(1958\)](#) formulated the existence of the solar wind even before the first satellites measured it in situ in 1959 ([Gringauz et al. 1960](#); [Neugebauer & Snyder 1966](#)). The idea of a space mission flying through the solar corona dates back to the founding year of NASA in 1958 ([McComas et al. 2008](#)). Since then several space missions have measured the solar wind in situ at a wide range of heliocentric distances. In the case of Voyager 1, this was as far away as 140 au<sup>1</sup> in October 2017, having crossed the heliosopause into interstellar space at a distance of 121 au ([Gurnett et al. 2013](#)). Various spacecraft have provided a wealth of solar-wind measurements near Earth's orbit, with WIND ([Lepping et al. 1995](#); [Ogilvie et al. 1995](#)), SOHO ([Domingo et al. 1995](#)), ACE

([Stone et al. 1998](#)), and DSCOVR ([Burt & Smith 2012](#)) currently providing observations while orbiting around the L1 point 1.5 million km ahead of Earth in the sunward direction. Additional measurements at other solar distances were provided by planetary missions to Venus and Mercury, such as PVO ([Colin 1980](#)) or MESSENGER ([Belcher et al. 1991](#)). Ulysses was the first probe that orbited the Sun out of the ecliptic plane and thus could measure solar wind even at polar latitudes ([McComas et al. 1998](#)). The in situ solar-wind measurements closest to the Sun to date were made by the Helios missions. Helios 1, launched in 1974, reached distances of 0.31 au. Helios 2, launched two years later, approached the Sun as close as 0.29 au ([Rosenbauer et al. 1977](#)). The NASA Parker Solar Probe<sup>2</sup> (PSP), formerly Solar Probe Plus, six years after its planned launch date in mid 2018, will reach its closest perihelia at a distance of 9.86 solar radii ( $R_{\odot}$ ), that is, 0.0459 au

<sup>1</sup> <https://voyager.jpl.nasa.gov/>

<sup>2</sup> <http://parkersolarprobe.jhuapl.edu/>

(Fox et al. 2016). This distance will be achieved through seven Venus gravity assists with orbital periods of 88–168 days. In its prime mission time 2018–2025 PSP provides 24 orbits with perihelia inside 0.25 au (Fox et al. 2016). Even its first perihelion, 93 days after launch in 2018, will take PSP to an unprecedented distance of 0.16 au ( $35.7 R_{\odot}$ ). In comparison, the ESA Solar Orbiter mission with a planned launch in February 2019 will have its closest perihelia at 0.28 au (Müller et al. 2013).

The key PSP science objectives are to “trace the flow of energy that heats and accelerates the solar corona and solar wind, determine the structure and dynamics of the plasma and magnetic fields at the sources of the solar wind, and explore mechanisms that accelerate and transport energetic particles” as stated in Fox et al. (2016). To achieve these goals, PSP has four scientific instruments on board: FIELDS for the measurement of magnetic fields and AC/DC electric fields (Bale et al. 2016), SWEAP for the measurement of flux of electrons, protons, and alphas (Kasper et al. 2016), ISOIS for the measurement of solar energetic particles (SEPs; McComas et al. 2016) and WISPR for the measurement of coronal and inner heliospheric structures (Vourlidas et al. 2016).

The study presented in this paper is undertaken in the Coronagraphic German And US SolarProbePlus Survey (CGAUSS) project, which is the German contribution to the PSP mission as part of the Wide-field Imager for Solar PRobe (WISPR). WISPR will contribute to the PSP science goals by deriving the three-dimensional structure of the solar corona through which the in situ measurements are made to determine the sources of the solar wind. It will provide density power spectra over a wide range of structures (e.g., streamers, pseudostreamers and equatorial coronal holes) for determining the roles of turbulence, waves, and pressure-balanced structures in the solar wind. It will also measure the physical properties, such as speed and density jumps of SEP-producing shocks and their coronal mass ejection (CME) drivers as they evolve in the corona and inner heliosphere (Vourlidas et al. 2016). In order to help optimize the WISPR and PSP preplanning of the science operations, knowledge of the expected solar-wind environment is needed. For this purpose the solar-wind environment is extrapolated down to the closest perihelion of  $9.86 R_{\odot}$  distance to the Sun using in situ solar-wind data from the Helios probes and near 1 au data from various satellites compiled in the OMNI solar-wind database.

Generally, two types of solar wind are observed in the heliosphere – slow and fast streams (Neugebauer & Snyder 1966; Schwenn 1983). Slow solar wind has typical speeds of  $<400 \text{ km s}^{-1}$  and fast solar wind has speeds  $>600 \text{ km s}^{-1}$  (Schwenn 1990, p. 144). Their different compositions and characteristics indicate different sources and generation processes (McGregor et al. 2011b). Fast streams are found to originate from coronal holes as confirmed by Ulysses’ out-of-ecliptic measurements (McComas et al. 1998). The source of slow wind, and its eventually different types (Schwenn 1983), is still a subject of controversial discussions because several scenarios are possible to explain its origin from closed magnetic structures in the solar corona, such as intermittent reconnection at the top of helmet streamers and from coronal hole boundaries (Kilpua et al. 2016). The occurrence frequency of these slow and fast streams varies strongly with solar activity and their interactions lead to phenomena such as stream interaction regions which may persist for many solar rotations (“co-rotating” interaction regions) if the coronal source regions are quasi-stationary (Balogh et al. 1999). Embedded in the slow and fast solar-wind streams are transient flows of CMEs – the faster ones driving shock waves ahead (Gosling et al. 1974). Their rate follows the

solar activity cycle and varies in near 1 au measurements between only one CME every couple of days during solar cycle minima up to multiple CMEs observed over several days at times of solar maxima, that is, the CME-associated flow share of the solar wind raises from about 5% up to about 50% (Richardson & Cane 2012).

It is not known which specific solar-wind type or structure PSP will encounter at a given time during its mission, therefore we extrapolate the probability distributions of the major solar-wind parameters from existing solar-wind measurements and take solar cycle dependencies into account. As a baseline we describe the solar-wind environment through the key quantities of a magnetized plasma: magnetic field strength, density and temperature. Furthermore, the bulk flow velocity is the defining parameter of the two types of solar wind. Solar-wind quantities, like flux densities, mass flux, and plasma beta, can be directly derived from these four parameters. In the analyses, we treat the solar wind as a proton plasma – the average helium abundance is about 4.5% and in slow wind at solar cycle minimum is even less than 2% (Feldman et al. 1978; Schwenn 1983; Kasper et al. 2012).

Our approach is to obtain analytical representations of the shapes of the solar-wind parameter’s frequency distributions in Sect. 2, of their solar activity dependence in Sect. 3 and of their solar distance scaling in Sect. 4. The solar-wind parameters’ frequency distributions and solar activity dependence is derived from near-Earth solar wind and sunspot number (SSN) time series with a duration of almost five solar cycles. Their distance dependency is derived from Helios solar-wind measurements covering more than two thirds of the distance to the Sun and more than half a solar cycle. From a combination of the obtained frequency distributions, SSN dependence functions, and solar distance dependence functions, a general solar-wind model is built in Sect. 5, representing the solar activity and distance behavior. Finally, this empirical model is fed with SSN predictions and extrapolated to PSP’s planned orbital positions in Sect. 6.

## 2. Frequency distributions of the solar-wind parameters

The solar-wind parameters are highly variable due to short-term variations from structures such as slow and fast wind streams, interaction regions, and CMEs, whose rate and properties depend on the phase of the solar activity cycle. Hence, for deriving characteristic frequency distributions for the solar-wind parameters, measurements over long-term time spans are needed. The abundance of the near-Earth hourly OMNI data set is ideally suited for this purpose, because to date it spans almost five solar cycles.

The OMNI 2 data set (King & Papitashvili 2005) combines solar-wind magnetic field and plasma data collected by various satellites since 1963, currently by WIND and by ACE. This intercalibrated multi-spacecraft data is time-shifted to the nose of the Earth’s bow shock. The data is obtained from the OMNIWeb interface<sup>3</sup> at NASA’s Space Physics Data Facility (SPDF), Goddard Space Flight Center (GSFC). In this study the whole hourly data until 31 December 2016 is used, starting from 27 November 1963 (for the temperature from 26 July 1965). The data coverage of the different parameters is in the range 67–74%, corresponding to a total duration of 36–40 yr. We note that a test-comparison of hourly averaged data with higher-time-resolution data for the available shorter time span 1981–2016 did not show significant differences in our results. According to the OMNI

<sup>3</sup> <http://omniweb.gsfc.nasa.gov/>

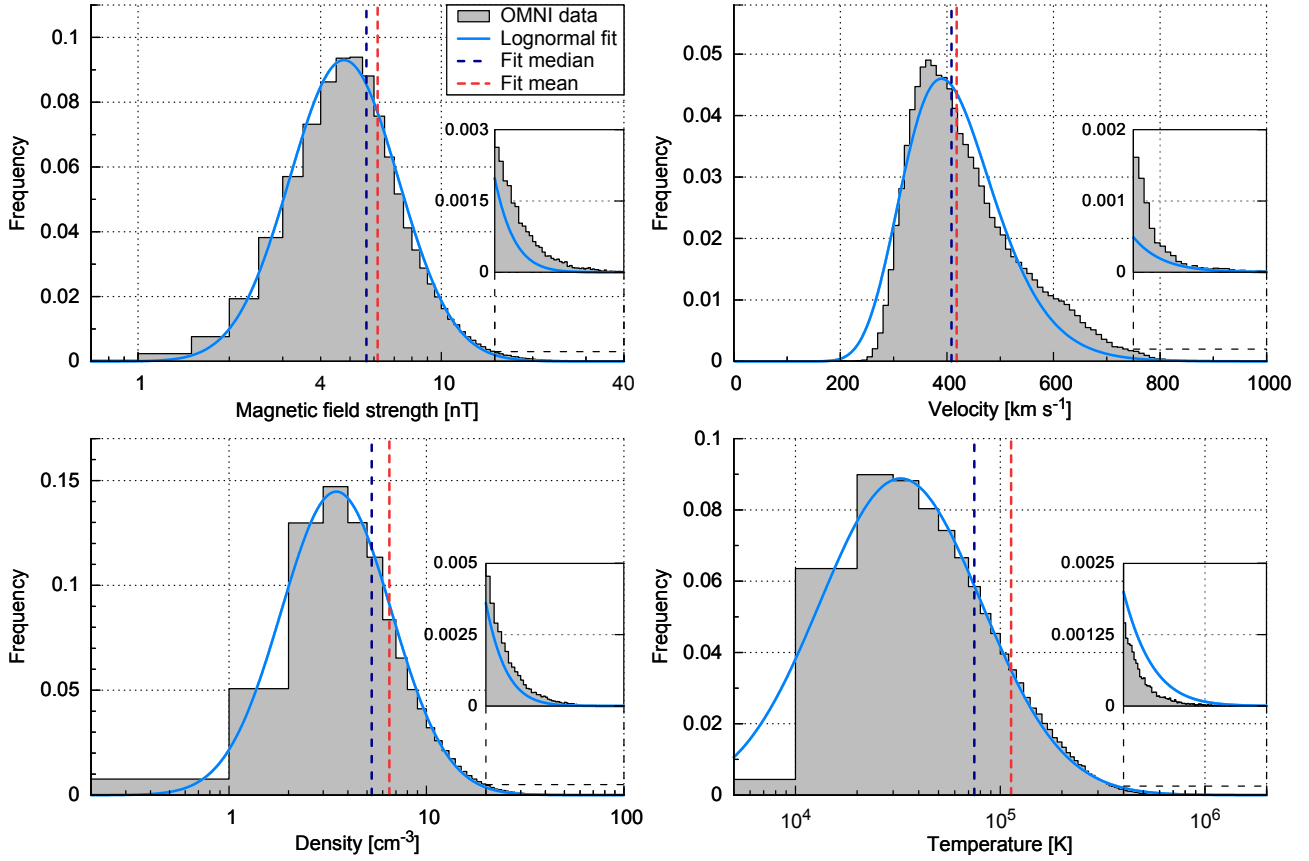


**Fig. 1.** Frequency distributions of the four solar-wind parameters and their lognormal fits derived from the hourly OMNI data set. The histograms have bins of 0.5 nT, 10 km s<sup>-1</sup>, 1 cm<sup>-3</sup>, and 10 000 K. The fits' median and mean values are indicated as well. The *insets* show zoomed-in views of the high-value tails of the distributions.

data precision and maximal parameter ranges we specify bin sizes of 0.5 nT for the magnetic field strength, 10 km s<sup>-1</sup> for the velocity, 1 cm<sup>-3</sup> for the density, and 10 000 K for the temperature. The frequency distributions of the solar-wind magnetic field strength, proton velocity, density and temperature are shown in Fig. 1. The solar-wind magnetic field strength is in the range 0.4–62 nT, the velocity in the range 156–1189 km s<sup>-1</sup>, the density in the range 0–117 cm<sup>-3</sup>, the temperature in the range 3450–6.63 × 10<sup>6</sup> K, and the mean data values are at 6.28 nT, 436 km s<sup>-1</sup>, 6.8 cm<sup>-3</sup>, and 1.05 × 10<sup>5</sup> K. These ranges and mean values are as statistically expected from previous analyses of near 1 au solar-wind data (e.g., Table 3.3 in Bothmer & Daglis 2007, p. 39). Much higher or lower peak values at 1 au have been observed in extraordinary events, such as the 23 July 2012 CME with a speed of over 2000 km s<sup>-1</sup> and a peak field strength of about 100 nT that was observed by STEREO A (Russell et al. 2013), or the solar-wind disappearance event observed in May 1999 with density values even down to 0.2 cm<sup>-3</sup> (Lazarus 2000).

The frequency distributions of the solar-wind parameters, magnetic field strength, proton density, and temperature, can be well approximated by lognormal distributions, whereas the proton velocity's frequency has a differing shape, as shown in Veselovsky et al. (2010). We investigate how well all four solar-wind parameters' frequency distributions can be represented by lognormal functions, which we use in the process of a least squares regression fitting. The lognormal function,

$$W(x) = \frac{1}{\sigma \sqrt{2\pi}x} \exp\left(-\frac{(\ln x - \mu)^2}{2\sigma^2}\right), \quad (1)$$

depends on the location  $\mu$  and the shape parameter  $\sigma$ . Changes in  $\mu$  affect both the horizontal and vertical scaling of the function whereas  $\sigma$  influences its shape. The distribution's median  $x_{\text{med}}$  and mean  $x_{\text{avg}}$  (average) positions are easily interpreted and are directly calculated from  $\mu$  and  $\sigma$ :

$$x_{\text{med}} = \exp(\mu) \iff \mu = \ln(x_{\text{med}}), \quad (2)$$

$$x_{\text{avg}} = \exp\left(\mu + \frac{\sigma^2}{2}\right) \iff \sigma = \sqrt{2 \ln\left(\frac{x_{\text{avg}}}{x_{\text{med}}}\right)}. \quad (3)$$

It is apparent that the mean is always larger than the median. Replacing the variables  $\mu$  and  $\sigma$  with these relations, the lognormal function (1) becomes

$$W(x) = \frac{1}{2\sqrt{\pi \ln\left(\frac{x_{\text{avg}}}{x_{\text{med}}}\right)}x} \exp\left(-\frac{\ln^2\left(\frac{x}{x_{\text{med}}}\right)}{4 \ln\left(\frac{x_{\text{avg}}}{x_{\text{med}}}\right)}\right). \quad (4)$$

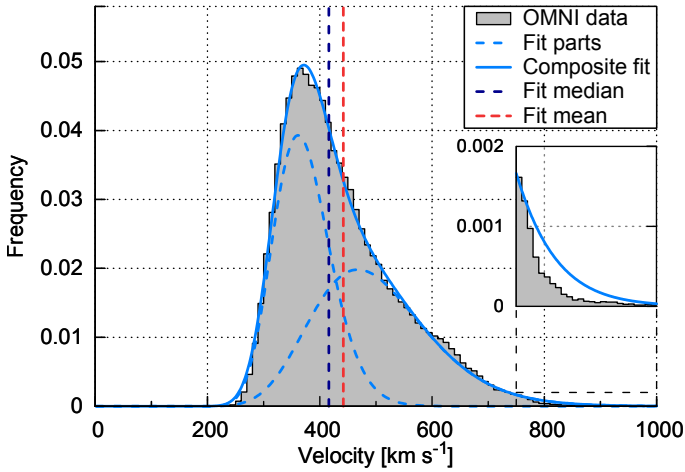
The values of  $x_{\text{med}}$  and  $x_{\text{avg}}$  obtained from fitting the individual solar-wind frequency distributions are listed in Table 1.

From visual inspection, the resulting fit curves describe the shape of the magnetic field strength, the density and the temperature distributions well, as can be seen in Fig. 1. However, for the velocity, the fit function appears not to be as good in describing the measured distribution's more complex shape around its peak and in the higher velocity range. This also can be inferred from the sum of absolute residuals (SAR) between data and fit, listed in Table 1 as a percentage of the distribution area, being almost three times larger than those from the other parameters. In order to find a better fit result for the velocity distribution, we

**Table 1.** Resulting fit coefficients from the fitting of the lognormal function (4) to the shape of the solar-wind parameters' frequency distributions from near 1 au OMNI hourly data.

Parameter	Median $x_{\text{med}}$	Mean $x_{\text{avg}}$	Balance $c$	SAR [%]
Magnetic field [nT]	5.661(16)	6.164(18)	–	6.83
Velocity [ $10^2 \text{ km s}^{-1}$ ]	4.085(19)	4.183(20)	–	18.69
Density [ $\text{cm}^{-3}$ ]	5.276(24)	6.484(34)	–	6.48
Temperature [ $10^4 \text{ K}$ ]	7.470(17)	11.301(32)	–	5.78
Velocity [ $10^2 \text{ km s}^{-1}$ ]	$W_1$	4.89(14)	5.00(14)	–
	$W_2$	3.68(20)	3.72(20)	–
	$W_{\text{II}}$	4.16(14) <sup>a</sup>	4.42(14) <sup>a</sup>	–
			0.504(62)	–

**Notes.** For the velocity, the fit parameters of the double lognormal function (5) are also listed, as well as the median and mean values of the resulting velocity fit. The numbers in parentheses are the errors on the corresponding last digits of the quoted value. They are calculated from the estimated standard deviations of the fit parameters. For each parameter, the sum of absolute residuals between data and fit (in percentage of the distribution area) is also listed. <sup>(a)</sup> Error estimates derived from the individual fit part errors.

**Fig. 2.** Velocity frequency distribution (same as in Fig. 1) and its compositional lognormal fit. The fit's median and mean values and its two fit parts are indicated as well. The *inset* is a zoomed-in view of the high value tail of the distribution.

assume that the velocity distribution can be made up of at least two overlapping branches (McGregor et al. 2011a). Therefore a compositional approach is chosen by combining two lognormal functions (4), involving more fit variables:

$$W_{\text{II}}(x) = c \cdot W_1(x) + (1 - c) \cdot W_2(x). \quad (5)$$

The balancing parameter  $c$  ensures that the resulting function remains normalized as it represents a probability distribution. The fitting of  $W_{\text{II}}(x)$  to the velocity's frequency distribution yields the values of the now five fit parameters ( $c$ ,  $x_{\text{med},1}$ ,  $x_{\text{avg},1}$ ,  $x_{\text{med},2}$  and  $x_{\text{avg},2}$ ) as listed in Table 1 together with the median and mean values of the composed distribution, which can be derived by solving

$$\int W_{\text{II}}(x) dx = 0 \quad \text{and} \quad \int x W_{\text{II}}(x) dx = 0. \quad (6)$$

This more complex fit function is more accurate in describing the velocity's frequency distribution as shown in Fig. 2. Thus in the following Sections we keep the double lognormal ansatz for all velocity frequency fits.

For the bulk of the solar wind these static lognormal functions describe the parameters' distributions well. The abnormally high parameter values in the distribution functions can be

attributed to shock/CME events in agreement with the results of the OMNI solar-wind investigations by Richardson & Cane (2012). The simple lognormal fit functions underestimate the frequencies in their high-value tails, except for the temperature's tail which is overestimated, as seen in the insets of Fig. 1. This appears to be because CMEs do not come with abnormally high temperatures, but rather with temperatures lower than those of the average solar wind (Forsyth et al. 2006). The velocity's compositional lognormal fit only slightly overestimates its tail as seen in the inset of Fig. 2. The slow and fast part contribute almost equally ( $c \approx 0.5$ ) to the long-term velocity distribution function.

### 3. Solar activity dependence of the solar-wind frequency distributions

In the next step we investigate how the long-term solar-wind distribution functions presented in the previous section depend on general solar activity. Therefore we examine their correlation with the SSN, being a commonly used long-term solar activity index, and determine the time lags with the highest correlation coefficients.

For the correlations we fit lognormal functions to the frequency distributions as in Sect. 2, but implement linear relations to the yearly SSN, allowing shifting of the distribution functions with SSN. For the velocity the approach is different insofar as its two components are kept fixed and instead their balance is modified with the changing SSN. Thus we obtain solar-activity-dependent models for the frequency distributions of all four solar-wind parameters.

The international sunspot number (1963–2016) is provided by the online catalog<sup>4</sup> at the World Data Center – Sunspot Index and Long-term Solar Observations (WDC-SILSO), Solar Influences Data Analysis Center (SIDC), Royal Observatory of Belgium (ROB).

Yearly medians of the solar-wind parameters and the yearly SSN together with the solar cycle number are shown in the upper part of Fig. 3. The reason for correlating the SSN to the solar-wind median values is because the position of a lognormal function is defined by its median. The data are averaged to yearly values to avoid seasonal effects during the Earth's orbit around the Sun caused by its variations in solar latitude and distance. The solar-wind velocity, density, and temperature depend

<sup>4</sup> <http://www.sidc.be/silso/>



**Table 2.** Resulting fit coefficients from the OMNI data, based on the linear SSN dependencies (7) and (8).

Parameter	Median		Mean scaling factor $a_{\text{avg}}$	Balance		SSN lag [years]
	SSN factor $a_{\text{med}}$	baseline $b_{\text{med}}$		SSN factor $c_a$	baseline $c_b$	
Magnetic field [nT]	$1.309(19) \times 10^{-2}$	4.285(17)	$8.786(78) \times 10^{-2}$	–	–	0
Density [ $\text{cm}^{-3}$ ]	$3.81(25) \times 10^{-3}$	4.495(26)	$3.050(27) \times 10^{-1}$	–	–	6
Temperature [ $10^4$ K]	$1.974(26) \times 10^{-2}$	5.729(19)	$6.541(28) \times 10^{-1}$	–	–	3
Velocity [ $10^2 \text{ km s}^{-1}$ ]	$W_1'$ $W_2'$	– –	3.633(12) 4.831(81)	$1.008(37) \times 10^{-2}$ $2.31(20) \times 10^{-2}$	-1.799(95)e-3 0.638(32)	3

**Notes.** For the velocity the fit parameters from the double lognormal fit (5) and their balancing function (9) are given. The numbers in parentheses are the errors on the corresponding last digits of the quoted value. They are calculated from the estimated standard deviations of the fit parameters. The listed SSN time lags are used for the fits.

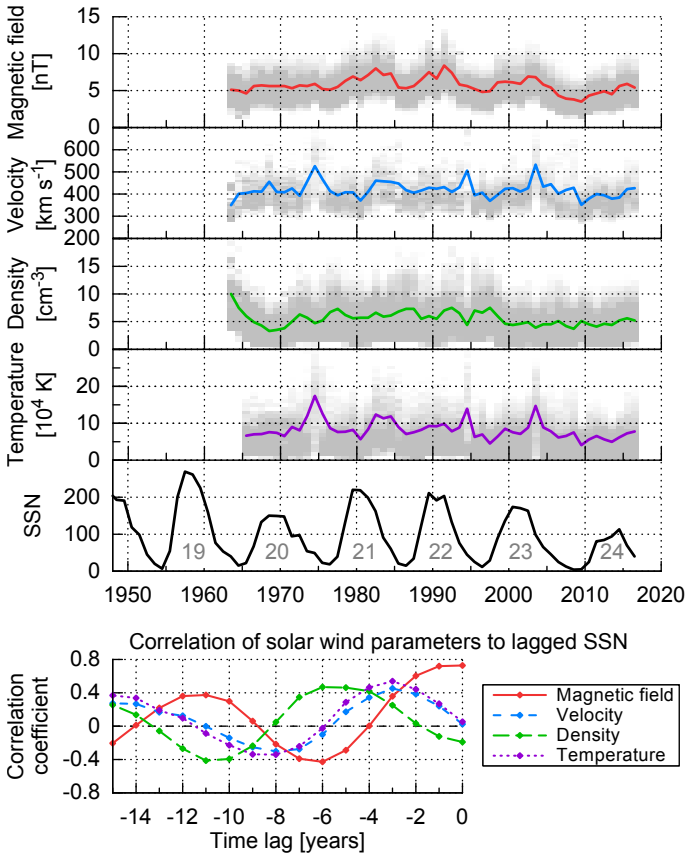


**Fig. 3.** Solar-wind parameter yearly frequencies (gray shading) with yearly medians (lines) derived from OMNI data and the yearly SSN from the SILSO World Data Center (1963–2016) with solar cycle number (top). Their correlation coefficients with the yearly SSN are calculated for time lags back to –15 yr (bottom).

on the state of the solar cycle (Schwenn 1983). For instance the fast solar wind occurs at times when polar coronal holes extend to lower latitudes, a typical feature of the declining phase of the solar cycle as pointed out by Bothmer & Daglis (2007, p. 75, Fig. 3.52). Therefore the solar-wind velocity, density, and temperature maxima exhibit time lags relative to the SSN maxima.

The correlation coefficients of the solar wind parameters with the yearly SSN shown in the bottom part of Fig. 3 are calculated for time lags back to –15 yr to cover a time span longer than a solar cycle. As expected, the amplitudes of the variations in the correlations of all parameters decline with increasing time lag and show a period of about 11 yr. The highest correlation coefficient of 0.728 to the SSN is found for the magnetic field

strength; it has no time lag. This finding is anticipated because the SSN is found to be directly proportional to the evolution of the photospheric magnetic flux (Smith & Balogh 2003). Velocity and temperature show time lags of 3 yr with peak correlation coefficients of 0.453 and 0.540. The density with a correlation coefficient of 0.468 has a time lag of 6 yr, which is in agreement with the density anticorrelation to the SSN reported by Bougeret et al. (1984).

Next we create solar-activity-dependent analytical representations of the solar wind frequency distributions. This is achieved by shifting the median positions of the lognormal distributions as a linear function of the SSN. To enable these shifts, we add a linear SSN dependency to the median,

$$x_{\text{med}}(\text{ssn}) = a_{\text{med}} \cdot \text{ssn} + b_{\text{med}}, \quad (7)$$

using a factor to the SSN  $a_{\text{med}}$  with a baseline  $b_{\text{med}}$ . We relate the mean with a scaling factor to the median to transfer its SSN dependency:

$$x_{\text{avg}}(\text{ssn}) = (1 + a_{\text{avg}}) \cdot x_{\text{med}}(\text{ssn}). \quad (8)$$

These relations, substituted into the lognormal function (4), lead to a new SSN-dependent function  $W'(x, \text{ssn})$ . This function is then fitted to the yearly data, using the yearly SSN as input parameter. The SSN is offset with the individual time lags determined before for each parameter, to benefit from the higher correlation. The values of the three resulting fit coefficients ( $a_{\text{med}}$ ,  $b_{\text{med}}$ , and  $a_{\text{avg}}$ ) are presented in Table 2.

Naturally, the fit models match with the general data trends, as can be seen from Fig. 4, though single year variations are not replicated by the model (e.g., the high velocity and temperature values in 1974, 1994, and 2003). The comparison of this model with the yearly data median values with respect to the lagged SSN shows that the medians obtained from the modeling have a similar slope, as shown in Fig. 5.

Again, the solar-wind velocity needs a special treatment because of the application of the double lognormal distribution (5). Since it is well known that slow and fast solar-wind stream occurrence rates follow the solar cycle, we keep the two velocity components' positions SSN-independent ( $x_{\text{med}} = b_{\text{med}}$ ) and vary instead their balance with the SSN:

$$c(\text{ssn}) = c_a \cdot \text{ssn} + c_b. \quad (9)$$

The fit result (see Table 2) yields a model in which three years after solar cycle minimum (SSN of zero) the contribution of slow solar wind to the overall solar wind distribution reaches a maximum value (about 64%) and decreases with increasing SSN as shown in Fig. 6.



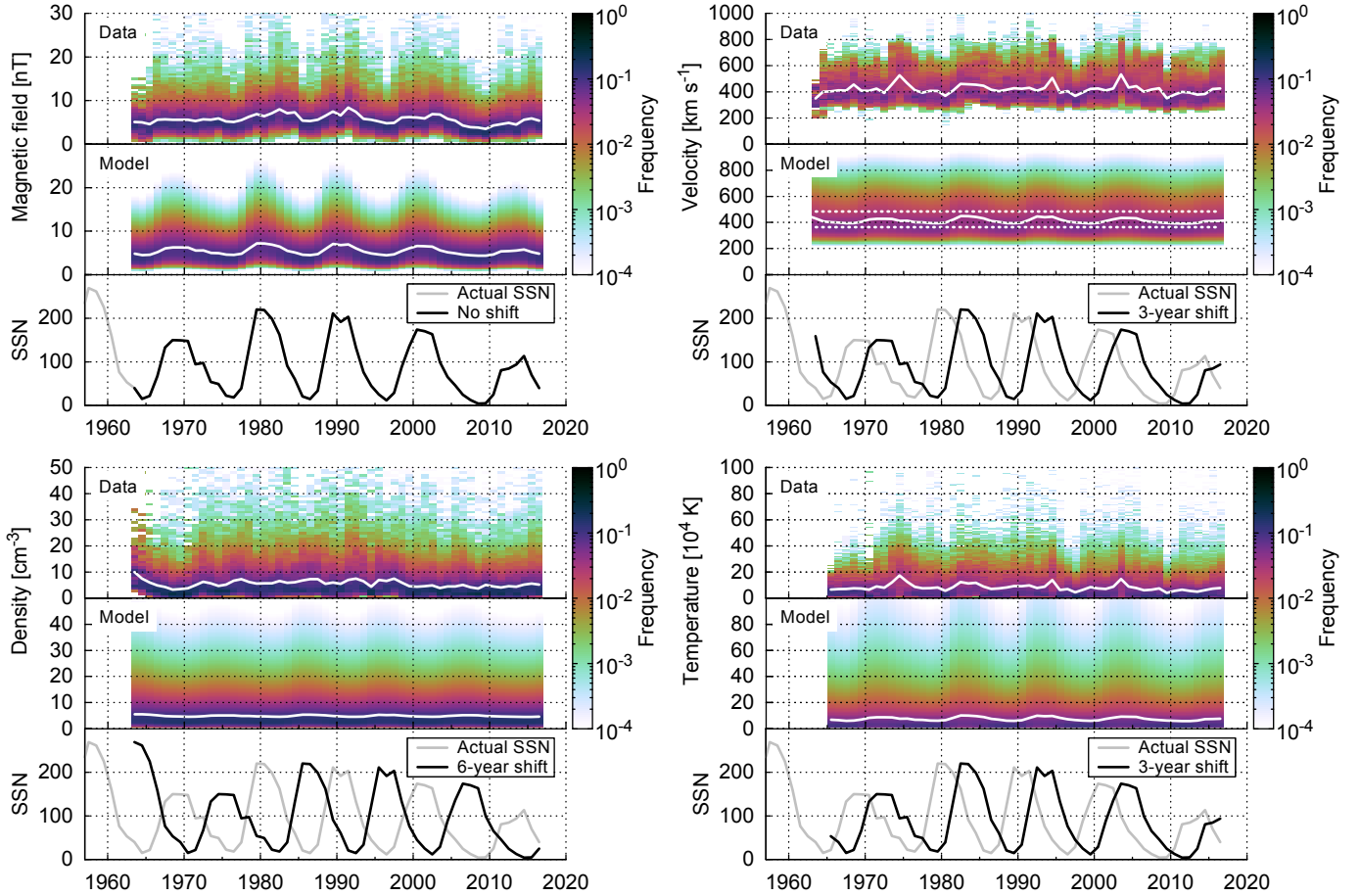


**Fig. 4.** Solar wind parameter yearly data frequencies and lognormal fit models, both with their median values (white lines) over the OMNI time period 1963–2016. The corresponding yearly SSN and the shifted SSN for the models are indicated by gray and black lines. The velocity median is derived from the SSN-weighted constant lognormal parts (dotted lines).

To investigate the amount of slow and fast wind contributions depending on solar activity, we apply the commonly used constant velocity threshold of  $v_{th} = 400 \text{ km s}^{-1}$  (Schwenn 1990, p. 144). The linear fit to the yearly data ratio and the derived model ratio show a good agreement (see Fig. 6). The to-some-degree steeper balance parameter of the double fit function used in this model cannot be compared directly with specific velocity thresholds between slow and fast solar wind. However, it appears to be a more realistic approach than just taking a specific velocity threshold for the slow and fast wind, in agreement with the overlapping nature of the velocity flows reported by McGregor et al. (2011a).

#### 4. Solar distance dependency

In order to derive heliocentric distance relationships of the bulk solar wind distribution functions, we apply and fit power law dependencies to the Helios data. We then examine how the fits may be extrapolated towards the Sun and in particular in to the PSP orbit. We use the fitting methods of Sect. 2 for the distance-binned combined data from both Helios probes. Helios' highly elliptical orbits in the ecliptic covered a solar distance range of 0.31–0.98 au in case of Helios 1 and 0.29–0.98 au in case of Helios 2. Launched during solar cycle minimum, the data of both probes cover the rise to the maximum of cycle 21, covering  $\sim 6.5$  yr at varying distances to the Sun.

We investigate hourly averages of the Helios data in the same way as with the OMNI data. The Helios 1 merged

hourly data from the magnetometer and plasma instruments (Rosenbauer et al. 1977) include  $\sim 12.5$  orbits for the time range 10 December 1974 to 14 June 1981, and those for Helios 2 include  $\sim 8$  orbits for the time span 1 January 1976 to 4 March 1980. The data are retrieved from the Coordinated Data Analysis Web (CDAWeb) interface at NASA's GSFC/SPDF<sup>5</sup>.

The Helios 1 magnetometer data coverage for this data set is about 43% (i.e., 2.8 yr), and that of Helios 2 amounts to 54% (i.e., 2.3 yr). The plasma data coverage is 76% (i.e., 5.0 yr) in case of Helios 1 and 92% (i.e., 3.9 yr) in case of Helios 2. Thus, using this data, we point out that its time coverage is unequally distributed over the solar cycle. Considering the data gap distributions, the amount of data during solar cycle minimum up to mid 1977, that is, the transition from minimum to maximum, covers about 68% of this period whereas during maximum of cycle 21 data are available only 38% of the time. This Helios data bias towards solar minimum is one reason why in this study the Helios solar wind data are not used to derive long-term frequency distributions and solar-cycle dependencies for the key solar wind parameters.

The radial dependencies of the key solar-wind parameters over the distance range 0.29–0.98 au measured by both Helios probes are plotted in Fig. 7, together with their median and mean values for different solar distances, calculated for the minimal distance resolution 0.01 au of the data set. Assuming a radial solar-wind outflow, it is expected that the distance

<sup>5</sup> <http://spdf.gsfc.nasa.gov/>

**Table 3.** Fit coefficients for the median and mean solar distance dependencies (10) of the four solar wind parameters derived from the combined Helios 1 and 2 data.

Parameter	Median		Mean		Crossing distance [au]	Yearly variation $\Delta e$
	$d_{\text{med}}$	$e_{\text{med}}$	$d_{\text{avg}}$	$e_{\text{avg}}$		
Magnetic field [nT]	5.377(92)	-1.655(17)	6.05(10)	-1.546(18)	0.339(11)	0.11
Velocity [ $10^2 \text{ km s}^{-1}$ ]	4.107(28)	0.058(13)	4.356(24)	0.049(10)	$0.7(83) \times 10^3$	0.012
Density [ $\text{cm}^{-3}$ ]	5.61(27)	-2.093(46)	7.57(30)	-2.010(38)	0.027(73)	0.072
Temperature [ $10^4 \text{ K}$ ]	7.14(23)	-0.913(39)	9.67(21)	-0.792(28)	0.082(85)	0.050

**Notes.** The numbers in parentheses are the errors on the corresponding last digits of the quoted value. They are calculated from the estimated standard deviations of the fit parameters. The crossing distances indicate where the median and mean fits intersect each other. The yearly variation is the weighted standard deviation derived from the yearly fit exponents seen in Fig. 9.

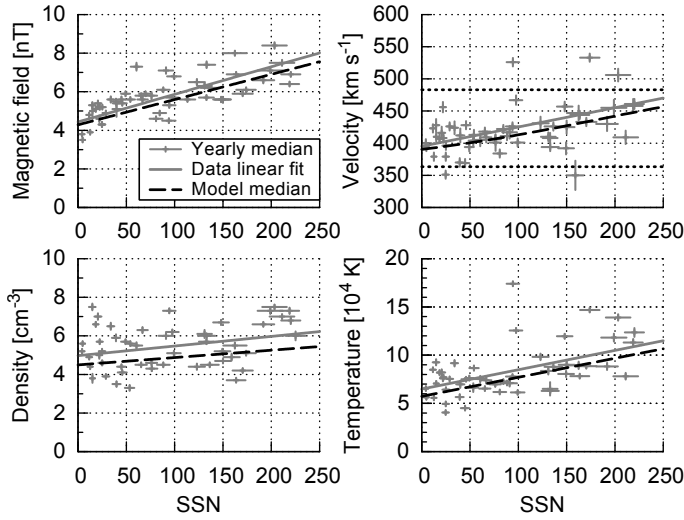


**Fig. 5.** Solar-wind parameter medians with respect to the lagged SSN. The yearly data medians (+) with their weighted linear fit (solid lines) are obtained from OMNI data. The error bars denote the SSN standard deviation and the relative weight from the yearly data coverage. The SSN-dependent median (dashed lines) is derived from the lognormal model fit. For the velocity the median is derived from the SSN-weighting (9) of the slow and fast model parts (dotted lines), whose magnitudes are SSN independent.

dependence of the solar-wind parameters over the Helios data range 0.29–0.98 au can be described through power law scaling. Therefore we use the power law function,

$$x(r) = d \cdot r^e, \quad (10)$$

for the regression fit of the median and mean, with  $r$  being the solar distance in astronomical units,  $d$  the magnitude at 1 au, and  $e$  the exponent. The fits are weighted through the different data counts per bin. The obtained coefficients for the median and mean power law fits ( $d_{\text{med}}$ ,  $e_{\text{med}}$ ,  $d_{\text{avg}}$ , and  $e_{\text{avg}}$ ) are listed in Table 3 and their corresponding curves are shown in Fig. 7.

Our derived exponents agree with those found in existing studies from the Helios observations: Mariani et al. (1978) derived the exponents for the magnetic field strength separately for the fast and slow solar wind as  $B_{\text{fast}} \propto r^{-1.54}$  and  $B_{\text{slow}} \propto r^{-1.61}$ , ours is  $B_{\text{avg}} \propto r^{-1.55}$ . The velocity exponent  $v_{\text{avg}} \propto r^{0.049}$  matches with the values found by Schwenn (1983, 1990), who derived the distance dependencies for both Helios spacecraft separately as  $v_{\text{H1}} \propto r^{0.083}$  and  $v_{\text{H2}} \propto r^{0.036}$ . The calculated density exponent  $n_{\text{avg}} \propto r^{-2.01}$  agrees well with the Helios plasma density model derived by Bougeret et al. (1984) yielding  $n \propto r^{-2.10}$ . The temperature exponent  $T_{\text{avg}} \propto r^{-0.79}$  is similar to those in the studies

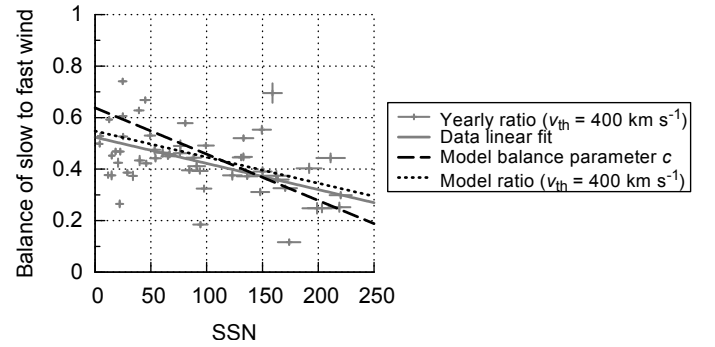


**Fig. 6.** Ratio of slow to fast solar wind for a SSN lagged by 3 yr. The yearly ratios (+) and their weighted linear fit (solid line) are obtained from OMNI data with a threshold velocity of  $v_{\text{th}} = 400 \text{ km s}^{-1}$ . The error bars denote the SSN standard deviation and the relative weight from the yearly data coverage. The model's balance parameter (9) and derived ratio (same threshold) are plotted as dashed and dotted lines.

by Hellinger et al. (2011, 2013), who also derived the exponents separately for the fast and the slow solar wind:  $T_{\text{fast}} \propto r^{-0.74}$  and  $T_{\text{slow}} \propto r^{-0.58}$ .

The mean and median velocity fit exponents acquired from the Helios data are very similar, which indicates that they can be kept identical so that the basic shape of the frequency distribution does not change with distance. Conversely, the mean and median fits for the magnetic field strength cross each other at 0.339 au (see Table 3) and the mean becomes slightly lower than the median at smaller distances. Thus, below that distance the frequency distribution can no longer be well described by a lognormal function, because the mean of a lognormal function has to be larger than its median (as pointed out in Sect. 2), that is, the location of the crossing indicates that the parameter's distribution is no longer of a lognormal shape thereafter. The fits for the proton temperature show a similar behavior, having an extrapolated intersection at 0.082 au. Therefore the extrapolation of the magnetic field and temperature distribution frequencies to the PSP orbit by applying lognormal functions is limited. The crossing points limit the regions where the distribution's shapes can still be considered lognormal.

In order to still fit and extrapolate lognormal functions with the data, we assume that the shapes can be considered lognormal at all distances. For the frequency distribution fit function to be discussed in the following paragraph, we reduce the fit exponents  $e_{\text{med}}$  and  $e_{\text{avg}}$  to only one. We note that this simplification leads to slightly larger modeling errors, especially in case of the magnetic field strength.

Next we retrieve the frequency distributions of the four solar wind parameters in solar distance bins of 0.01 au, choosing the

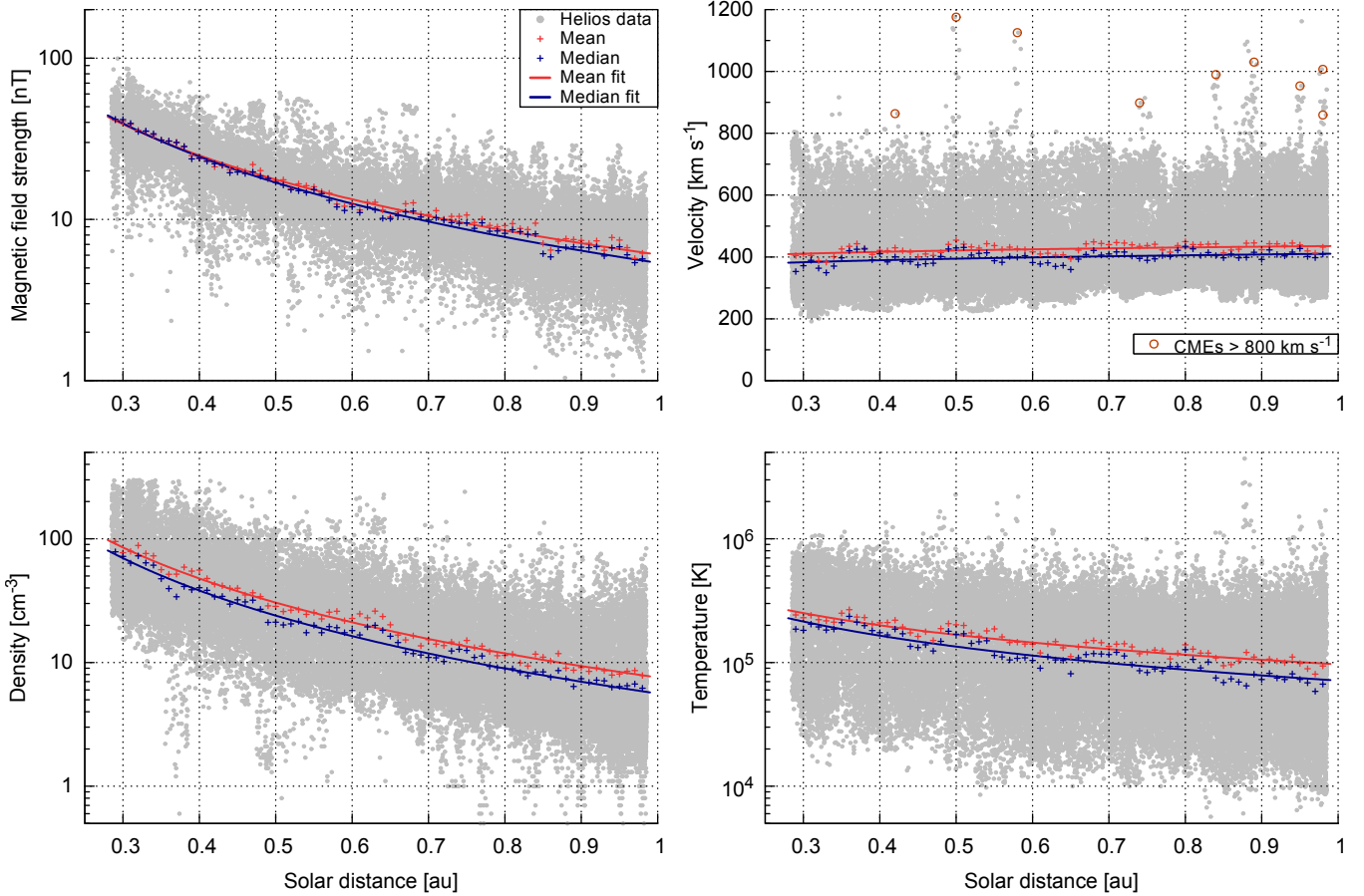


**Fig. 7.** Helios hourly data plots of the four solar wind parameters over solar distance. The mean and median per 0.01 au data bin and their fit curves are plotted as well. The Helios data has a native distance resolution of 0.01 au, thus, to make the distribution visible in these plots, we added a random distance value of up to  $\pm 0.005$  au. The high velocity data points above  $800 \text{ km s}^{-1}$  (circled red) are identified as CME events (e.g., Sheeley et al. 1985; Bothmer & Schwenn 1996, 1998).

**Table 4.** Fit coefficients for the distance-dependent single lognormal function, based on Eq. (4) combined with (10) from the combined Helios data.

Parameter	Median $d'_{\text{med}}$	Mean $d'_{\text{avg}}$	Exponent $e'$	Balance $c'$	Seasonal variation $\Delta d$ [%]
Magnetic field [nT]	5.358(25)	5.705(28)	-1.662(11)	–	2.8
Density [ $\text{cm}^{-3}$ ]	5.424(33)	6.845(47)	-2.114(20)	–	3.6
Temperature [ $10^4 \text{ K}$ ]	6.357(64)	10.72(14)	-1.100(20)	–	1.9
Velocity [ $10^2 \text{ km s}^{-1}$ ]	$W''_1$	3.707(13)	3.748(16)	0.0990(51) 0.557(45)	0.17
	$W''_2$	5.26(13)	5.42(11)		
	$W''_{\text{II}}$	4.13(13) <sup>a</sup>	4.47(11) <sup>a</sup>	–	–

**Notes.** Regarding the velocity, the double lognormal function (5) is used instead. The numbers in parentheses are the errors on the corresponding last digits of the quoted value. They are calculated from the estimated standard deviations of the fit parameters. The seasonal variations are calculated from Earth's orbital solar distance variation and the derived exponents. <sup>(a)</sup> Velocity median and mean 1 au values for the resulting function. Error estimates derived from the individual fit part errors.

same resolution as for the OMNI data analyzed in Sect. 2 – the distributions and their median values are plotted in Fig. 8. For simplification, as mentioned before, we treat the exponents of the median and mean fit functions as being identical, using one fit parameter for both. Implementing the power law distance dependency (10) into the lognormal function (4), we get the fit parameters  $d'_{\text{med}}$ ,  $d'_{\text{avg}}$  and the common exponent  $e'$ . Again, we use the double lognormal function (5) for the velocity distribution fit – resulting in  $W''_{\text{II}}(x, r)$ . The additional fit parameters are the balancing parameter  $c'$  and for the second lognormal part  $d'_{\text{med},2}$

and  $d'_{\text{avg},2}$ . The resulting fit coefficients for the four solar wind parameters are presented in Table 4.

The velocity balancing parameter  $c' = 0.557$  is in good agreement with the results for the SSN dependency (9), because with a mean SSN of 59 during the Helios time period,  $c(59) = 0.53$ , as can be seen from Fig. 6.

The power law lognormal models and the power law double lognormal model for the velocity, which result from the fitting, are plotted in Fig. 8 together with their median values. The model's magnetic field strength is broader around values

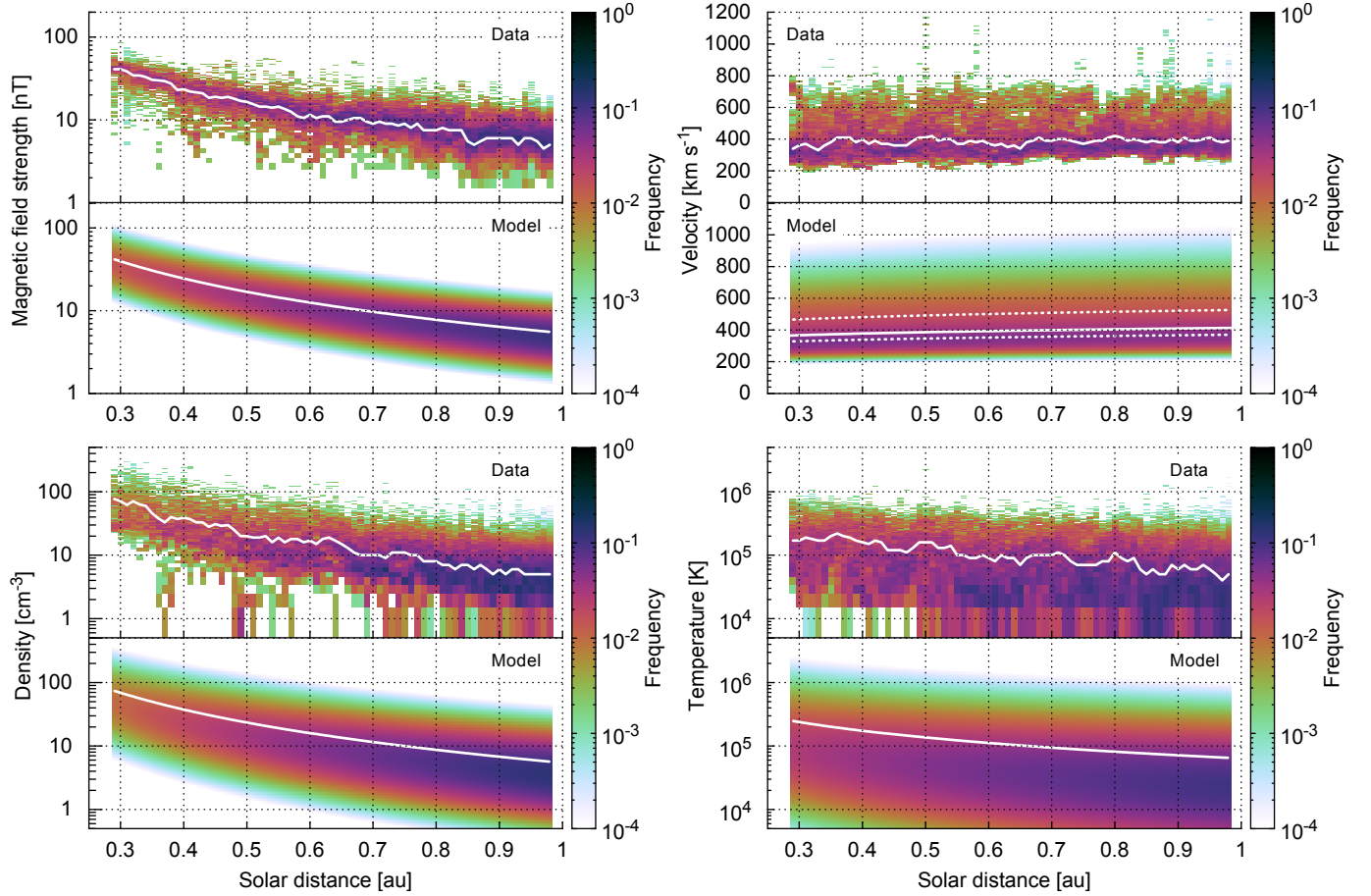


**Fig. 8.** Frequency distributions of the four solar-wind parameters with respect to solar distance. Plotted are the binned Helios data and the power law lognormal fit models with their median values (white lines). The double lognormal model is used for the velocity, its slow and fast parts are indicated by dotted lines.

of 40 nT at the lower distance boundary than the data's frequency distribution implies. This behavior is expected because of the applied distance-independent shape approximation. The velocity and temperature models' upper values generally show a higher abundance than the actual data; see also zoom boxes in Figs. 1 and 2. The high-velocity tail that increases with distance arises from using the same exponent for both slow and fast components. This effect is not seen in the data; more specifically, not only the slowest wind but also the fastest wind is expected to converge to more average speeds (Sanchez-Diaz et al. 2016).

## 5. Empirical solar-wind model

In order to estimate the solar-wind environment for the PSP orbit, we combine the results from the solar-wind frequency distributions' solar-activity relationships and their distance dependencies derived from the OMNI and Helios data. The result is an empirical solar-wind model for the inner heliosphere which is then extrapolated to the PSP orbit in Sect. 6.

This solar-wind model for the radial distance dependence is representative for the time of the Helios observations around the rise of solar cycle 21. The variations of the yearly power law fit exponents from fitting the solar-distance dependency (10) are shown in Fig. 9 together with the yearly SSN for the time period 1974–1982. It can be seen that during the Helios time period there might be some systematic variation of the exponents with solar activity – at least for the velocity and temperature

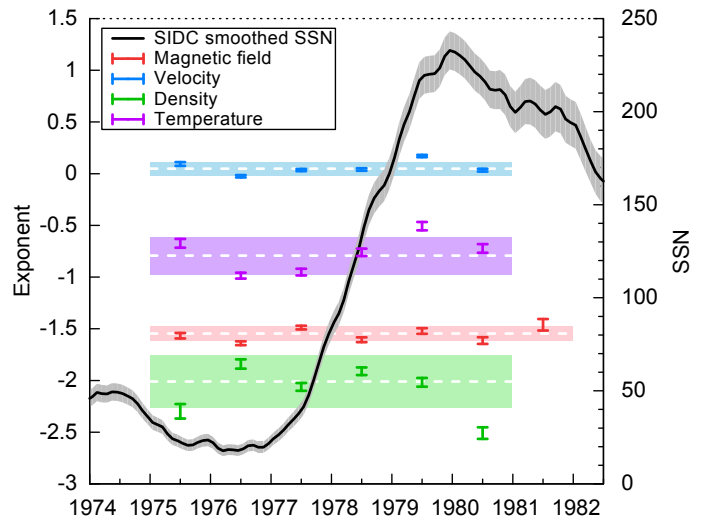


**Fig. 9.** Helios yearly variation of the solar-wind parameter power exponents for the dependence on radial distance together with the SIDC 13-month smoothed monthly SSN. The weighted standard deviations and average values for all years are indicated by the shaded areas. In this plot, the 21 days since Helios launch in the year 1974 are omitted because a distance range of merely 0.95–0.98 au was covered that year.

exponents. However, for simplicity we assume that the distance scaling laws can be treated as time independent and include



the calculated exponents' yearly variations  $\Delta e$ , summarized in Table 3, as relative uncertainties.

Since we neglect possible variations of the distance scaling laws, we combine the frequency distribution's median solar activity dependency (7) derived for 1 au from the OMNI data with the power law exponents (10) derived from the Helios data:

$$x_{\text{med}}(ssn, r) = (a_{\text{med}} \cdot ssn + b_{\text{med}}) \cdot r^{e'}. \quad (11)$$

Thus, implementing the median and mean relations into the lognormal function (4), we obtain the combined model function  $W'''(x, ssn, r)$  and for the velocity  $W''_{\text{II}}(x, ssn, r)$  with the double lognormal function (5). The corresponding median and mean relations for each solar-wind parameter, based on the values resulting from our analyses, are listed below. Their numerical values are the fit parameters from Table 2 and the exponents from Table 4.

- The magnetic field strength relations, depending on solar activity and solar distance, are:

$$B_{\text{med}}(ssn, r) = (0.0131 \text{ nT} \cdot ssn + 4.29 \text{ nT}) \cdot r^{-1.66}, \quad (12)$$

$$B_{\text{avg}}(ssn, r) = 1.0879 \cdot B_{\text{med}}(ssn, r). \quad (13)$$

- The proton velocity relations for the slow and fast components, depending on solar distance, are:

$$v_{\text{med}}^{\text{slow}}(r) = 363 \text{ km s}^{-1} \cdot r^{0.099}, \quad v_{\text{med}}^{\text{fast}}(r) = 483 \text{ km s}^{-1} \cdot r^{0.099}, \quad (14)$$

$$v_{\text{avg}}^{\text{slow}}(r) = 1.0101 \cdot v_{\text{med}}^{\text{slow}}(r), \quad v_{\text{avg}}^{\text{fast}}(r) = 1.023 \cdot v_{\text{med}}^{\text{fast}}(r). \quad (15)$$

The share of both components balanced with solar activity is found to be:

$$c(ssn) = -0.00180 \cdot ssn + 0.64. \quad (16)$$

- The derived relations of the proton density are:

$$n_{\text{med}}(ssn, r) = (0.0038 \text{ cm}^{-3} \cdot ssn + 4.50 \text{ cm}^{-3}) \cdot r^{-2.11}, \quad (17)$$

$$n_{\text{avg}}(ssn, r) = 1.305 \cdot n_{\text{med}}(ssn, r). \quad (18)$$

- The derived proton temperature relations are:

$$T_{\text{med}}(ssn, r) = (197 \text{ K} \cdot ssn + 57\,300 \text{ K}) \cdot r^{-1.10}, \quad (19)$$

$$T_{\text{avg}}(ssn, r) = 1.654 \cdot T_{\text{med}}(ssn, r). \quad (20)$$

These relations average over seasonal variations because they are based on yearly data. The OMNI data are time-shifted to the nose of the Earth's bow shock; this leads to yearly solar distance variations of  $\pm 1.67\%$  as it orbits the Sun. The resulting maximal solar-wind parameter variation amplitudes over the year can thus be derived from the derived power law exponents. They are estimated to be smaller than 4% as seen in Table 4. Bruno et al. (1986) and Balogh et al. (1999) have pointed out that the solar-wind parameters vary with latitudinal separation from the heliospheric current sheet. Its position in heliographic latitude is highly variable around the solar equator (Schwenn 1990) and, furthermore, the Earth's orbit varies over the course of the year by  $\pm 7.2^\circ$  in latitude. Since this latitudinal separation is highly variable and requires significant effort to calculate for an extended time series, we have ignored this aspect in this analysis.

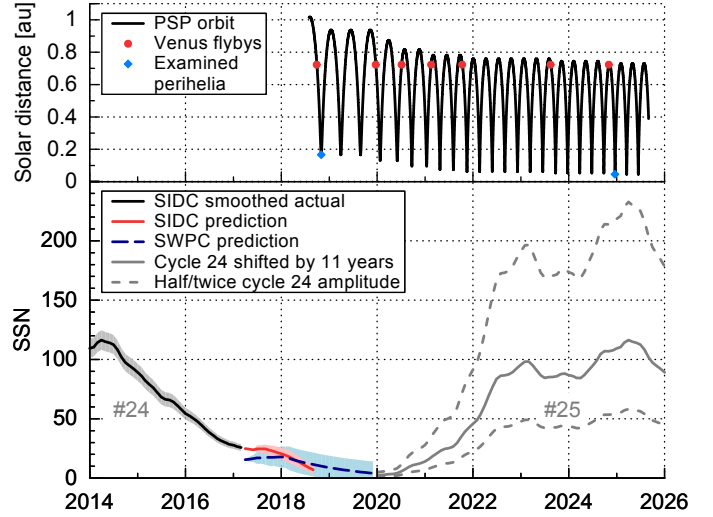


**Fig. 10.** PSP's solar distance during its mission time (*top*). Consecutive Venus flybys bring its perihelia nearer to the Sun. Actual and predicted SSN (*bottom*), that is, SIDC 13-month smoothed monthly actual SSN, SIDC Standard Curves Kalman filter prediction and SWPC prediction with their corresponding expected ranges (shaded areas). The SSN from previous cycle 24, shifted by 11 yr, is plotted together with two alternative trends of half and twice its amplitude.

## 6. Model extrapolation to PSP orbit

To estimate PSP's solar-wind environment during its mission time for its orbital positions, predictions of the SSN during the mission are incorporated into the empirical solar-wind model, derived in the previous sections, and extrapolations down to the PSP perihelion region are performed.

PSP is planned to launch in mid 2018. With its first Venus flyby it will swing into Venus' orbital plane, reaching a first perihelion with a distance of 0.16 au just 93 days after launch, in November 2018. Seven additional Venus flybys allow the perihelion distance to be reduced to a minimum of  $9.86 R_{\odot}$ . This distance will be reached with the 22nd perihelion in December 2024 (Fox et al. 2016), as plotted in the top panel of Fig. 10.

We extrapolate the derived empirical solar-wind models to PSP's orbital distance range and compare the results with those from the existing models shown in Fig. 11. The model and its extrapolation are visualized for the SSN range between solar minimum and maximum ( $0 \leq ssn \leq 200$ ), indicated by the shaded regions in the figure. The magnetic field strength is found to increase from median values of about 43 nT at 0.25 au to 715 nT at 0.046 au for a SSN of zero. Taking a SSN of 200 increases the values to 69 nT and 1152 nT. Our extrapolation results are slightly flatter than those derived from the analytical magnetic field model by Banaszkiewicz et al. (1998), who constructed an analytical dipole plus quadrupole plus current sheet (DQCS) model for solar minimum. We note that one cannot easily compare the absolute values of our study with the values obtained by Banaszkiewicz et al. (1998) because the DQCS model assumes solar wind originating from coronal holes at higher heliographic latitudes only, neglecting the slow solar-wind belt. We suggest that the difference in slope is due to the previously mentioned (Sect. 4) changing shape of the frequency distribution with heliocentric distance, which for smaller distances deviates more from the model's lognormal distribution. The average velocity is found to decrease from  $340 \text{ km s}^{-1}$  at 0.25 au to about  $290 \text{ km s}^{-1}$  at 0.046 au 3 yr after a SSN of zero occurred, whereas using a SSN of 200 it decreases from  $390 \text{ km s}^{-1}$



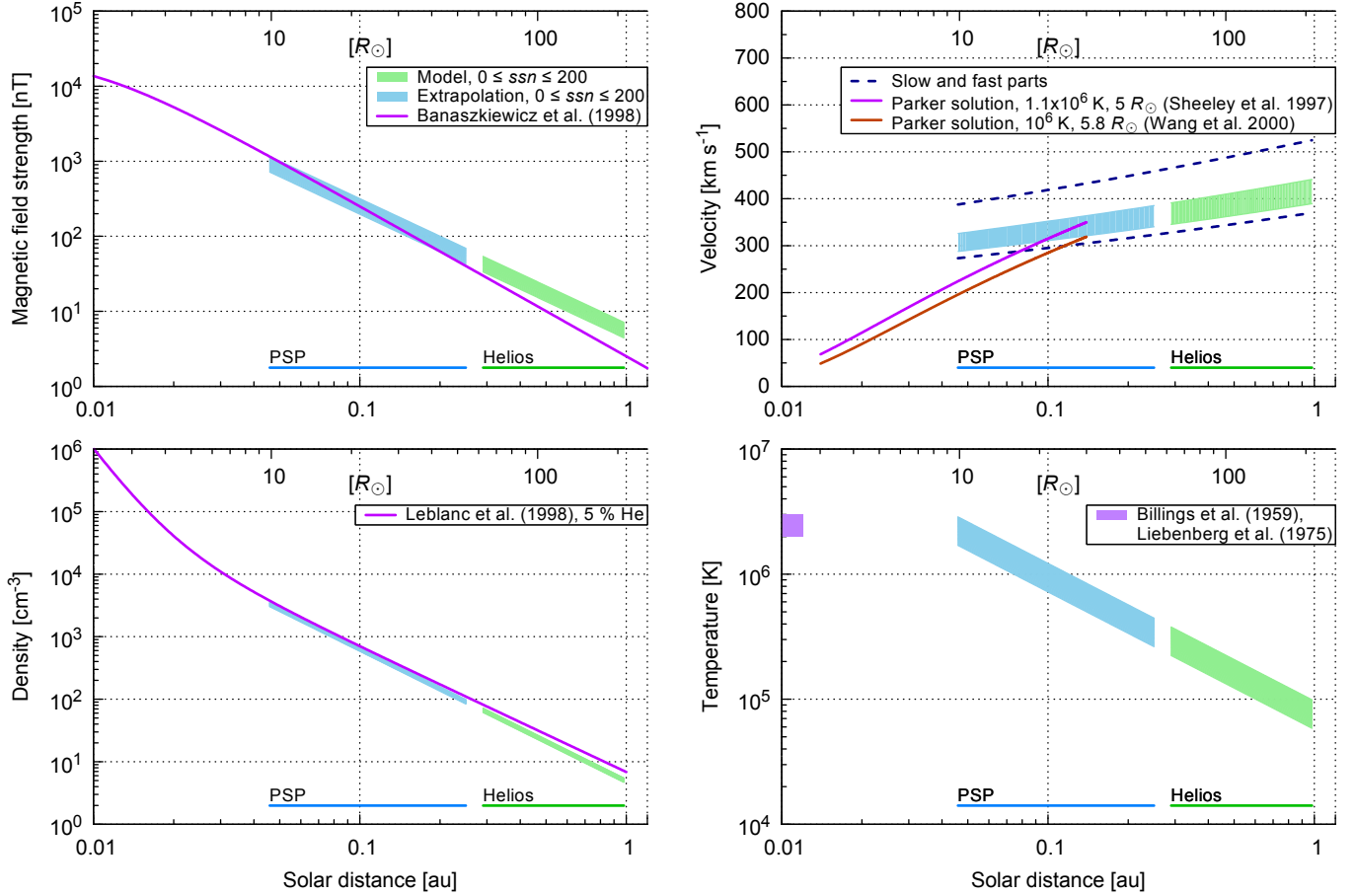


**Fig. 11.** Radial extrapolation of the solar-wind parameters to the PSP orbit region. The median values from the models, obtained from Helios and OMNI measurements, are extrapolated to the PSP region for SSN values between solar minimum and maximum, that is,  $0 \leq \text{ssn} \leq 200$ . The lower edges of the shaded areas correspond to solar minimum, the upper edges to solar maximum. Also plotted are the radial dependencies of the analytic DQCS magnetic field model for solar minimum from Banaszekiewicz et al. (1998), the slow wind velocity models from Sheeley et al. (1997) and Wang et al. (2000), the density model from Leblanc et al. (1998) and the range of temperature measurements from Billings (1959) and Liebenberg et al. (1975).

to 330 km s<sup>-1</sup>. Comparing the results with the measurements by Sheeley et al. (1997) and Wang et al. (2000) shows an overestimation in our extrapolated slow solar-wind velocity values for distances below approximately  $20 R_\odot$ . They used LASCO coronagraph observations to track moving coronal features (blobs) in the distance range  $2\text{--}30 R_\odot$  to determine speed profiles and sources of the slow solar wind and they derived temperature and sonic point values for slow solar wind with the isothermal expansion model from Parker (1958). Therefore, it generally can be expected that PSP will encounter a slower solar-wind environment close to the Sun than our model estimates. Thus PSP will measure solar-wind acceleration processes (McComas et al. 2008), maybe even still at  $30 R_\odot$  as the study by Sheeley et al. (1997) suggests. The proton density increases from about 84 cm<sup>-3</sup> at 0.25 au to about 3018 cm<sup>-3</sup> at 0.046 au 6 yr after a SSN of zero occurred. Being almost independent of the SSN, the values for a SSN of 200 are only 17% larger. The results are in good agreement with those of Leblanc et al. (1998), who derived an electron density model from type III radio burst observations. Their model shows that the density distance dependency scales with  $r^{-2}$  and steepens just below  $10 R_\odot$  with  $r^{-6}$ . We assumed a solar-wind helium abundance of 5% to convert these electron densities to proton densities. The extrapolated proton temperature increases from about 260 000 K at 0.25 au to about 1 690 000 K at 0.046 au 3 yr after a SSN of zero occurred and from 440 000 K to 2 860 000 K for a SSN of 200. Knowing

that near-Sun coronal temperatures are in the range of 2–3 MK (Billings 1959; Liebenberg et al. 1975), the model overestimates the extrapolated temperatures at the PSP perihelion distance.

Aside from the solar distance, the derived solar-wind parameter models depend on the SSN. Short-term predictions of the SSN can be used for the solar-wind predictions of PSP's early perihelia and also for refining the solar-wind predictions during PSP's mission. Several sources are available for SSN short-term predictions. The SIDC provides 12-month SSN forecasts<sup>6</sup> obtained from different methods (e.g., Kalman filter Standard Curve method). The SSN prediction of NOAA's Space Weather Prediction Center (SWPC) for the time period until the end of 2019 follows a consensus of the Solar Cycle 24 Prediction Panel<sup>7</sup>. The SSN for PSP's first perihelion will be small – certainly below 20 – whereas the SSN during the closest perihelia, which will commence at the end of 2024 at the likely maximum phase of cycle 25, cannot be predicted at this time. However, Hathaway & Upton (2016) found indications that the next solar cycle will be similar in size to the current cycle 24. Therefore we simply assume a pattern similar to the last cycle for the prediction of the next solar cycle and thus shift the last cycle by 11 yr. Additionally, we consider as possible alternatives

<sup>6</sup> <http://sidc.be/silso/forecasts>

<sup>7</sup> <http://www.swpc.noaa.gov/products/solar-cycle-progression>

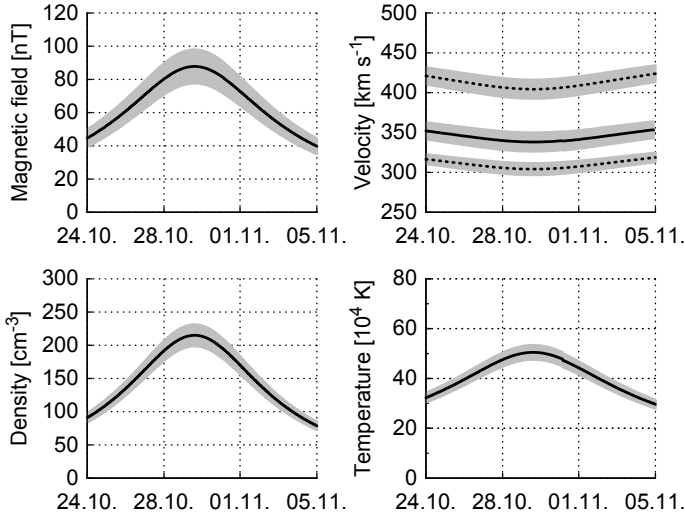


**Fig. 12.** Estimated solar-wind parameter medians (black lines) and their error bands (gray) during 12 days in 2018 with PSP's first perihelion at about 0.16 au. For the velocity the combined median is calculated and also the SSN-independent slow and fast parts are plotted (dotted lines).

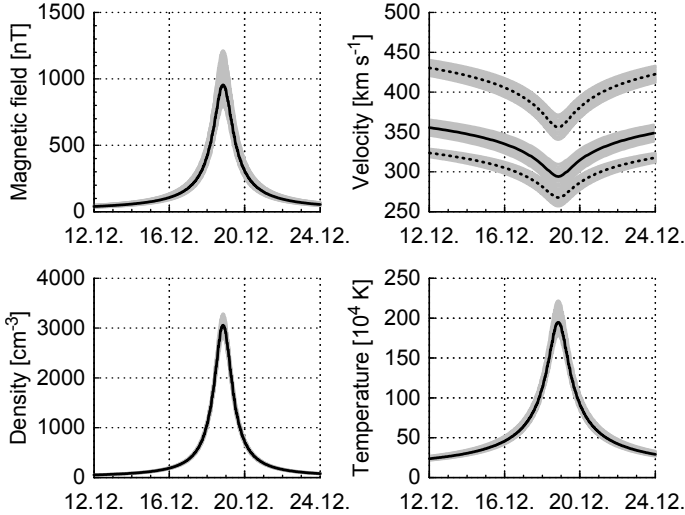


**Fig. 13.** Estimated solar-wind parameter medians (black lines) and their error bands (gray) during 12 days in 2024 with PSP's 22nd (the first closest) perihelion at 0.0459 au. For the velocity the combined median is calculated and also the SSN-independent slow and fast parts are plotted (dotted lines).

SSN patterns of half and twice its amplitude as shown in the bottom panel of Fig. 10.

Implementing the SSN predictions for the PSP mission time and the orbital trajectory data, we can infer which solar-wind parameter magnitudes can be expected. Figures 12 and 13 show the median values (7) of the considered different solar-wind parameters for 12-day periods, comprising the first perihelion in November 2018 and the first closest perihelion in December 2024. In the beginning of the mission median values of about 87 nT, 340 km s<sup>-1</sup>, 214 cm<sup>-3</sup>, and 503 000 K are estimated to be measured at 0.16 au, increasing to about 943 nT, 290 km s<sup>-1</sup>, 2951 cm<sup>-3</sup>, and 1 930 000 K during the first closest approach at 0.046 au. Monthly SSNs – shifted by the time lags specific to the solar-wind parameters – are used in the calculation of the solar-wind predictions. These SSNs are either actual smoothed values from the SIDC with their reported standard deviations, short-term predictions from the SWPC with

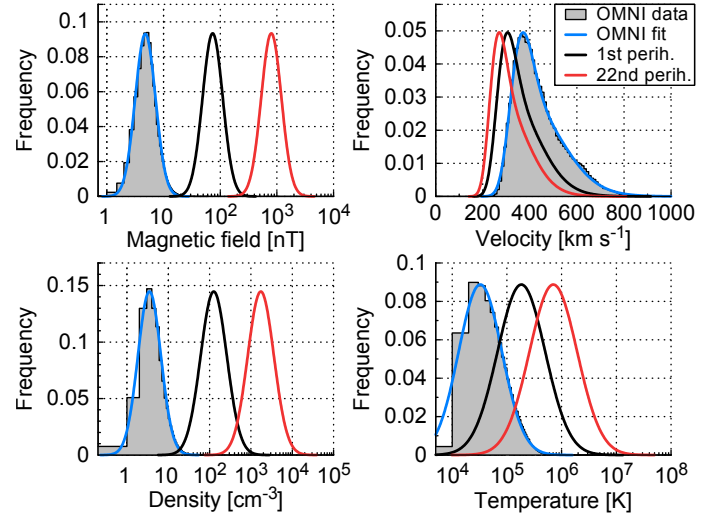


**Fig. 14.** Frequency distributions of the four solar-wind parameters (same as in Figs. 1 and 2) and those estimated with the solar-wind model for PSP's 1st and 22nd (first closest) perihelion. In these figures the frequencies of both extrapolated curves are scaled for visibility to the same height as the 1 au distribution.

their expected ranges, or actual smoothed values from the SIDC shifted by 11 yr with half/twice their values as uncertainties. The error bands given in both figures, calculated from error propagation, include these SSN ranges and the derived fit parameter errors.

Finally the estimated solar-wind environment can be derived from the function  $W'''(x, ssn, r)$ . The estimated frequency distributions of the four solar-wind parameters at PSP's 1st and 22nd (first closest) perihelion are plotted in Fig. 14. Again, we point out that the velocity and temperature distributions for the 22nd perihelion are only upper limits and the actual values to be encountered by PSP are expected to be smaller.

## 7. Discussion and summary

The scientific objective of this study, being part of the CGAUSS project – the German contribution to the WISPR instrument – is to model the solar-wind environment for the PSP mission to be launched mid 2018. For this purpose we started the development of the empirical solar-wind environment model for the near-ecliptic PSP orbit. We derived lognormal representations of the in situ near-Earth solar-wind data collected in the OMNI database, using the frequency distributions of the key solar-wind parameters, magnetic field strength, proton velocity, density, and temperature. Throughout the different analyses in our study, the velocity's frequency distribution is treated as a composition of a slow and a fast wind distribution. Each velocity part is fitted with a lognormal function, which allows for the overlap of both velocity ranges. The OMNI multi-spacecraft solar-wind data is intercalibrated and covers almost five solar cycles. It thus represents solar wind gathered at different phases of solar activity in the ecliptic plane. In the next step we investigated the yearly variation of the solar-wind distribution functions along with the SSN over 53 yr and derived linear dependencies of the solar-wind parameters with the SSN. The radial dependencies of the solar-wind distribution functions were then analyzed, using Helios 1 and 2 data for the distance range 0.29–0.98 au in bins of 0.01 au, deriving power law fit functions that were used to scale the previously calculated SSN-dependent 1 au distribution fit functions to the PSP orbit,

taking into account SSN predictions for the years 2018–2025, encompassing the prime mission up to the closest approach of  $9.86 R_{\odot}$ . The reason for performing the analysis this way is based on the fact that the OMNI solar-wind database is much larger than the Helios database.

For determining solar-activity- and solar-distance-dependent relations for the median and mean solar-wind values, we could have used the simpler approach of combining the radial dependence of averaged Helios data with averaged 1 au OMNI data scaled with the SSN. It is expected that the results of a simpler analysis would have similar distance scaling results, as can be inferred from the exponents in Tables 3 and 4. However, in our study we are not only interested in averages but rather in bulk distributions, that is, the whole range of values that might occur. For the determination of the frequency distributions the use of the more complex fit model is important, because the distance between median and mean values determines the width of the lognormal distributions.

It is clear that the calculated distribution functions only represent first-order estimates of the real solar wind to be encountered by PSP. The solar-wind environment to be encountered will depend at times of PSP on the structure of the solar corona and underlying photospheric magnetic field and on the evolution and interaction of individual solar-wind streams and superimposed CMEs and shocks. However, the derived results are in good agreement with existing studies about near-Sun solar-wind magnetic field strengths and densities as shown in Sect. 6. The extrapolation results of the velocity and the temperature differ from the direct measurements seen in existing studies. This suggests that below about  $20 R_{\odot}$  PSP may dive into the region where the acceleration and heating of the solar wind is expected to occur (see Fig. 11). The near-Sun solar-wind velocity at PSP perihelion is also expected to be slower than our model estimates, because the solar wind is assumed to be accelerated up to the height of the Alfvénic critical surface, which is predicted to lie on average around  $17 R_{\odot}$  (e.g., Sittler & Guhathakurta 1999; Exarhos & Moussas 2000), scaling with solar activity within a range of between  $15 R_{\odot}$  at solar minimum and  $30 R_{\odot}$  at solar maximum (Katsikas et al. 2010; Goelzer et al. 2014).

We have not specifically investigated the occurrences of extreme solar-wind parameters caused by CMEs or enhanced values due to stream interaction or co-rotating interaction regions. The Helios solar-wind measurements plotted over radial distance in Fig. 7 show several extreme values far above the usual solar-wind velocities, which are associated with individual CMEs. The results by Sachdeva et al. (2017) indicate that due to solar-wind drag, the speeds of fast CMEs will commonly slow down substantially from early distances of a few solar radii. Therefore, it is expected that PSP will encounter CMEs with much higher speeds than those observed during the Helios mission. Also, the magnetic field, density and temperature values are expected to be much larger than in the average solar wind in individual fast-shock-associated CME events. PSP will thus also substantially improve our understanding of the near-Sun evolution of CMEs and their expansion with radial distance.

With the resulting CGAUSS empirical solar-wind model for PSP, the following main results for the bulk solar-wind parameters and estimations for their median values at PSP's first perihelion in 2018 at a solar distance of 0.16 au and at PSP's closest perihelia beginning in 2024 at 0.046 au ( $9.86 R_{\odot}$ ) are obtained:

- The dependency of the magnetic field strength on solar activity and radial distance appears to be valid above  $20 R_{\odot}$ ,

however near PSP's closest perihelia, the actual values might be found to be slightly higher.

- The estimated magnetic field strength median values obtained from relation (12) for PSP's 1st and 22nd perihelion are 87 nT and 943 nT.
- The radial dependencies of the proton velocity median values for slow and fast solar wind (14) appear to be valid above about  $20 R_{\odot}$  solar distance; below they overestimate the actual solar-wind velocities obtained from remote measurements. The share of their frequency distributions to the overall solar-wind velocity distribution (5) depends on solar activity with their balance relation (16). Thus, at solar minimum, with a SSN of around zero, the slow-wind component contributes about 64% and drops to 28% during solar maximum conditions with a SSN around 200.
- The calculated median velocity values for PSP's 1st and 22nd perihelion are  $340 \text{ km s}^{-1}$  and  $290 \text{ km s}^{-1}$ .
- The proton density relation appears to be valid throughout the full PSP orbital distance range, even down to about  $8 R_{\odot}$ .
- The estimated density median values obtained from relation (17) for PSP's 1st and 22nd perihelion are  $214 \text{ cm}^{-3}$  and  $2951 \text{ cm}^{-3}$ .
- The derived correlation function for the proton temperature appears to provide overly high temperature values around PSP's closest perihelion in comparison to coronal measurements.
- The estimated temperature median values obtained from relation (19) for PSP's 1st and 22nd perihelion are 503 000 K and 1 930 000 K.

The results of the modeled solar-wind environment will be useful to help optimize the WISPR and in situ instrument science plannings and PSP mission operations. This also applies for the Heliospheric Imager (SoloHI; Howard et al. 2013) and the in situ instruments on board the Solar Orbiter spacecraft.

**Acknowledgements.** The authors acknowledge support of the Coronagraphic German and US SolarProbePlus Survey (CGAUSS) project for WISPR by the German Aerospace Center (DLR) under grant 50 OL 1601 as national contribution to the Parker Solar Probe mission. The authors thank the Helios and OMNI PIs/teams for creating and making available the solar-wind in situ data. The Helios and the OMNI data are supplied by the NASA Space Science Data Coordinated Archive and the Space Physics Data Facility at NASA's Goddard Space Flight Center. Additional thanks for maintaining and providing the international sunspot number series goes to the World Data Center – Sunspot Index and Long-term Solar Observations at the Solar Influences Data Analysis Center, Royal Observatory of Belgium. The PSP SPICE kernel was kindly provided by Angelos Vourlidas. The authors thank the referee for the careful review of this manuscript and helpful comments and suggestions.

## References

- Bale, S. D., Goetz, K., Harvey, P. R., et al. 2016, *Space Sci. Rev.*, 204, 49
- Balogh, A., Bothmer, V., Crooker, N. U., et al. 1999, *Space Sci. Rev.*, 89, 141
- Banaszkiewicz, M., Axford, W. I., & McKenzie, J. F. 1998, *A&A*, 337, 940
- Belcher, J. W., Slavin, J. A., Armstrong, T. P., et al. 1991, Mercury Orbiter: Report of the Science Working Team (Washington, United States)
- Biermann, L. 1951, *ZAp*, 29, 274
- Billings, D. E. 1959, *ApJ*, 130, 961
- Bothmer, V., & Daglis, I. A. 2007, *Space Weather – Physics and Effects* (Praxis Publishing)
- Bothmer, V., & Schwenn, R. 1996, *Adv. Space Res.*, 17, 319
- Bothmer, V., & Schwenn, R. 1998, *Annales Geophysicae*, 16, 1
- Bougeret, J.-L., King, J. H., & Schwenn, R. 1984, *Sol. Phys.*, 90, 401
- Bruno, R., Villante, U., Bavassano, B., Schwenn, R., & Mariani, F. 1986, *Sol. Phys.*, 104, 431
- Burt, J., & Smith, B. 2012, in IEEE Aerospace Conference, 1
- Colin, L. 1980, *J. Geophys. Res.*, 85, 7575
- Domingo, V., Fleck, B., & Poland, A. I. 1995, *Sol. Phys.*, 162, 1
- Exarhos, G., & Moussas, X. 2000, *A&A*, 356, 315

- Feldman, W. C., Asbridge, J. R., Bame, S. J., & Gosling, J. T. 1978, *J. Geophys. Res.*, **83**, 2177
- Forsyth, R. J., Bothmer, V., Cid, C., et al. 2006, *Space Sci. Rev.*, **123**, 383
- Fox, N. J., Velli, M. C., Bale, S. D., et al. 2016, *Space Sci. Rev.*, **204**, 7
- Goelzer, M. L., Schwadron, N. A., & Smith, C. W. 2014, *J. Geophys. Res. (Space Phys.)*, **119**, 115
- Gosling, J. T., Hildner, E., MacQueen, R. M., et al. 1974, *J. Geophys. Res.*, **79**, 4581
- Gringauz, K. I., Bezrokhikh, V. V., Ozerov, V. D., & Rybchinskii, R. E. 1960, *Soviet Physics Doklady*, **5**, 361
- Gurnett, D. A., Kurth, W. S., Burlaga, L. F., & Ness, N. F. 2013, *Science*, **341**, 1489
- Hathaway, D. H., & Upton, L. A. 2016, *J. Geophys. Res. (Space Phys.)*, **121**, 10
- Hellinger, P., Matteini, L., Štverák, Š., Trávníček, P. M., & Marsch, E. 2011, *J. Geophys. Res. (Space Phys.)*, **116**, A09105
- Hellinger, P., Trávníček, P. M., Štverák, Š., Matteini, L., & Velli, M. 2013, *J. Geophys. Res. (Space Phys.)*, **118**, 1351
- Howard, R. A., Vourlidas, A., Korendyke, C. M., et al. 2013, in *Solar Physics and Space Weather Instrumentation V*, *Proc. SPIE*, **8862**, 88620
- Kasper, J. C., Stevens, M. L., Korreck, K. E., et al. 2012, *ApJ*, **745**, 162
- Kasper, J. C., Abiad, R., Austin, G., et al. 2016, *Space Sci. Rev.*, **204**, 131
- Katsikas, V., Exarhos, G., & Moussas, X. 2010, *Adv. Space Res.*, **46**, 382
- Kilpua, E. K. J., Madjarska, M. S., Karna, N., et al. 2016, *Sol. Phys.*, **291**, 2441
- King, J. H., & Papitashvili, N. E. 2005, *J. Geophys. Res. (Space Phys.)*, **110**, A02104
- Lazarus, A. J. 2000, *Science*, **287**, 2172
- Leblanc, Y., Dulk, G. A., & Bougeret, J.-L. 1998, *Sol. Phys.*, **183**, 165
- Lepping, R. P., Acuña, M. H., Burlaga, L. F., et al. 1995, *Space Sci. Rev.*, **71**, 207
- Liebenberg, D. H., Bessey, R. J., & Watson, B. 1975, *Sol. Phys.*, **44**, 345
- Mariani, F., Ness, N. F., Burlaga, L. F., Bavassano, B., & Villante, U. 1978, *J. Geophys. Res.*, **83**, 5161
- McComas, D. J., Bame, S. J., Barraclough, B. L., et al. 1998, *Geophys. Res. Lett.*, **25**, 1
- McComas, D. J., Acton, L. W., Balat-Pichelin, M., et al. 2008, *Solar Probe Plus: Report of the Science and Technology Definition Team*, Tech. Rep. NASA/TM-2008-214161, National Aeronautics and Space Administration, Goddard Space Flight Center, Greenbelt, MD
- McComas, D. J., Alexander, N., Angold, N., et al. 2016, *Space Sci. Rev.*, **204**, 187
- McGregor, S. L., Hughes, W. J., Arge, C. N., Odstreil, D., & Schwadron, N. A. 2011a, *J. Geophys. Res. (Space Phys.)*, **116**, A03106
- McGregor, S. L., Hughes, W. J., Arge, C. N., Owens, M. J., & Odstreil, D. 2011b, *J. Geophys. Res. (Space Phys.)*, **116**, A03101
- Müller, D., Marsden, R. G., St. Cyr, O. C., & Gilbert, H. R. 2013, *Sol. Phys.*, **285**, 25
- Neugebauer, M., & Snyder, C. W. 1966, *J. Geophys. Res.*, **71**, 4469
- Ogilvie, K. W., Chornay, D. J., Fritzenreiter, R. J., et al. 1995, *Space Sci. Rev.*, **71**, 55
- Parker, E. N. 1958, *ApJ*, **128**, 664
- Richardson, I. G., & Cane, H. V. 2012, *J. Space Weather and Space Climate*, **2**, A2
- Rosenbauer, H., Schwenn, R., Marsch, E., et al. 1977, *J. Geophys. Res. Geophysik*, **42**, 561
- Russell, C. T., Mewaldt, R. A., Luhmann, J. G., et al. 2013, *ApJ*, **770**, 38
- Sachdeva, N., Subramanian, P., Vourlidas, A., & Bothmer, V. 2017, *Sol. Phys.*, **292**, 118
- Sanchez-Diaz, E., Rouillard, A. P., Lavraud, B., et al. 2016, *J. Geophys. Res. (Space Phys.)*, **121**, 2830
- Schwenn, R. 1983, in *NASA Conference Publication*, 228
- Schwenn, R. 1990, *Large-Scale Structure of the Interplanetary Medium*, eds. R. Schwenn, & E. Marsch (Berlin, Heidelberg: Springer), 99
- Sheeley, Jr., N. R., Howard, R. A., Michels, D. J., et al. 1985, *J. Geophys. Res.*, **90**, 163
- Sheeley, N. R., Wang, Y.-M., Hawley, S. H., et al. 1997, *ApJ*, **484**, 472
- SILSO World Data Center 1963–2016, *International Sunspot Number Monthly Bulletin and online catalogue*
- Sittler, Jr., E. C., & Guhathakurta, M. 1999, *ApJ*, **523**, 812
- Smith, E. J., & Balogh, A. 2003, in *Solar Wind Ten*, eds. M. Velli, R. Bruno, F. Malara, & B. Bucci, *AIP Conf. Ser.*, **679**, 67
- Stone, E. C., Frandsen, A. M., Mewaldt, R. A., et al. 1998, *Space Sci. Rev.*, **86**, 1
- Veselovsky, I. S., Dmitriev, A. V., & Suvorova, A. V. 2010, *Cosmic Research*, **48**, 113
- Vourlidas, A., Howard, R. A., Plunkett, S. P., et al. 2016, *Space Sci. Rev.*, **204**, 83
- Wang, Y.-M., Sheeley, N. R., Socker, D. G., Howard, R. A., & Rich, N. B. 2000, *J. Geophys. Res.*, **105**, 25133



## 7 Conclusions

In this work I addressed solar wind problems relevant to space weather and to the Parker Solar Probe mission. Predictive models related to solar wind were developed in both studies. In the first study, I modeled the impact of solar wind and CMEs on geomagnetic activity, and in the second study I developed an empirical solar wind model for the inner heliosphere. Here, I briefly summarize the principal results and conclusions of both studies and give an outlook on further objectives based on this work.

### 7.1 Geomagnetic impact of the solar wind

This study, presented in [Chapter 4](#), estimates the impact of solar wind on the planetary geomagnetic disturbance indicator  $Kp$  and predicts it for CMEs and streams in particular. The analyses are based on 35 years (1981–2016) of near-Earth solar wind data from the minutely OMNI data set and  $Kp$  data from the GFZ Potsdam. The separation into CME and stream data is done via the Solar Wind Structures list created by [Richardson et al. \(2000\)](#). The CME data consists of CME-associated flows, including leading compressed material, and the stream data consists of a mixture of slow and fast wind, including interaction regions. The solar wind electric field proxy  $vB_z$ , the velocity of CMEs, and the velocity of streams were each correlated with the  $Kp$  index. Empirical dependencies were determined from the mean values of the relative  $Kp$  frequency distributions. Functional relations were derived by fitting logarithmic functions to these mean  $Kp$  values. The obtained  $Kp$  relations were evaluated for their prediction performance. The resulting predictive models are presented in the following and the conclusions thereafter.

- The functional dependency of the yearly  $Kp$  average on the SSN of the previous year is

$$Kp(ssn) = 0.281 \cdot \ln(ssn) + 1.05.$$

The associated  $Kp$  error is approximately 0.3 but seasonal effects add yearly variations with a  $Kp$  magnitude of up to 1.3.

- The two-part relation of the  $Kp$  index with the 3-hour minima of the solar wind electric field proxy  $vB_z$  is

$$Kp(vB_z) = \begin{cases} Kp_-(vB_z) & \text{for } (vB_z + 163) < 0, \\ Kp_+(vB_z) & \text{for } (vB_z + 163) \geq 0, \end{cases}$$

with  $vB_z$  in units of  $[\text{km s}^{-1} \text{ nT}]$ . The individual parts are derived to be

$$\begin{aligned} Kp_-(vB_z) &= 1.258 \cdot \ln((vB_z + 163)^2 + 1.416 \times 10^6) - 17.04, \\ Kp_+(vB_z) &= 0.467 \cdot (Kp_-(vB_z) - Kp_-(-163)) + Kp_-(-163). \end{aligned}$$

The mean absolute deviation (MAD) of this relation has a mean  $Kp$  size of 0.7. This relation provides proper predictions, that is, significantly better than random, in the  $Kp$  range from 1.0 to 8.7.

- The relation between the  $Kp$  index and the 3-hour velocity maxima of CME-associated flows, including shocked and compressed solar wind plasma, is

$$Kp_{\text{CME}}(v) = 10.6 \cdot \ln(v + 810) - 73,$$

with the velocity in units of  $[\text{km s}^{-1}]$ . Its MAD has a mean  $Kp$  size of about 1.1. This relation has a proper prediction range between a  $Kp$  of 1.3 and 6.3. Strong geomagnetic storms exceeding  $Kp = 7.0$  are being underestimated on average by about 3  $Kp$  values.



- The empirical relation between the  $Kp$  index and the 3-hour velocity maxima of solar wind streams, including fast and slow wind and interaction regions, is

$$Kp_{\text{Stream}}(v) = 5.88 \cdot \ln(v + 299) - 37.0,$$

with the velocity in units of  $[\text{km s}^{-1}]$ . Its MAD has a mean  $Kp$  size of about 0.7. This relation has a proper  $Kp$  range of 0.3–4.3. This is well below the threshold of geomagnetic storms ( $Kp = 5$ ), and thus the relation is good in predicting lower geomagnetic activity but not storms.

The correlations between  $Kp$  and the solar wind electric field and velocity were done separately for high-resolution solar wind data that was processed in a different manner, that is, 3-hour averages and 3-hour extrema. The processing of 3-hour  $vB_z$  minima leads to a significantly higher correlation coefficient as compared with the 3-hour averages ( $r_{\min} = -0.72$  versus  $r_{\text{avg}} = -0.36$ ), whereas correlating 3-hour velocity maxima results in nearly the same correlation as 3-hour averages ( $r_{\max} = 0.622$  versus  $r_{\text{avg}} = 0.613$ ). These findings support the notions that averaging over 3-hour intervals leads to short-term geoeffective features in the magnetic field  $z$ -component being missed, and that the magnetosphere indeed responds directly to short-term solar wind variations in the order of minutes. Thus, for an efficient  $Kp$  prediction via  $vB_z$ , it is of key importance to capture the magnetic features by using 3-hour minima of high-resolution data. As short-term variations in  $B_z$  cannot yet be predicted from remote observations, the solar wind electric field is not well suited as a basis for remote forecast situations. In contrast, as the underlying data resolution makes no difference for the solar wind velocity, it is best suited for remote forecast situations.

The  $Kp$  predictive models derived from CME and stream velocity show a significant difference in magnitude and in trend – their initial separation of about 1  $Kp$  value grows slightly at higher velocities. This confirms the initial assumption that the isolated treatment of CME and stream velocities is beneficial for the prediction accuracy of the  $Kp$  index. Both relations are derived from velocity data that is below  $1100 \text{ km s}^{-1}$ . Assuming the CME relation holds true for even higher speeds, an extension could predict the geomagnetic impact of faster CMEs as well. However, the maximum  $Kp$  of 9.0 is reached at a CME velocity of  $1500 \text{ km s}^{-1}$ .

The derived predictive models are based on the velocity and the magnetic field  $z$ -component, which comprise only a fraction of the relevant solar wind–magnetosphere coupling parameters. The evaluation of their prediction performance shows that they indeed cannot compete with models based on full-fledged solar wind coupling functions, nor with current prediction models based on artificial neural networks. That said, the models perform well for what they represent and they still enable empirical estimations of the average geomagnetic activity for special space weather forecast situations.  $Kp$  can directly be quantified from in-situ measurements of the solar wind electric field. As early predictions of CME and stream magnetic fields obtained from remote observations are currently either non-existent or come with high uncertainties,  $Kp$  relations, derived exclusively for the arrival velocities of CMEs and streams, are provided.

**Outlook.** Many questions remain unanswered regarding the relationship between solar wind properties and  $Kp$  index: Would an even higher time resolution in the order of seconds further resolve these short-term geoeffective magnetic features and subsequently enhance the  $Kp$  predictions? Are there other ways of data processing that can achieve even higher correlations with  $Kp$ ? It would be interesting to uncover to what extent full-fledged coupling functions, such as Newell’s universal coupling function, are impacted by the underlying processing of the high-resolution data.

The ground geomagnetic disturbances, generated by rare and extremely fast CME events with velocities above  $1500 \text{ km s}^{-1}$ , may be resolved and estimated by redefining and extending the conversion between the  $Kp$  and  $ap$  indices.  $Kp$  is connected to the ground disturbance field strength at the  $\pm 50^\circ$  latitudes via the equivalent  $ap$  index. By extending the derived  $Kp$  relations above 9.0, the absolute field disturbances at the ground can be estimated.

Smaller-scale solar wind structures, such as CIRs and HCSs, may be isolated for their  $Kp$  impact. The CME-associated flows can be filtered into their substructures, such as the compressed solar wind plasma and the MC plasma, and their  $Kp$  impact evaluated individually.

Spacecraft missions positioned at special locations would be beneficial for earlier and more accurate space weather forecasting. Suggested locations are sub-L1, a position slightly closer to the Sun than L1 which would enable earlier warnings from in-situ solar wind and CME measurements, and L5, which would provide early CME velocity and arrival time warnings from coronagraph images (Vourlidas 2015), similar to what the STEREO mission achieved at this position.

## 7.2 Sun–Earth evolution of the solar wind

This study is presented in [Chapter 5](#), however, its essential portion is published in [Venzmer & Bothmer \(2018\)](#), which is included as [Chapter 6](#) in this thesis. The study builds an empirical solar wind model for the inner heliosphere restricted to the ecliptic, which accounts for the variations of the solar activity cycle and for solar distance. In order to obtain empirical estimates of the solar wind environment the PSP spacecraft is to encounter, this solar wind model is extrapolated down to PSP’s planned near-Sun perihelia and also considers the expected solar activity during PSP’s mission. The final model consists of individual sub-models that consider the solar wind parameters magnetic field strength, proton velocity, density, and temperature. The sub-models are composed of empirically determined frequency distributions that are being shifted with solar distance and solar activity.

The parameters’ frequency distributions were obtained from 53 years (1963–2016) of near-Earth solar wind measurements from the hourly OMNI data set. Analytical representations of the frequency distributions were derived and were fitted with lognormal functions except for the velocity, whose fast and slow regimes were considered by using a double lognormal distribution. The solar activity dependencies were derived from nearly five solar cycles of monthly SSN data. Solar wind measurements made by the Helios 1 and Helios 2 probes in the 1970s were analyzed to model the parameters’ solar distance scalings via power-law fits. The Helios data cover more than two thirds of the distance to the Sun (0.29–0.98 au). Furthermore, an alternative model for the magnetic field strength was derived, which changes the solar distance dependency to support a Parker magnetic field geometry. The obtained lognormal functions, SSN dependencies, and solar distance dependencies were combined to build models of the parameters that represent the solar activity and distance behavior. The near-Sun extrapolations of the resulting models were compared to existing studies that infer the local magnitude of the solar wind parameters from remote observations. Eventually, these empirical models were supplied with predictions of the SSN and extrapolated to the planned orbital trajectory of PSP.

The resulting models represent the frequency distributions of the solar wind parameters by lognormal functions, whose location and shape are defined by their median and mean. The derived relations for the median and mean values are a result of lognormal function fits and they deviate slightly from the actual median and mean values of the solar wind parameters. Thus, the derived relations are to be used as input to the lognormal function, Equation (4) in [Venzmer & Bothmer \(2018\)](#). The frequency distributions are being shifted by the median and mean relations, which depend on solar distance  $r$  measured in [au], and on solar activity measured via the SSN. The resulting relations and the predicted values for PSP’s first perihelion in November 2018 and its first closest perihelion in December 2024 are listed here.

- The relations for the median and mean of the magnetic field strength are:

$$\begin{aligned} B_{\text{med}}(\text{ssn}, r) &= (0.0131 \text{ nT} \cdot \text{ssn} + 4.29 \text{ nT}) \cdot r^{-1.66}, \\ B_{\text{avg}}(\text{ssn}, r) &= 1.0879 \cdot B_{\text{med}}(\text{ssn}, r). \end{aligned}$$

The estimated median value for PSP’s first perihelion is 87 nT and that for the first closest perihelion is 943 nT.

- An alternative relation for the field strength median has been derived, which considers the differing distance scaling of the individual vector components. The relation only differs in its solar distance dependency, that is, it accounts for the Parker field geometry:

$$B_{\text{med}}^{\text{Parker}}(\text{ssn}, r) = (0.0131 \text{ nT} \cdot \text{ssn} + 4.29 \text{ nT}) \cdot \sqrt{(r^{-1.858})^2 + (r^{-1.32})^2}.$$

This model neglects the azimuthal field component and assumes that the Parker spiral angle at 1 au has an average value of  $-45^\circ$  or  $135^\circ$ , corresponding to a constant solar wind velocity of  $414 \text{ km s}^{-1}$ . This model yields higher extrapolated near-Sun values than the simple power-law dependent model does. The estimated median value of 94 nT for PSP’s first perihelion is 8 % higher and the value of 1241 nT for the first closest perihelion is even 32 % higher.

- The model for the velocity distribution is built in a different way, combining two lognormal functions to consider for the slow and fast solar wind components (see the Equation (5) in [Venzmer & Bothmer](#)

2018). Here, the solar activity dependence is introduced by varying the share of both components and not by shifting their positions, that is, a balancing parameter depending on the SSN regulates the share of both components:

$$c(ssn) = -0.00180 \cdot ssn + 0.64.$$

As a result, the median and mean relations for both lognormal functions depend only on solar distance:

$$\begin{aligned} v_{\text{med}}^{\text{slow}}(r) &= 363 \text{ km s}^{-1} \cdot r^{0.099}, & v_{\text{med}}^{\text{fast}}(r) &= 483 \text{ km s}^{-1} \cdot r^{0.099}, \\ v_{\text{avg}}^{\text{slow}}(r) &= 1.0101 \cdot v_{\text{med}}^{\text{slow}}(r), & v_{\text{avg}}^{\text{fast}}(r) &= 1.023 \cdot v_{\text{med}}^{\text{fast}}(r). \end{aligned}$$

The estimated median value for PSP's first perihelion is  $340 \text{ km s}^{-1}$  and that for the first closest perihelion is  $290 \text{ km s}^{-1}$ .

- The derived median and mean relations for the density are:

$$\begin{aligned} n_{\text{med}}(ssn, r) &= (0.0038 \text{ cm}^{-3} \cdot ssn + 4.50 \text{ cm}^{-3}) \cdot r^{-2.11}, \\ n_{\text{avg}}(ssn, r) &= 1.305 \cdot n_{\text{med}}(ssn, r). \end{aligned}$$

The estimated median value for PSP's first perihelion is  $214 \text{ cm}^{-3}$  and that for the first closest perihelion is  $2951 \text{ cm}^{-3}$ .

- The derived median and mean relations for the temperature are:

$$\begin{aligned} T_{\text{med}}(ssn, r) &= (197 \text{ K} \cdot ssn + 5.73 \times 10^4 \text{ K}) \cdot r^{-1.10}, \\ T_{\text{avg}}(ssn, r) &= 1.654 \cdot T_{\text{med}}(ssn, r). \end{aligned}$$

The estimated median value for PSP's first perihelion is  $5.03 \times 10^5 \text{ K}$  and that for the first closest perihelion is  $1.93 \times 10^6 \text{ K}$ .

The IMF is known to conform to the Parker field geometry in the outer heliosphere, therefore, the predictions of the second IMF model are considered to be more reliable. The extrapolation of the velocity model to solar distances below  $20 R_{\odot}$  yields speeds that overestimate those obtained from remote observations. In particular, the estimated velocity for slow wind at  $10 R_{\odot}$  is about  $270 \text{ km s}^{-1}$ , whereas remote observations show velocities around  $200 \text{ km s}^{-1}$ . This indicates that solar wind acceleration takes place up to solar distances of  $20 R_{\odot}$ . Also, the near-Sun extrapolation of the temperature model overestimates its magnitude in comparison to coronal measurements, that is, temperatures of 2–3 MK are estimated for solar distances of  $10 R_{\odot}$ , whereas it is known that these temperatures already exist in the corona close to the Sun. This suggests that plasma heating takes place up to these solar distances. Thus, from the results presented in this study, I conclude that the regions where solar wind acceleration and heating occurs will indeed be probed by the PSP spacecraft. However, only the near-Sun in-situ measurements of PSP itself will ultimately reveal the accuracy of the solar wind model predictions.

*Outlook.* This work presents average predictions for the key solar wind parameters – predictions about the near-Sun properties of internal solar wind structures lie outside the scope of this thesis. Thus, further investigations should be done to extrapolate different solar wind structures as, for example, the properties of CMEs and MCs differ from those of the bulk solar wind distance scaling laws (Bothmer & Schwenn 1998). Furthermore, the dependence of the contribution of solar wind structures on solar activity can influence the derived fit parameters. In addition, a number of modifications could be integrated into the solar wind model, such as flux conservation, the IMF–velocity dependence, seasonal effects, and the distance behavior of different solar wind structure types.

To refine the distance dependency of the solar wind model in the Helios distance range, additional solar wind data could be included in the analyses. For example, data from the spacecraft Mariner 10 and MESSENGER that studied Mercury which has a perihelion distance of 0.3 au. Furthermore, the Solar Orbiter spacecraft, which is scheduled for launch in 2020, carries in-situ instruments as well. When reaching its operational orbit in 2023, it will provide more solar wind data from the solar distance range 0.28–0.9 au and from heliolatitudes up to  $\pm 25^\circ$ . Ultimately, the upcoming solar wind measurements made by PSP, beginning in November 2018 with its first perihelion at 0.16 au, can be integrated into the solar wind model to adjust its near-Sun part with empirical data.

## A Appendix

### A.1 Solar surface differential rotation

The differential rotation of the solar surface is visible from sunspot observations and was first discovered by [Scheiner \(1630\)](#). It is caused by transport of angular momentum away from the rotation axis due to the Sun's inner thermal convective circulation.

[Bartels \(1934\)](#) set the average synodic solar rotation period to 27 days for the definition of his solar rotation number. The Bartels Rotation Number counts the solar rotations starting with 8 February 1832. Later, Carrington determined a more accurate average solar rotation period of 27.2753 days, which is valid for solar latitudes of  $\pm 16^\circ$ , where sunspots usually are found. He defined the Carrington Rotation Number based upon this period, starting with 9 November 1853.

The Sun's sidereal differential angular velocity can be approximated by the function ([Beck 2000](#)):

$$\omega_{\odot}(\theta) = \omega_{\text{eq}} + B \sin^2(\theta) + C \sin^4(\theta), \quad (\text{A.1})$$

with the heliolatitude  $\theta$ , the equatorial angular velocity  $\omega_{\text{eq}} = 14.37^\circ \text{d}^{-1}$ , and the coefficients  $B = -2.33^\circ \text{d}^{-1}$  and  $C = -1.56^\circ \text{d}^{-1}$ . I plot this function in [Figure A.1](#) for illustration. Thus, the solar equatorial sidereal rotation period is  $T_{\odot}^{\text{eq}} = 25.05 \text{ d}$  and the synodic period is

$$\begin{aligned} T_{\odot}^{\text{eq, syn}} &= \left( \frac{1}{T_{\odot}^{\text{eq}}} - \frac{1}{T_{\text{E}}} \right)^{-1} \\ &= 26.90 \text{ d}, \end{aligned} \quad (\text{A.2})$$

with a Julian year as the Earth's orbital rotation period,  $T_{\text{E}} = 365.25 \text{ d}$ .

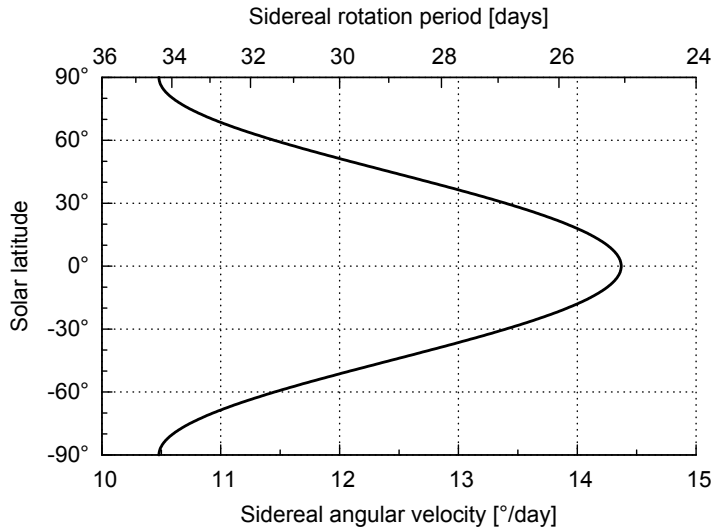


**Figure A.1** Diagram showing the angular velocity of the sidereal solar surface differential rotation over solar latitude. The upper x-axis shows the corresponding sidereal rotation period.

The differential rotation differs locally in the different surface structures, such as sunspots and CHs. The angular velocity slows down with sunspot age and changes with how deep the structure is rooted in the interior ([Pulkkinen & Tuominen 1998](#)). The average differential rotation profile is asymmetric in both hemispheres and also varies slightly with solar activity. Thus, [Equation A.1](#) is not a definite function, in fact, the average rotation rate is even observed to slow down during the last couple of solar cycles.

## A.2 Electric field at the magnetopause

The Lorentz force law defines the electric and magnetic field vectors  $\mathbf{E}$  and  $\mathbf{B}$ :

$$\mathbf{F} = q(\mathbf{E} + \mathbf{v} \times \mathbf{B}). \quad (\text{A.3})$$

The equation describes the force  $\mathbf{F}$  that acts on a charge  $q$  with velocity  $\mathbf{v}$ . The full Ohm's law accounts for the Lorentz force:

$$\mathbf{j} = \sigma(\mathbf{E} + \mathbf{v} \times \mathbf{B}) \quad \Longleftrightarrow \quad \mathbf{E} = -\mathbf{v} \times \mathbf{B} + \frac{\mathbf{j}}{\sigma}.$$

Solar wind is often approximated as an ideal magnetohydrodynamic (MHD) plasma having an infinite conductivity ( $\sigma = \infty$ ). In this case electric fields do not generate electric currents ( $\mathbf{j}/\sigma = 0$ ):

$$\mathbf{E} = -\mathbf{v} \times \mathbf{B}. \quad (\text{A.4})$$

Assuming a strictly radial solar wind flow, that is, in x-direction when using GSM coordinates ( $v_y = v_z = 0$ ), the resulting electric field components become

$$\mathbf{E} = \begin{bmatrix} 0 \\ -v_x \cdot B_z \\ v_x \cdot B_y \end{bmatrix}. \quad (\text{A.5})$$

Reconnection occurs where the magnetic fields of the solar wind and magnetopause are antiparallel. Due to the magnetosphere's dipole topology, the magnetospheric field is always orientated along the GSM z-axis at the equator and central meridian of the sunward magnetopause ( $B_y = 0$ ). In this region, the only remaining electric field component that contributes is

$$E_y = -v_x \cdot B_z. \quad (\text{A.6})$$

At the rest of the magnetopause surface facing the solar wind, the magnetospheric field deviates from the z-direction, in particular at higher latitudes. However, reconnection can occur there too if the solar wind magnetic field clock angle is oriented accordingly, see also [Figure 2.29](#). Thus, it makes sense to use the magnetic field's clock angle, which is defined as  $\theta_c = \tan^{-1}(B_y/B_z)$ , instead of just the field's  $B_z$  component. The electric field becomes then

$$\mathbf{E} = \begin{bmatrix} 0 \\ -v_x \cdot |\mathbf{B}_{yz}| \cdot \cos(\theta_c) \\ v_x \cdot |\mathbf{B}_{yz}| \cdot \sin(\theta_c) \end{bmatrix}, \quad (\text{A.7})$$

with  $E_y$  containing the half-wave rectifier, see also [Figure 2.35](#).

## A.3 Plasma beta

The thermal pressure of a plasma is defined as  $p = nk_B T$ , with the number density  $n$  and the Boltzmann constant  $k_B$ . However, according to MHD, the magnetic energy density  $w_{\text{mag}} = B^2/(2\mu_0)$ , with the magnetic field strength  $B$  and the permeability constant  $\mu_0$ , behaves like an additional pressure that adds to the thermal pressure of a plasma ([Kivelson & Russell 1995](#), p. 50). The ratio of the thermal pressure to the magnetic pressure determines the behavior of the plasma. If the thermal pressure dominates the magnetic pressure (warm plasma), the plasma movements transport the magnetic field, else the plasma movements are guided by the magnetic field lines (cold plasma). This ratio is called plasma beta:

$$\begin{aligned} \beta &= \frac{p}{p_{\text{mag}}} \\ &= \frac{2\mu_0 n k_B T}{B^2}. \end{aligned} \quad (\text{A.8})$$

The plasma at the photosphere has typical beta values around 14 and that of the low corona around 0.2 ([Gary 2001](#)). Further up, beta rises again and the region where it equals 1 is defined as the source surface for the solar wind ([Schatten et al. 1969](#)). This surface is typically located at about  $1.2\text{--}2.5 R_\odot$  ([Gary 2001](#)).

The solar wind usually has plasma beta values higher than 1 – the solar magnetic field is carried away into the heliosphere. Together with the solar rotation, this effect creates the spiral form of the interplanetary magnetic field (Parker spiral). Yet in some solar wind structures, such as magnetic clouds,  $\beta \ll 1$  and thus the magnetic field can still contain the plasma. Indeed, a change in plasma beta is a good predictor for the location of magnetic flux ropes in CME structures ([Riley & Richardson 2013](#); [Savani et al. 2013](#)).



## A.4 Alfvén velocity

The incompressible wave mode within MHD plasmas, the shear Alfvén wave, consists of periodic disturbances in the magnetic field orthogonal to its direction (Alfvén 1942). Alfvén waves are prevalent in open coronal regions and therefore occur in fast solar wind (Cranmer & van Ballegoijen 2005). Their propagation velocity is an important parameter to characterize a plasma. In an ideal incompressible MHD plasma (viscosity  $\mu = 0$  and electrical conductivity  $\sigma = \infty$ ) the kinetic and magnetic energy density are of equal value (Kivelson & Russell 1995, p. 51):

$$w_{\text{kin}} = w_{\text{mag}} \quad \Longleftrightarrow \quad \frac{\rho v^2}{2} = \frac{B^2}{2\mu_0},$$

with the permeability constant  $\mu_0$  and the total mass density  $\rho$  of the charged plasma particles. Thus, the Alfvén velocity can be calculated via

$$v_A = \frac{|B|}{\sqrt{\mu_0 \rho}}. \quad (\text{A.9})$$

The wave's phase velocity is  $v_{\text{ph}} = v_A \cdot \cos(\alpha)$ , with  $\alpha$  as the angle between wave propagation direction and magnetic field line, that is, Alfvén waves travel along magnetic field lines. They consist of periodic disturbances in the magnetic field, the electric field, the plasma velocity, and the current density. Plasma density, pressure, and magnetic field magnitude are not affected by them.

Additionally, there exist two types of compressional wave modes within MHD plasmas, the fast-mode wave and the slow-mode wave. The phase speeds of the three MHD waves meet  $v_{\text{fast}} \geq v_A \geq v_{\text{slow}}$  (Kivelson & Russell 1995, p. 52). The solar distance where the solar wind speed exceeds the Alfvén speed is called the Alfvén critical surface. It lies on average around  $17 R_\odot$  (Sittler & Guhathakurta 1999; Exarhos & Moussas 2000). Within solar wind at 1 au, the typical frequency of Alfvén waves is 1–4 per hour and their average velocity is  $v_A = 56.8 \text{ km s}^{-1}$  (Veselovsky et al. 2010).

## A.5 Sun–Earth distance and rotation axes tilt

All interactions between Sun and Earth are governed by the geometry of Earth's orbit and the orientations of both bodies' rotation axes. The Earth orbit defines the ecliptic plane which is a convenient reference base for a few coordinate systems, see Appendix A.6.

The Sun–Earth distance can be derived from the orbital parameters of Earth<sup>1</sup>, the semimajor axis  $a = 1 \text{ au}$  and the eccentricity  $e = 0.0167$ . Hence, the perihelion and aphelion distances are:

$$\begin{aligned} r_p &= a(1 - e) & \text{and} & & r_a &= a(1 + e) \\ &= 0.9833 \text{ au}, & & & &= 1.0167 \text{ au}, \end{aligned}$$

The exact solar distance at a given point in time can be obtained from the HORIZONS online ephemeris system<sup>2</sup>, hosted by the Solar System Dynamics group at NASA's Jet Propulsion Laboratory. In the year 2017, the Earth's perihelion was on 5 January. The cosine approximation

$$r_E(t) = 1 - 0.0167 \cdot \cos\left(2\pi\left(t - 2017 - \frac{5}{365}\right)\right), \quad (\text{A.10})$$

with  $t$  in years, suffices for the plot of the seasonal changes in Earth's solar distance presented in Figure A.2. The total distance variation of 3.34 % has implications for the magnitude of the solar wind quantities measured at Earth, as most of them follow a power law distance dependency. Thus for example, the density varies about 6.7 % between summer and winter because it scales with  $r^{-2}$ .

The heliosphere is structured by the orientation of the solar rotation axis, e.g., the overall solar wind properties change with angular distance from the solar equator. The solar equator is inclined to the ecliptic (Carrington 1863, p. 13) by  $i_\odot = 7.25^\circ$  (Russell 1971). Thus, viewed from Earth, the projected solar rotation axis tilt angle varies as the Earth is moving on its orbit. The seasonal change is plotted in Figure A.2, where the projected tilt at a given time is calculated by modulating  $i_\odot$  with a sine, using the equation in Hapgood (1992) and the time of vernal equinox. The projected tilt is zero at the equinoxes – the vernal equinox in 2016 was on 20 March.

<sup>1</sup>NASA/JPL Solar System Dynamics, Keplerian Elements: [https://ssd.jpl.nasa.gov/?planet\\_pos](https://ssd.jpl.nasa.gov/?planet_pos)

<sup>2</sup>NASA/JPL HORIZONS Web-Interface: <http://ssd.jpl.nasa.gov/horizons.cgi>

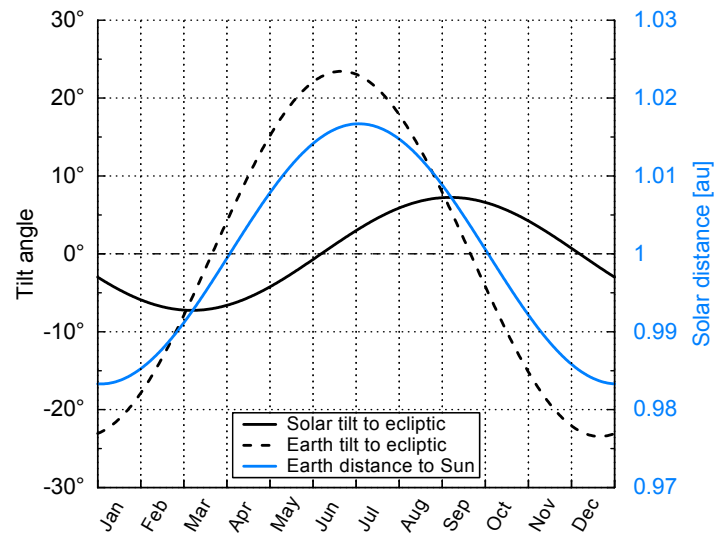


**Figure A.2** Seasonal changes of the Sun's and the Earth's tilt angles to the ecliptic and of the Earth's solar distance. The curves are approximated with trigonometric functions.

The orientation of the Earth's rotation axis to the Sun defines the solar wind flow angle onto the magnetosphere. The Earth's obliquity of the ecliptic is  $23.44^\circ$  (Luzum et al. 2011) and the resulting seasonal variation, seen in Figure A.2, influences the solar wind coupling efficiency with the magnetosphere and is reflected in geomagnetic activity as well.

## A.6 GSE, GSM, and HGI coordinate systems

A wise choice of coordinate system often eases the understanding and the calculation of a given problem, notably in geo- and astrophysics there exist an abundance of different coordinate systems. The coordinate systems used in this work are Earth- and Sun-centered and are described in the following. Three different Cartesian systems are applied: GSE, GSM, and HGI coordinates.

### Geocentric Solar Ecliptic coordinates

The Geocentric Solar Ecliptic (GSE) coordinates are centered at Earth and oriented with the ecliptic plane. The system's x-axis points in direction of the Sun and its z-axis in direction of the ecliptic north pole (Russell 1971; Hapgood 1992). The y-axis completes the right-handed orthogonal system. Thus compared to a fixed coordinate system, the GSE system completes one rotation around its z-axis per year.

GSE coordinates are preferably used when looking at near-Earth solar wind measurements, e.g., in this work they are applied for plotting the ACE solar wind measurements in Figures 2.14 and 2.22.

### Geocentric Solar Magnetospheric coordinates

The Geocentric Solar Magnetospheric (GSM) coordinates are also centered at Earth but oriented with its magnetic dipole axis. The x-axis points in direction of the Sun and the z-axis is parallel to the projection of the magnetic dipole axis on the plane normal to the x-axis (Russell 1971; Hapgood 1992). Its direction is towards the negative magnetic pole located near the geographic North Pole. The dipole axis is defined by the centered geomagnetic dipole which is the best approximation to the International Geomagnetic Reference Field (Thébault et al. 2015). Again, the y-axis completes the right-handed orthogonal system. Relative to the GSE system, the GSM system shows a wobbling rotation around its x-axis. The amplitude varies in time and is derived by the tilt of the Earth's rotation axis to the ecliptic normal ( $23.44^\circ$ ) and the tilt of the dipole axis, which itself slightly changes over the years. Most of the last century, the tilt had an angle near  $11.5^\circ$  from the geographic poles, yet the current (2015) angular distance is  $9.53^\circ$  (Thébault et al. 2015).

GSM coordinates are useful in problems regarding the magnetosphere. These coordinates are applied throughout Chapter 4.

## Heliographic Inertial coordinates

The Heliographic Inertial (HGI) coordinates are centered at the Sun and oriented with its rotation axis. The z-axis points northward parallel to the Sun's rotation axis. The x-axis is parallel to the intersection line between the solar equatorial plane and the ecliptic plane (Burlaga 1984), which are inclined by  $7.25^\circ$ . This x-axis points to the longitude of the ascending node which was at  $74.367^\circ$  on 1 January 1900 at 12:00 UT, but increases slowly with time (about  $1.4^\circ$  per century) due to the Earth's precession<sup>3</sup>. The y-axis completes the right-handed orthogonal system. Over one year, the position of Earth oscillates within an HGI latitude range of  $\pm 7.25^\circ$ .

HGI coordinates are useful when looking at processes concerning the solar wind in the heliosphere. These coordinates are applied for the processing of the Helios data, e.g., in Figures 3.7 and 3.8.

## A.7 True skill statistic

The true skill statistic (TSS) or true skill score is a means for measuring the predictive value of a variable. It was developed by Hanssen & Kuipers (1965) for evaluating different predictors for rain and dry weather conditions. Therefore it is also often called the Hanssen-Kuipers skill score or the Hanssen-Kuipers discriminant. As with other skill scores, the TSS is based on a  $2 \times 2$  contingency table that categorizes forecasted and observed events, see the Table A.1. The following ratios, derived from this kind of table, reveal relevant information about the

**Table A.1** Generic contingency table for categorizing forecasted and observed events. The designations for the event counts are given in parentheses.

		Observed	
		Yes	No
Forecasted	Yes	Hit ( $n_H$ )	False alarm ( $n_{FA}$ )
	No	Miss ( $n_M$ )	Correct null ( $n_{CN}$ )

forecast quality (Doswell et al. 1990): The proportion of correct predictions

$$PC = \frac{n_H + n_{CN}}{n_H + n_{FA} + n_M + n_{CN}}, \quad (\text{A.11})$$

the probabilities of detection and of false detection (i.e., the hit rate and the false alarm rate)

$$POD = \frac{n_H}{n_H + n_M} \quad \text{and} \quad POFD = \frac{n_{FA}}{n_{FA} + n_{CN}},$$

as well as the false alarm and detection failure ratios

$$FAR = \frac{n_{FA}}{n_{FA} + n_H} \quad \text{and} \quad DFR = \frac{n_M}{n_M + n_{CN}}.$$

The TSS is the difference between the hit rate and the false alarm rate<sup>4</sup> and thus it is calculated as follows (Hanssen & Kuipers 1965, Eq. 15):

$$\begin{aligned} TSS &= POD - POFD \\ &= \frac{n_H \cdot n_{CN} - n_{FA} \cdot n_M}{(n_H + n_M)(n_{FA} + n_{CN})}. \end{aligned} \quad (\text{A.12})$$

Its value is in the range from  $-1$  to  $1$ , with  $1$  representing an ideal prediction,  $0$  a random prediction, and  $-1$  an ideal negative prediction. The TSS is positive if the hit rate is higher than the false alarm rate.

In the case of rare event forecasting, the contingency table is dominated by correct nulls and the TSS approaches the hit rate. Doswell et al. (1990) show that the Heidke skill score is superior in these situations, in that it considers correct null forecasts in a controlled way. They recommend to use the Heidke skill score in preference to TSS for rare event forecasting. Other often applied skill scores are the threat score, also called critical success index or Gilbert score, and the equitable threat score. However, the TSS is commonly applied to evaluate and compare space weather prediction methods, particularly in forecasting the  $K_p$  index (Detman & Joselyn 1999; Wing et al. 2005; Savani et al. 2017). The TSS is used in the verification analysis of operational geomagnetic storm forecasts as well, for example at the SIDC<sup>5</sup>.

<sup>3</sup>Numbers according to NASA's COHWeb documentation: [https://omniweb.gsfc.nasa.gov/coho/html/cw\\_data.html](https://omniweb.gsfc.nasa.gov/coho/html/cw_data.html)

<sup>4</sup>False alarm rate – not to be confused with false alarm ratio.

<sup>5</sup>SIDC's Verification Analysis of the SIDC Forecast website: [http://sidc.be/forecastverification/K\\_index\\_storm\\_5+.php](http://sidc.be/forecastverification/K_index_storm_5+.php)

## A.8 Lognormal distribution

This is a brief description of the lognormal probability distribution. The lognormal distribution is the distribution of a random variable  $X$  if the logarithm of  $X$  conforms to a normal distribution (Bronstein et al. 2000, p. 780). Its shape is highly asymmetric, however the Gaussian bell curve is recognizable in a semi-log plot, see Figure A.3. Its probability density function is

$$f(x) = \frac{1}{\sigma \sqrt{2\pi}x} e^{-\frac{(\ln x - \mu)^2}{2\sigma^2}}, \quad (\text{A.13})$$

with the location ( $\mu$ ) and the shape parameter ( $\sigma$ ). Changes in  $\mu$  affect both the horizontal and vertical scaling of the function, whereas  $\sigma$  has an influence on its shape, see the graphs with different  $\mu$  and  $\sigma$  in Figure A.4.

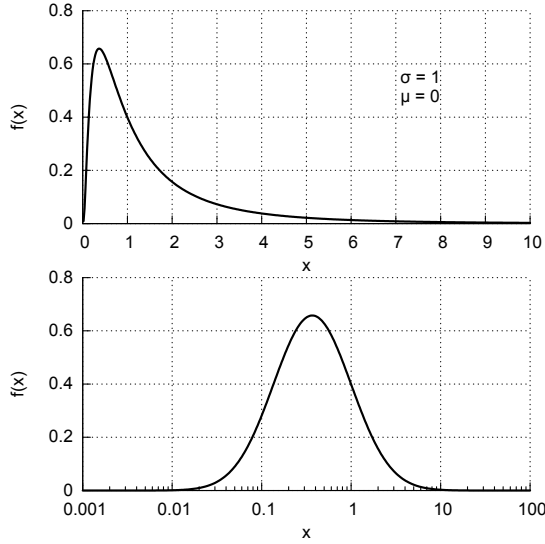


**Figure A.3** Lognormal probability density function plotted in a linear (top panel) and semi-log (bottom panel) way. Both distributions have the parameters  $\sigma = 1$  and  $\mu = 0$ .

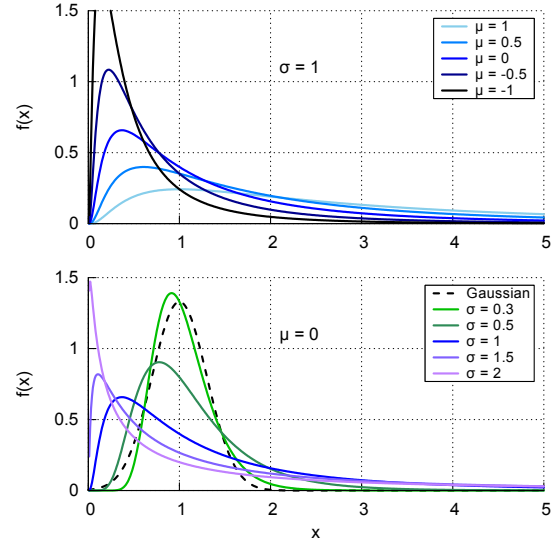


**Figure A.4** Sets of five different lognormal distributions plotted with a fixed  $\sigma$  (top panel) and a fixed  $\mu$  (bottom panel). The Gaussian curve is drawn for comparison.

A lognormal distribution adheres to the general properties noted in the following. As it is a probability distribution, its area is normalized:

$$\int_0^{\infty} f(x) dx = 1.$$

For a lognormally distributed random variable, the geometric moments mean, standard deviation, and variance are calculated from:

$$\mu_g = e^{\mu}, \quad \sigma_g = e^{\sigma}, \quad \text{var}_g = e^{\sigma^2}.$$

Whereas its arithmetic moments are derived from:

$$\mu_a = e^{\mu + \frac{\sigma^2}{2}}, \quad \sigma_a = e^{\mu + \frac{\sigma^2}{2}} (e^{\sigma^2} - 1), \quad \text{var}_a = \sigma_a^2.$$

Further useful characteristics are the positions of the median and the mode:

$$x_{\text{median}} = e^{\mu}, \\ x_{\text{mode}} = e^{\mu - \sigma^2}.$$

Note that for the lognormal distribution its median is equal to its geometric mean. In the limit of  $\sigma \ll 1$  the lognormal shape converges to a Gaussian, see the lower panel of Figure A.4.

Most distributions in nature deviate from the simple Gaussian shape and are to some extent skewed. Indeed, almost all natural quantities which can only be positive are lognormally distributed. Such distributions are found in all fields of sciences (Limpert et al. 2001), for example in biology (size and weight of individuals in populations; species abundance), in medicine (latency periods and survival times of diseases), in social sciences (age of marriage), in linguistics (lengths of words and sentences), in economics (household income), and in geophysics (distribution of mineral resources in the Earth's crust). Obviously measurements of certain solar wind quantities and geomagnetic indices conform to lognormal distributions as well.

## A.9 Acronyms

### List of generic acronyms:

CH	coronal hole
CIR	co-rotating interaction region
CME	coronal mass ejection
<i>Dst</i>	disturbance storm time
DQCS	dipole + quadrupole + current sheet
EUV	extreme ultraviolet
GNSS	global navigation satellite system
GSE	geocentric solar ecliptic
GSM	geocentric solar magnetospheric
HCS	heliospheric current sheet
HGI	heliographic inertial
HMF	heliospheric magnetic field
HPS	heliospheric plasma sheet
HSS	high speed stream
ICME	interplanetary coronal mass ejection
IMF	interplanetary magnetic field
<i>Kp</i>	planetare Kennziffer
MAD	mean absolute deviation
MC	magnetic cloud
MHD	magnetohydrodynamic
MVA	minimum variance analysis
SAR	sum of absolute residuals
SEP	solar energetic particle
SIR	stream interaction region
SSN	sunspot number
TEC	total electron content
TSS	true skill statistic
WSSR	weighted sum of squared residuals

### List of specific acronyms:

ACE	Advanced Composition Explorer
AFFECTS	Advanced Forecast For Ensuring Communications Through Space
AIA	Atmospheric Imaging Assembly
BSS	Bothmer-Schwenn scheme
CAT	CME Analysis Tool
CCMC	Community Coordinated Modeling Center
CDAWeb	Coordinated Data Analysis Web
CEDAR	Coupling, Energetics and Dynamics of Atmospheric Regions
CGAUSS	Coronagraphic German And US SolarProbePlus Survey
DDC	DoomsDayCalculator
DSCOVR	Deep Space Climate Observatory
EVE	EUV Variability Experiment
GCS	Graduated Cylindrical Shell
GFZ	GeoForschungsZentrum
GSFC	Goddard Space Flight Center
HELCATS	Heliographic Cataloging, Analysis and Techniques Service
HMI	Helioseismic Magnetic Imager
IAGA	International Association of Geomagnetism and Aeronomy
ISGI	International Service of Geomagnetic Indices
L1	Lagrange point 1
LASCO	Large Angle and Spectrometric COronagraph
MAG	name of the Magnetometer on the ACE spacecraft
MDI	Michelson Doppler Imager
MMS	Magnetospheric Multiscale
NASA	National Aeronautics and Space Administration
NOAA	National Oceanic and Atmospheric Administration
OMNI	name of the multi-source data set
OPTIMAP	OPerational Tool for Ionospheric Mapping And Prediction
PSP	Parker Solar Probe
ROB	Royal Observatory of Belgium
SDO	Solar Dynamics Observatory
SIDC	Solar Influences Data Center
SOHO	Solar and Heliospheric Observatory
SPDF	Space Physics Data Facility
STEREO	Solar TERrestrial RELations Observatory
SWEPAM	Solar Wind Electron Proton Alpha Monitor
SWPC	Space Weather Prediction Center
SWS	Solar Wind Structures
WDC-SILSO	World Data Center-Sunspot Index and Long-term Solar Observations
WISPR	Wide-field Imager for Solar Probe



## A.10 Astronomical constants

The nominal distance units astronomical unit (au) and solar radius ( $R_{\odot}$ ) are used extensively in this work. The astronomical unit is about the average distance between Earth's perihelion and aphelion. The 2009 Resolution B2 of the International Astronomical Union (IAU) defines it as being exactly  $1 \text{ au} = 149\,597\,870.700 \text{ km}$  (Luzum et al. 2011). The nominal solar radius is the distance from the Sun's center to its photosphere and the IAU 2015 Resolution B3 defines its value exactly as  $1 R_{\odot} = 695\,700 \text{ km}$  (Prša et al. 2016). Thus  $1 \text{ au}$  equals about  $215.0 R_{\odot}$ .

Notable resources for astronomical constants:

- IAU 2009 values and best estimates, IAU Division I Working Group, Numerical Standards for Fundamental Astronomy, Luzum et al. (2011).
- The Astronomical Almanac Online, U.S. Nautical Almanac Office (2017):  
[http://asa.usno.navy.mil/static/files/2016/Astronomical\\_Constants\\_2016.pdf](http://asa.usno.navy.mil/static/files/2016/Astronomical_Constants_2016.pdf)

## References

- Alfvén, H. 1942, *Existence of Electromagnetic-Hydrodynamic Waves*, Nature, 150, 405, [\[DOI\]](#), [\[ADS\]](#).
- Aubry, M. P., Russell, C. T. & Kivelson, M. G. 1970, *Inward motion of the magnetopause before a substorm*, J. Geophys. Res., 75, 7018, [\[DOI\]](#), [\[ADS\]](#).
- Bahcall, J. N., Pinsonneault, M. H. & Wasserburg, G. J. 1995, *Solar models with helium and heavy-element diffusion*, Reviews of Modern Physics, 67, 781, [\[DOI\]](#), [\[ADS\]](#).
- Bala, R. & Reiff, P. 2012, *Improvements in short-term forecasting of geomagnetic activity*, Space Weather, 10, S06001, [\[DOI\]](#), [\[ADS\]](#).
- Bale, S. D., Goetz, K., Harvey, P. R. et al. 2016, *The FIELDS Instrument Suite for Solar Probe Plus. Measuring the Coronal Plasma and Magnetic Field, Plasma Waves and Turbulence, and Radio Signatures of Solar Transients*, Space Sci. Rev., 204, 49, [\[DOI\]](#), [\[ADS\]](#).
- Balogh, A. & Jokipii, J. R. 2009, *The Heliospheric Magnetic Field and Its Extension to the Inner Heliosheath*, Space Sci. Rev., 143, 85, [\[DOI\]](#), [\[ADS\]](#).
- Balogh, A., Bothmer, V., Crooker, N. U. et al. 1999, *The Solar Origin of Corotating Interaction Regions and Their Formation in the Inner Heliosphere*, Space Sci. Rev., 89, 141, [\[DOI\]](#), [\[ADS\]](#).
- Bame, S. J., Asbridge, J. R., Feldman, W. C. & Gosling, J. T. 1977, *Evidence for a structure-free state at high solar wind speeds*, J. Geophys. Res., 82, 1487, [\[DOI\]](#), [\[ADS\]](#).
- Bame, S. J., McComas, D. J., Barraclough, B. L. et al. 1992, *The ULYSSES solar wind plasma experiment*, Astron. Astrophys., Suppl. Ser., 92, 237, [\[ADS\]](#).
- Banaszkiewicz, M., Axford, W. I. & McKenzie, J. F. 1998, *An analytic solar magnetic field model*, Astron. Astrophys., 337, 940, [\[ADS\]](#).
- Bartels, J. 1934, *Twenty-seven day recurrences in terrestrial-magnetic and solar activity, 1923-1933*, Terrestrial Magnetism and Atmospheric Electricity (Journal of Geophysical Research), 39, 201, [\[DOI\]](#), [\[ADS\]](#).
- . 1962, *Zur Vorgeschichte der Weltraumforschung*, Naturwissenschaften, 49, 313, [\[DOI\]](#), [\[ADS\]](#).
- Bartels, J., Heck, N. H. & Johnston, H. F. 1939, *The three-hour-range index measuring geomagnetic activity*, Terrestrial Magnetism and Atmospheric Electricity (Journal of Geophysical Research), 44, 411, [\[DOI\]](#), [\[ADS\]](#).
- Bartels, J. & Veldkamp, J. 1949, *International Data on Magnetic Disturbances, First Quarter, 1949*, J. Geophys. Res., 54, 295, [\[DOI\]](#), [\[ADS\]](#).
- Beck, J. G. 2000, *A comparison of differential rotation measurements - (Invited Review)*, Solar Phys., 191, 47, [\[DOI\]](#), [\[ADS\]](#).
- Biermann, L. 1951, *Kometenschweife und solare Korpuskularstrahlung*, Z. Astrophys., 29, 274, [\[ADS\]](#).
- Billings, D. E. 1959, *Distribution of Matter with Temperature in the Emission Corona.*, Astrophys. J., 130, 961, [\[DOI\]](#), [\[ADS\]](#).
- Borrini, G., Wilcox, J. M., Gosling, J. T., Bame, S. J. & Feldman, W. C. 1981, *Solar wind helium and hydrogen structure near the heliospheric current sheet - A signal of coronal streamers at 1 AU*, J. Geophys. Res., 86, 4565, [\[DOI\]](#), [\[ADS\]](#).
- Bosman, E., Bothmer, V., Nisticò, G. et al. 2012, *Three-Dimensional Properties of Coronal Mass Ejections from STEREO/SECCHI Observations*, Solar Phys., 281, 167, [\[DOI\]](#), [\[ADS\]](#).
- Bothmer, V. & Daglis, I. A. 2007, *Space Weather – Physics and Effects* (Praxis Publishing), [\[ADS\]](#), [\[DOI\]](#).
- Bothmer, V. & Mrotzek, N. 2017, *Comparison of CME and ICME Structures Derived from Remote-Sensing and In Situ Observations*, Solar Phys., 292, 157, [\[DOI\]](#), [\[ADS\]](#).
- Bothmer, V. & Schwenn, R. 1995, *The Interplanetary and Solar Causes of Major Geomagnetic Storms.*, Journal of Geomagnetism and Geoelectricity, 47, 1127, [\[DOI\]](#), [\[ADS\]](#).
- . 1998, *The structure and origin of magnetic clouds in the solar wind*, Annales Geophysicae, 16, 1, [\[DOI\]](#), [\[ADS\]](#).

- Boyle, C. B., Reiff, P. H. & Hairston, M. R. 1997, *Empirical polar cap potentials*, J. Geophys. Res., 102, 111, [\[DOI\]](#), [\[ADS\]](#).
- Bronstein, I. N., Semendjajew, K. A., Musiol, G. & Mühlig, H. 2000, *Taschenbuch der Mathematik* (Verlag Harri Deutsch), [\[link\]](#).
- Burlaga, L., Sittler, E., Mariani, F. & Schwenn, R. 1981, *Magnetic loop behind an interplanetary shock - Voyager, Helios, and IMP 8 observations*, J. Geophys. Res., 86, 6673, [\[DOI\]](#), [\[ADS\]](#).
- Burlaga, L. F. 1984, *MHD processes in the outer heliosphere*, Space Sci. Rev., 39, 255, [\[DOI\]](#), [\[ADS\]](#).
- . 1988, *Magnetic clouds and force-free fields with constant alpha*, J. Geophys. Res., 93, 7217, [\[DOI\]](#), [\[ADS\]](#).
- Burlaga, L. F. & Behannon, K. W. 1982, *Magnetic clouds - Voyager observations between 2 and 4 AU*, Solar Phys., 81, 181, [\[DOI\]](#), [\[ADS\]](#).
- Burlaga, L. F., Goldstein, M. L., McDonald, F. B. & Lazarus, A. J. 1985, *Cosmic ray modulation and turbulent interaction regions near 11 AU*, J. Geophys. Res., 90, 12, [\[DOI\]](#), [\[ADS\]](#).
- Burlaga, L. F., Lepping, R. P., Behannon, K. W. & Klein, L. W. 1984, *Large-scale interplanetary magnetic fields - Voyager 1 and 2 observations between 1 AU and 9.5 AU*, J. Geophys. Res., 89, 10659, [\[DOI\]](#), [\[ADS\]](#).
- Burlaga, L. F., Ness, N. F., Wang, Y.-M. & Sheeley, N. R. 2002, *Heliospheric magnetic field strength and polarity from 1 to 81 AU during the ascending phase of solar cycle 23*, Journal of Geophysical Research (Space Physics), 107, 1410, [\[DOI\]](#), [\[ADS\]](#).
- Cane, H. V. & Richardson, I. G. 2003, *Interplanetary coronal mass ejections in the near-Earth solar wind during 1996-2002*, Journal of Geophysical Research (Space Physics), 108, 1156, [\[DOI\]](#), [\[ADS\]](#).
- Carrington, R. C. 1859, *Description of a Singular Appearance seen in the Sun on September 1, 1859*, Mon. Not. R. Astron. Soc., 20, 13, [\[DOI\]](#), [\[ADS\]](#).
- . 1863, *Observations of the Spots on the Sun from November 9, 1853 to March 24, 1861 made at Redhill* (Williams and Norgate, London), [\[link\]](#).
- Chen, J., Howard, R. A., Brueckner, G. E. et al. 1997, *Evidence of an Erupting Magnetic Flux Rope: LASCO Coronal Mass Ejection of 1997 April 13*, Astrophys. J., Lett., 490, L191, [\[DOI\]](#), [\[ADS\]](#).
- Cho, K.-S., Bong, S.-C., Moon, Y.-J. et al. 2011, *Relationship between multiple type II solar radio bursts and CME observed by STEREO/SECCHI*, Astron. Astrophys., 530, A16, [\[DOI\]](#), [\[ADS\]](#).
- Christensen-Dalsgaard, J., Gough, D. O. & Thompson, M. J. 1991, *The depth of the solar convection zone*, Astrophys. J., 378, 413, [\[DOI\]](#), [\[ADS\]](#).
- Christensen-Dalsgaard, J., Dappen, W., Ajukov, S. V. et al. 1996, *The Current State of Solar Modeling*, Science, 272, 1286, [\[DOI\]](#), [\[ADS\]](#).
- Clark, D. H. & Stephenson, F. R. 1978, *An Interpretation of the Pre-Telescopic Sunspot Records from the Orient*, Quart. J. R. Astron. Soc., 19, 387, [\[ADS\]](#).
- Cliver, E. W., Kahler, S. W., Shea, M. A. & Smart, D. F. 1982, *Injection onsets of 2 GeV protons, 1 MeV electrons, and 100 keV electrons in solar cosmic ray flares*, Astrophys. J., 260, 362, [\[DOI\]](#), [\[ADS\]](#).
- Cliver, E. W., Laurenza, M., Storini, M. & Thompson, B. J. 2005, *On the Origins of Solar EIT Waves*, Astrophys. J., 631, 604, [\[DOI\]](#), [\[ADS\]](#).
- Coleman, Jr., P. J., Smith, E. J., Davis, Jr., L. & Jones, D. E. 1969, *The radial dependence of the interplanetary magnetic field: 1.0-1.5 AU*, J. Geophys. Res., 74, 2826, [\[DOI\]](#), [\[ADS\]](#).
- Cortie, A. L. 1912, *Sun-spots and terrestrial magnetic phenomena, 1898-1911*, Mon. Not. R. Astron. Soc., 73, 52, [\[DOI\]](#), [\[ADS\]](#).
- Coxon, J. C., Milan, S. E., Clausen, L. B. N., Anderson, B. J. & Korth, H. 2014, *The magnitudes of the regions 1 and 2 Birkeland currents observed by AMPERE and their role in solar wind-magnetosphere-ionosphere coupling*, Journal of Geophysical Research (Space Physics), 119, 9804, [\[DOI\]](#), [\[ADS\]](#).
- Cranmer, S. R., Gibson, S. E. & Riley, P. 2017, *Origins of the Ambient Solar Wind: Implications for Space Weather*, Space Sci. Rev., 212, 1345, [\[DOI\]](#), [\[ADS\]](#).
- Cranmer, S. R. & van Ballegoijen, A. A. 2005, *On the Generation, Propagation, and Reflection of Alfvén Waves from the Solar Photosphere to the Distant Heliosphere*, Astrophys. J., Suppl. Ser., 156, 265, [\[DOI\]](#), [\[ADS\]](#).

- Cremades, H. & Bothmer, V. 2004, *On the three-dimensional configuration of coronal mass ejections*, *Astron. Astrophys.*, 422, 307, [DOI], [ADS].
- Crooker, N. U., Huang, C.-L., Lamassa, S. M. et al. 2004, *Heliospheric plasma sheets*, *Journal of Geophysical Research (Space Physics)*, 109, A03107, [DOI], [ADS].
- Danziger, I. J. 1970, *The Cosmic Abundance of Helium*, *Ann. Rev. Astron. Astrophys.*, 8, 161, [DOI], [ADS].
- Davies, K. 1990, *Ionospheric Radio* (Institution of Engineering and Technology), [link], [DOI].
- de Keyser, J., Dunlop, M. W., Owen, C. J. et al. 2005, *Magnetopause and Boundary Layer*, *Space Sci. Rev.*, 118, 231, [DOI], [ADS].
- Detman, T. & Joselyn, J. 1999, *Real-time Kp predictions from ACE real time solar wind*, in *American Institute of Physics Conference Series*, Vol. 471, American Institute of Physics Conference Series, ed. S. R. Habbal, R. Esser, J. V. Hollweg, & P. A. Isenberg, 729–732, [ADS].
- Doswell, III, C. A., Davies-Jones, R. & Keller, D. L. 1990, *On Summary Measures of Skill in Rare Event Forecasting Based on Contingency Tables*, *Weather and Forecasting*, 5, 576, [DOI], [ADS].
- Dungey, J. W. 1961, *Interplanetary Magnetic Field and the Auroral Zones*, *Physical Review Letters*, 6, 47, [DOI], [ADS].
- . 1963, *The structure of the exosphere or advances in velocity space*, ed. C. DeWitt, J. Hieblot, & A. Lebeau, *Geophysics: The Earth's Environment* (Gordon and Breach, New York), 505–550, [ADS].
- Elliott, H. A., Jahn, J.-M. & McComas, D. J. 2013, *The Kp index and solar wind speed relationship: Insights for improving space weather forecasts*, *Space Weather*, 11, 339, [DOI], [ADS].
- Exarhos, G. & Moussas, X. 2000, *An estimation of the shape and temporal variation of the solar wind sonic, Alfvénic and fast magnetosonic surfaces*, *Astron. Astrophys.*, 356, 315, [ADS].
- Fairfield, D. H. 1971, *Average and unusual locations of the Earth's magnetopause and bow shock*, *J. Geophys. Res.*, 76, 6700, [DOI], [ADS].
- Fairfield, D. H. & Cahill, Jr., L. J. 1966, *Transition region magnetic field and polar magnetic disturbances*, *J. Geophys. Res.*, 71, 155, [DOI], [ADS].
- Feldman, W. C., Asbridge, J. R., Bame, S. J. & Gosling, J. T. 1978, *Long-term variations of selected solar wind properties - IMP 6, 7, and 8 results*, *J. Geophys. Res.*, 83, 2177, [DOI], [ADS].
- Fisher, R. R. & Munro, R. H. 1984, *Coronal transient geometry. I - The flare-associated event of 1981 March 25*, *Astrophys. J.*, 280, 428, [DOI], [ADS].
- Forbush, S. E. 1937, *On the Effects in Cosmic-Ray Intensity Observed During the Recent Magnetic Storm*, *Physical Review*, 51, 1108, [DOI], [ADS].
- Fox, N. J., Velli, M. C., Bale, S. D. et al. 2015, *The Solar Probe Plus Mission: Humanity's First Visit to Our Star*, *Space Sci. Rev.*, [DOI], [ADS].
- Gary, G. A. 2001, *Plasma Beta above a Solar Active Region: Rethinking the Paradigm*, *Solar Phys.*, 203, 71, [DOI], [ADS].
- Goelzer, M. L., Schwadron, N. A. & Smith, C. W. 2014, *An analysis of Alfvén radius based on sunspot number from 1749 to today*, *Journal of Geophysical Research (Space Physics)*, 119, 115, [DOI], [ADS].
- Gold, T. 1959, *Motions in the Magnetosphere of the Earth*, *J. Geophys. Res.*, 64, 1219, [DOI], [ADS].
- . 1962, *Magnetic Storms*, *Space Sci. Rev.*, 1, 100, [DOI], [ADS].
- Gonzalez, W. D., Joselyn, J. A., Kamide, Y. et al. 1994, *What is a geomagnetic storm?*, *J. Geophys. Res.*, 99, 5771, [DOI], [ADS].
- Gopalswamy, N. 2016, *History and development of coronal mass ejections as a key player in solar terrestrial relationship*, *Geoscience Letters*, 3, 8, [DOI], [ADS].
- Gopalswamy, N., Akiyama, S., Yashiro, S. & Mäkelä, P. 2010, *Coronal Mass Ejections from Sunspot and Non-Sunspot Regions*, *Astrophysics and Space Science Proceedings*, 19, 289, [DOI], [ADS].
- Gopalswamy, N., Akiyama, S., Yashiro, S. et al. 2014, *Anomalous expansion of coronal mass ejections during solar cycle 24 and its space weather implications*, *Geophys. Res. Lett.*, 41, 2673, [DOI], [ADS].
- Gopalswamy, N., Yashiro, S., Liu, Y. et al. 2005, *Coronal mass ejections and other extreme characteristics of the 2003 October-November solar eruptions*, *Journal of Geophysical Research (Space Physics)*, 110, A09S15, [DOI], [ADS].

- Gosling, J. T. 1993, *The solar flare myth*, J. Geophys. Res., 98, 18937, [DOI], [ADS].
- Gosling, J. T., Baker, D. N., Bame, S. J. & Zwickl, R. D. 1986, *Bidirectional solar wind electron heat flux and hemispherically symmetric polar rain*, J. Geophys. Res., 91, 11352, [DOI], [ADS].
- Gosling, J. T., Hildner, E., MacQueen, R. M. et al. 1974, *Mass ejections from the sun - A view from SKYLAB*, J. Geophys. Res., 79, 4581, [DOI], [ADS].
- Gosling, J. T., Hundhausen, A. J., Pizzo, V. & Asbridge, J. R. 1972, *Compressions and rarefactions in the solar wind: Vela 3*, J. Geophys. Res., 77, 5442, [DOI], [ADS].
- Gosling, J. T., Pizzo, V. & Bame, S. J. 1973, *Anomalous low proton temperatures in the solar wind following interplanetary shock waves—evidence for magnetic bottles?*, J. Geophys. Res., 78, 2001, [DOI], [ADS].
- Gosling, J. T. & Pizzo, V. J. 1999, *Formation and Evolution of Corotating Interaction Regions and their Three Dimensional Structure*, Space Sci. Rev., 89, 21, [DOI], [ADS].
- Gringauz, K. I., Bezrokhikh, V. V., Ozerov, V. D. & Rybchinskii, R. E. 1960, *A Study of the Interplanetary Ionized Gas, High-Energy Electrons and Corpuscular Radiation from the Sun by Means of the Three-Electrode Trap for Charged Particles on the Second Soviet Cosmic Rocket*, Soviet Physics Doklady, 5, 361, [ADS].
- Gurnett, D. A., Kurth, W. S., Burlaga, L. F. & Ness, N. F. 2013, *In Situ Observations of Interstellar Plasma with Voyager 1*, Science, 341, 1489, [DOI], [ADS].
- Hanssen, A. W. & Kuipers, W. J. A. 1965, *On the Relationship Between the Frequency of Rain and Various Meteorological Parameters: (With reference to the problem of objective forecasting)* (Staatsdrukkerij- en Uitgeverijbedrijf, 'S-Gravenhage), 72, [link].
- Hapgood, M. A. 1992, *Space physics coordinate transformations - A user guide*, Planet. Space Sci., 40, 711, [DOI], [ADS].
- Hathaway, D. H. 2015, *The Solar Cycle*, Living Reviews in Solar Physics, 12, 4, [DOI], [ADS].
- Hathaway, D. H. & Upton, L. A. 2016, *Predicting the amplitude and hemispheric asymmetry of solar cycle 25 with surface flux transport*, Journal of Geophysical Research (Space Physics), 121, 10, [DOI], [ADS].
- Hellinger, P., Trávníček, P. M., Štverák, Š., Matteini, L. & Velli, M. 2013, *Proton thermal energetics in the solar wind: Helios reloaded*, Journal of Geophysical Research (Space Physics), 118, 1351, [DOI], [ADS].
- Hildner, E., Gosling, J. T., MacQueen, R. M. et al. 1976, *Frequency of coronal transients and solar activity*, Solar Phys., 48, 127, [DOI], [ADS].
- Holappa, L., Mursula, K. & Asikainen, T. 2014, *A new method to estimate annual solar wind parameters and contributions of different solar wind structures to geomagnetic activity*, Journal of Geophysical Research (Space Physics), 119, 9407, [DOI], [ADS].
- Hollweg, J. V. 1985, *Energy and Momentum Transport by Waves in the Solar Atmosphere*, in Advances in Space Plasma Physics, ed. W. Grossmann, E. M. Campbell, & B. Buti, 77, [ADS].
- Hollweg, J. V. & Isenberg, P. A. 2002, *Generation of the fast solar wind: A review with emphasis on the resonant cyclotron interaction*, Journal of Geophysical Research (Space Physics), 107, 1147, [DOI], [ADS].
- Hughes, W. J. 1995, *Chapter 9: The magnetopause, magnetotail, and magnetic reconnection*, ed. M. Kivelson & C. Russell, Introduction to Space Physics (Cambridge University Press, Cambridge), 227–287, [ADS].
- Hundhausen, A. J. 1977, *An interplanetary view of coronal holes.*, in Coronal Holes and High Speed Wind Streams, ed. J. B. Zirker, 225–329, [ADS].
- Hundhausen, A. J., Sawyer, C. B., House, L., Illing, R. M. E. & Wagner, W. J. 1984, *Coronal mass ejections observed during the solar maximum mission - Latitude distribution and rate of occurrence*, J. Geophys. Res., 89, 2639, [DOI], [ADS].
- Huttunen, K. & Koskinen, H. 2004, *Importance of post-shock streams and sheath region as drivers of intense magnetospheric storms and high-latitude activity*, Annales Geophysicae, 22, 1729, [DOI], [ADS].
- Joint Committee for Guides in Metrology. 2008, *JCGM 100: Evaluation of Measurement Data - Guide to the Expression of Uncertainty in Measurement*, Tech. rep., JCGM, [link].
- Jokipii, J. R. & Thomas, B. 1981, *Effects of drift on the transport of cosmic rays. IV - Modulation by a wavy interplanetary current sheet*, Astrophys. J., 243, 1115, [DOI], [ADS].
- Jones, G. H., Balogh, A. & Smith, E. J. 2003, *Solar magnetic field reversal as seen at Ulysses*, Geophys. Res. Lett., 30, 8028, [DOI], [ADS].



- Kahler, S. W., Hildner, E. & Van Hollebeke, M. A. I. 1978, *Prompt solar proton events and coronal mass ejections*, Solar Phys., 57, 429, [DOI], [ADS].
- Kasper, J. C., Stevens, M. L., Korreck, K. E. et al. 2012, *Evolution of the Relationships between Helium Abundance, Minor Ion Charge State, and Solar Wind Speed over the Solar Cycle*, Astrophys. J., 745, 162, [DOI], [ADS].
- Kasper, J. C., Abiad, R., Austin, G. et al. 2016, *Solar Wind Electrons Alphas and Protons (SWEAP) Investigation: Design of the Solar Wind and Coronal Plasma Instrument Suite for Solar Probe Plus*, Space Sci. Rev., 204, 131, [DOI], [ADS].
- Katsikas, V., Exarhos, G. & Moussas, X. 2010, *Study of the solar Slow Sonic, Alfvén and Fast Magnetosonic transition surfaces*, Advances in Space Research, 46, 382, [DOI], [ADS].
- Kilpua, E. K. J., Madjarska, M. S., Karna, N. et al. 2016, *Sources of the Slow Solar Wind During the Solar Cycle 23/24 Minimum*, Solar Phys., 291, 2441, [DOI], [ADS].
- King, J. H. & Papitashvili, N. E. 2005, *Solar wind spatial scales in and comparisons of hourly Wind and ACE plasma and magnetic field data*, Journal of Geophysical Research (Space Physics), 110, 2104, [DOI], [ADS].
- Kivelson, M. G. & Russell, C. T. 1995, *Introduction to Space Physics* (Cambridge University Press, Cambridge), 586, [ADS].
- Klimchuk, J. A. 2006, *On Solving the Coronal Heating Problem*, Solar Phys., 234, 41, [DOI], [ADS].
- Kojima, M., Fujiki, K., Ohmi, T. et al. 1999, *Low-speed solar wind from the vicinity of solar active regions*, J. Geophys. Res., 104, 16993, [DOI], [ADS].
- Kraaikamp, E. & Verbeeck, C. 2015, *Solar Demon - an approach to detecting flares, dimmings, and EUV waves on SDO/AIA images*, Journal of Space Weather and Space Climate, 5, A18, [DOI], [ADS].
- Krieger, A. S., Timothy, A. F. & Roelof, E. C. 1973, *A Coronal Hole and Its Identification as the Source of a High Velocity Solar Wind Stream*, Solar Phys., 29, 505, [DOI], [ADS].
- Landi, E., Alexander, R. L., Gruesbeck, J. R. et al. 2012, *Carbon Ionization Stages as a Diagnostic of the Solar Wind*, Astrophys. J., 744, 100, [DOI], [ADS].
- Lem, S. & Kandel, M. 1984, *His Master's Voice* (Houghton Mifflin Harcourt), [link].
- Liebenberg, D. H., Bessey, R. J. & Watson, B. 1975, *Coronal emission line profile observations at total solar eclipses. II - 30 May 1965 results, deconvolution and interpretation*, Solar Phys., 44, 345, [DOI], [ADS].
- Limpert, E., Stahel, W. A. & Abbt, M. 2001, *Log-normal Distributions across the Sciences: Keys and Clues: On the charms of statistics, and how mechanical models resembling gambling machines offer a link to a handy way to characterize log-normal distributions, which can provide deeper insight into variability and probability—normal or log-normal: That is the question*, BioScience, 51, 341, [DOI], [link].
- Lockwood, M. 2013, *Reconstruction and Prediction of Variations in the Open Solar Magnetic Flux and Interplanetary Conditions*, Living Reviews in Solar Physics, 10, 4, [DOI], [ADS].
- Luhmann, J. G., Ledvina, S. A. & Russell, C. T. 2004, *Induced magnetospheres*, Advances in Space Research, 33, 1905, [DOI], [ADS].
- Luhmann, J. G., Walker, R. J., Russell, C. T. et al. 1984, *Patterns of potential magnetic field merging sites on the dayside magnetopause*, J. Geophys. Res., 89, 1739, [DOI], [ADS].
- Luzum, B., Capitaine, N., Fienga, A. et al. 2011, *The IAU 2009 system of astronomical constants: the report of the IAU working group on numerical standards for Fundamental Astronomy*, Celestial Mechanics and Dynamical Astronomy, 110, 293, [DOI], [ADS].
- Machol, J. L., Reinard, A. A., Viereck, R. A. & Biesecker, D. A. 2013, *Identification and replacement of proton-contaminated real-time ACE solar wind measurements*, Space Weather, 11, 434, [DOI], [ADS].
- MacQueen, R. M. 1980, *Coronal transients - A summary*, Philosophical Transactions of the Royal Society of London Series A, 297, 605, [DOI], [ADS].
- MacQueen, R. M., Eddy, J. A., Gosling, J. T. et al. 1974, *The Outer Solar Corona as Observed from Skylab: Preliminary Results*, Astrophys. J., Lett., 187, L85, [DOI], [ADS].
- Madjarska, M. S., Doyle, J. G. & van Driel-Gesztelyi, L. 2004, *Evidence of Magnetic Reconnection along Coronal Hole Boundaries*, Astrophys. J., Lett., 603, L57, [DOI], [ADS].

- Manoharan, P. K., Gopalswamy, N., Yashiro, S. et al. 2004, *Influence of coronal mass ejection interaction on propagation of interplanetary shocks*, Journal of Geophysical Research (Space Physics), 109, A06109, [DOI], [ADS].
- Mariani, F., Ness, N. F., Burlaga, L. F., Bavassano, B. & Villante, U. 1978, *The large-scale structure of the interplanetary magnetic field between 1 and 0.3 AU during the primary mission of HELIOS 1*, J. Geophys. Res., 83, 5161, [DOI], [ADS].
- Marubashi, K. 1997, *Interplanetary magnetic flux ropes and solar filaments*, Washington DC American Geophysical Union Geophysical Monograph Series, 99, 147, [DOI], [ADS].
- Marubashi, K., Akiyama, S., Yashiro, S. et al. 2015, *Geometrical Relationship Between Interplanetary Flux Ropes and Their Solar Sources*, Solar Phys., 290, 1371, [DOI], [ADS].
- Marubashi, K. & Lepping, R. P. 2007, *Long-duration magnetic clouds: a comparison of analyses using torus- and cylinder-shaped flux rope models*, Annales Geophysicae, 25, 2453, [DOI], [ADS].
- Maunder, E. W. 1890, *Prof. Spoerer's researches on Sun-spots*, Mon. Not. R. Astron. Soc., 50, 251, [DOI], [ADS].
- . 1904, *Note on the distribution of sun-spots in heliographic latitude, 1874-1902*, Mon. Not. R. Astron. Soc., 64, 747, [DOI], [ADS].
- Mays, M. L., Taktakishvili, A., Pulkkinen, A. et al. 2015, *Ensemble Modeling of CMEs Using the WSA-ENLIL+Cone Model*, Solar Phys., 290, 1775, [DOI], [ADS].
- McComas, D. J., Bame, S. J., Barker, P. et al. 1998, *Solar Wind Electron Proton Alpha Monitor (SWEPAM) for the Advanced Composition Explorer*, Space Sci. Rev., 86, 563, [DOI], [ADS].
- McComas, D. J., Ebert, R. W., Elliott, H. A. et al. 2008a, *Weaker solar wind from the polar coronal holes and the whole Sun*, Geophys. Res. Lett., 35, L18103, [DOI], [ADS].
- McComas, D. J., Velli, M., Lewis, W. S. et al. 2007, *Understanding coronal heating and solar wind acceleration: Case for in situ near-Sun measurements*, Reviews of Geophysics, 45, RG1004, [DOI], [ADS].
- McComas, D. J., Acton, L. W., Balat-Pichelin, M. et al. 2008b, *Solar Probe Plus: Report of the Science and Technology Definition Team*, Tech. Rep. NASA/TM-2008-214161, National Aeronautics and Space Administration, Goddard Space Flight Center, Greenbelt, MD, [link].
- McComas, D. J., Alexashov, D., Bzowski, M. et al. 2012, *The Heliosphere's Interstellar Interaction: No Bow Shock*, Science, 336, 1291, [DOI], [ADS].
- McComas, D. J., Alexander, N., Angold, N. et al. 2016, *Integrated Science Investigation of the Sun (ISIS): Design of the Energetic Particle Investigation*, Space Sci. Rev., 204, 187, [DOI], [ADS].
- McGregor, S. L., Hughes, W. J., Arge, C. N., Odstrcil, D. & Schwadron, N. A. 2011a, *The radial evolution of solar wind speeds*, Journal of Geophysical Research (Space Physics), 116, A03106, [DOI], [ADS].
- McGregor, S. L., Hughes, W. J., Arge, C. N., Owens, M. J. & Odstrcil, D. 2011b, *The distribution of solar wind speeds during solar minimum: Calibration for numerical solar wind modeling constraints on the source of the slow solar wind*, Journal of Geophysical Research (Space Physics), 116, A03101, [DOI], [ADS].
- Merkin, V. G., Lyon, J. G. & Claudepierre, S. G. 2013, *Kelvin-Helmholtz instability of the magnetospheric boundary in a three-dimensional global MHD simulation during northward IMF conditions*, Journal of Geophysical Research (Space Physics), 118, 5478, [DOI], [ADS].
- Miesch, M. S. 2005, *Large-Scale Dynamics of the Convection Zone and Tachocline*, Living Reviews in Solar Physics, 2, 1, [DOI], [ADS].
- Milan, S. E. 2009, *Both solar wind-magnetosphere coupling and ring current intensity control of the size of the auroral oval*, Geophys. Res. Lett., 36, L18101, [DOI], [ADS].
- Milan, S. E., Provan, G. & Hubert, B. 2007, *Magnetic flux transport in the Dungey cycle: A survey of daytime and nighttime reconnection rates*, Journal of Geophysical Research (Space Physics), 112, A01209, [DOI], [ADS].
- Moore, F. R. 1977, *Geomagnetic Disturbance and the Orientation of Nocturnally Migrating Birds*, Science, 196, 682, [DOI], [ADS].
- Ness, N. F. 1970, *Magnetometers for Space Research*, Space Sci. Rev., 11, 459, [DOI], [ADS].
- Ness, N. F. & Wilcox, J. M. 1965, *Sector Structure of the Quiet Interplanetary Magnetic Field*, Science, 148, 1592, [DOI], [ADS].

- Neugebauer, M. & Snyder, C. W. 1966, *Mariner 2 Observations of the Solar Wind, 1, Average Properties*, J. Geophys. Res., 71, 4469, [DOI], [ADS].
- Newell, P. T., Sotirelis, T., Liou, K., Meng, C.-I. & Rich, F. J. 2007, *A nearly universal solar wind-magnetosphere coupling function inferred from 10 magnetospheric state variables*, Journal of Geophysical Research (Space Physics), 112, A01206, [DOI], [ADS].
- Newell, P. T., Sotirelis, T., Liou, K. & Rich, F. J. 2008, *Pairs of solar wind-magnetosphere coupling functions: Combining a merging term with a viscous term works best*, Journal of Geophysical Research (Space Physics), 113, A04218, [DOI], [ADS].
- Opher, M., Drake, J. F., Swisdak, M. et al. 2011, *Is the Magnetic Field in the Heliosheath Laminar or a Turbulent Sea of Bubbles?*, Astrophys. J., 734, 71, [DOI], [ADS].
- Opher, M., Drake, J. F., Zieger, B. & Gombosi, T. I. 2015, *Magnetized Jets Driven By the Sun: the Structure of the Heliosphere Revisited*, Astrophys. J., Lett., 800, L28, [DOI], [ADS].
- Ossendrijver, M. 2003, *The solar dynamo*, Astron. Astrophys. Rev., 11, 287, [DOI], [ADS].
- Otto, A. & Nykyri, K. 2003, *Kelvin-Helmholtz instability and magnetic reconnection: Mass transport at the LLBL*, Washington DC American Geophysical Union Geophysical Monograph Series, 133, 53, [DOI], [ADS].
- Owens, M. J. & Forsyth, R. J. 2013, *The Heliospheric Magnetic Field*, Living Reviews in Solar Physics, 10, 5, [DOI], [ADS].
- Owens, M. J., Merkin, V. G. & Riley, P. 2006, *A kinematically distorted flux rope model for magnetic clouds*, Journal of Geophysical Research (Space Physics), 111, A03104, [DOI], [ADS].
- Pagel, A. C., Crooker, N. U., Zurbuchen, T. H. & Gosling, J. T. 2004, *Correlation of solar wind entropy and oxygen ion charge state ratio*, Journal of Geophysical Research (Space Physics), 109, A01113, [DOI], [ADS].
- Parker, E. N. 1958, *Dynamics of the Interplanetary Gas and Magnetic Fields.*, Astrophys. J., 128, 664, [DOI], [ADS].
- Perreault, P. & Akasofu, S.-I. 1978, *A study of geomagnetic storms*, Geophysical Journal, 54, 547, [DOI], [ADS].
- Phan, T. D., Escoubet, C. P., Rezeau, L. et al. 2005, *Magnetopause Processes*, Space Sci. Rev., 118, 367, [DOI], [ADS].
- Pizzo, V., Millward, G., Parsons, A. et al. 2011, *Wang-Sheeley-Arge-Enlil Cone Model Transitions to Operations*, Space Weather, 9, 03004, [DOI], [ADS].
- Pizzo, V. J. 1991, *The evolution of corotating stream fronts near the ecliptic plane in the inner solar system. II - Three-dimensional tilted-dipole fronts*, J. Geophys. Res., 96, 5405, [DOI], [ADS].
- Planck Collaboration, Ade, P. A. R., Aghanim, N. et al. 2016, *Planck 2015 results. XIII. Cosmological parameters*, Astron. Astrophys., 594, A13, [DOI], [ADS].
- Prša, A., Harmanec, P., Torres, G. et al. 2016, *Nominal Values for Selected Solar and Planetary Quantities: IAU 2015 Resolution B3*, Astron. J., 152, 41, [DOI], [ADS].
- Pulkkinen, P. & Tuominen, I. 1998, *Velocity structures from sunspot statistics in cycles 10 to 22. I. Rotational velocity*, Astron. Astrophys., 332, 748, [ADS].
- Richardson, I. G. & Cane, H. V. 2012, *Near-earth solar wind flows and related geomagnetic activity during more than four solar cycles (1963-2011)*, Journal of Space Weather and Space Climate, 2, A2, [DOI], [ADS].
- Richardson, I. G., Cliver, E. W. & Cane, H. V. 2000, *Sources of geomagnetic activity over the solar cycle: Relative importance of coronal mass ejections, high-speed streams, and slow solar wind*, J. Geophys. Res., 105, 18203, [DOI], [ADS].
- Riley, P. & Richardson, I. G. 2013, *Using Statistical Multivariable Models to Understand the Relationship Between Interplanetary Coronal Mass Ejecta and Magnetic Flux Ropes*, Solar Phys., 284, 217, [DOI], [ADS].
- Rosenbauer, H., Schwenn, R., Marsch, E. et al. 1977, *A survey on initial results of the HELIOS plasma experiment*, Journal of Geophysics Zeitschrift Geophysik, 42, 561, [ADS].
- Rotter, T., Veronig, A. M., Temmer, M. & Vršnak, B. 2012, *Relation Between Coronal Hole Areas on the Sun and the Solar Wind Parameters at 1 AU*, Solar Phys., 281, 793, [DOI], [ADS].
- Russell, C. T. 1971, *Geophysical coordinate transformations.*, Cosmic Electrodynamics, 2, 184, [ADS].

- . 2007, *The coupling of the solar wind to the Earth's magnetosphere*, ed. V. Bothmer & I. A. Daglis, Space Weather- Physics and Effects, 103, [\[DOI\]](#), [\[ADS\]](#).
- Russell, C. T., Le, G. & Kuo, H. 1996, *The occurrence rate of flux transfer events*, Advances in Space Research, 18, 197, [\[DOI\]](#), [\[ADS\]](#).
- Russell, C. T. & McPherron, R. L. 1973, *Semiannual variation of geomagnetic activity*, J. Geophys. Res., 78, 92, [\[DOI\]](#), [\[ADS\]](#).
- Russell, C. T., Wang, Y. L. & Raeder, J. 2003, *Possible dipole tilt dependence of dayside magnetopause reconnection*, Geophys. Res. Lett., 30, 1937, [\[DOI\]](#), [\[ADS\]](#).
- Russell, C. T., Mewaldt, R. A., Luhmann, J. G. et al. 2013, *The Very Unusual Interplanetary Coronal Mass Ejection of 2012 July 23: A Blast Wave Mediated by Solar Energetic Particles*, Astrophys. J., 770, 38, [\[DOI\]](#), [\[ADS\]](#).
- Sachdeva, N., Subramanian, P., Vourlidas, A. & Bothmer, V. 2017, *CME Dynamics Using STEREO and LASCO Observations: The Relative Importance of Lorentz Forces and Solar Wind Drag*, Solar Phys., 292, 118, [\[DOI\]](#), [\[ADS\]](#).
- Sánchez Almeida, J., Bonet, J. A., Viticchié, B. & Del Moro, D. 2010, *Magnetic Bright Points in the Quiet Sun*, Astrophys. J., Lett., 715, L26, [\[DOI\]](#), [\[ADS\]](#).
- Sanchez-Diaz, E., Rouillard, A. P., Lavraud, B. et al. 2016, *The very slow solar wind: Properties, origin and variability*, Journal of Geophysical Research (Space Physics), 121, 2830, [\[DOI\]](#), [\[ADS\]](#).
- Savani, N. P., Vourlidas, A., Shiota, D. et al. 2013, *A Plasma  $\beta$  Transition within a Propagating Flux Rope*, Astrophys. J., 779, 142, [\[DOI\]](#), [\[ADS\]](#).
- Savani, N. P., Vourlidas, A., Szabo, A. et al. 2015, *Predicting the magnetic vectors within coronal mass ejections arriving at Earth: 1. Initial architecture*, Space Weather, 13, 374, [\[DOI\]](#), [\[ADS\]](#).
- Savani, N. P., Vourlidas, A., Richardson, I. G. et al. 2017, *Predicting the magnetic vectors within coronal mass ejections arriving at Earth: 2. Geomagnetic response*, Space Weather, 15, 441, [\[DOI\]](#), [\[ADS\]](#).
- Schatten, K. H. & Sofia, S. 1987, *Forecast of an exceptionally large even-numbered solar cycle*, Geophys. Res. Lett., 14, 632, [\[DOI\]](#), [\[ADS\]](#).
- Schatten, K. H., Wilcox, J. M. & Ness, N. F. 1969, *A model of interplanetary and coronal magnetic fields*, Solar Phys., 6, 442, [\[DOI\]](#), [\[ADS\]](#).
- Scheiner, C. 1630, *Rosa Ursina*, [\[ADS\]](#), [\[DOI\]](#).
- Schröder, W., ed. 2004, *Some aspects of the earlier history of solar-terrestrial physics: Zur Entstehung der solar-terrestrischen Physik.*, [\[ADS\]](#).
- Schwenn, R. 1983, *The average solar wind in the inner heliosphere: Structures and slow variations*, in NASA Conference Publication, Vol. 228, NASA Conference Publication, [\[ADS\]](#).
- Schwenn, R. 1990, *Large-Scale Structure of the Interplanetary Medium*, ed. R. Schwenn & E. Marsch, Physics of the Inner Heliosphere I, 99, [\[ADS\]](#).
- Sheeley, N. R., Hakala, W. N. & Wang, Y.-M. 2000, *Detection of coronal mass ejection associated shock waves in the outer corona*, J. Geophys. Res., 105, 5081, [\[DOI\]](#), [\[ADS\]](#).
- Siscoe, G. L. & Huang, T. S. 1985, *Polar cap inflation and deflation*, J. Geophys. Res., 90, 543, [\[DOI\]](#), [\[ADS\]](#).
- Sittler, Jr., E. C. & Guhathakurta, M. 1999, *Semiempirical Two-dimensional MagnetoHydrodynamic Model of the Solar Corona and Interplanetary Medium*, Astrophys. J., 523, 812, [\[DOI\]](#), [\[ADS\]](#).
- Smith, C. W., L'Heureux, J., Ness, N. F. et al. 1998, *The ACE Magnetic Fields Experiment*, Space Sci. Rev., 86, 613, [\[DOI\]](#), [\[ADS\]](#).
- Smith, E. J. 2001, *The heliospheric current sheet*, J. Geophys. Res., 106, 15819, [\[DOI\]](#), [\[ADS\]](#).
- Smith, E. J. & Wolfe, J. H. 1976, *Observations of interaction regions and corotating shocks between one and five AU - Pioneers 10 and 11*, Geophys. Res. Lett., 3, 137, [\[DOI\]](#), [\[ADS\]](#).
- Snyder, C. W., Neugebauer, M. & Rao, U. R. 1963, *The Solar Wind Velocity and Its Correlation with Cosmic-Ray Variations and with Solar and Geomagnetic Activity*, J. Geophys. Res., 68, 6361, [\[DOI\]](#), [\[ADS\]](#).
- Sonnerup, B. U. O. & Cahill, Jr., L. J. 1967, *Magnetopause Structure and Attitude from Explorer 12 Observations*, J. Geophys. Res., 72, 171, [\[DOI\]](#), [\[ADS\]](#).



- Stamper, R., Lockwood, M., Wild, M. N. & Clark, T. D. G. 1999, *Solar causes of the long-term increase in geomagnetic activity*, J. Geophys. Res., 104, 28325, [DOI], [ADS].
- Sterling, A. C., Moore, R. L. & Harra, L. K. 2011, *Lateral Offset of the Coronal Mass Ejections from the X-flare of 2006 December 13 and Its Two Precursor Eruptions*, Astrophys. J., 743, 63, [DOI], [ADS].
- Subramanian, P. & Dere, K. P. 2001, *Source Regions of Coronal Mass Ejections*, Astrophys. J., 561, 372, [DOI], [ADS].
- Subramanian, S., Madjarska, M. S. & Doyle, J. G. 2010, *Coronal hole boundaries evolution at small scales. II. XRT view. Can small-scale outflows at CHBs be a source of the slow solar wind*, Astron. Astrophys., 516, A50, [DOI], [ADS].
- Sugiura, M. & Kamei, T. 1991, *Equatorial Dst Index 1957–1986*, IAGA Bulletin No. 40, [link].
- Temmer, M., Hinterreiter, J. & Reiss, M. A. 2018, *Coronal hole evolution from multi-viewpoint data as input for a STEREO solar wind speed persistence model*, Journal of Space Weather and Space Climate, 8, A18, [DOI], [ADS].
- Temmer, M. & Nitta, N. V. 2015, *Interplanetary Propagation Behavior of the Fast Coronal Mass Ejection on 23 July 2012*, Solar Phys., 290, 919, [DOI], [ADS].
- Temmer, M., Vršnak, B., Rollett, T. et al. 2012, *Characteristics of Kinematics of a Coronal Mass Ejection during the 2010 August 1 CME-CME Interaction Event*, Astrophys. J., 749, 57, [DOI], [ADS].
- Thébault, E., Finlay, C. C., Beggan, C. D. et al. 2015, *International Geomagnetic Reference Field: the 12th generation*, Earth, Planets, and Space, 67, 79, [DOI], [ADS].
- Thernisien, A. F. R., Howard, R. A. & Vourlidas, A. 2006, *Modeling of Flux Rope Coronal Mass Ejections*, Astrophys. J., 652, 763, [DOI], [ADS].
- Thompson, M. J., Christensen-Dalsgaard, J., Miesch, M. S. & Toomre, J. 2003, *The Internal Rotation of the Sun*, Ann. Rev. Astron. Astrophys., 41, 599, [DOI], [ADS].
- Tousey, R. 1973, *The solar corona.*, in Space Research Conference, Vol. 2, Space Research Conference, ed. M. J. Rycroft & S. K. Runcorn, 713–730, [ADS].
- Tsurutani, B. T., Smith, E. J., Gonzalez, W. D., Tang, F. & Akasofu, S. I. 1988, *Origin of interplanetary southward magnetic fields responsible for major magnetic storms near solar maximum (1978-1979)*, J. Geophys. Res., 93, 8519, [DOI], [ADS].
- U.S. Nautical Almanac Office. 2017, *Astronomical Almanac for the Year 2018 and Its Companion, the Astronomical Almanac Online* (U.S. Government Publishing Office), [link].
- Vanselow, K. H., Jacobsen, S., Hall, C. & Garthe, S. 2017, *Solar storms may trigger sperm whale strandings: explanation approaches for multiple strandings in the North Sea in 2016*, International Journal of Astrobiology, 1–9, [DOI].
- Vaquero, J. M. 2007, *Letter to the Editor: Sunspot observations by Theophrastus revisited*, Journal of the British Astronomical Association, 117, 346, [ADS].
- Venzmer, M. S. & Bothmer, V. 2018, *Solar-wind predictions for the Parker Solar Probe orbit. Near-Sun extrapolations derived from an empirical solar-wind model based on Helios and OMNI observations*, Astron. Astrophys., 611, A36, [DOI], [ADS].
- Veselovsky, I. S., Dmitriev, A. V. & Suvorova, A. V. 2010, *Algebra and statistics of the solar wind*, Cosmic Research, 48, 113, [DOI], [ADS].
- Vourlidas, A. 2014, *The flux rope nature of coronal mass ejections*, Plasma Physics and Controlled Fusion, 56, 064001, [DOI], [ADS].
- . 2015, *Mission to the Sun-Earth L<sub>5</sub> Lagrangian Point: An Optimal Platform for Space Weather Research*, Space Weather, 13, 197, [DOI], [ADS].
- Vourlidas, A., Lynch, B. J., Howard, R. A. & Li, Y. 2013, *How Many CMEs Have Flux Ropes? Deciphering the Signatures of Shocks, Flux Ropes, and Prominences in Coronagraph Observations of CMEs*, Solar Phys., 284, 179, [DOI], [ADS].
- Vourlidas, A., Howard, R. A., Plunkett, S. P. et al. 2016, *The Wide-Field Imager for Solar Probe Plus (WISPR)*, Space Sci. Rev., 204, 83, [DOI], [ADS].
- Vršnak, B., Temmer, M. & Veronig, A. M. 2007, *Coronal Holes and Solar Wind High-Speed Streams: I. Forecasting the Solar Wind Parameters*, Solar Phys., 240, 315, [DOI], [ADS].



- Vršnak, B., Temmer, M., Žic, T. et al. 2014, *Heliospheric Propagation of Coronal Mass Ejections: Comparison of Numerical WSA-ENLIL+Cone Model and Analytical Drag-based Model*, *Astrophys. J., Suppl. Ser.*, 213, 21, [\[DOI\]](#), [\[ADS\]](#).
- Wang, Y.-M. 2013, *On the Strength of the Hemispheric Rule and the Origin of Active-region Helicity*, *Astrophys. J., Lett.*, 775, L46, [\[DOI\]](#), [\[ADS\]](#).
- Wang, Y.-M., Sheeley, N. R., Socker, D. G., Howard, R. A. & Rich, N. B. 2000, *The dynamical nature of coronal streamers*, *J. Geophys. Res.*, 105, 25133, [\[DOI\]](#), [\[ADS\]](#).
- Wang, Y.-M. & Sheeley, Jr., N. R. 1990, *Solar wind speed and coronal flux-tube expansion*, *Astrophys. J.*, 355, 726, [\[DOI\]](#), [\[ADS\]](#).
- Wang, Y.-M., Sheeley, Jr., N. R., Walters, J. H. et al. 1998, *Origin of Streamer Material in the Outer Corona*, *Astrophys. J., Lett.*, 498, L165, [\[DOI\]](#), [\[ADS\]](#).
- Webb, D. F. 1991, *The solar cycle variation of the rates of CMEs and related activity*, *Advances in Space Research*, 11, 37, [\[DOI\]](#), [\[ADS\]](#).
- Webb, D. F. & Howard, T. A. 2012, *Coronal Mass Ejections: Observations*, *Living Reviews in Solar Physics*, 9, 3, [\[DOI\]](#), [\[ADS\]](#).
- Webb, D. F. & Hundhausen, A. J. 1987, *Activity associated with the solar origin of coronal mass ejections*, *Solar Phys.*, 108, 383, [\[DOI\]](#), [\[ADS\]](#).
- Weber, E. J. & Davis, Jr., L. 1967, *The Angular Momentum of the Solar Wind*, *Astrophys. J.*, 148, 217, [\[DOI\]](#), [\[ADS\]](#).
- Wilson, R. M. 1987, *Geomagnetic response to magnetic clouds*, *Planet. Space Sci.*, 35, 329, [\[DOI\]](#), [\[ADS\]](#).
- Wing, S., Johnson, J. R., Jen, J. et al. 2005, *Kp forecast models*, *Journal of Geophysical Research (Space Physics)*, 110, A04203, [\[DOI\]](#), [\[ADS\]](#).
- Winterhalter, D., Smith, E. J., Burton, M. E., Murphy, N. & McComas, D. J. 1994, *The heliospheric plasma sheet*, *J. Geophys. Res.*, 99, 6667, [\[DOI\]](#), [\[ADS\]](#).
- Zhang, G. & Burlaga, L. F. 1988, *Magnetic clouds, geomagnetic disturbances, and cosmic ray decreases*, *J. Geophys. Res.*, 93, 2511, [\[DOI\]](#), [\[ADS\]](#).
- Zhang, J., Richardson, I. G., Webb, D. F. et al. 2007, *Solar and interplanetary sources of major geomagnetic storms ( $Dst \leq -100$  nT) during 1996-2005*, *Journal of Geophysical Research (Space Physics)*, 112, A10102, [\[DOI\]](#), [\[ADS\]](#).
- Zhang, Q.-H., Lockwood, M., Foster, J. C. et al. 2015, *Direct observations of the full Dungey convection cycle in the polar ionosphere for southward interplanetary magnetic field conditions*, *Journal of Geophysical Research (Space Physics)*, 120, 4519, [\[DOI\]](#), [\[ADS\]](#).
- Zhao, H. & Zong, Q.-G. 2012, *Seasonal and diurnal variation of geomagnetic activity: Russell-McPherron effect during different IMF polarity and/or extreme solar wind conditions*, *Journal of Geophysical Research (Space Physics)*, 117, A11222, [\[DOI\]](#), [\[ADS\]](#).
- Zhao, J., Bogart, R. S., Kosovichev, A. G., Duvall, Jr., T. L. & Hartlep, T. 2013, *Detection of Equatorward Meridional Flow and Evidence of Double-cell Meridional Circulation inside the Sun*, *Astrophys. J., Lett.*, 774, L29, [\[DOI\]](#), [\[ADS\]](#).
- Zheng, Y., Macneice, P., Odstrcil, D. et al. 2013, *Forecasting propagation and evolution of CMEs in an operational setting: What has been learned*, *Space Weather*, 11, 557, [\[DOI\]](#), [\[ADS\]](#).

## Acknowledgments

There are a number of people I want to thank, without whom the realization and results of my thesis certainly would have been different. First and foremost, I thank my PhD supervisor Volker Bothmer for supervising my doctorate, for letting me work so freely, and for providing helpful discussions and comments. I am grateful to Volker Bothmer and Ansgar Reiners for constituting my advisory committee and also for kindly agreeing to evaluate my work as thesis committee.

My appreciation goes to all members of the Institute for Astrophysics for facilitating such a pleasant work environment. I thank all current and former associates of the space weather group for their friendly company on my way – in particular Jens, Johannes, Niclas, and Giuseppe for our lively discussions, which were every now and then even scientifically motivated ;)

I especially thank my eternal office mates Eckhard, Jonas, and Adam: Eckhard for instantly integrating me at the start of my PhD and the good friendship since, Jonas for the committed debates during the beginning, and Adam for accompanying me through the last difficulties on the way. I am thankful to Giuseppe and Tal for proofreading late drafts of this manuscript and providing helpful comments and suggestions. I acknowledge the office for cozily accommodating me all the long hours, in particular the couch for giving me strength, and the Shadow Worker for guarding the office. I honor the brands Star Wars and LEGO for providing lots of merchandise and distractions.

I am grateful to my family and friends for supporting me at all times. Those who are not mentioned above but deserve it are thanked hereby as well. A shout-out to the Sun for creating the solar wind and harboring all life we know of (yet).